P−P and P−Sb Coordination Chemistry

by

Saurabh Sunil Chitnis
B. Art. Sc., McMaster University, 2010

A Dissertation Submitted in Partial Fulfillment of the
Requirements for the Degree of

DOCTOR OF PHILOSOPHY

in the Department of Chemistry

P−P and P−Sb Coordination Chemistry

by

Saurabh Sunil Chitnis
B. Art. Sc., McMaster University, 2010

Supervisory Committee

Dr. Neil Burford, Supervisor
(Department of Chemistry, University of Victoria)

Dr. Robin G. Hicks, Departmental Member
(Department of Chemistry, University of Victoria)

Dr. J. Scott McIndoe, Departmental Member
(Department of Chemistry, University of Victoria)

Dr. Sadik Dost, Outside Member
(Faculty of Engineering, University of Victoria)

ABSTRACT

Supervisory Committee

Dr. Neil Burford, Supervisor
(Department of Chemistry, University of Victoria)

Dr. Robin G. Hicks, Departmental Member
(Department of Chemistry, University of Victoria)

Dr. J. Scott McIndoe, Departmental Member
(Department of Chemistry, University of Victoria)

Dr. Sadik Dost, Outside Member
(Faculty of Engineering, University of Victoria)

The coordination chemistry of compounds featuring P−P and P−Sb bonds has been investigated to define the fundamental features of bonding in these systems. New reaction methodologies to form P−P bonds have been evolved based on careful consideration of bond strengths in the gas and condensed phase. Insights revealed from systematic studies of molecular structures have been used to augment and expand the scope of existing models for structural prediction (*e.g.* VSEPR theory). Unique classes of *catena*-antimony compounds have been discovered, illustrating a remarkable structural and electronic diversity for this heavy *p*-block metal. Detailed mechanistic examinations have revealed a previously unrecognized mode of ligand activation for phosphine complexes of very electrophilic acceptors. Stable sources of the hitherto unisolated and highly reactive *tris*-triflate reagents, $E(OTf)_3$ (E = P, As, Sb, Bi), have been prepared and their coordination chemistry as Lewis acids and oxidizing agents has been mapped. Collectively, the findings described here span a range of coordination

chemistry paradigms for *p*-block elements that may be broadly applicable across the periodic table. A robust plan has been proposed for applying these insights towards the preparation of fundamentally interesting molecular frameworks and towards new strategies for small molecule activation.

Contents

List of Figures

List of Schemes

List of Tables

ACKNOWLEDGEMENTS

I am greatly indebted to Prof. Neil Burford for the *outstanding* graduate experience that I have enjoyed over the past four and a half years under his supervision. The customary freedom in the Burford group to independently design and manage research projects has significantly enhanced my sense of ownership over the work in this thesis. Neil has also given me a truly enviable opportunity to get involved in all aspects of installing, maintaining and customizing a world-class synthetic laboratory, and I have learned a tremendous amount from working closely with him on writing and reviewing manuscripts. Our frequent discussions on fundamental aspects of main group chemistry have infected me with his deep passion for the subject, and prevented my enthusiasm for research from ever floundering throughout my time in the group. I hope to continue benefiting from his excellent mentorship in the future.

I would also like to thank Prof. Jan J. Weigand and the Weigand group for hosting a very stimulating six month research internship in his lab at Technische Universität - Dresden. The state-of-the-art training I received during this time has given me the confidence to tackle even the most daunting synthetic challenges.

I would like to acknowledge the vital collaboration I have enjoyed with Dr. Robert McDonald and Dr. Michael J. Ferguson at the University of Alberta. Nearly all of the diffraction experiments described in this thesis have been performed by them and their efforts to accommodate my sensitive samples and provide me with high-quality results in a timely fashion are greatly appreciated.

I am grateful for the unwavering financial support from the Government of Canada in the form of numerous undergraduate and graduate research fellowships administered by the Natural Sciences and Engineering Council. In particular, I would like to acknowledge the Vanier Canada Graduate Scholarships program for enabling me to work as a dedicated researcher without demands on my time due to financial considerations. I am cognizant of the responsibilities these taxpayer investments imply and their collective weight inspires me to work harder.

Finally, I am fortunate for having had the constant support of my family and close friends during the last few years. I would like, in particular, to thank past and present members of the Burford and Fyles groups for making every day an enjoyable and laughter-filled adventure. I am happily aware that that a number of friendships forged here will be milestones in the landscape of my life.

LIST OF ABBREVIATIONS AND SYMBOLS

$^\circ$: degree

Å : angstrom

Ar : generic aromatic substituent

AIM : atoms-in-molecules

avg. : average

bipy : 2,2'-bipyridine

Bu : *n*-butyl

cf. : compare

ca. : approximately

CPMAS : cross polarization magic angle spinning

Cy : cyclohexyl

DFT : density functional theory

dmap : 4-dimethylaminopyridine

dmpm : bis(dimethylphosphino)methane

dppe : bis(diphenylphosphino)ethane

dppm : bis(diphenylphosphino)methane

ϵ : dielectric constant

e.g. : for example

Et : ethyl

Et_2O : diethyl ether

FT-IR : fourier-transform infrared spectroscopy

g : grams

HOMO : highest occupied molecular orbital

Hz : hertz

i.e. : that is

% : per cent

^{i}Pr : isopropyl

K : Kelvin

LUMO : lowest unoccupied molecular orbital

m : medium intensity (*in FT-IR*)

m : multiplet (*in NMR*)

m/z : mass-to-charge ratio

Me : methyl

MeCN : acetonitrile

Mes : mesityl (2,4,6,-trimethylphenyl)

NHC : N-heterocyclic carbene

$^n J_{XY}$: *n*-bond coupling between nuclei X and Y

NMR : nuclear magnetic resonance

NPA : natural population analysis

OTf : triflate (trifluoromethanesulfonate)

PCM : polarization continuum model

Ph : phenyl

ppm : parts per million

Pr : *n*-propyl

q : quartet (*in NMR*)

R : generic organic substituent

$\mathbf{r_{(cov)}}$: covalent radius

$\mathbf{r_{(vdW)}}$: van der Waals radius

Σ : sum of

s : singlet (*in NMR*)

s : strong intensity (*in FT-IR*)

tbbipy : 4,4'-^{t}Bu$_2$-2,2'-*bipyridine*

TMS : Me_3Si

t : triplet (*in NMR*)

^{t}**Bu** : *tert*-butyl

vide infra : see below

vide supra : see above

vs. : versus

VSEPR : valence shell electron pair repulsion

VT-NMR : variable temperature NMR

w : weak intensity (*in FT-IR*)

Δ : difference or change in a quantity

Δ**G** : Δ in free energy

Δ**H** : Δ in enthalpy

Δ**S** : Δ in entropy

LIST OF PUBLICATIONS

Research presented in this dissertation has appeared in the following publications:

S. S. Chitnis, B. Peters, E. Conrad, N. Burford, R. McDonald, and M. J. Ferguson, 'Structural Diversity for Phosphine Complexes of Stibenium and Stibinidenium Cations', *Chem. Commun.*, **2010**, *47*, 12331-12333.

S. S. Chitnis, E. MacDonald, N. Burford, U. Werner-Zwanziger, N. Burford, and R. McDonald, 'P-P Menschutkin Preparation of Prototypical Phosphinophosphonium Salts', *Chem. Commun.*, **2012**, *48*, 7359-7361.

E. MacDonald, L. Doyle, S. S. Chitnis, U. Werner-Zwanziger, N. Burford, and A. Decken, 'Me_3P Complexes of P-block Lewis Acids $SnCl_4$, $[SnCl_3]^{1+}$, and $[SnCl_2]^{2+}$', *Chem. Commun.*, **2012**, *48*, 7922-7924.

S. S. Chitnis, N. Burford, and M. J. Ferguson, '2,2-Bipyridine Complexes of Antimony: Sequential Fluoride Ion Abstraction from SbF_3 by Exploiting the Fluoride Ion Affinity of $[Me_3Si]^{1+}$', *Angew. Chem. Int. Ed.*, **2013**, *52*, 4863-4866.

S. S. Chitnis, Y-y. Carpenter, N. Burford, R. McDonald, and M. J. Ferguson, 'Assembly of a cyclo-tetrastibinotetraphosphonium Tetracation by Reductive Elimination', *Angew. Chem. Int. Ed.*, **2013**, *52*, 2042-2045.

S. S. Chitnis, N. Burford, A. Decken, and M. J. Ferguson, 'Coordination Complexes of Bismuth Triflates with THF and Diphosphine Ligands', *Inorg. Chem.*, **2013**, *52*, 7242-7248.

S. S. Chitnis, N. Burford, R. McDonald, and M. J. Ferguson, 'Prototypical Phosphine Complexes of Antimony(III)', *Inorg. Chem.*, **2014**, *53*, 5359-5372.

S. S. Chitnis, J. M. Whalen, and N. Burford, 'Influence of Charge and Coordination Number on Bond Dissociation Energies, Distances and Vibrational Frequencies for the Phosphorus-Phosphorus Bond', *J. Am. Chem. Soc.*, **2014**, *136*, 12498-12506.

S. S. Chitnis, and N. Burford, 'Phosphine Complexes of Lone Pair Bearing Acceptors', *Dalton Trans.*, **2015**, *44*, 17-29.

S. S. Chitnis, A. P. M. Robertson, N. Burford, J. J. Weigand, and R. Fischer, 'Synthesis and Reactivity of Cyclo-tetra(stibinophosphonium) Tetracations: Redox and Coordination Chemistry of Phosphine-Antimony Complexes', *Chem. Sci.*, **2015**, *6*, 2559-2574.

A. P. M. Robertson, S. S. Chitnis, H. A. Jenkins, R. McDonald, M. J. Ferguson, and N. Burford, 'Establishing the Coordination Chemistry of Antimony(V) Cations: Systematic Assessment of $Ph_4Sb(OTf)$ and $Ph_3Sb(OTf)_2$ as Lewis Acceptors', *Chem. Eur. J.*, **2015**, In Press.

"There is no book so bad...that it does not have something good in it."
—Miguel de Cervantes Saavedra, *Don Quixote*

Chapter 1

Introduction

Of the four fundamental forces, electromagnetism is the most relevant to the realm of chemistry, being responsible for attraction or repulsion between charged particles such as protons and electrons. In the practice of synthetic chemistry, this force is codified as the central concept of Lewis acidity and basicity, which provides an overarching framework to predict a vast array of chemical transformations involving spin-paired electrons. This predictability is rooted in the axiom that transfer of electron density to a Lewis acid (A) from a Lewis base (B) forms a chemical bond (—) between two nuclei, yielding the compound (A—B). The following examples illustrate this process:

$$\mathrm{A} + \mathrm{B} \longrightarrow \mathrm{A{-}B} \tag{1.1}$$

$$[\mathrm{H}]^{1+} + [\mathrm{Cl}]^{1-} \longrightarrow \mathrm{H{-}Cl} \tag{1.2}$$

$$[\mathrm{Me}]^{1+} + [\mathrm{Cl}]^{1-} \longrightarrow \mathrm{Me{-}Cl} \tag{1.3}$$

$$[\mathrm{Me}]^{1+} + [\mathrm{Me}]^{1-} \longrightarrow \mathrm{Me{-}Me} \tag{1.4}$$

There is no requirement that A or B have an overall charge as shown in equations $1.2 - 1.4$, since molecules are not fundamental particles with fixed charges, but rather aggregates of fundamental particles that can have induced charge distributions depending upon the myriad aggregation patterns available. Thus neutral molecules may exhibit regions of electron density depletion or accumulation, permitting bond formation by interaction between a region of high density in neutral molecule B with a region of low density in neutral molecule A. Such topological variations in electron

density enable even two positively charged or two negatively charged molecules to engage in bonding. Some examples of bonding involving uncharged or similarly charged A or B are given in equations $1.5 - 1.9$:

$$BH_3 + NH_3 \longrightarrow [H_3B{-}NH_3] \tag{1.5}$$

$$[H]^{1+} + NH_3 \longrightarrow [HNH_3]^{1+} \tag{1.6}$$

$$HF + [F]^{1-} \longrightarrow [FHF]^{1-} \tag{1.7}$$

$$[Cl]^{1-} + [SbCl_4]^{1-} \longrightarrow [ClSbCl_4]^{2-} \tag{1.8}$$

$$[H_3NNH_2]^{1+} + [H]^{1+} \longrightarrow [H_3NNH_3]^{2+} \tag{1.9}$$

As these examples show, the fundamental concept of coordination chemistry, *coordinate bonding*, is a very general one and the study of any bonding interaction that involves transfer of electron density from one centre to another lies within the purview of coordination chemistry. Another concept that is common in the vernacular of coordination chemistry is that of a *coordination complex*, generally referring to a molecule featuring a coordinate bond between a Lewis acid and a Lewis base. Classification of a compound as a coordination complex depends upon the perceived nature of the bond(s) in question and the precise definition of coordinate bonds is a contentious topic. A number of qualifying criteria have been proposed[1] but each has limitations.

For instance, classifying coordinate bonds as being relatively long and weak is difficult since these criteria assume the presence of non-existent standard bond lengths and strengths that may serve as benchmark values. This is particularly problematic for new bonding frameworks for which no prior examples exist or insufficient examples exist to define a standard value. Moreover bond strengths in cationic complexes are often greater than in neutral derivatives, and bond lengths shorter, making cationic coordination complexes difficult to classify using these criteria.

A more convincing indicator is the higher equilibrium constant for heterolytic cleavage over homolytic cleavage for a coordinate bond but experimental values for both dissociation processes are extremely difficult to obtain and compare for the same bond. Often substitution of one neutral functional group (usually a Lewis base) by another (a stronger Lewis base) at an acceptor centre in a putative coordination

complex is interpreted as a preference for heterolytic cleavage. But it is usually unclear whether the displacement is occurring *via* an associative or dissociative mechanism. and this ambiguity is significant since the former offers no information about the equilibrium constant for heterolytic cleavage of the broken bond. This is because the associative transition state features both the outgoing and incoming substituents bound to the acceptor and is a different species altogether than the complex under consideration*. Moreover, in some situations where such ligand exchange can be effectively demonstrated, it is questionable whether such chemistry constitutes a sufficient criterion for defining a coordinate bond because it encompasses species such as phosphine oxides ($R_3P{=}O$), protonated amines ($[R_3N{-}H]^{1+}$), ketones ($R_2C{=}O$), and even fluorophosphonium cations ($[R_3P{-}F]^{1+}$) – compounds that exhibit transfer of atomic oxygen, protons, or fluoronium cations to neutral acceptors under the appropriate conditions.

Thus the coordinate bonding model has come under some criticism[2–5] for wanton application and for being inclusive to the point of absurdity. An extreme example of its application might be to describe the bonding situation in centrosymmetric polyatomic ions such as $[Me_3PPMe_3]^{2+}$, where the indistinguishable nature of fundamental particles means that neither phosphine can be experimentally identified as being the donor or the acceptor. However, it is precisely here that the value of the coordinate model, *as a conceptual tool to enlarge the scope of envisioned reactivity*, becomes evident (Scheme 1.0.1).

The Lewis structure of $[Me_3PPMe_3]^{2+}$ has two identical phosphorus atoms with a positive formal charge at each phosphonium centre. It is known that methyl groups adjacent to cationic phosphonium centres bear acidic protons, since deprotonation yields a compound stabilized by ylidic resonance.[6] Thus looking at just the Lewis structure, one might predict that addition of a base should yield products due to deprotonation of one of the six methyl groups. On the other hand a coordinate bonding model can be used to describe $[Me_3PPMe_3]^{2+}$ as a phosphine-coordinated phosphodiium ($[Me_3P]^{2+}$), and the P-C bonds can also be described as dative interactions between Me_2PPMe_2 or $[Me_3PPMe_2]^{1+}$ and two or one $[CH_3]^{1+}$ cations, respectively. The consequential

*Arguably, *acceptor* rather than *ligand* exchange is a more rigorous criterion to demonstrate heterolytic cleavage since the former precludes any associative mechanism. In this context, a variety of strong and neutral Lewis acids are available, which are ideally suited to assess the possibility of heterolytic cleavage in a coordination complex.

experimental predictions are that the phosphine ligand may be substituted by a more Lewis basic ligand to release free PMe_3 and that the dication should be accessible by methylation of Me_2PPMe_2 or $[Me_3PPMe_2]^{1+}$.

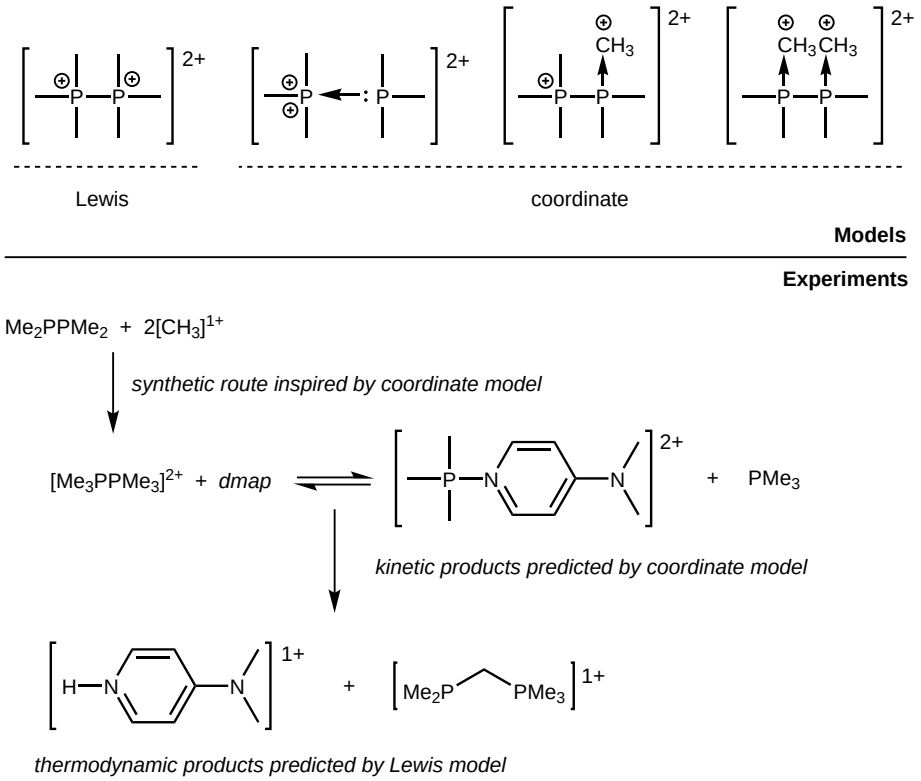

Scheme 1.0.1. Bonding models, synthesis and reactivity of $[Me_3PPMe_3]^{2+}$.

Methylation of phosphine lone pairs in Me_2PPMe_2 to give $[Me_3PPMe_3]^{2+}$ has been confirmed experimentally,[7] and, as described in Chapter 5, addition of *dmap* to a solution of $[Me_3PPMe_3]^{2+}$ immediately gives free PMe_3 and the new species $[(dmap)PMe_3]^{2+}$, consistent with the ligand exchange predicted by the dative model. However after four hours only $[(dmapH)]^{1+}$ and $[Me_2PCH_2PMe_3]^{1+}$ are observed in the reaction mixture, consistent with deprotonation of a methyl group followed by rearrangement, as predicted by using the Lewis model. In this example, the kinetic products are predicted by the dative model, while the thermodynamic products are predicted by using the Lewis model. Neither view single-handedly provides a complete picture of the reactivity of $[Me_3PPMe_3]^{2+}$.

In light of these considerations, it is clear that neither a coordinate nor a Lewis bonding model should be assumed prejudicially as the exclusive descriptor for the

bonding in a compound, but both should be used in conjunction. All models are approximations of natural phenomena and can only be judged by their experimental utility. This thesis therefore deliberately invokes a very broad definition of 'Coordination Chemistry', referencing both the synthetic methodology employed to make a specific bond and the discussion of the resulting compound within the context of established coordination chemistry terminology, particularly where such discussion engenders a unification between main group and transition metal chemistry concepts. This flexible definition predicts, for example, that the hypothetical molecule $[(Me_3P)SbCl_4]^{1+}$ may be accessible by *coordination* of $P^{III}Me_3$ to the $[Sb^{V}Cl_4]^{1+}$ cation and that, in addition to a simple dissociation back into the starting reagents, it may also be susceptible to a *reductive elimination* of $[Me_3P^{V}Cl]^{1+}$ to give $Sb^{III}Cl_3$. The emphasis on such conceptual unification is a deliberate choice, in line with a modern re-envisioning of main group chemistry as not only a source of foundational pedagogical concepts about structure and bonding, but also as a source of stoichiometric and catalytic reagents capable of effecting valuable chemical transformations.[8–11]

The compounds prepared in this thesis are fundamentally interesting because their molecular and electronic structures have important implications for existing theories of structure prediction (*e.g.* VSEPR theory) and chemical bonding. In addition, their reactivity patterns reveal hitherto unrecognized similarities with transition metal coordination chemistry, with consequences for the ongoing development of catalysis platforms derived from main group elements. Finally, the new molecules revealed here represent a logical evolution of structural complexity in inorganic frameworks and the new reaction methodologies used to access them enlarge the toolkit of chemical transformations accessible to the synthetic inorganic chemist.

1.1 The Pnictogen Elements

The elements of group 15 (N, P, As, Sb, Bi) have historically been called the pnictogens, from the ancient Greek word for strangulation, an allusion to the suffocation hazard many of their gaseous compounds present. While not an IUPAC-approved term, the prevalence of 'pnictogens' in the chemical literature makes it the most meaningful and least cumbersome collective noun for the group 15 elements.

The pnictogens exhibit an ns^2np^3 electronic structure and three oxidation states

(+I, +III, and +V) as closed-shell species. Key nuclear properties are collected in Table 1.1.1. A decrease in the Pauling electronegativity and ionization energy values is observed descending the group. One important consequence of these trends is the behaviour of binary pnictogen compounds PnX_3 (X = H or halogen), which exhibit polar-covalent Pn-X bonds for the lighter elements and ionic Pn-X bonds for the heavier ones. In other words, the increasingly metallic nature of the heavy elements renders their binary compounds sources of hydrides or halides with significant implications for coordination chemistry.

The nuclear spins of the elements show that only the phosphorus nuclide (^{31}P, $I = {}^{+}1/2$, 100 % abundance) is amenable to facile study by NMR techniques. The chemical shift range for commonly-encountered organo- or organohalophosphines is from −100 to +300 ppm. Factors influencing ^{31}P NMR chemical shifts include the electronegativity of the attached substituent, and the coordination number as well as steric bulk at the phosphorus centre being probed. In broad terms, phosphorus centres attached to very electronegative or bulky groups resonate downfield with respect to those with electropositive or small groups. Resonances for four-coordinate phosphonium centres also appear downfield and with narrower linewidths relative to three-coordinate phosphines. Finally, a greater variation in chemical shifts is observed for three-coordinate and alkyl-substituted phosphorus centres than for four- or five-coordinate and aryl-substituted centres. A detailed discussion of these trends and a theoretical account of their origins is given elsewhere.[12] The high sensitivity of ^{31}P NMR chemical shifts to local electronic structure and the relatively short acquisitions times for ^{31}P NMR experiments, together with the readily tunable electronic and steric features of phosphines, form a constellation of favourable chemical properties underlying the choice of phosphines as a bespoke family of ligands in the coordination chemistry presented here.

Table 1.1.1. Selected elemental properties (energies in kJ mol^{-1}, lengths in Å) for the pnictogen elements.

Property	Nitrogen	Phosphorus	Arsenic	Antimony	Bismuth
Atomic Number	7	15	33	51	83
Natural Isotopes (% abundance)	^{14}N (99.6)	^{31}P (100)	^{75}As (100)	^{121}Sb (57.4),	^{209}Bi (100)
	^{15}N (0.4)			^{123}Sb (42.6)	
Nuclear Spin (I)	+1 (^{14}N)	$+1/2$	$-3/2$	$+5/2$ (^{121}Sb)	$-9/2$
	$-1/2$ (^{15}N)			$+7/2$ (^{123}Sb)	
Ionization Energies					
$[M] \longrightarrow [M]^{1+}$	1402	1012	947	834	703
$[M]^{1+} \longrightarrow [M]^{2+}$	2856	1907	1798	1794	1610
$[M]^{2+} \longrightarrow [M]^{3+}$	4578	2914	2735	2443	2466
$[M]^{3+} \longrightarrow [M]^{4+}$	7475	4964	4837	4260	4372
$[M]^{4+} \longrightarrow [M]^{5+}$	9445	6274	6043	5400	5400
Electron Affinity (kJ mol^{-1})	7	72	78	101	91
Pauling Electronegativity	3.04	2.19	2.18	2.05	2.02
Atomic Radius	0.65	1.00	1.25	1.46	1.55
Covalent Radius	0.71	1.11	1.21	1.39	1.48
van der Waals Radius	1.55	1.80	2.00	2.20	2.40

An important consideration in the context of pnictogen coordination chemistry is the trend in increasing covalent and van der Waals radii for the elements. For the heaviest member of this group, bismuth, coordination numbers as high as nine are commonly observed[13] in the solid state and hypervalency is the norm rather than an exception. On the other hand, hypervalent nitrogen compounds are unknown and the ability to accommodate more than eight electrons has only been demonstrated beginning with phosphorus. The most familiar set of compounds in this context are the pnictogen pentahalides, which are powerful Lewis acids and oxidizers. The trigonal bipyramidal geometries of pnictogen pentahalides are representative of those observed for pentavalent pnictogen compounds in the +V oxidation state. By comparison, those in the +III oxidation state adopt a pyramidal geometry as typified by the pnictogen trihalides.

The structural chemistry of pnictogen complexes is discussed in several chapters of this thesis and for comparison parameters for a selection of prototypical compounds are gathered in Table 1.1.2. The trends in bond lengths reflect the larger covalent radii of heavier elements and increase in the order: $NX_3 \ll PX_3 < AsX_3 \ll SbX_3 < BiX_3$. The X-E-X angles show a marked decrease from nitrogen (*ca.* $105 - 110°$) to the heavier elements (*ca.* $90 - 100\,°$). In Valence Bond theory terms, the trend reflects a transition from high *s*-orbital contribution to the E-X bonding orbitals (described as sp^3 hybridization) in amines, to essentially purely *p*-orbital character for the E-X bonding orbitals in the heavier analogues. The corollary to this transition is that the lone pair at the heavier pnictogen centres also exhibits greater *s*-orbital character (more diffuse and polarizable) than hybrid sp^3-orbital character (more directional and less polarizable). Experimentally, these electronic features are manifested in the hard donor properties of amines relative to their heavier analogues (soft donors) and as a greater umbrella inversion barrier for heavier pnictines (> 130 kJ mol^{-1}) than found in amines (*ca.* 25 kJ mol^{-1}), since traversing through a trigonal-planar (sp^2 hybridized) transition state is required for inversion.[14,15]

Calculated values of the relative *s* and *p* orbital components are illustrated graphically in Figure 1.1.1 and the significant divergence from idealized sp^3 hybridization scheme for amines reflects the increasing disparity between the radial extents of n*s* and n*p* orbitals with increasing value of the principle quantum number. The unique condition of zero radial nodes in the $2p$ atomic orbitals enables a close match between

2s and 2p orbitals, enabling effective hybridization for the elements of the second row but, as illustrated by the structural data in Table 1.1.2 and Figure 1.1.1, this orbital coincidence represents an exception rather than the norm in main group chemistry.

Table 1.1.2. Selected bond lengths (Å) and angles (°) in the gas-phase structures of some prototypical pnictogen compounds.[16]

	NH_3	PH_3	AsH_3	SbH_3	BiH_3
E−H	1.012	1.421	1.511	1.700	1.776
H−E−H	106.7	93.3	92.1	91.6	90.5
	NCl_3	PCl_3	$AsCl_3$	$SbCl_3$	$BiCl_3$
E−Cl	1.759	2.039	2.165	2.334	2.424
Cl−E−Cl	107.1	100.3	98.6	97.1	97.5
	NMe_3	PMe_3	$AsMe_3$	$SbMe_3$	$BiMe_3$
E−C	1.458	1.847	1.979	–	2.263
C−E−C	110.9	98.6	98.8	–	97.1

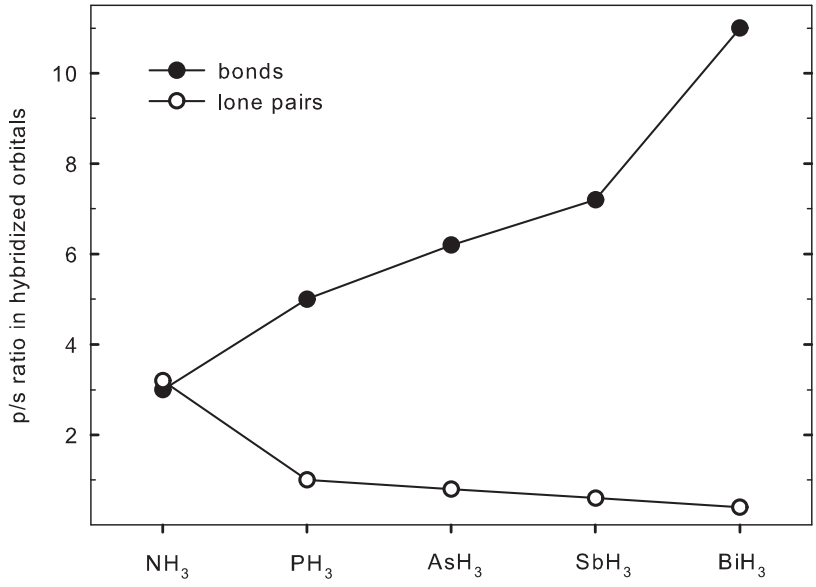

Figure 1.1.1. Relative s- and p-orbital contributions ($\frac{p}{s}$ ratio) in the hybridized bonding and lone pair orbitals in EH_3 at the B3LYP/def2-TZVP level.[17]

The majority of complexes described here contain phosphine ligands as the donor and pnictogen centres as acceptors in their +III oxidation state. Such complexes feature bonding frameworks where the acceptor site bears a lone pair that is stereochemically active and available for further reactivity. By comparison, phosphine complexes of transition metals rarely feature distinct lone pair stereochemistry and prediction of their molecular structures requires careful investigation of electronic structure and molecular orbital occupations rather than application of semi-empirical rules such as VSEPR theory. To put the findings of this thesis into context, the following section offers a brief, non-comprehensive, introduction to phosphine complexes of lone pair bearing acceptors in the main group. The topic has been reviewed in significant detail elsewhere.[18,19] A number of examples introduced briefly in this section reappear in later chapters where a full discussion is offered.

1.2 Phosphine Complexes of Lone Pair Bearing Lewis Acceptors

Complexes of lone pair bearing acceptors and one phosphine ligand have been structurally characterized for the majority of *p*-block elements (summarized in Figure 1.2.1), but remain rare as few examples are known for most elements. A limited number of main group elements form *bis*-phosphine complexes and *tris*-phosphine complexes have only been reported for gallium,[20] indium,[20] thallium[21] and antimony.[22] Phosphine complexes of boron(I) or aluminium(I) are not known even though complexes of these centres with N-heterocyclic carbene (NHC) or diketiminate ligands have been reported.[23–27]

For the sake of brevity, the inclusion criterion for compounds in Figure 1.2.1 is based on experimental considerations. For compounds such as phosphorus ylides, carbodiphosphoranes (carbones), $[(PPh_3)N_2(PPh_3)]$,[28] derivatives of $[(R_3P)I_2]$,[29,30] and $[(Ph_2(\textit{mecarb})P)I_2(PPh_2(\textit{mecarb}))]$[31] a coordinate bonding model augments the Lewis description with new predictions that have been experimentally borne out. However, for phosphine chalcogenides R_3PE (E = O, S, Se, Te), derivatives of Hendricksons reagent ($[R_3POPR_3]^{2+}$),[32] and halophosphonium cations $[R_3PX]^{1+}$ (X = F, Cl, Br) the Lewis model adequately describes the experimental observables, and invoking the donor/acceptor model does not yet add to the description in a useful way.

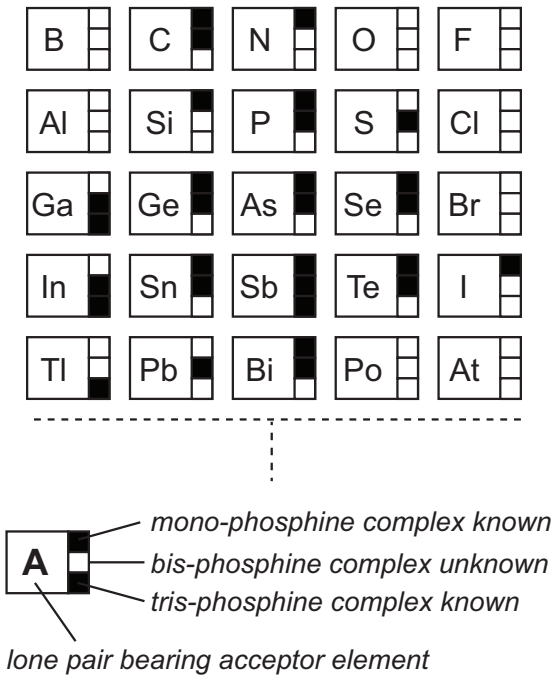

Figure 1.2.1. The *p*-block elements with marks indicating those elements for which complexes with one, two or three phosphine ligands have been structurally characterized and for which the acceptor site contains at least one lone pair.

Reinterpretation of their bonding in light of future experimental evidence remains a possibility.

1.2.1 Structural Diversity

Figure 1.2.2 gives an overview of the formulae that are possible for *mono*-, *bis*-, and *tris*-phosphine complexes of lone pair bearing *p*-block acceptors. Based on the structural data available (almost exclusively in the solid state), the observed molecular geometries at the acceptor centres are dictated primarily by a balance between the steric activity of the lone pair and the covalent radius of the element. For example, antimony or bismuth complexes of the form $[(Ph_3P)_2EPh_2]^{1+}$ (E = Sb, Bi) are accessible,[33] whereas the analogous phosphorus complexes of the form $[(R_3P)_2PR_2]^{1+}$ have not been reported. Attempts to prepare *bis*-phosphine complexes of phosphenium acceptors, $[PR_2]^{1+}$, using chelating donors result in the diphosphine donor bridging two phosphenium acceptors, as in the example of $[Ph_2P{-}(dppe){-}PPh_2]^{2+}$.[34] Further distinction between the coordination chemistry of phosphorus and its heavier congeners is evidenced by the reactions of excess trialkylphosphines with PCl_3 or $SbCl_3$. While the former undergoes a redox process resulting in formation of triphosphenium and chlorophosphonium cations, $[(R_3P)_2P]^{1+}$ and $[R_3PCl]^{1+}$,[35] $SbCl_3$ is redox resistant and derivatives of $[(R_3P)_2SbCl_3]$ (R = Me, Ph, Cy) are obtained[36] in which the larger coordination sphere of antimony can accommodate five bond pairs and a lone pair. In general, halides of the heavier *p*-block elements behave as classical transition metal acceptors, and interion as well as nearest-neighbour contacts tend to participate in the coordination geometry of the acceptor giving hypervalent environments.

Lone Pair Stereochemistry and VSEPR Configurational Diversity

Since orbital hybridization is difficult to achieve in molecules derived from heavy elements, lone pairs are accommodated primarily in *s*-type orbitals while bonding occurs primarily through the *p*-orbitals. As a result, bond angles in the first coordination sphere are close to 90° for three-coordinate geometries and when interion contacts are considered, distorted square-based-pyramidal or octahedral arrangements occur for five- and six-coordinate geometries, respectively, as shown in the examples presented in Figure 1.2.3 for recently reported complexes.[36]

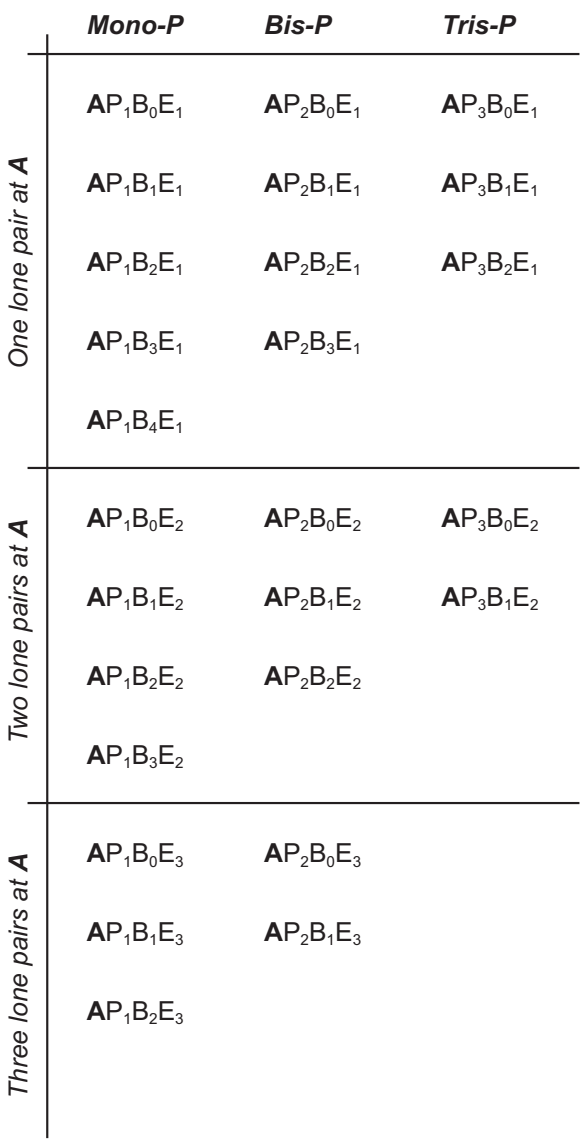

Figure 1.2.2. Generic formulae for the 26 possible *mono*-, *bis*-, and *tris*-phosphine complexes of a lone pair bearing acceptor, A, organized according to the type of electron pair around the acceptor. Assuming a maximum of six electron pairs around A, P = phosphine donor, B = substituent electron pair (*e.g.* alkyl, aryl, halogen *etc.*) and E = non-bonding lone pair.

The P−Sb−Cl angles of $[(Me_3P)SbCl_2]^{1+}$ cation (Figure 1.2.3*a*) in its triflate salt are 90.71(3)° and 90.62(3)°, while the Cl−Sb−Cl angle is 92.78(3)°. A six-coordinate geometry is observed at antimony by considering the interion contacts, and the average O_1−Sb−O_3 and O_2−Sb−O_3 angles of 115.4°, suggesting the presence of a stereochemically active lone pair. Similarly, the average Cl−Sb−Cl angle of the $[(Me_3P)_2SbCl_4]^{1-}$ anion (Figure 1.2.3*b*) in its magnesium salt is 89.47°, but the average P−Sb−Cl angle is compressed to 84.39° (*cf.* 90° expected for an ideal square-based pyramid), consistent with steric pressure from the presence of a lone pair *trans* to the phosphine interaction. Importantly, this effect is replicated in the gas-phase calculated geometry of the free ion at the MP2/def2-TZVPP level, precluding solid-state packing as its cause, and the calculated electronic structure also shows significant accumulation of electron density at the Sb atom in the HOMO (Figure 1.2.3*c*) of the anion.

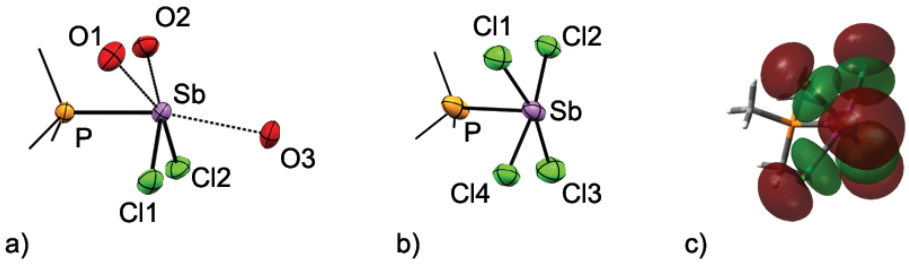

Figure 1.2.3. Molecular structure of *a*) $[(Me_3P)SbCl_2]^{1+}$ with three weak interion contacts, *b*) $[(Me_3P)SbCl_4]^{1-}$, and *c*) HOMO of $[(Me_3P)SbCl_4]^{1-}$ as calculated at the MP2/def2-TZVPP level.

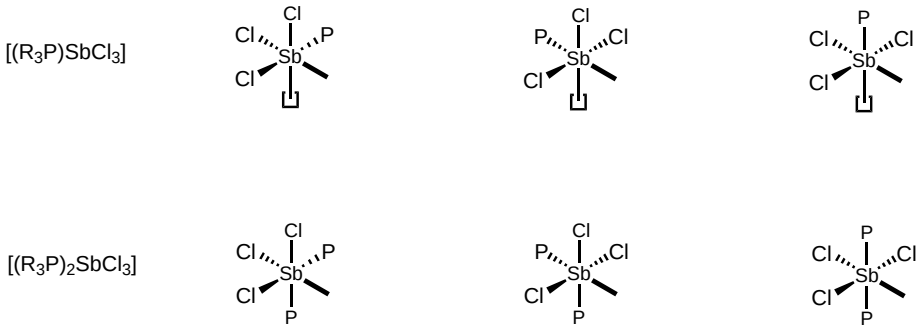

Scheme 1.2.1. Potential configurational outcomes (only VSEPR-consistent structures are considered) in an octahedral frame for chloroantimony complexes composed of three chloride substituents and one or two phosphine ligands (P = PR_3). Bold line = lone pair, square = vacant coordination site.

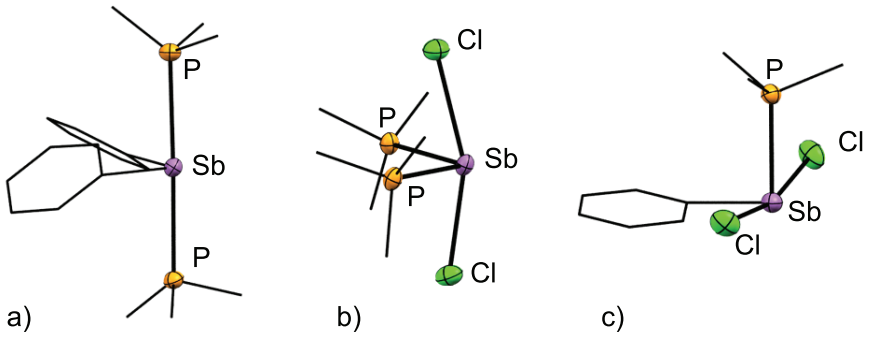

Figure 1.2.4. Structural diversity for four- and five-coordinate phosphine complexes of antimony acceptors: *a*) $[(Me_3P)_2SbPh_2]^{1+}$, *b*) $[(Me_3P)_2SbCl_2]^{1+}$, and *c*) $[(Me_3P)SbPhCl_2]$.

The potential configurational diversity within a given four- or five-coordinate VSEPR geometry for phosphine complexes of antimony(III) chloride is illustrated in Scheme 1.2.1. While the overall geometry is predicted by VSEPR theory, few guidelines are present to determine which configuration is preferred. This preference has recently been assessed experimentally and described in terms of a *trans*-influence series for various functional groups (lone pair, aryl, phosphine, halide *etc.*) around antimony acceptors (see Chapter 3).[36] For example, differences between the solid-state structures of $[(Me_3P)_2SbPh_2]^{1+}$ and $[(Me_3P)_2SbCl_2]^{1+}$ (Figure 1.2.4*a* and 1.2.4*b*) in their triflate salts demonstrate the differing outcomes of axial or equatorial phosphine positioning based upon the other substituents present at antimony. The series also correctly predicts configurations adopted by complexes with three different substituents as in the case of the neutral complex $[(PMe_3)SbPhCl_2]$, where the phenyl group and PMe_3 are *cis* to each other, with the two chlorine substituents *trans* to each other (Figure 1.2.4*c*). The findings also hold true for anionic derivatives such as $[(Me_3P)SbCl_4]^{1-}$, where the phosphine ligand adopts an apical rather than basal site (Figure 1.2.3*b*).

Importantly, the relative *trans*-labilizing influence of phosphines and substituents, derived for antimony acceptors, applies generally for to other group 15 acceptors. For example, all NHC (strong σ-donor) adducts of ECl_3 (E = P, As, Sb, Bi) adopt structures in which the ligand is *cis*-configured with respect to all halides while all phosphine sulfide (weak σ-donor) adducts adopt structures where the ligand is *trans* to a halide.[37–40] The unique nature of lone pair bearing complexes is highlighted by the fact that the relative *trans*-labilizing influence described above is not operative in the absence of a lone pair. For example, $[(Me_3P)_2InCl_3]$[41] and $[(Me_3P)_2SnCl_4]$[42] exhibit *trans*-configured PMe_3 ligands wheareas lone pair bearing $[(Me_3P)_2SbCl_3]$[36] shows *cis*-configured phosphines.

Electronic Structure from Molecular Structure

Beyond highlighting the configurational ambiguity of VSEPR structures, consideration of lone pair stereochemical activity at the acceptor sites also provides insights into the electronic structure of complexes. The most significant example of this relationship between electronic and molecular structure comes from compounds of the formula $(R_3P)_2C$, which have been described as *bis*-phosphine complexes of carbon on the basis of quantum-chemical calculations[43] and reactivity studies (*vide infra*). Foreshadowing

their ability to behave as double-bases (*i.e.* engage two Lewis acids simultaneously), the structures of several derivatives adopt a bent geometry at the carbon atom with a P-C-P angle of *ca.* 140°, consistent with one or two stereochemically active lone pairs at the acceptor site. The bent geometry definitively refutes the alternative allenic electronic structure ($R_3P{=}C{=}PR_3$), which is expected to yield a linear geometry around carbon.

Another example is furnished by the phosphine coordination chemistry of M(I), where M = In or Ga.[20] The *tris*-phosphine complexes $[(Ph_3P)_3M]^{1+}$ have pyramidal geometries, as expected for AX_3E compounds, and P−M−P angles around 95°, consistent with occupation of the three *p*-orbitals by the ligands and a residual lone pair on the metal (Figure 1.2.5*a*). When $^tBu_3P$ is employed as a ligand, due to steric factors, only two of the phosphines bind the metal centres, giving a bent geometry with P−M−P angles of *ca.* 117° (Figure 1.2.5*b*). Quantum-chemical analysis of model pyramidal and bent structures showed that the former geometry yields an essentially *s*-type lone pair, while the latter results in a sp^2-type lone pair in the P−M−P plane and an unoccupied *p*-orbital as the LUMO.[20] Consequently, the *tris*-phosphine complexes have the potential to behave as σ-donors *via* the metal centre and the *bis*-phosphine complexes are simultaneous σ-donors and π-acceptors. Although experimental evidence for these two modes of reactivity has not yet been reported, the structural outcomes clearly offer insight into the electronic structure with potential consequences for the acceptor-centred coordination chemistry of the phosphine complex.

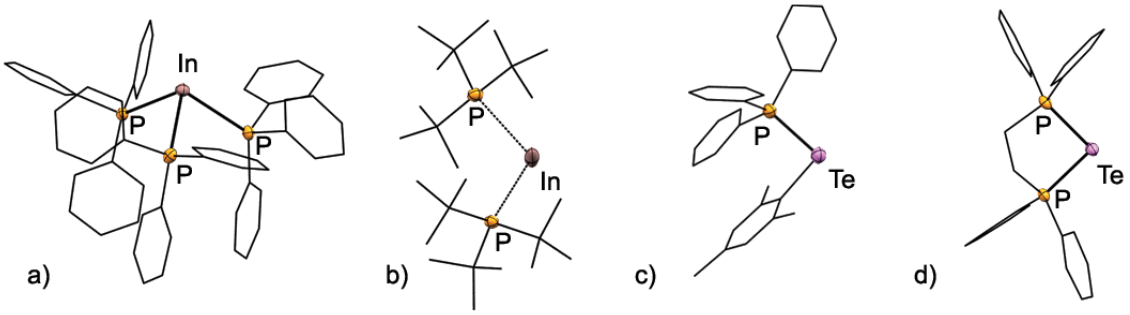

Figure 1.2.5. Molecular structures of *a*) $[(Ph_3P)_3In]^{1+}$, *b*) $[(^tBu_3P)_2In]^{1+}$, *c*) $[(Ph_3P)TeMes]^{1+}$, and *d*) $[(dppe)Te]^{2+}$ in the solid state.

In complexes where the acceptor site has more than one lone pair, the structural

outcomes are somewhat trivial as only limited VSEPR-consistent configurations are possible. Therefore phosphine complexes of group 16 acceptors yield bent or T-shaped geometries (Figure 1.2.5*c* and 1.2.5*d*), although some slight variation within the motifs exist .[44–49] For the group 17 diatomic, I_2, the presence of three lone pairs and two bonding pairs at the acceptor necessitates a linear geometry. The acceptor chemistry of molecular I_2 has been studied in some detail and an analysis of ligand steric effects has been reported.[30] As shown in Table 1.2.1, complexes of I_2 with strongly donating phosphines lead to shorter P−I bond distances and longer I−I distances, indicating that the acceptor orbital is the I−I σ^* orbital. Consistently, with very basic trialkylphosphines, solid- and solution-phase species described as $[R_3PI][I]$ are formed due to complete displacement of an iodide from molecular I_2 by a phosphine ligand. The arrested-displacement embodied in the so-called 'spoke' complexes (Figure 1.2.6*a*) of the form $[(R_3P)XX]$ is a snapshot of the familiar hypervalent transition state for S_N2 nucleophilic displacement in an alkyl halide. On the basis of ligand-exchange experiments and bond strengths these complexes have been intepreted either as phosphine adducts of I_2 or as iodide adducts of iodophosphonium cations, the latter description emphasizing the preference for soft/soft iodide/iodine interactions over soft/hard iodide/phosphonium interactions.[29]

Remarkably, molecular I_2 can even accept two phosphine ligands and the linear P−I−I−P framework (Figure 1.2.6*b*) has been reported[31] using a very weakly-coordinating carboranyl phosphine ligand PPh_2(*mecarb*). The P−I−I−P interaction persists in halocarbon solutions, and this may be due to kinetic factors or additional intramolecular stabiliziation *via* weak contacts. With more strongly donating phosphines, spoke complexes or phosphonium salts are formed.[50] The phosphine coordination chemistry of molecular I_2 illustrates that very weakly-coordinating ligands have the ability to stabilize unusual *hypervalent* bonding motifs, complementing the ability of very strongly-coordinating ligands such as carbenes to stabilize unusual *hypovalent* bonding motifs.

1.2.2 Acceptor-centred Reactivity

In addition to the interesting coordination chemistry described above, phosphine complexes of lone pair bearing acceptors also show a variety of reactions. These have been collated into three broad categories to facilitate discussion: i) ligand exchange,

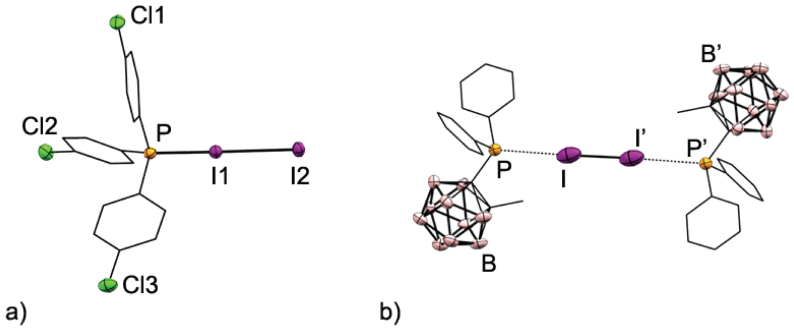

Figure 1.2.6. Molecular structures of *a*) a spoke wheel complex $[(p{-}\mathrm{ClPh})_3\mathrm{PI}_2]$, and *b*) $[((mecarb)\mathrm{Ph}_2\mathrm{P})_2\mathrm{I}_2]$ in the solid state.

Table 1.2.1. Key bond distances (Å) in selected phosphine-diiodine adducts, $[\mathrm{R}_3\mathrm{PII}]$.[30] Asterisk denotes the presence of two unique molecules in the unit cell.

Complex	d(P–I)	d(I–I)
$[(p{-}\mathrm{FC}_6\mathrm{H}_4)_3\mathrm{PII}]$*	2.507(3)	3.0807(12)
	2.461(3)	3.1529(11)
$[(p{-}\mathrm{ClC}_6\mathrm{H}_4)_3\mathrm{PII}]$	2.488(2)	3.1332(9)
$[\mathrm{Ph}_3\mathrm{PII}]$	2.481(4)	3.161(2)
$[(p{-}\mathrm{MeC}_6\mathrm{H}_4)_3\mathrm{PII}]$	2.472(5)	3.1815(13)
$[(p{-}(\mathrm{SMe})\mathrm{C}_6\mathrm{H}_4)_3\mathrm{PII}]$	2.468(2)	3.1946(8)
$[(p{-}(\mathrm{OMe})\mathrm{FC}_6\mathrm{H}_4)_3\mathrm{PII}]$	2.448(4)	3.2123(7)

ii) coordination and oxidation of lone pair bearing acceptor centres, and iii) reductive coupling.

Ligand Exchange

Reaction of $[(ClPh_2P)PPh_2]^{1+}$ with PPh_3 or NHC results in displacement of the weaker base by the stronger one to give $[(Ph_3P)PPh_2]^{1+}$ or $[(NHC)PPh_2]^{1+}$, respectively.[51] The equilibrium between bound phosphinophosphonium complexes and their unbound constituents in some cases also enables acceptor exchange. Addition of Ph_2PCl to a solution of $[(Ph_3P)PPhCl]^{1+}$, liberates $PhPCl_2$ and yields the $[(Ph_3P)PPh_2]^{1+}$ cation.[52] This observation is interpreted as abstraction of chloride from Ph_2PCl by $[PhClP]^{1+}$, since the latter is a more Lewis acidic phosphenium cation than $[Ph_2P]^{1+}$ due to the presence of an electronegative chlorine substituent at the phosphorus centre. Enhancement of Lewis acidity in phosphenium cations with very electronegative substituents was also noted in a computational study.[53]

Detailed mechanistic investigation of ligand exchange has been done for the P−P case, where both S_N1 and S_N2 pathways are implicated depending upon the steric bulk of the donor and the stability of the acceptor in the absence of a donor.[54] For instance, displacement of the PPh_3 ligand from the phospholophosphonium cation $[(Ph_3P)PC_4Et_4]^{1+}$ shows second-order kinetics consistent with an S_N2-type mechanism. The most likely transition state is calculated to be only 18 kJ mol^{-1} above the starting materials, and features a see-saw geometry at the acceptor centre, with two identical and mutually-*trans* phosphine interactions. In contrast, a dissociative pathway is evidenced in the reaction of PMe_3 with *bis*-(arylamino)phosphenium cations[55] and a computational analysis[54] found no hypercoordinate transition state for these types of substitution reactions. The enhanced steric bulk of the arylamino groups and the inherent stability of phosphenium cations attached to a π-donating heteroatom[56] results in the dominance of an S_N1 pathway in substitution reactions involving these acceptors.

Ligand exchange at heavier main group centres such as antimony and bismuth likely proceeds *via* associative mechanisms (S_N2 or AE), made possible by the larger covalent radii of these elements, which permits higher coordination numbers and stable hypervalent geometries. For example, while the reaction of PMe_3 with $PhPCl_2$ yields $[(Me_3P)_2PPh]^{2+}$,[57] the related reaction of PMe_3 with $PhSbCl_2$ yields the non-ionic,

hypervalent neutral adduct $[(Me_3P)SbPhCl_2]$.[36] Displacement of a chloride ion is not observed even in the presence of excess phosphine. By comparison, ligand exchange occurs readily in cationic phosphine complexes of antimony.[58]

An intriguing feature of some ligand exchange reactions is the strong preference for homoleptically substituted acceptor centres. As shown in Scheme 1.2.2, the mixed PPh_3/PMe_3 derivative is not observed when a one equivalent of PMe_3 is added to a solution of $[(Ph_3P)RPPR(PPh_3)]^{2+}$.[52] Instead, a 1:1 mixture of the starting material and *bis*-PMe_3 substituted dication $[(Me_3P)RPPR(PMe_3)]^{2+}$ is obtained. Upon addition of two equivalents of PMe_3, conversion to $[(Me_3P)RPPR(PMe_3)]^{2+}$ is observed, together with quantitative liberation of PPh_3. Analogous experiments targeting displacement of a single stibine ligand from $[(Ph_3Sb)RPPR(SbPh_3)]^{2+}$ by an equivalent of arsine or phosphine ligand consistently give only the homoleptic derivatives, $[(Ph_3Pn)RPPR(PnPh_3)]^{2+}$ (Pn = As, P) and unreacted starting material.[59] The reason for this preference remains a mystery.

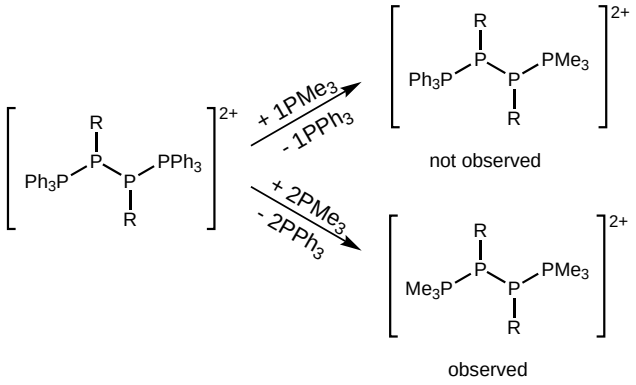

Scheme 1.2.2. Ligand exchange in 2,3-diphosphino-1,4-diphosphonium dications.

An intramolecular ligand exchange reaction is observed in 1,3-diphosphino-2-phosphonium monocations, $[R_2PP(R_2)PR_2]^{1+}$, which highlights the lability of coordinate P−P bonds (Scheme 1.2.3). These cations are readily generated by the reaction of diphosphines (R_2PPR_2) with chlorophosphines (R'_2PCl) in the presence of a halide abstractor. When R = Me and R' = Ph, the expected asymmetrically-substituted cation $[Me_2PP(Me_2)PPh_2]^{1+}$ is obtained. However when R = Ph and R' = Me, only the symmetrically substituted $[Ph_2PP(Me_2)PPh_2]^{1+}$ is observed.[60] An intramolecular ligand exchange is proposed that involves dissociation of a $[Ph_2P]^{1+}$ fragment from the $[Ph_2PP(Ph_2)PMe_2]^{1+}$ cation and re-association at the more basic alkylphosphine site

of the resulting neutral diphosphine, Ph_2PPMe_2. When R = Me and R' = Ph, this rearrangement is inhibited by the high Lewis acidity of $[Me_2P]^{1+}$ (calculated fluoride-ion-affinity of 960 kJ mol^{-1}),[53] which disfavours dissociation of $[Me_2PP(Me_2)PPh_2]^{1+}$ into $[Me_2P]^{1+}$ and neutral Me_2PPPh_2. Even if such dissociation occurs meagrely, the subsequent re-association engages the more basic dimethylphosphine moiety of Me_2PPPh_2, giving the observed product.

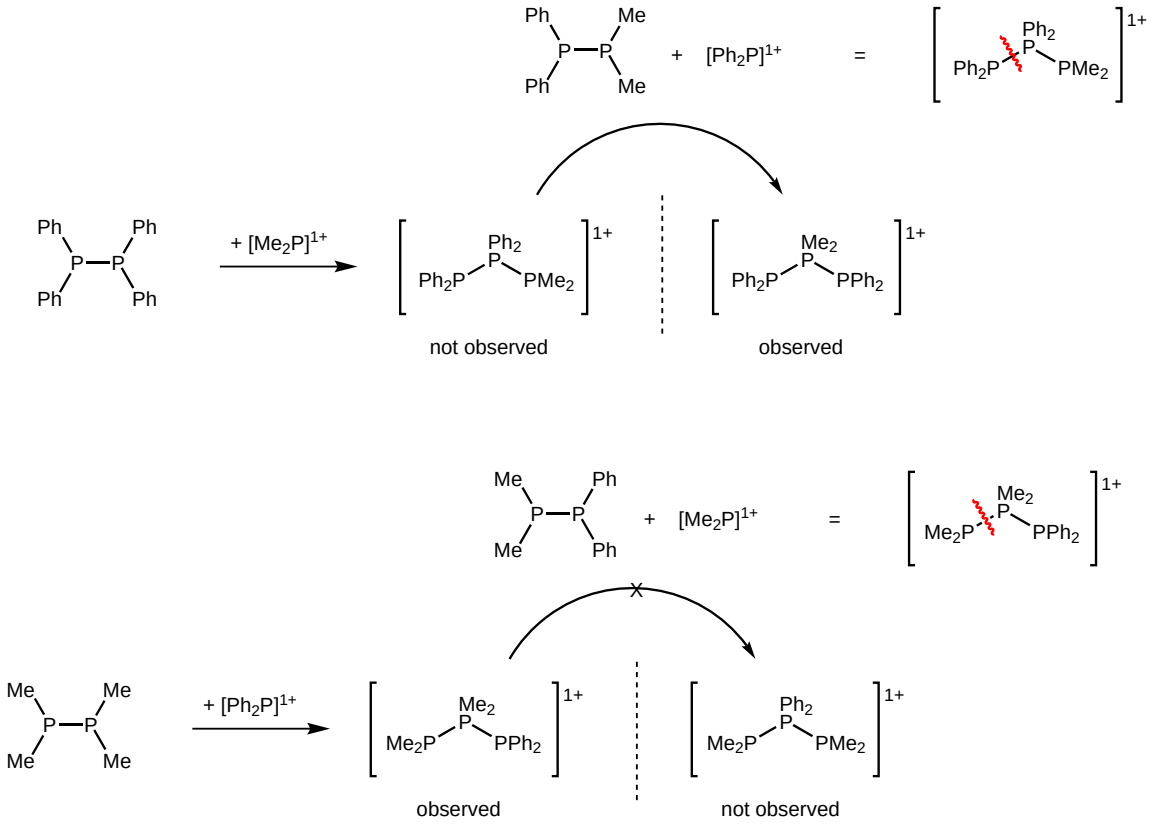

Scheme 1.2.3. Proposed mechanism for insertion of phosphenium cations into P−P bonds.

Coordination & Oxidation of Acceptor Lone Pair

The complexes discussed here feature a distinct acceptor-centred lone pair, potentially capable of binding to another acceptor or being oxidized. Lewis-basic behaviour for phosphine stabilized complexes has only been reported towards a few acceptor elements. In group 14, the most diverse examples are from the coordination chemistry of phosphonium ylides and double ylides (carbodiphosphoranes). Both species feature

a highly-nucleophilic carbon acceptor with a maximum of one and two lone pairs, respectively, available for coordination (Scheme 1.2.4). The use of phosphorus ylides as ligands in main group chemistry is rare. The structures of $[(Ph_3PCMe_2)BH_3]$,[61] $[(Ph_3PCMe_2)GeCl_2]$,[61] and $[(Ph_3PCHMe)SbCl_3]$[62] are shown in Figure 1.2.7, representing complexes of ylides with prototypical neutral Lewis acids from groups 13, 14 and 15.

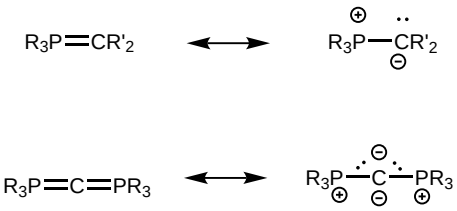

Scheme 1.2.4. Resonance structures for phosphonium ylides (top) and carbones (bottom).

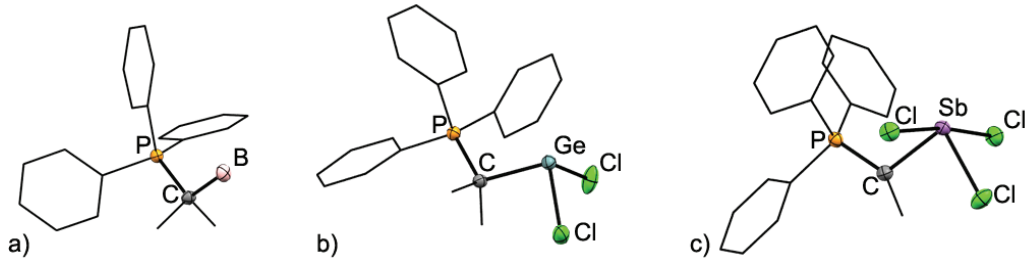

Figure 1.2.7. Molecular structures of *a*) $[(Ph_3PCMe_2)BH_3]$, *b*) $[(Ph_3PCMe_2)GeCl_2]$, and *c*) $[(Ph_3PCMeH)SbCl_3]$ in the solid state.

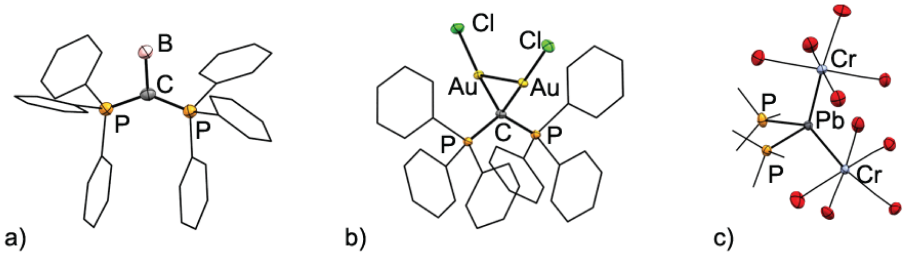

Figure 1.2.8. Molecular structures of *a*) $[(Ph_3P)_2CBH_3]$, *b*) $[(Ph_3P)_2C(AuCl)_2]$, and *c*) $[(Me_3P)_2Pb(Cr(CO)_5)_2]$ in the solid state.

Investigations into the electronic structure of carbones revealed them to be good σ- and π-donors (*cf.* NHCs which are σ-donors and π-acceptors), capable of binding to

one or two Lewis acids.[63] These predictions have been confirmed experimentally and prototypical structures of carbone complexes with one and two acceptors are shown in Figures 1.2.8*a* and 1.2.8*b*).

Complexes featuring lead, $[(R_3P)_2Pb(Cr(CO)_5)_2]$ (R = Me, Et, and ^{n}Bu), show P−Pb−P angles in the 86.93(5) − 95.00(4)° range and Cr−Pb−Cr angles in the 127.73(5) − 129.80(3)° range (Figure 1.2.8*c*).[64] While these complexes were made by displacement of halides from the Pb^{II} precursors, $[X_2Pb(Cr(CO)_5)_2]^{2-}$ (X= Cl, Br, I), they can also be interpreted as chromium complexes of a dibasic Pb^0 donor, a plumbylone, as such complexes are predicted to be stable in theoretical studies.[65] An uncoordinated plumbylone has not been reported and ligand displacement from the chromium centre in these complexes may be one route to their discovery.

The potential for the phosphine centre in phosphinophosphonium cations to behave as a donor is demonstrated (Scheme 1.2.5*a*) by the isolation of the gallium complex $[Me_2ClPP(Me_2)GaCl_3]^{1+}$,[66] spectroscopic characterization[67] of derivatives of $[RCl_2PP(R)(Cl)GaCl_3]^{1+}$ cations, and isolation of transition metal complexes like the tungsten complex of a cyclic phosphinophosphonium (Scheme 1.2.4*b*).[68] As previously noted, the phosphine centre in $[Me_3PPMe_2]^{1+}$ can be alkylated to give $[Me_3PPMe_3]^{2+}$, and $[Me_3PPMe_2{}^tBu]^{2+}$,[7] which is analogous to methylation of a triphosphenium cation (Scheme 1.2.4*c*).[69] Single[70] and double[71] coordination of transition metals at lone pairs of neutral P^I centres has also been reported (Scheme 1.2.4*d*-*f*, Figures 1.2.9*a* and 1.2.9*b*). The broad array of coordination chemistry that is now established for phosphine stabilized cationic and neutral P^I, and P^{III} centres bodes well for the application of these species as an interesting family of ligands in the context of transition metal catalysis. The observation that other heavy acceptor centres such as antimony and bismuth show marked lone pair stereochemistry in their phosphine complexes suggests the possibility of engaging these centres in further coordination, as reported for phosphorus.

Examples of acceptor-centred two-electron oxidation are rare in main group phosphine complexes as the phosphine ligand is itself susceptible to oxidation but some examples are known (Figure 1.2.9*c*). Phosphonium sila-ylides, silicon analogues of phosphonium ylides, are transient species that can be isolated in rare instances using bulky substituents and intramolecular coordination.[72,73] For one family of complexes, a variety of two-electron oxidations have been demonstrated including activation of

small alkenes, CO, and CO_2, exemplifying the highly nucleophilic nature of the silicon atom in these systems (Scheme 1.2.6).[73–75]

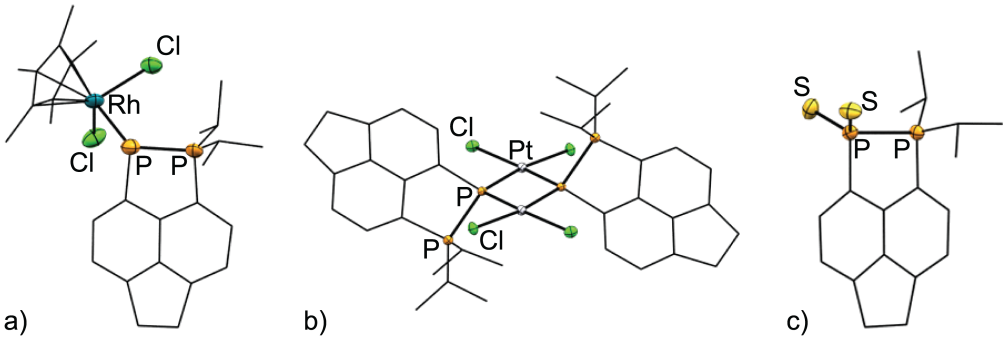

Figure 1.2.9. Acceptor-centred *a*) single coordination, *b*) double coordination, and *c*) oxidation for phosphine-stabilized phosphorus^{I} acceptors.

Reductive Coupling

Reductive coupling of phosphine-stabilized halo-element centres is analogous to reductive coupling of carbene-stabilized halo-element centres. However, compared to carbenes, phosphines are more susceptible to oxidation and can therefore react simultaneously as a ligand and as a reducing agent. For example, the reaction of $PhPCl_2$ with excess TMSOTf and excess PPh_3, initially gives the chlorophosphinophosphonium cation, $[(Ph_3P)PPhCl]^{1+}$ as a triflate salt. However, the ^{31}P-NMR spectrum of the reaction mixture after 48 hours shows an AA'BB' pattern corresponding to $[(Ph_3P)PhPPPh(PPh_3)]^{2+}$ and a singlet due to $[Ph_3PCl]^{1+}$.[76] The tetraphosphorus dication can be equivalently viewed as containing either two central P^{I} phosphine centres bound to terminal P^{IV} phosphonium centres, or two central P^{II} phosphenium centres bound to two terminal P^{III} phosphine centres, depending upon the perceived localization of charge. The overall reaction is summarized in Scheme 1.2.7 and exemplifies the use of a phosphine as both a ligand and a reducing agent.

Reactions involving $SbPh_3$ instead of PMe_3 give the heteroleptically substituted $[(Ph_3Sb)RPPR(SbPh_3)]^{2+}$ dications together with the $[Ph_3SbCl]^{1+}$ cation as the oxidation product. These mixed P−Sb cations demonstrate an unusual reversal of traditional donor (non-metal) and acceptor (metal) roles and undergo the expected displacement of the stibine ligands in the presence of more basic $AsPh_3$ or PPh_3 donors as discussed earlier in the context of ligand exchange reactivity.

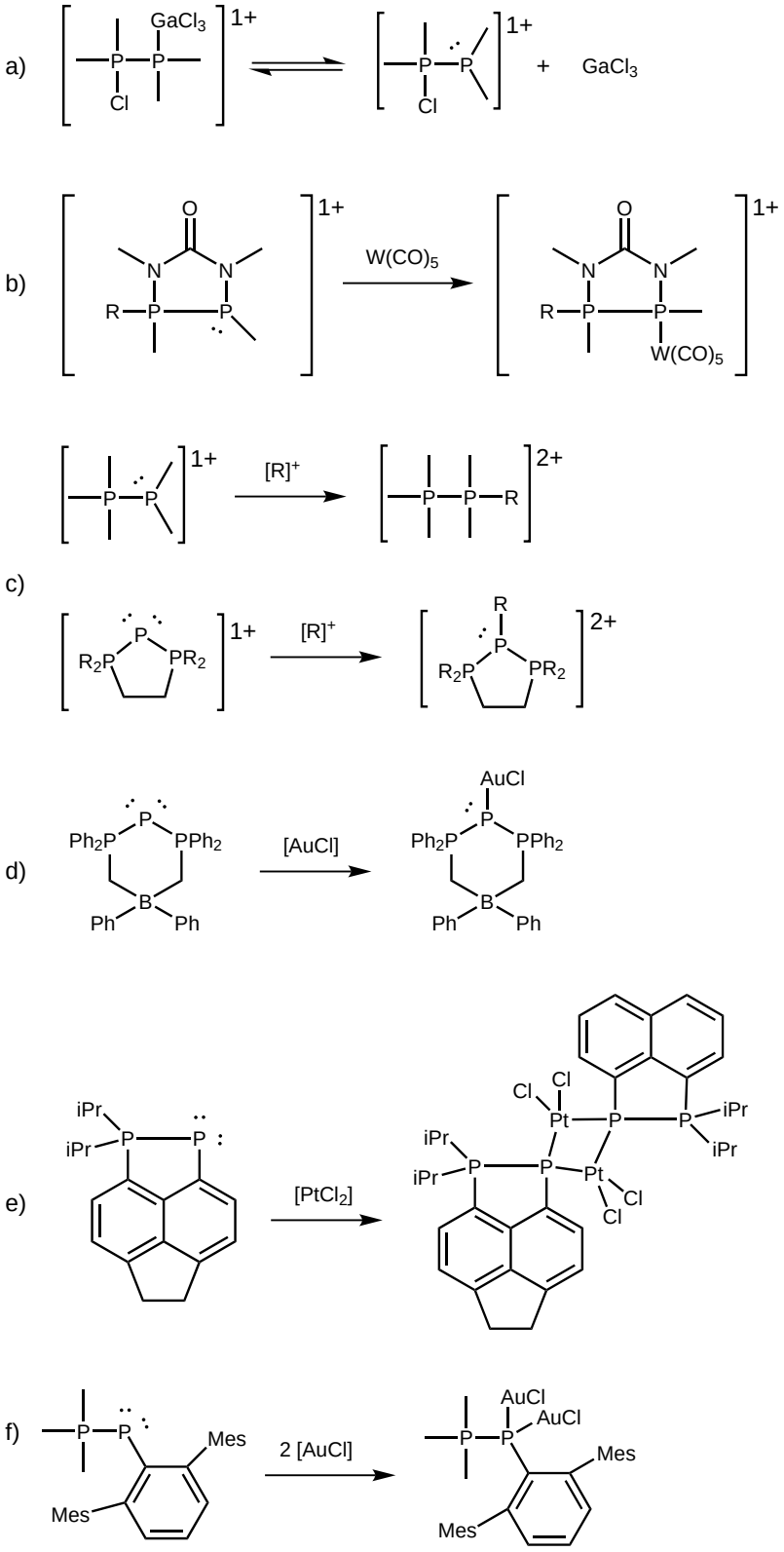

Scheme 1.2.5. Selected examples of phosphine complexes behaving as donors *via* acceptor-centred lone pairs.

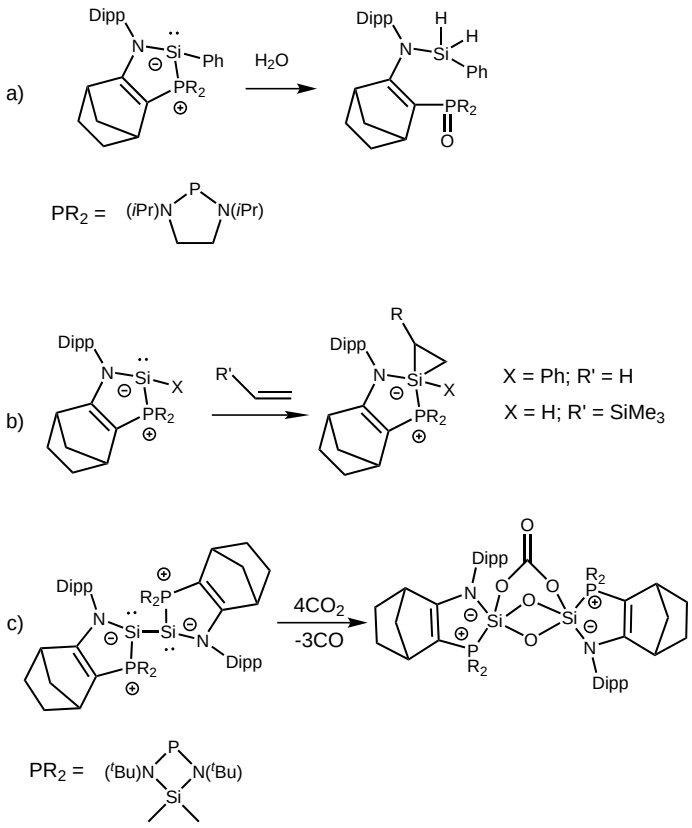

Scheme 1.2.6. Silicon-centred two-electron oxidation in phosphonium sila-ylides.

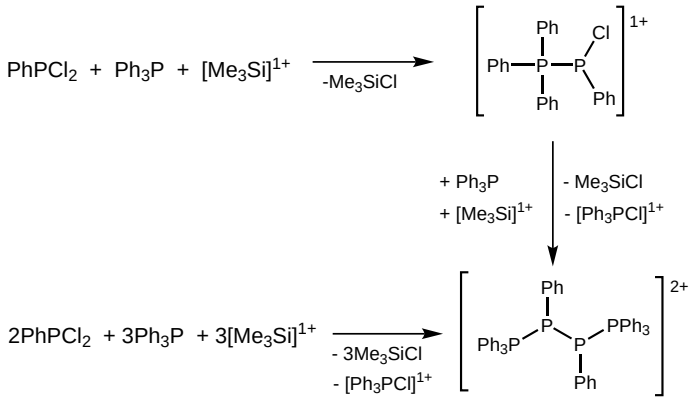

Scheme 1.2.7. Synthesis and reductive coupling of chlorophosphinophosphonium cations.

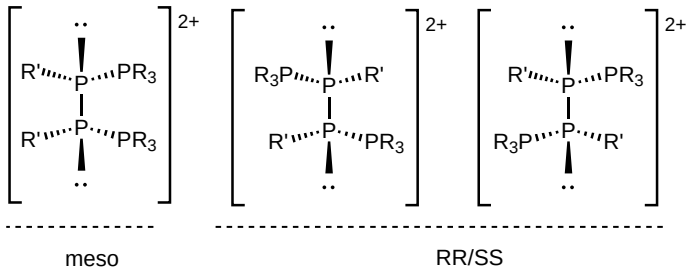

Scheme 1.2.8. Stereochemical outcomes for 2,3-diphosphonium-1,4-diphosphonium dications.

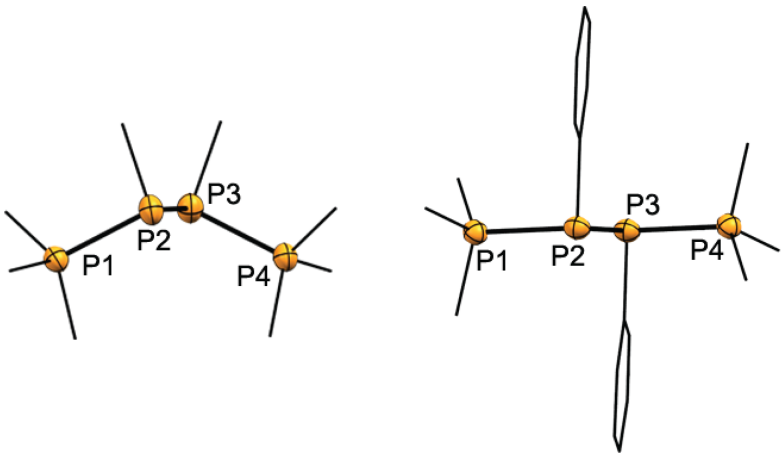

Figure 1.2.10. Molecular structures of the *RR/SS*-$[(Me_3P)(Me)PP(Me)(PMe_3)]^{2+}$ (left) and *meso*-$[(Me_3P)(Ph)PP(Ph)(PMe_3)]^{2+}$ (right) in the solid state.

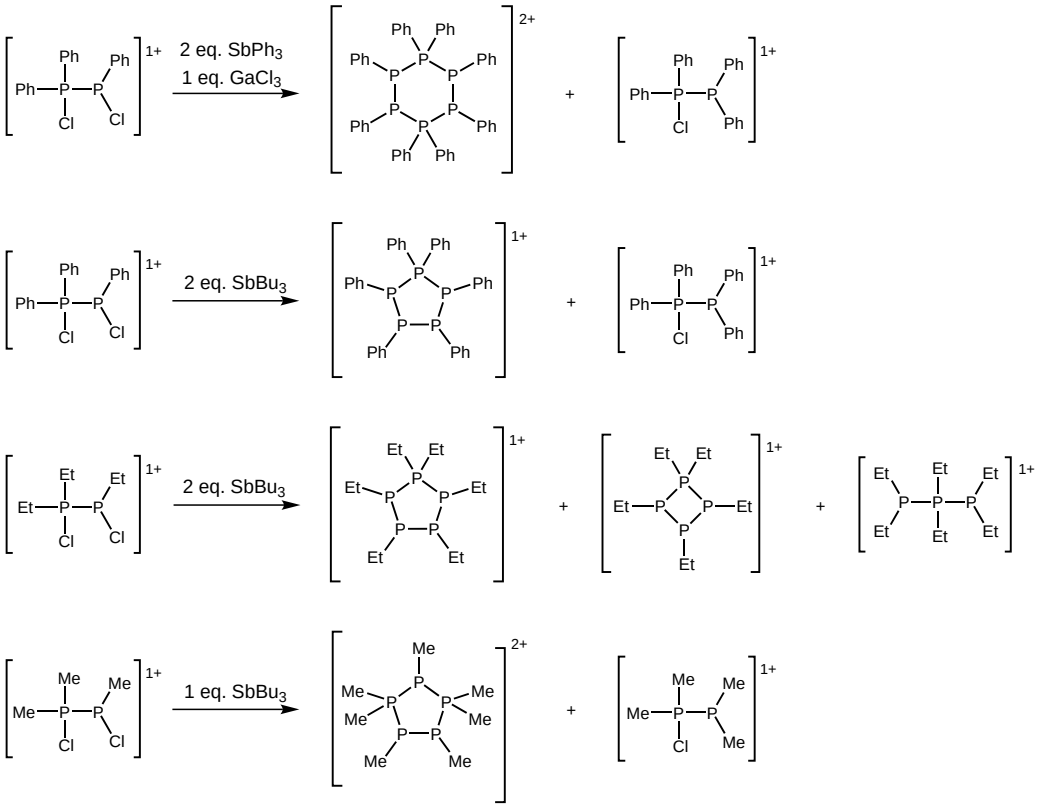

Scheme 1.2.9. Formation of cyclic and linear *catena*-phosphorus cations *via* reductive coupling of chlorophosphinochlorophosphonium cations.

The presence of a lone pair at the acceptor sites in $[(Ph_3Pn)PhPPPh(PnPh_3)]^{2+}$ (Pn = P, As, Sb) dications gives rise to unique stereochemical outcomes due to the high umbrella inversion barriers at tricoordinate phosphorus centres (Scheme 1.2.8).[77] The distribution of meso or *RR*/*SS* diastereomers depends on the substituent at the acceptor phosphorus centre. When R = Ph or Me and R = Me, only the *RR*/*SS* enantiomers are observed, whereas when R = Me or Ph and R = Ph, both the *meso* and *RR*/*SS* forms are observed (Figure 1.2.10). The underlying reasons for the substituent dependence are not definitively understood.

A seemingly trivial change from the use of PR_3 to R_2PCl as the donor phosphine unlocks numerous secondary reductive coupling pathways yielding di-, tri-, tetra-, penta-, or hexa-phosphorus containing cations depending upon the choice of reducing agent and substituent at the phosphorus centres (Scheme 1.2.9). In each case, the oxidation product is $[R_3SbCl]^{1+}$. The moderate inversion barrier at the tricoordinate, lone-pair bearing phosphorus centres results in temperature-sensitive spin systems and diastereomeric mixtures at room temperature.[78]

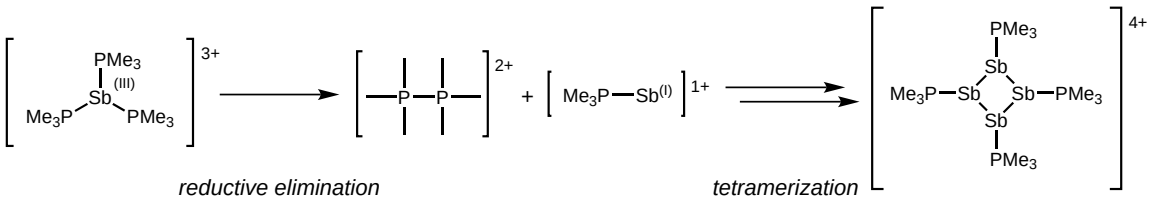

Scheme 1.2.10. Proposed mechanism for assembly of a *cyclic*-tetra(stibinophosphonium) tetracation by reductive elimination from P−Sb^I complexes.

The reductive coupling methodology has been extended to include phosphine complexes of lone-pair bearing Sb^{III} centres. A series of compounds featuring anionic, neutral, monocationic and dicationic chloroantimony centres bound by one or two phosphine ligands have been reported.[36,58] The highly-electrophilic *tris*-phosphine cation, $[(Me_3P)_3Sb]^{3+}$, was isolated, but is unstable and undergoes elimination of a diphosphonium dication, $[Me_3PPMe_3]^{2+}$, at ambient temperatures and cyclizes to give the unique reductively coupled Sb^I tetraphosphine complex, $[(Me_3P)_4Sb_4]^{4+}$ as a quantitative product (Scheme 1.2.10).[22] The oxidative coupling of two PMe_3 units giving $[Me_3PPMe_3]^{2+}$, from the reaction of PMe_3 with $Ph_3Pn(OTf)_2$ (Pn = Sb and Bi), has also been revealed recently.[79]

1.2.3 Summary

Phosphine complexes of lone pair bearing acceptors are now known for almost all elements in groups 13-17, except boron, aluminum, oxygen, and some halogens. However, few examples are known for most elements and, in particular, *tris*-phosphine complexes are only known for four elements. In some cases, such as the group 14 tetrylones, interpretation of compounds as phosphine coordination complexes has only recently been made, and the consequent predictions verified experimentally. Such examples highlight the need for a flexible understanding of the bonding situation in compounds that may not be classically recognized as coordination complexes. As a contribution to this evolving understanding, Chapter 2 provides a case study where oft-assumed correlations between theoretical bonding models and experimental observables are evaluated for the P−P bond. Independent of the bonding models employed, the steric activity of lone pairs at acceptor centres, as assessed from analysis of experimental solid-state structures, offers interesting stereochemical outcomes. Numerous configurational possibilities exist as demonstrated for antimony or bismuth acceptors.

Detailed in Chapter 3 and 4 are insights gleaned from a systematic study of these configurational options and their contribution towards filling gaps in VSEPR theory, which is the primary model used to predict structures in main group chemistry. Section 1.1.2 describes a number of phosphine complexes showing acceptor-centred reactivity including ligand/acceptor exchange, coordination/oxidation and reductive coupling. The most interesting of these, in the context of advancing fundamental main group chemistry and of comparison to transition metal chemistry, is the redox reactivity exhibited by phosphine complexes. This is described in detail for complexes of antimony acceptors in Chapter 5 together with the possibility of general application across the periodic table.

The possibility of modulating the structural and reaction chemistry presented here by appropriate choice of steric and electronic features in the phosphine ligand employed, offers multiple axes of further investigation and the most significant of these are collated in Chapter 8.

Chapter 2

The P−P Bond

The stable and isolable organophosphorus frameworks in Scheme 2.0.1 offer a rare opportunity to assess systematic variations in the fundamental properties of the P−P bond as a function of charge and coordination number. The structure of **2.1** is well-established in the solid state[80] and the gas phase.[81] The phosphinophosphonium cation $[\mathbf{2.2}]^{1+}$ has been characterized in the solid state in triflate[7] and chloride[57] salts, and the diphosphonium $[\mathbf{2.3}]^{2+}$ in its triflate salt.[7] The neutral compounds tetramethyldiphosphine sulfide (**2.4**),[82] tetramethyldiphosphine disulfide (**2.5**),[83] and the triflate salt[84] of the pentamethylphosphoniumphosphine sulfide cation ($[\mathbf{2.6}]^{1+}$) have also been structurally characterized in the solid state.

Calculated and experimental (wherever possible) values for bond strengths, lengths, and stretching frequencies in this series of molecules are presented and trends in these data as a function of substitution and charge evaluated. These features are often assumed to be strongly correlated with one another and this assumption is tested for the P−P case. The resulting insights should apply broadly to a wide swathe of organophosphorus compounds and may have implications for *catena*-element compounds in general.

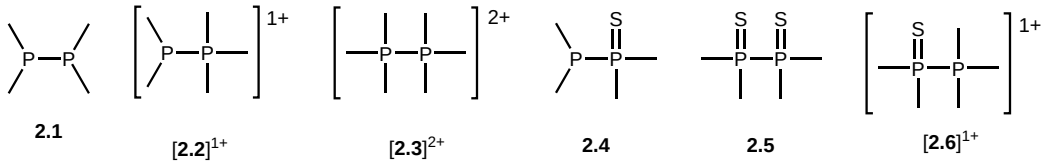

Scheme 2.0.1. Prototypical tricoordinate and tetracoordinate P−P bonded frameworks.

2.1 Bond Strengths

The strength of a covalent bond (E−E') is an important characteristic that determines the reactivity of a molecule and provides insight into its electronic structure. Energies for homolytic and heterolytic dissociation for a given bond can differ substantially. For instance, the S−B bond in [Me_2SBH_3] undergoes facile heterolytic dissociation to give Me_2S and BH_3 (Scheme 2.1.1*a*, E = B, E' = S), while homolytic dissociation into a dimethylsulfide radical cation and borane radical anion is not observed because the electron affinity of BH_3 (0.038 ± 0.015 eV)[85] is much smaller than the ionization energy of Me_2S (8.706 ± 0.010 eV).[86] Consequently, the S−B bond is described as a 'coordinate bond' (or 'dative bond'), and illustrated using the arrow notation, $Me_2S{\rightarrow}BH_3$. In contrast, heterolytic dissociation of a bond such as the C−C bond in ethane requires separation of oppositely charged fragments and is intuitively more endergonic than homolytic dissociation (Scheme 2.1.1*b*, E = E' = C). As a result, vernacular usage of the term 'bond strength' in compounds representing cases *a* and *b* in Scheme 2.1.1 implicitly connote the energy required for heterolytic and homolytic dissociation, respectively.[1–3] By comparison, the thermodynamic difference between the two dissociation routes is ambiguous for bonds in charged molecules (*c* and *d* in Scheme 2.1.1) because it is not *a priori* known whether the production of radical species is more or less favourable than separation of a strong Lewis acid (cation) from a Lewis base (donor). This ambiguity is addressed here by means of high-level quantum-chemical calculations of the various bond cleavage pathways accessible to the compounds in Scheme 2.0.1.

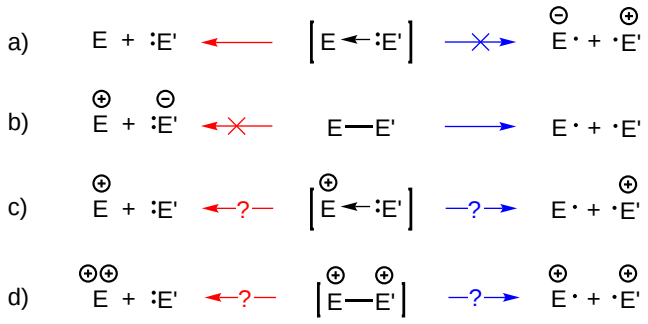

Scheme 2.1.1. Heterolytic (red) and homolytic (blue) dissociation pathways for an E−E' bond.

Similar calculations have been performed previously for subsets of the compounds

considered, but systematic variations have not been assessed explicitly across the series nor have all the possible dissociation routes been considered. For **2.1**, a homolytic dissociation energy was calculated to be in the 220-260 kJ mol^{-1} range.[87] For cations of the class $[Me_3PPR_2]^{1+}$ (of which $[\mathbf{2.2}]^{1+}$ is a prototypical alkyl case), a gas-phase computational study concluded that heterolytic P−P bond dissociation to give $[R_2P]^{1+}$ and PMe_3 was preferred by *ca.* 130 kJ mol^{-1} when R is a π-donating substituent (R = Me_2N), and homolytic dissociation to give Me_2P and $[PMe_3]^{1+}$ was preferred by *ca.* 30 kJ mol^{-1} when R is a σ-donating substituent (R = Me).[88] These difference arise because phosphenium cations $[R_2P]^{1+}$ are resonance stabilized by π-donor substituents, whereas the stability of radical species generally increases with alkyl substitution. An Atoms-In-Molecules (AIM) investigation concluded that the homolytic P−P bond energies calculated from electron densities at bond critical points increased in the order: **2.1** (183 kJ mol^{-1}) < $[\mathbf{2.2}]^{1+}$ (188 kJ mol^{-1}) < $[\mathbf{2.3}]^{2+}$ (190 kJ mol^{-1}).[89]

To comprehensively evaluate the energy content of the P−P bond as a function of charge and coordination number, the Gibbs energies and enthalpies of various P−P bond dissociation processes were calculated at the MP2/cc-pVTZ level at 298 K for the frameworks in Scheme 2.0.1. The results for these gas-phase calculations are compiled in Scheme 2.1.2. The trends in bond enthalpy are reflected in the Gibbs energies as all dissociation processes considered are entropically favourable. Therefore only enthalpy values have been plotted in Figure 2.1.1, which shows trends across the charge and coordination number series. In general, heterolytic processes are more endothermic than homolytic ones but the distinction is small for monocations. For example, the heterolytic dissociation enthalpy of **2.1** into $[PMe_2]^{+}$ and $[PMe_2]^{1-}$ is 735 kJ mol^{-1} more than the homolytic dissociation into two PMe_2 radicals, and a similar distinction is expected for ethane. In contrast, for $[\mathbf{2.2}]^{1+}$, heterolytic dissociation is only 15 kJ mol^{-1} greater than homolytic dissociation. Moreover, the homolytic dissociation of $[\mathbf{2.2}]^{1+}$ is substantially greater than homolytic dissociation of all other frameworks considered except the phosphoniumphosphine sulfide cation, $[\mathbf{2.6}]^{1+}$. The homolytic and heterolytic P−P dissociations of **2.5** have enthalpies that are similar to those of **2.1**, and the former pathway is preferred in both compounds. Heterolytic dissociation of the P−P bond appears to be prohibitively endothermic except in $[\mathbf{2.2}]^{1+}$, $[\mathbf{2.3}]^{2+}$ and $[\mathbf{2.6}]^{1+}$ in which P−P dissociation can occur without separation of oppositely charged ions. The small heterolytic dissociation value for $[\mathbf{2.2}]^{1+}$ and

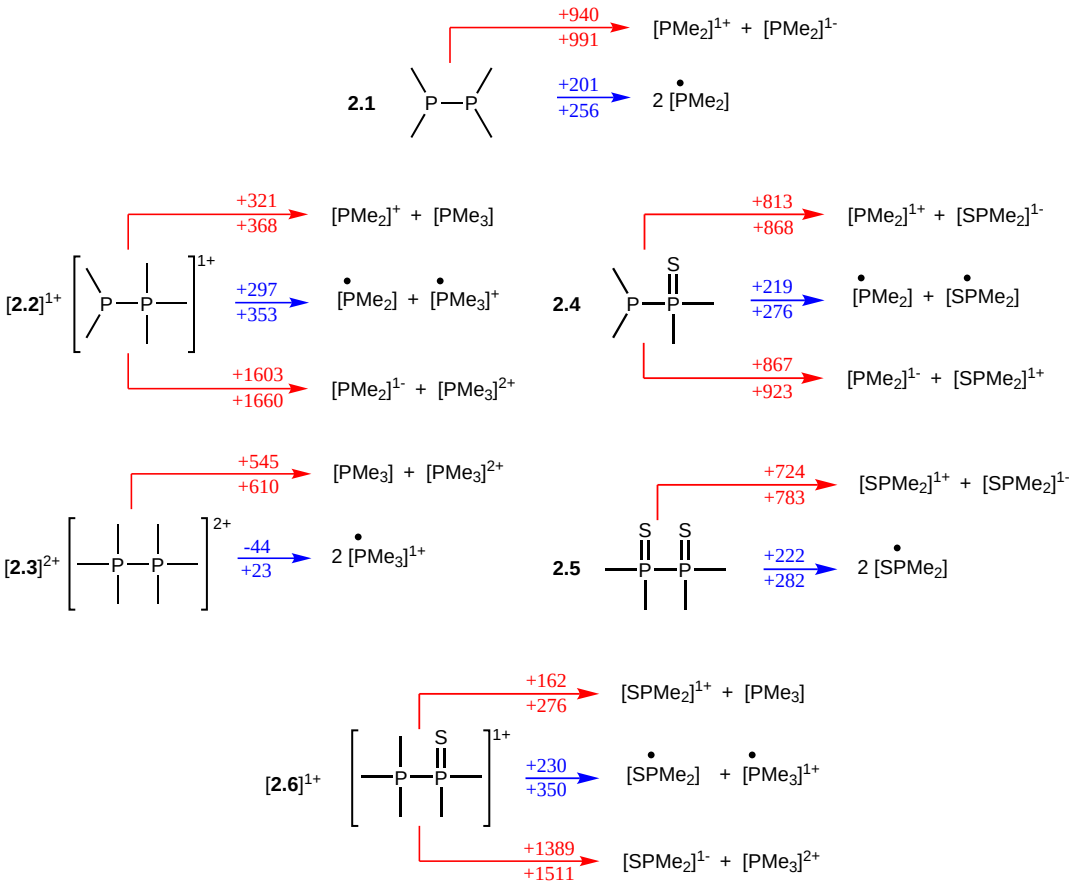

Scheme 2.1.2. Calculated (MP2/cc-pVTZ) reaction Gibbs energies (kJ mol^{-1}, above arrow) and enthalpies (kJ mol^{-1}, below arrow) for the P−P bond dissociation in some prototypical organophosphorus compounds. Pathways in red and blue denote heterolytic and homolytic processes, respectively.

$[\mathbf{2.6}]^{1+}$ predicts that these cations may undergo displacement of the PMe_3 group by a stronger donor such as an N-heterocyclic carbene (NHC) to give the corresponding $[(NHC)P(S)Me_2]^{1+}$ cations, a derivative of which has been prepared *via* a different synthetic route.[90]

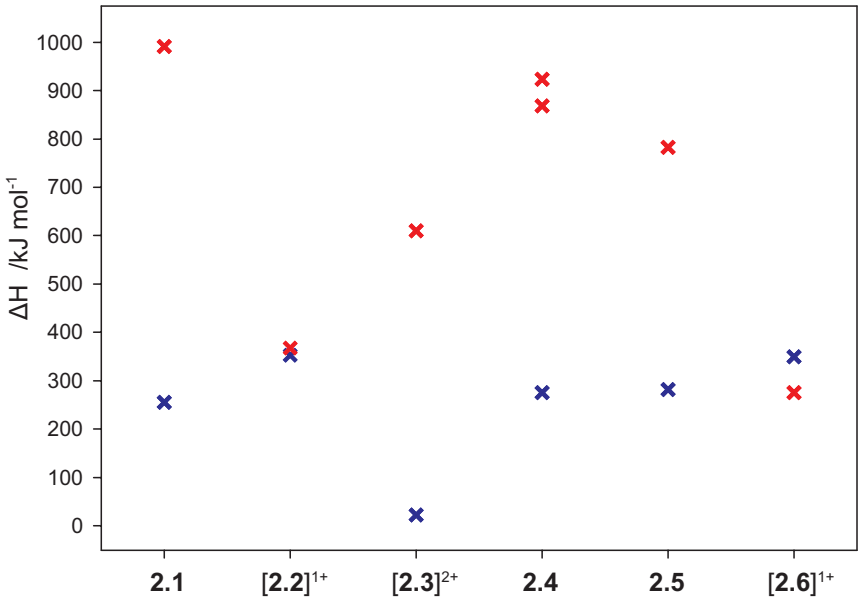

Figure 2.1.1. Homolytic and heterolytic dissociation pathways for an E−E' bond. Pathways in red and blue denote heterolytic and homolytic processes, respectively.

Methylation of **2.1** to give $[\mathbf{2.2}]^{1+}$ effects an increase in the homolytic P−P bond enthalpy of 97 kJ mol^{-1}, and the value for $[\mathbf{2.2}]^{1+}$ (353 kJ mol^{-1}) is of the order of the corresponding C−C bond dissociation enthalpy in simple alkanes such as ethane (377 ± 1 kJ mol^{-1}).[16] This result illustrates the energetic consequences of the similar electronegativities of carbon and phosphorus, as well as the isolobality between alkanes and phosphonium cations, a feature that has enabled the isolation of a diverse family of cationic *catena*-phosphorus compounds representing phosphorus analogues of hydrocarbon frameworks.[19,91] In this context, it is interesting to note that the energy of the dominant P−P σ-bonding MO shows the trend: **2.1** (−11.0 eV) > $[\mathbf{2.2}]^{1+}$ (−16.4 eV) > $[\mathbf{2.3}]^{2+}$ (−21.1 eV), evidencing the dramatic reduction in MO energies upon introduction of cationic charge (Figure 2.1.2). However, correlation of this trend in bonding-MO stabilization with stronger P−P bonds across the charge-variant series is not observed. Specifically, while implication of a substantially strong P−P bond in $[\mathbf{2.2}]^{1+}$ is consistent with the relative homolytic bond enthalpies of

2.1 and $[\mathbf{2.2}]^{1+}$, the relatively low energy of the primary P−P σ-bonding MO in $[\mathbf{2.3}]^{2+}$ is incongruent with calculated metastability of this cation in the gas phase with respect to homolytic dissociation into two $[PMe_3]^{1+}$ radical cations ($\Delta G_{rxn} = -44$ kJ mol^{-1}, $\Delta H_{rxn} = +23$ kJ mol^{-1}). Consideration of these numbers together with those for the sulfur containing derivatives suggests that frameworks involving one or two tetracoordinate centres adopt a relatively strong P−P bond, except in the case of $[\mathbf{2.3}]^{2+}$ (*vide infra*), where any stabilizing influence due to cationic charge is constrained by Coulombic destabilization due to high charge concentration. Therefore, successful isolation of polycations such as $[\mathbf{2.3}]^{2+}$ necessarily depends upon the choice of anions and solid-state thermodynamics. Enhancement by approximately 70 kJ mol^{-1} of the P−P homolytic bond enthalpy due to the presence of a single cationic charge is also evidenced by comparison of the P−P dissociation enthalpies of $[\mathbf{2.2}]^{1+}$ (353 kJ mol^{-1}) and **2.4** (276 kJ mol^{-1}), as well as comparison of $[\mathbf{2.6}]^{1+}$ (350 kJ mol^{-1}) and **2.5** (282 kJ mol^{-1}).

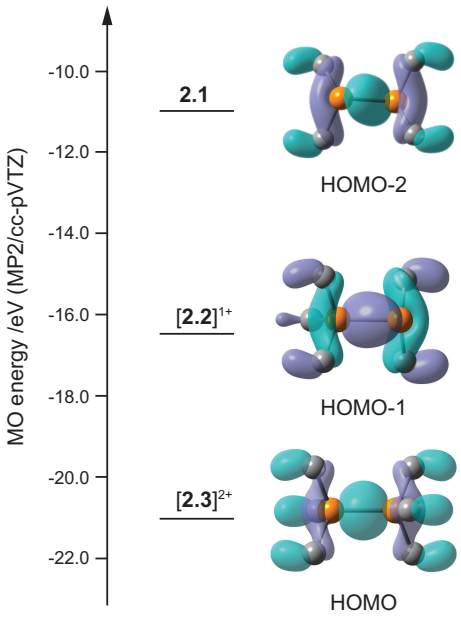

Figure 2.1.2. calculated (MP2/cc-pVTZ) energies and isosurfaces for the principle P−P σ-bonding orbital in **2.1**, $[\mathbf{2.2}]^{1+}$, and $[2.3]^{2+}$.

Despite the facility of homolytic P−P dissociation in $[\mathbf{2.3}]^{2+}$, a stable *bis*-triflate salt of $[\mathbf{2.3}]^{2+}$ has been obtained from three distinct reactions (Scheme 2.1.3): *a*) methylation of $[\mathbf{2.2}][OTf]$,[7] *b*) nucleophilic displacement of *dmap* by PMe_3 from $[(dmap)PMe_3][OTf]_2$,[84] and *c*) reductive elimination from $[(Me_3P)_3Sb][OTf]_3$ or from

$[(Me_3P)_2SbPh_3][OTf]_2$.[22,79] To assess the importance of lattice enthalpies in the formation of an MX_2 salt, as in the case of [**2.3**][$OTf]_2$ from these reactions, Born-Haber-Fajans cycles for the thermodynamically favoured stepwise methylation of **2.1** to give [**2.2**][OTf] and [**2.3**][$OTf]_2$ were constructed (Scheme 2.1.4).

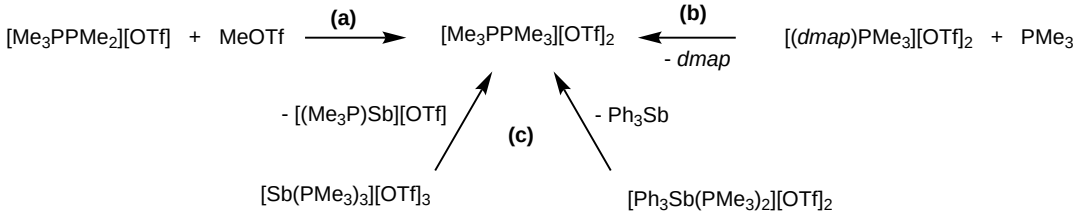

Scheme 2.1.3. Three experimental routes to [**2.3**][$OTf]_2$: *a*) methylation, *b*) nucleophilic displacement, and *c)* oxidative coupling.

The lattice enthalpies of the salts of [**2.2**][OTf] and [**2.3**][$OTf]_2$ were estimated using the Volume-Based-Thermodynamics (VBT) proposed initially by Kapustinksy[92] and further refined for main group ionic species by Glasser and Jenkins.[93] The volume of [**2.3**][$OTf]_2$ was obtained from its crystal structure.[7] Since the solid-state structure of [**2.2**][OTf] is not known, the volume of $[\mathbf{2.2}]^{1+}$ was obtained from [**2.2**][Cl] and added to an average volume for the triflate anion observed in several M[OTf] salts (M = Li, Na, K, NH_4).[94] The enthalpies of vapourization for MeOTf and **2.1** were derived from Trouton's rule using experimentally known boiling points.[16] The most reliable gas-phase enthalpy of dissociation for MeOTf into $[Me]^{1+}$ and $[OTf]^{1-}$ has been reported using calculations at the MP2/aug-cc-pVnZ (n = D, T, Q) level, extrapolated to the complete basis set limit.[94] The P−C bond dissociation enthalpies were calculated at the MP2/cc-pVTZ level.

The P−C bond resulting from the methylation of [**2.2**][OTf] is much weaker (177 kJ mol^{-1}) than that resulting from the first methylation (621 kJ mol^{-1}) and the large difference between the two values evidences the greater Lewis basicity of neutral **2.1** compared to cationic $[\mathbf{2.2}]^{1+}$. Nevertheless, the relatively large lattice enthalpy of [**2.3**][$OTf]_2$ (1432 kJ mol^{-1}) is sufficient to make methylation of [**2.2**][OTf] thermodynamically favoured. A similar analysis is carried out in Scheme 2.1.5 for nucleophilic displacement of *dmap* by PMe_3 from [(*dmap*)PMe_3][$OTf]_2$. The sublimation enthalpy of *dmap* was obtained as a sum of its reported enthalpy of fusion[95] and calculated (Trouton's rule using experimental boiling point) enthalpy of vapourization.[16] Thermochemical analyses of the two reductive elimination pathways (Scheme 2.1.3*c*) are

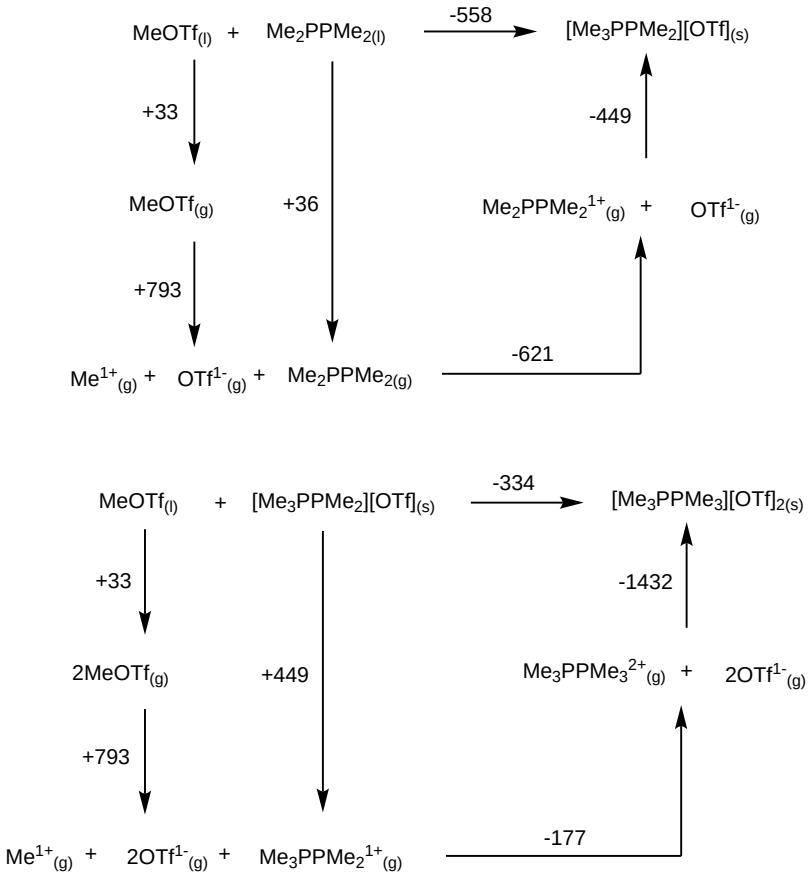

Scheme 2.1.4. Born-Haber-Fajans cycles for the formation of [**2.2**][OTf] and [**2.3**][OTf]$_2$ *via* stepwise methylation of **2.1**. All values are given in kJ mol^{-1}.

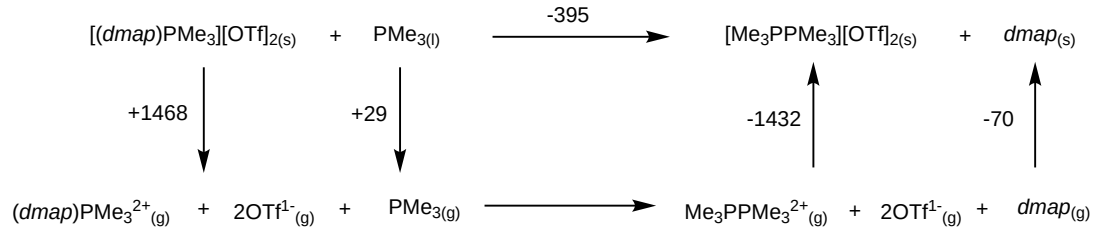

Scheme 2.1.5. Born-Haber-Fajans cycles for the formation of [**2.3**][OTf]$_2$ *via* nucleophilic displacement of *dmap* by PMe_3 from the $[(dmap)PMe_3]^{2+}$ cation. All values are given in kJ mol^{-1}.

precluded by the unknown sublimation enthalpies for the solids.

Scheme 2.1.6 shows the corollary thermochemical cycles for the decomposition of [**2.3**][OTf]$_2$ in the solid state to give free PMe_3 and [PMe_3][OTf]$_2$ (heterolytic P−P dissociation) or to give two equivalents of [PMe_3][OTf] (homolytic P−P dissociation). To estimate the lattice enthalpy of [PMe_3][OTf]$_2$, the volume of the $[PMe_3]^{2+}$ was approximated as 50% of the experimentally-known value for the $[Me_3PPMe_3]^{2+}$ ion, and represents a conservative estimate rather than an accurate value. Nevertheless, due to the large endothermic term arising from heterolytic dissociation of $[\mathbf{2.3}]^{2+}$ in the gas phase, the error in this volume can be as large as 50 % while still yielding a 200 kJ mol^{-1} barrier to the overall decomposition. The volume of the $[PMe_3]^{1+}$ radical cation was calculated as 40% of the known volume of PMe_3 based on the experimental observation that there is a $24 - 44$ % contraction of volume going from neutral PR_3 to the $[PR_3]^{1+}$ radical cation based on examples where crystallographic data for both species exist.[96–99] Since lattice enthalpy is inversely proportional to ionic volume, the 40% volume contraction assumed here provides an upper limit for the lattice enthalpy of [PMe_3][OTf]. Although these assumptions are necessarily crude due to the unavailability of experimental data, the energetic barriers calculated for processes are large enough to be significant and the results demonstrate why [**2.3**][OTf]$_2$ is thermodynamically stable in the solid state with respect to P−P dissociation, despite the manifest facility of the process in gaseous $[\mathbf{2.3}]^{2+}$.*

The similarity of the semi-empirical homolytic (+447 kJ mol^{-1}) and heterolytic (+490 kJ mol^{-1}) P−P bond dissociation enthalpies in the solid state suggests that solutions of [**2.3**][OTf]$_2$ may exhibit reactivity consistent with both dissociation modes depending upon the reaction conditions. Although these experiments have not been the reported, a reactivity study of the closely related salt, hexapropyldiphosphonium diperchlorate, [Pr_3PPPr_3][ClO_4]$_2$, showed that reaction with dipropyldisulfide (PrS-SPr) yields [Pr_3P−SPr][ClO_4], thereby implicating homolytic P−P and S−S dissociation.[101] In addition, solutions of [Pr_3PPPr_3][ClO_4]$_2$ react with fluoride in

*An important limitation of Born-Haber-Fajans thermochemical analysis is that kinetic barriers to dissociation, which may also play a role in stabilizing the diphosphonium dication, are not considered. A thorough computational assessment of the transition state and any intermediates along the dissociation reaction coordinate will undoubtedly reveal further insight, but such an analysis has not yet been attempted. Dissociation curves for homolytic bond cleavage involving 1,2-dications can be deceptively complicated since excited states are known to be prevalent and even for a seemingly simple dissociations, the possibility of multiple pathways featuring electronic state crossover cannot be precluded.[100]

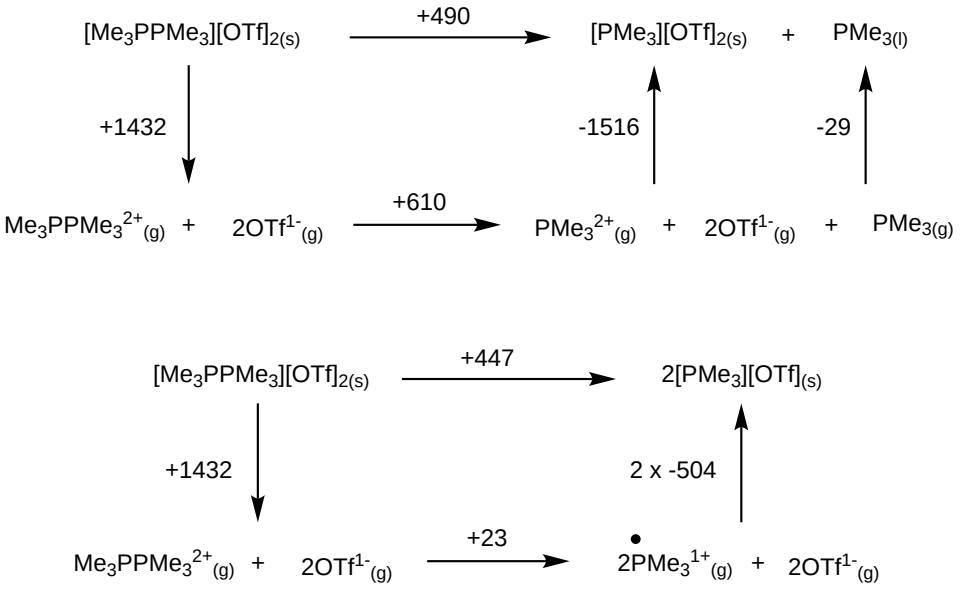

Scheme 2.1.6. Born-Haber-Fajans cycles for heterolytic (top) and homolytic (bottom) dissociation of the P−P bond in [**2.3**][OTf]$_2$. All values are given in kJ mol^{-1}.

$[NEt_4][F]$ to yield Pr_3PF_2 and free PPr_3, indicative of heterolytic P−P bond dissociation.[101]

In the context of the ambiguity highlighted in Scheme 2.1.1, the energy calculations presented here suggest that in *catena*-phosphorus monocations, homolytic and heterolytic P−P bond cleavage are both equally favoured but for dications the former may be preferred, at least in the gas phase. Therefore, stability in salts of $[\mathbf{2.3}]^{2+}$ requires careful anion choice and lattice enthalpy considerations, but derivatives of $[\mathbf{2.2}]^{1+}$ feature a strong P−P bond that is comparable to C−C bonds. As illustrated in the next section, the strength of this bond has now yielded the most atom-efficient route possible for the synthesis of phosphinophosphonium salts.

2.1.1 The P−P Menschutkin Reaction

The Menschutkin reaction yields alkylammonium halide salts from an alkyl halide and an amine,[102] representing interaction of a Lewis basic nitrogen centre with a Lewis acidic carbon center to eliminate a halide anion. The reaction offers a facile approach to N−C bond formation, and the methodology should be broadly applicable across the periodic table so long as *i)* the strength of the donor-acceptor interaction is greater than the strength of the acceptor-halide interaction, and *ii)* the acceptor centre is coordinatively saturated so that an increase in the coordination number is not favourable. For example, select imine derivatives have been shown to displace a chloride from chloroaminophosphines to give oniophosphines.[103] There is also scattered NMR spectroscopic data and elemental analytical data indicating Pn-Pn' bond formation (Pn = P, As, Sb) in reactions of pnictines with halopnictines.[104–108] However in the absence of solid-state structures, distinction between hypervalent molecular adducts or ion-separated salts cannot be made unambiguously.

This section provides definitive confirmation of a homoatomic P−P Menschutkin reaction and demonstrates that Me_2PCl and Ph_2PCl are both sufficiently Lewis acidic to engage alkylphosphines as donors to form P−P bonds yielding phosphinophosphonium frameworks. The reaction has been used to prepare the chloride salt of the prototypical organophosphinophosphonium cation, $[Me_3PPMe_2]^{1+}$, which has been comprehensively characterized and compared with salts formed *via* activation of chlorophosphines by added Lewis acid and with salts containing weakly coordinating anions.

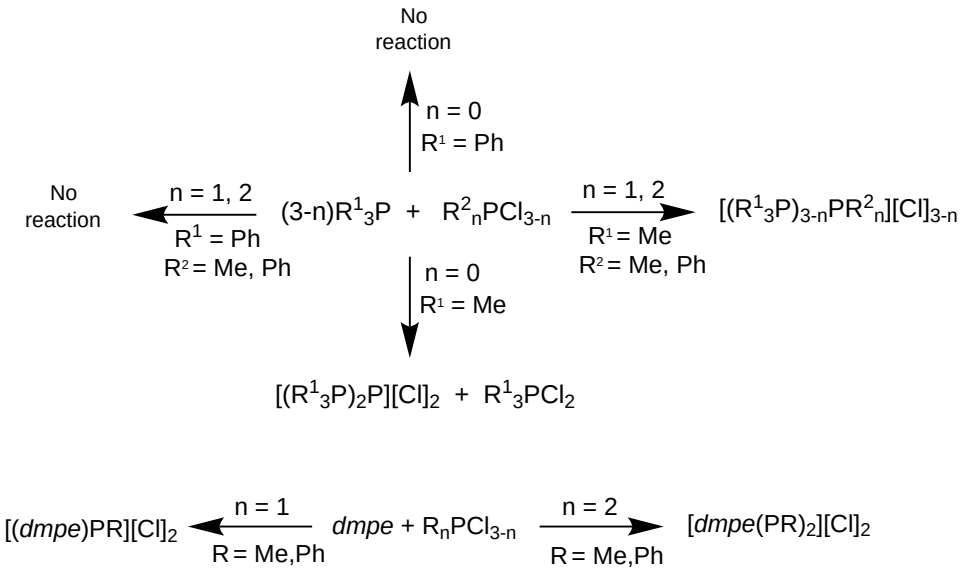

Scheme 2.1.7. P−P Menschutkin synthesis of phosphinophosphonium cations.

Table 2.1.1 lists the products identified by ^{31}P Cross Polarization Magic Angle Spinning (CP-MAS) NMR† spectroscopy from mixtures of PR^1_3 (R^1 = Me, Ph) with $R^2_nPCl_{3-n}$ (R^2 = Me, Ph; n = 0, 1, 2) or *dmpe* as illustrated in Scheme 2.1.7. PMe_3 reacts with Me_2PCl or $MePCl_2$ either in the gas phase (as vapours at room temperature), in neat mixtures, or in organic solvents to give [**2.2**][Cl] and $[(Me_3P)_2PMe][Cl]_2$, respectively, and *dmpe* reacts with Me_2PCl or $MePCl_2$ upon contact to give compounds $[dmpe(PMe_2)_2][Cl]_2$ and $[(dmpe)PMe)][Cl]_2$, respectively. All reactions proceed quantitatively and rapidly according on the stoichiometry of the mixture. Reactions of PMe_3 or *dmpe* with Ph_2PCl and $PhPCl_2$ in CH_2Cl_2 give $[Me_3PPPh_2][Cl]$, $[(Me_3P)_2PPh][Cl]_2$, $[dmpe(PPh_2)_2][Cl]_2$ and $[(dmpe)PPh][Cl]_2$. Reaction of PMe_3 with PCl_3 yielded a mixture of insoluble polymeric material, Me_3PCl_2 and $[(Me_3P)_2P][Cl]$, identified by comparison of its ^{31}P chemical shifts and coupling constants with known triphosphenium cations.[109] The composition of the chloride salts was established by elemental analysis and ^{31}P NMR spectroscopy. The ionic formulation is supported by comparison of their chemical shifts and $^1J_{PP}$ coupling constants with those of the reported triflate derivatives (Table 2.1.1), several of which have now been structurally authenticated as ionic species.

Table 2.1.1. ^{31}P NMR data for P−P bonded cations in their chloride (triflate) salts.

Compound	Spin system	δ^{31}P (ppm)	$^1J_{PP}$ (Hz)
$[\mathbf{2.2}]^{1+}$	AX	+20, -66 (+18, -59)[7]	242, 256 (274)
$[(Me_3P)_2PMe]^{2+}$	AXX'	+20, -63 (+25, -63)[110]	broad (285, 295)
$[dmpe(PMe_2)_2]^{2+}$	AX	+30, -75 (+24, -58)	272 (broad)
$[(dmpe)PMe]^{2+}$	AXX'	+50, -86 (+53, -88)	296, 271 (278, 283)
$[Me_3PPPh_2]^{1+}$	AX	+15, -24 (+15, -23)[7]	broad (289)
$[(Me_3P)_2PPh]^{2+}$	AXX'	+31, -51 (+24, -46)[110]	broad (286, 298)
$[dmpe(PPh_2)_2]^{2+}$	AX	+19, -15 (+21, -21)[34]	broad (300)
$[(dmpe)PPh]^{2+}$	AXX'	+48, -77 (+53, -68)	broad (277, 275)
$[(Me_3P)_2P]^{1+}$	AXX'	+18, -146 (+15, -156)	434 (439, 438)

Figure 2.1.3 shows a representative ^{31}P CP-MAS NMR spectrum for the precipitate

†The solid-state CP-MAS NMR spectra presented in this section were obtained by Dr. Elizabeth MacDonald and Dr. Ulrike Werner-Zwanziger at Dalhousie University. Their contributions are gratefully acknowledged.

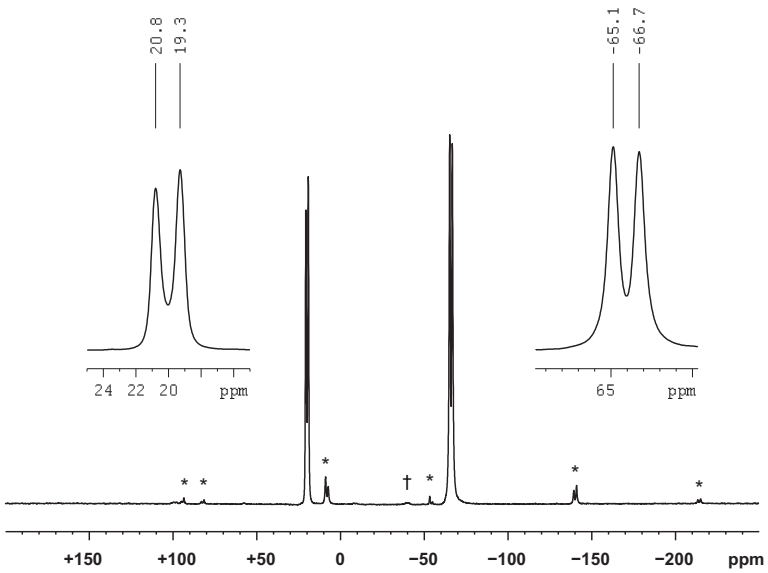

Figure 2.1.3. ^{31}P CP-MAS spectrum of [**2.2**][Cl]. Asterisks indicate isotropic peaks and dagger indicates unidentified impurities.

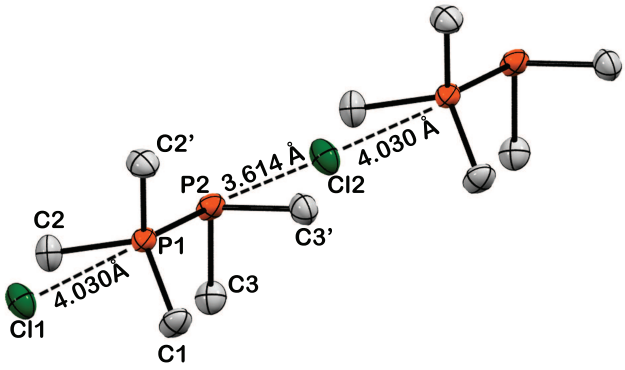

Figure 2.1.4. Solid-state structure of [**2.2**][Cl]. Hydrogen atoms have been omitted for clarity. Selected bond lengths (Å) and angles (°): P1−P2 = 2.1767(6), P1−C1 = 1.790(2), P1−C2/C2' = 1.7855(15), P2−C3/C3' = 1.8329(15), C1−P1−C2/C2' = 108.9, C2−P1−C2' = 106.3, C3−P2−C3' = 100.7, P1−P2−C3/C3' = 98.2, P1−P2−Cl2 = 178.4, C1−P1−P2−C3/C3' = 51.1.

of the reaction between PMe_3 and Me_2PCl. The distinctive doublets yield a $^1J_{PP}$ coupling constant of 249 Hz, which is consistent with that observed for [**2.2**][OTf] (274 Hz).[7] In contrast to reactions of PMe_3 or *dmpe*, ^{31}P NMR spectra of mixtures involving PPh_3 with Me_2PCl, $MePCl_2$, Ph_2PCl, $PhPCl_2$, and PCl_3 show only signals corresponding to starting materials, even after prolonged heating.

Crystals of [**2.2**][Cl] were obtained from a dilute MeCN solution, and found to be suitable for diffraction (Figure 2.2.1). In the solid state, $[\mathbf{2.2}]^{1+}$ adopts a staggered conformation about the P−P bond. The closest interion P−Cl distance (3.614 Å) occurs at P2, *trans* to P1, and is significantly longer than the sum of the van der Waals radii for the two elements ($\Sigma_{r,vdW}$ = 3.55 Å)[111]. The excellent ion separation supports formulation of this compound as a salt and provides the first unambiguous evidence of a P−P Menschutkin reaction. The nearly linear P1-P2-Cl2 angle (178.4 °) in the structure of $[\mathbf{2.2}]^{1+}$ is a vestigial remnant of the associative nucleophilic displacement process (S_N2) that led to its generation. The disphenoidal acceptor site (P2) featuring the incoming nucleophile (phosphine) and the outgoing halide on the same axis is the phosphorus analogue to the canonical trigonal bipyramidal acceptor carbon centre in the C−N Menschutkin reaction.

The Born-Haber-Fajans cycle for the formation of [**2.2**][Cl] shown in Scheme 2.1.8 (top cycle) has been constructed using experimentally measured enthalpies of vaporization (ΔH_{vap} for PMe_3[112] and Me_2PCl[113]), experimental and calculated values for the chloride-ion-affinities (ΔH_{CIA}) of $AlCl_3$[114] and $[Me_2P]^{1+}$, respectively , calculated value for the P−P bond strength in $[\mathbf{2.2}]^{1+}$ (ΔH_{PP}), and lattice enthalpies ($\Delta H_{lat.}$) calculated using Volume Based Thermodynamics,[93] to give the overall ΔH_{rxn} of −14.2 kJ mol^{-1}. The small magnitude of ΔH_{rxn} renders the overall thermodynamics sensitive to small changes in ΔH_{PP} and $\Delta H_{lat.}$ and these variations are the reason for previous reports of reaction mixtures containing longer-chained trialkylphosphines and alkyl- or arylhalophosphines producing thermally unstable adducts and redox decomposition products. In particular, the inverse relationship between $\Delta H_{lat.}$ and the volume of the interacting ions makes $\Delta H_{vap.}$ less negative for larger trialkylphosphines. However, when a powerful Lewis acid such as $AlCl_3$ is added, there is a clear thermodynamic drive towards formation of phosphinophosphonium salts, despite the slightly larger anionic volume (Scheme 2.1.8, bottom cycle).

The large value of ΔH_{CIA} for $[Me_2P]^{1+}$ (770 kJ mol^{-1}) precludes heterolytic disso-

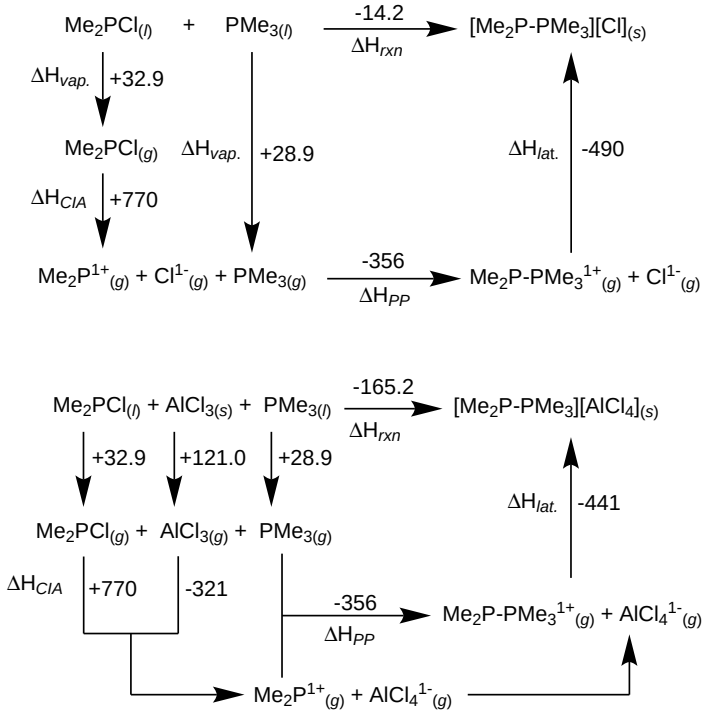

Scheme 2.1.8. Born-Haber-Fajans cycle for the formation of [**2.2**][Cl] and [**2.2**][$AlCl_4$]. All values are given in kJ mol^{-1}.

ciation of Me_2PCl as a plausible step prior to P−P bond formation, and consistently, the reaction proceeds rapidly even in non-polar solvents such as pentane and benzene. *Ab initio* calculations indicate that the LUMO for both Me_2PCl and Ph_2PCl is the P-Cl σ*-antibonding orbital. On this basis, the reaction is interpreted as a bimolecular Menschutkin process, driven by the ΔH_{PP} and $\Delta H_{lat.}$ of the phosphinophosphonium salt and facilitated by the occupation of the P-Cl σ*-MO in the acceptor by the lone pair HOMO of the donor phosphine (Figure 2.1.5). Appropriate consideration of these parameters should enable isolation of more diverse and complex *catena*-phosphorus frameworks.

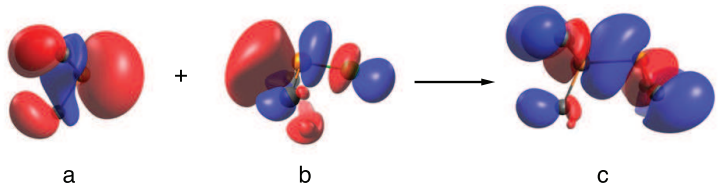

Figure 2.1.5. Pictorial representation of *a)* the HOMO in PMe_3, *b)* the LUMO in Me_2PCl, and *c)* the HOMO-1 P−P bonding molecular orbital in $[\mathbf{2.2}]^{1+}$.

2.2 Bond Lengths

Experimental solid-state structures are now known for all compounds in Scheme 2.0.1. The structure of cation $[\mathbf{2.2}]^{1+}$ in its chloride salt was described in the previous section. The solid-state structure of **2.5** (Figure 2.2.1) was redetermined at 173.15 K and refined to a R_1 value of 2.1%, since a previously-reported structure (295 K, R_1 = 8.9%)[83] was found to have unacceptably large estimated standard deviations for a detailed discussion.[‡] The compounds were also modelled in the gas phase at the PBE1PBE/aug-cc-pVTZ level in the absence of triflate or chloride anions. Calculated bond lengths are approximately 0.01 Å longer than experimental ones in the majority of cases, and this small discrepancy between compounds in the solid and gas phase is a well-known phenomenon[115] arising from the polarized environment of the crystal lattice and interion or intermolecular contacts.

[‡]Two unique molecules are found in the unit cell, with statistically different P−P and P−C bond lengths . For clarity, the discussion for this compound uses averaged values from the two molecules.

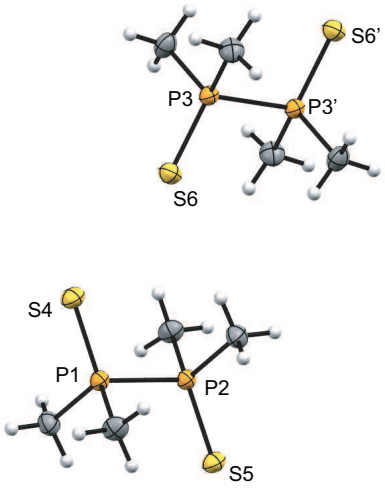

Figure 2.2.1. Molecular structure of **2.4** in the solid state.

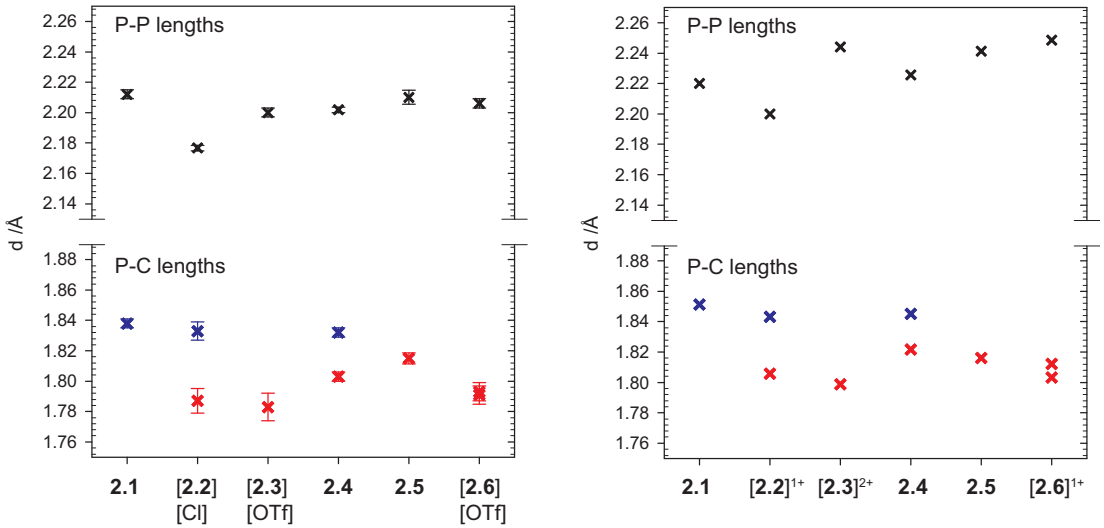

Figure 2.2.2. Experimental (left) and calculated (PBE1PBE/aug-cc-pVTZ, right) P−P and P−C bond lengths for some prototypical organophosphorus compounds. Calculated values are for gas-phase species in the absence of anions. Red and blue coloured data points denote P−C bonds involving four-coordinate and three-coordinate phosphorus centres, respectively.

Experimental and calculated variations in d_{PE}, where E = P or C, are illustrated in Figure 2.2.2, where the error bars for experimental values denote ±3 standard deviations for bond distances. The P−P bond in [**2.2**][Cl] is *ca.* 0.03 Å shorter than that in **2.1**, which is interpreted as being a consequence of the radial extent contraction and the associated energetic lowering of molecular orbitals upon introduction of cationic charge (see Figure 2.1.2). Between the phosphinophosphonium and the diphosphonium, a second unit of charge is introduced, and despite the lowering of the P−P bonding MO, d_{PP} increases by *ca.* 0.02 Å in [**2.3**][$\mathrm{OTf}]_2$. The lengthening in this case is attributed to Coulombic repulsion due to the adjacency of the two formally positive phosphonium centres in the dication, which apparently more than compensates for the MO stabilization.

The trend is qualitatively reproduced in the calculated values, although these show d_{PP} elongation for the diphosphonium that is nearly twice the experimental value, making it slightly longer than d_{PP} in **2.1**. The results suggest that the relatively long P−P bond in the anion-free, gas-phase model is attenuated in the solid state due to interion contacts, which is unsurprising for a dicationic formulation. Consistently, an AIM study of electron density obtained from a high-resolution X-ray diffraction experiment showed the presence of bond critical path between the CH_3 protons of the cation and the oxygen atoms of the triflate anions, interpreted as evidence of hydrogen bonding interactions.[89] Similar hydrogen bonding interactions are also evident in the solid-state structure of [**2.2**][Cl] (Figure 2.2.3). For the diphosphonium, partial quenching of the dicationic charge, *via* the proton mediated transfer of electron density from the anion to the cation, alleviates the Coulombic repulsion between two adjacent phosphoniums. However, in the gas phase, where such quenching is absent, the P−P bond spans the vexed gap between two formally cationic centres, experiencing the maximal extent of their mutual repulsion.

The P−P distances in the sulfur compounds also show small variations and calculated values increase with oxidation of the phosphorus centre with either sulfur or a methyl cation, the latter having a seemingly larger effect as demonstrated by the longer value of d_{PP} in cationic [**2.6**]$^{1+}$ than in neutral **2.5**. Here too the effect in the solid state appears to be attenuated by intermolecular and interion contacts.

Experimental and calculated values of d_{PC} involving tetracoordinate centers (Figure 2.2.2, red datapoints) are systematically, approximately 0.04 Å shorter than those

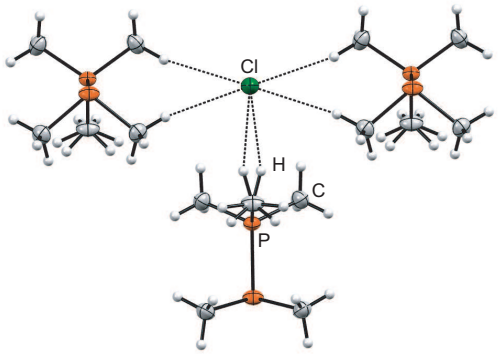

Figure 2.2.3. Molecular structure of [**2.2**][Cl] in the solid state showing hydrogen bonding interactions.

involving tricoordinate phosphine centers (Figure 2.2.2, blue datapoints), which are essentially equivalent to those in **2.1** (1.838 Å). For example, the P−C bonds at tetracoordinate centers in [**2.3**][OTf]$_2$, **2.5**, and [**2.6**][OTf] are similar to each other and are shorter than the P−C bonds at the tricoordinate centers in **2.1**, [**2.2**][OTf], and **2.4**. Contraction of the P−C bonds is interpreted as being consistent with partial delocalization of cationic charge over the hydrocarbyl frameworks in these compounds, as evidenced for the cations in the form of hydrogen bonding interactions involving the methyl groups.

2.3 Bond Stretching Frequencies

Figure 2.3.1 shows the room-temperature infrared spectra of **2.1**, [**2.2**][OTf] and [**2.3**][OTf]$_2$, together with the low-temperature (−75 °C) Raman spectra of powdered **2.1**, [**2.2**][OTf], and [**2.3**][OTf]$_2$. While, the P−P stretching mode (*ca.* 450 cm^{-1}) is infrared-silent in **2.1** and [**2.3**][OTf]$_2$, and weak in [**2.2**][OTf], it is Raman active and intense in all cases. At room temperature, **2.1** exists as an equilibrium mixture of *trans* (D_{2h}) and *gauche* (C_s) conformers in a 60:40 ratio.[116] Upon cooling to −75 °C, only the *trans* isomer is observed in the Raman spectrum of solid **2.1**. The presence of an inversion center in [**2.3**]$^{2+}$ is responsible for mutual exclusion of peaks between the infrared and Raman modes for the dication. Observation of this mutual exclusion also confirmed that factor group splitting of spectral lines arising from reduction of free-molecule point symmetry due to lattice interactions is insignificant for these compounds. In Figure 2.3.1, fourteen triflate anion frequencies (marked by asterisks) were assigned by comparison with a previous vibrational studies of this anion.[117–119] The assignments were further confirmed by comparing the low-temperature Raman spectrum of the chloride and triflate salts of the [**2.2**]$^{1+}$ cation (Figure 2.3.2).

Isotopic shifts for modes involving carbon atoms were used to obtain unambiguous assignment of the heavy atom stretching modes in these compounds. The C-13 enriched (99 atom %) isotopomer of **2.1** (**2.1***) was made *via* reduction of the enriched disulfide, **2.5***, which was in turn prepared from $^{13}CH_3Br$ and $SPCl_3$ using procedures established for the natural abundance analogue.[110] Stepwise methylation of **2.1*** with $^{13}CH_3$-OTf (*i.e.* C-13 enrichment of only the CH_3 carbon in MeOTf) yielded 99 % C-13 enriched cations [**2.2***]$^{1+}$, and [**2.3***]$^{2+}$ with triflate counterions at

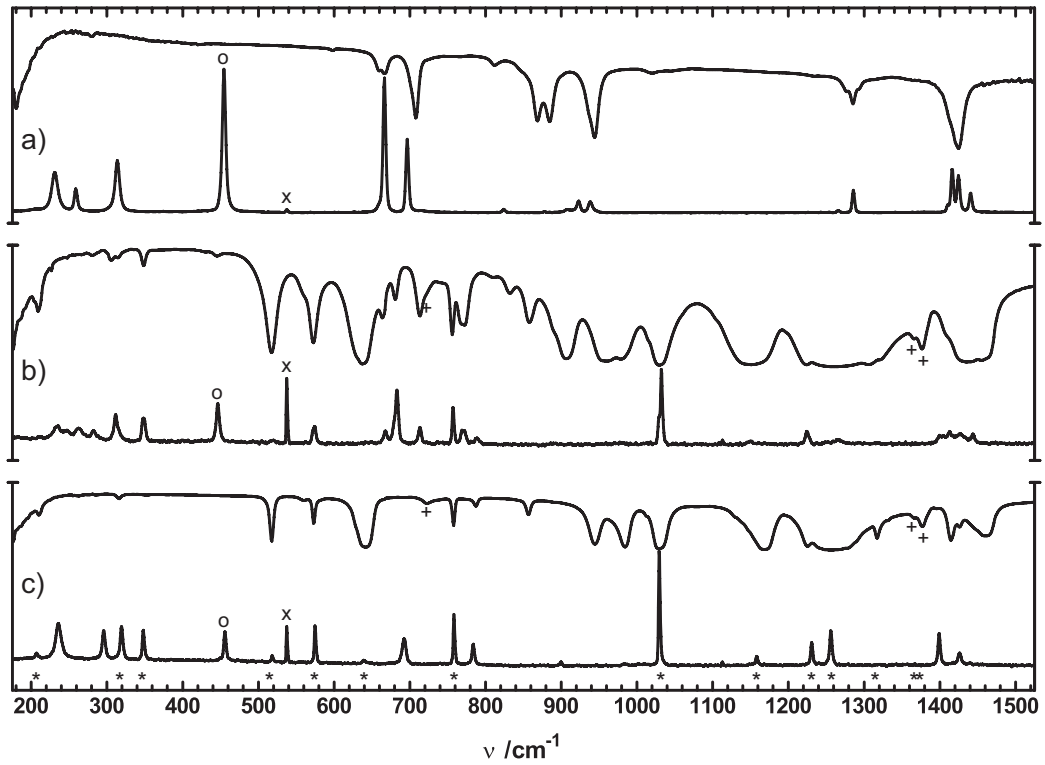

Figure 2.3.1. Raman (bottom, -75 °C, Pyrex tube, 1064 Å excitation) and infrared (top, 25 °C, CsI plates) spectra of a) **2.1**, [**2.2**][OTf], and [**2.3**][OTf]$_2$. Symbols denote anion modes (∗), the P-P stretching mode (o), Nujol modes (+), and an instrumental artifact (×).

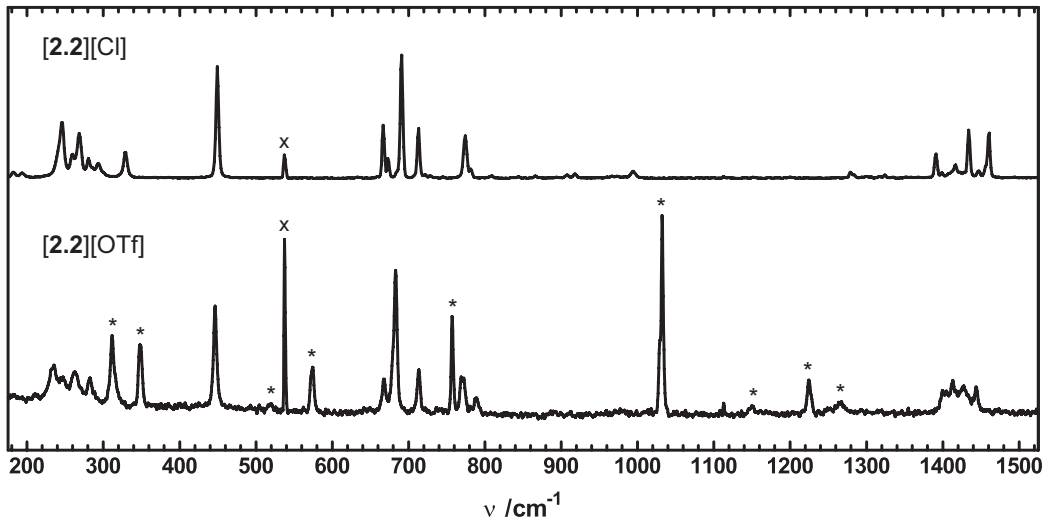

Figure 2.3.2. Raman spectrum of cation $[\mathbf{2.2}]^{1+}$ in its chloride and triflate salt. Asterisks denote peaks due to the triflate anion.

natural abundance levels.[§] The low-temperature Raman spectra of all isotopomers were obtained under identical conditions as their natural abundance analogues, yielding isotopic shift data for modes involving carbon atoms. As a representative example, Figure 2.3.3 compares spectra obtained for [**2.3**][OTf]$_2$ and [**2.3***][OTf]$_2$. The ν_{PP} frequencies (o) show minimal shifts (3 cm^{-1}) between the isotopomers, consistent with this vibrational mode being decoupled from any of the P−C stretching modes. By comparison, the ν_{EC} (E = P, H) modes show isotopic shifts of 11-16 cm^{-1}.

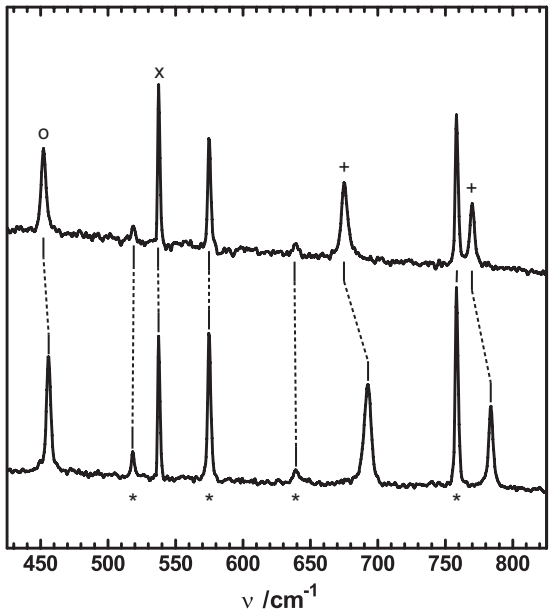

Figure 2.3.3. Raman spectrum (425−825 cm^{-1}) of [**2.3***][OTf]$_2$ (top) and [**2.3**][OTf]$_2$ (bottom). Symbols denote the P−P stretching mode (o), P−C stretching modes (+), and peaks due to natural abundance triflate anion (*) present in both salts.

Raman frequencies, intensities, and isotopic shifts were also calculated for the natural abundance and enriched gas-phase, anion free, species at the PBE1PBE/aug-cc-pVTZ level. As a benchmarking exercise, the suitability of HF, MP2 and a variety of hybrid DFT functionals was tested using experimental values of the P−P stretching frequencies in **2.1**, [**2.2**][OTf], and [**2.3**][OTf]$_2$, which fortuitously appears as the only peak in the P−P stretching region (400−500 cm^{-1} for single bonds). While calculations carried out at the MP2 level provided the closest match with experimental values of ν_{PP}, calculation of Raman intensities at this level with the large aug-cc-pVTZ basis

[§]The C-13 labelled compounds presented in this section were prepared by Dr. J. Marc Whalen, who also obtained their low temperature vibrational spectra. These contributions are gratefully acknowledged.

set was prohibitively memory-intensive. HF level calculations were accurate at low frequencies but deviated significantly from experimental values at higher frequencies. Therefore, the PBE1PBE functional was chosen for calculating intensities, isotopic shifts and visualizing atomic displacements.

The calculated values were compared with the experimental data to obtain corresponding pairs of experimental and calculated peaks and frequencies. Mutual exclusion of infrared and Raman modes also aided assignments for centrosymmetric **2.1** and [**2.3**]$^{2+}$. The atomic displacement vectors associated with each calculated mode were visualized to derive a set of approximate mode assignments, which describe the skeletal deformations that give rise to each peak in the experimental spectra. The data pertaining to the most important stretching modes are collated in Table 2.3.1 with atomic labels given in Scheme 2.3.1. Although the absolute values of the calculated frequencies vary, on average, by 13 cm^{-1}, the excellent match between observed and calculated isotopic shifts provides definitive confirmation of the assignments and their associations with the described molecular vibrations.

The infrared spectrum of **2.4** was obtained at room temperature and could be assigned straightforwardly without the need of isotopic enrichment. A vibrational analysis of **2.5** has been reported previously, comprehensively assigning the key stretching modes.[120] Similarly, the Raman spectrum of [**2.6**][OTf] has been reported previously.[84] Reported assignments were also corroborated by calculations (PBE1PBE/aug-cc-pVTZ) and the results are given in Tables 2.3.2, 2.3.3, and 2.3.4.

Table 2.3.1. Selected experimental and calculated Raman frequencies and intensities (in parentheses) for the natural abundance and C-13 enriched isotopomers of **2.1**, [**2.2**][OTf], and [**2.3**][$OTf]_2$.

		expt.			calcd.		approximate mode description
	2.1	**2.1***	Δ	**2.1**	**2.1***	Δ	
P−P	455(57)	456(78)	1	459(10)	459(10)	0	$\nu_{P_1P_2}$
P−C	666(53)	651(51)	15	677(29)	661(27)	16	$\nu_{P_1C_{11}+P_1C_{12}+P_2C_{21}+P_2C_{22}}$
	697(26)	683(26)	14	712(18)	699(17)	13	$\nu_{P_1C_{11}+P_2C_{22}-P_1C_{12}-P_2C_{21}}$
	[**2.2**][OTf]	[**2.2***][OTf]	Δ	[**2.2**]$^{1+}$	[**2.2***]$^{1+}$	Δ	
P−P	446(32)	444(55)	2	435(13)	432(14)	3	$\nu_{P_1P_2}$
P−C	668(12)	651(22)	17	672(3)	656(2)	16	$\nu_{P_1C_{11}+P_1C_{12}-P_2C_{21}-P_2C_{22}-P_2C_{23}}$
	683(42)	666(64)	17	681(31)	664(29)	17	$\nu_{P_1C_{11}+P_1C_{12}+P_2C_{22}+P_2C_{23}}$
	713(15)	699(27)	14	725(8)	710(7)	15	$\nu_{P_1C_{11}-P_1C_{12}}$
	769(13)	n.o.	–	766(6)	752(8)	14	$\nu_{P_2C_{22}-P_2C_{21}+P_2C_{23}}$
	773(12)	n.o.	–	773(5)	758(4)	15	$\nu_{P_2C_{21}-P_2C_{22}}$
	[**5.3**][$OTf]_2$	[**5.3***][$OTf]_2$	Δ	[**5.3**]$^{2+}$	[**5.3***]$^{2+}$	Δ	
P−P	456(24)	452(34)	4	428(17)	425(18)	3	$\nu_{P_1P_2}$
P−C	692(20)	675(14)	17	672(36)	656(32)	16	$\nu_{P_1C_{11}+P_1C_{12}+P_1C_{23}+P_2C_{21}+P_2C_{22}+P_2C_{23}}$
	784(17)	770(24)	14	766(9)	752(8)	14	$\nu_{P_1C_{11}+P_1C_{13}+P_2C_{21}+P_2C_{23}-P_1C_{12}-P_2C_{22}}$

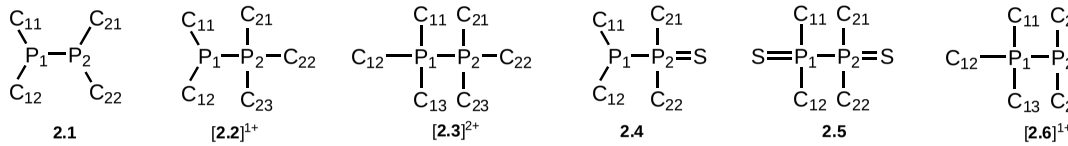

Scheme 2.3.1. Atom labelling scheme used in Tables 2.3.1, 2.3.2, 2.3.3, and 2.3.4.

Table 2.3.2. Selected experimental and calculated infrared frequencies for natural abundance **2.4**. Calculated intensities (km mol^{-1}) are given in parentheses.

	expt.	calcd.	approximate mode assignment
P−P	423 (m)	418 (5)	$\nu_{P_1P_2}$
P−C	586 (vs)	607 (43)	$\nu_{P_2C_{21}} + \nu_{P_2C_{22}} + \nu_{P_2S-P_1P_2}$
	670 (w)	684 (1)	$\nu_{P_1C_{11}} + \nu_{P_1C_{12}}$
	711 (m)	723 (2)	$\nu_{P_1C_{11}-P_1C_{12}}$
	722 (vs)	735 (46)	$\nu_{P_2C_{21}} + \nu_{P_2C_{22}}$
	745 (m)	741 (15)	$\nu_{P_2C_{21}-P_2C_{22}}$

Table 2.3.3. Selected experimental[120] and calculated Raman (R) or infrared (IR) frequencies for natural abundances **2.5**. Experimental intensities were not reported.

	expt.	calcd.	approximate mode assignment
P−P	435 (R)	438 (R)	$\nu_{P_1P_2}$
P−C	730 (R)	750 (R)	$\nu_{P_1C_{12}} + \nu_{P_2C_{22}} - \nu_{P_1C_{11}} - \nu_{P_2C_{21}}$
	733 (IR)	758 (IR)	$\nu_{P_1C_{11}} + \nu_{P_2C_{22}} - \nu_{P_1C_{12}} - \nu_{P_2C_{21}}$
	743 (R)	760 (R)	$\nu_{P_1C_{11}} + \nu_{P_1C_{12}} + \nu_{P_2C_{21}} + \nu_{P_2C_{22}}$
	746 (IR)	765 (IR)	$\nu_{P_1C_{11}} + \nu_{P_1C_{12}} - \nu_{P_2C_{21}} - \nu_{P_2C_{22}}$

Table 2.3.4. Selected experimental[84] and calculated Raman frequencies and intensities (in parentheses) for natural abundance $[\mathbf{2.6}]^{1+}$.

	expt.	calcd.	approximate mode description
P−P	442 (30)	415 (19)	$\nu_{P_1P_2}$
P−C	591 (28)	602 (21)	$\nu_{P_2C_{21}} + \nu_{P_2C_{22}} + \nu_{P_2S}$
	672 (27)	672 (26)	$\nu_{P_1C_{11}} + \nu_{P_1C_{12}} + \nu_{P_1C_{13}}$
	769 (14)	745 (8)	$\nu_{P_2C_{21}-P_2C_{22}}$

Experimental values of ν_{PP} exhibit the trend: $\mathbf{2.4} < \mathbf{2.5} < [\mathbf{2.6}]^{1+} < [\mathbf{2.2}]^{1+} < [\mathbf{2.3}]^{2+} \approx \mathbf{2.1}$. Derivatives with a sulfur-substituted, four-coordinate, phosphorus center show ν_{PP} frequencies that are slightly lower in energy than those in the corresponding cationic methylated analogues. Predictably, the ν_{PP} frequency for $[\mathbf{2.6}]^{1+}$, which contains both sulfur and methyl substitution at a tetracoordinate phosphorus center, lies in between those for $[\mathbf{2.3}]^{2+}$ and **2.5**. Derivatives that contain

both three- and four-coordinate phosphorus centers show lower ν_{PP} frequencies than frameworks that contain only four-coordinate centers. The effect is more pronounced in the sulfides (30 cm^{-1} variation) than the methylated cations (16 cm^{-1} variation). The results indicate that values of ν_{PP} are under certain conditions sensitive towards variation in the electronic and structural features of a PP-bonded compound.

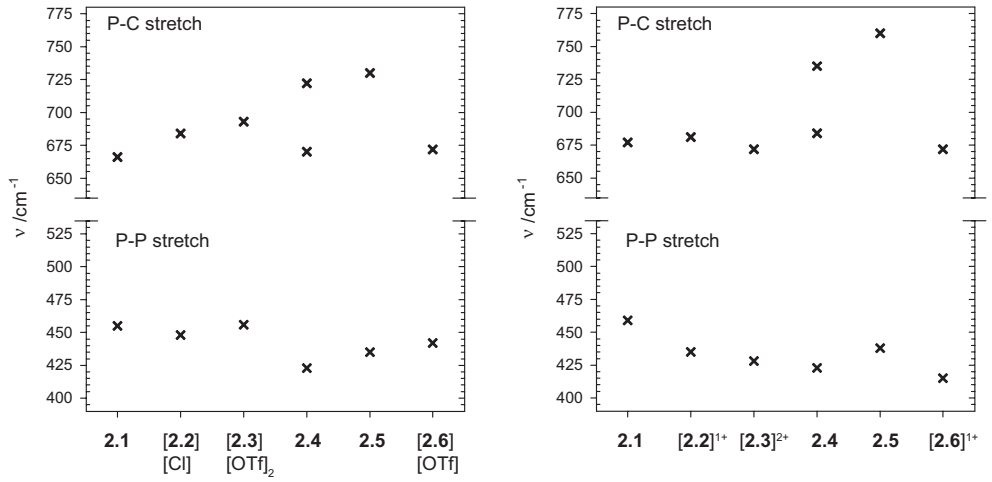

Figure 2.3.4. Experimental (left) and calculated (PBE1PBE/aug-cc-pVTZ, right) P−P and P−C bond stretching frequencies for some prototypical organophosphorus compounds. Only the symmetric P−C stretching modes involving all carbon atoms are plotted, except for **2.4**, where the symmetric stretches involving the two phosphorus atoms have different frequencies. Calculated values are for gas-phase species in the absence of anions.

The range of ν_{PC} values is significantly greater than that of ν_{PP} values, as illustrated in Figure 2.3.4. Only the symmetric stretching mode is plotted except for **2.4**, where there is no vibrational mode that involves a symmetric and in-phase stretching of all PC bonds, and therefore two frequencies, corresponding to discrete symmetric P−C stretches at P1 and at P2, are plotted. Similarly, for $[\mathbf{2.6}]^{2+}$, only the symmetric stretching mode involving the PMe_3 fragment is plotted since the mode involving the PMe_2S fragment shows strong coupling between the P−S and P−C stretches. P−C modes observed for compounds **2.1**, [**2.2**][OTf] and [**2.3**][$OTf]_2$ exhibit higher frequencies for frameworks with greater charge, and for stretches involving tetracoordinate centres. Furthermore, all ν_{PC} in $[\mathbf{2.2}]^{1+}$ and $[\mathbf{2.3}]^{2+}$ occur at a higher wavenumber than the symmetric ν_{PC} in crystalline (654 cm^{-1}) and gaseous (645 cm^{-1}) PMe_3.[121]

2.4 Influence of Charge and Coordination Number

The calculated P−P bond strengths for frameworks in Scheme 2.0.1 show that, independent of molecular charge or coordination number of the phosphorus centers, homolytic bond dissociation is thermochemically favoured over heterolytic bond dissociation. For $[\mathbf{2.2}]^{1+}$ and $[\mathbf{2.6}]^{1+}$, where heterolytic dissociation does not entail separation of opposite charges, the preference for homolytic dissociation is small. The calculated P−P bond dissociation energies for frameworks **2.1** and $[\mathbf{2.2}]^{1+}$ show that the cationic charge strengthens the P−P bond such that it is comparable with the C−C bond in alkanes, enabling the synthesis of phosphinophosphonium and phosphinodiphosphonium cations as their halide salts from direct combination of trialkylphosphines and halophosphines (Section 2.1.1).

Experimental P−P bond distances observed in the frameworks considered are independent of molecular charge or coordination number of the phosphorus centers, although gas-phase values, which are unmodified by anion interactions, show longer P−P bonds between two tetracoordinate centres than between two tricoordinate or one tetracaroodinate and one tricoordinate centres. Meanwhile, ν_{PP} for bonds that involve one tetracoordinate phosphorus center are significantly lower than those involving only tricoordinate centers or only tetracoordinate centers. Values of d_{PC} are distinctly shorter at quaternized phosphorus centres and correlate with higher ν_{PC} values. These trends in d_{PC} and ν_{PC} evidence an inductive electron donation from the methyl groups to the tetracoordinate phosphorus centre that, in the case of cations, results in distribution of the molecular cationic charge over the alkyl substituent.

There is no systematic correlation between d_{PP} and the calculated homolytic or heterolytic bond dissociation energies. Similarly, 'intuitive' correlations between the experimentally observed bond distances or stretching frequencies and the calculated homolytic or heterolytic P−P dissociation energies are absent in the data collected here, suggesting that oft-assumed relationships between bond lengths, strengths and force constants (*e.g.* Badger's rule, Gordy's rule) are potentially misleading when applied to the P−P bond.

2.5 Summary

A comprehensive experimental and computational assessment of the P−P bond in some prototypical organophosphorus compounds has been presented. The strength, length, and stretching frequency are basic features of a bond and define its chemical reactivity. A rare, complete catalogue of data for these observables has been compiled in this chapter for a series of experimentally known molecules.

Bond strengths have been calculated using a triple-ζ level basis set at the MP2 level and, wherever possible, solid-state effects have also been included in discussion of stability and bond strengths. The dramatic difference between the calculated stabilities of $[\mathbf{2.3}]^{2+}$ and $[\mathbf{2.3}][\mathrm{OTf}]_2$ is an arresting reminder that for cationic species, gas-phase stability calculations alone constitute a poor guide for synthetic methods. Semi-empirical thermochemical cycles show that although, in the gas phase, the diphosphonium dication $[\mathbf{2.3}]^{2+}$ is comparable in energy to two $[\mathrm{PMe_3}]^{1+}$ radical cations, it is the lattice enthalpy of $[\mathbf{2.3}][\mathrm{OTf}]_2$ in the solid state that enables isolation from a variety of reactions. This assessment of bond strengths answers some fundamental questions regarding homoatomic bonding (see Scheme 2.1.1*c* and *d*) and has inspired the most atom-economical route possible to phosphinophosphonium salts, namely the P−P Menschutkin reaction.

Previous structural data of inadequate quality (*e.g.* X-ray data for **2.5**) has been updated with new, high-resolution data to ensure statistical significance of findings. A combination of computational modelling and systematic isotopic labelling has yielded definitive assignments for the low-temperature vibrational spectra for these compounds. Taken together with the electronic and molecular structure evaluations described previously, these results provides important insights and a more definitive understanding of the P−P bond. It is envisioned that some of these findings will be broadly applicable to homoatomic bonding across the periodic table.

Chapter 3

Monoantimony Coordination Complexes

Unlike the P−P homoatomic bonding cases discussed thus far, heteroleptic P−Sb bonding cases feature the more recognizable coordination chemistry paradigm of a main group donor ligated to a metallic acceptor. The metallic nature of antimony makes antimony(III) halides a source of the $[Sb]^{3+}$ cation in the presence of suitable donors or strong Lewis acids. However, even neutral Sb^{III} compounds behave as Lewis acids since the low electronegativity of the element renders vacant σ^* Sb−X MOs of SbX_3 energetically accessible to ligands. The large covalent radius of antimony also facilitates coordination by preventing steric congestion. Thus a valence electron population as high as 12 can be accommodated within an octahedral framework around the metal, as exemplified in anions such as $[SbCl_5]^{2-}$. As a result of these features, many of which are shared by other heavy main group elements, a wide array of coordination environments are potentially accessible for antimony and several of these are described in this chapter.

A further consideration for the coordination chemistry of Sb^{III} is that the acceptor site, unlike most metal sites, features a localized and stereochemically active lone pair introducing the possibility of diverse configurational outcomes. VSEPR theory is the primary model employed to predict the structures of main group compounds and does so with remarkable accuracy in most cases. But when multiple substituents are present, in addition to a lone pair, it is often impossible to definitively predict the structure of a compound, and this situation is highlighted in a number of complexes

described in this chapter.

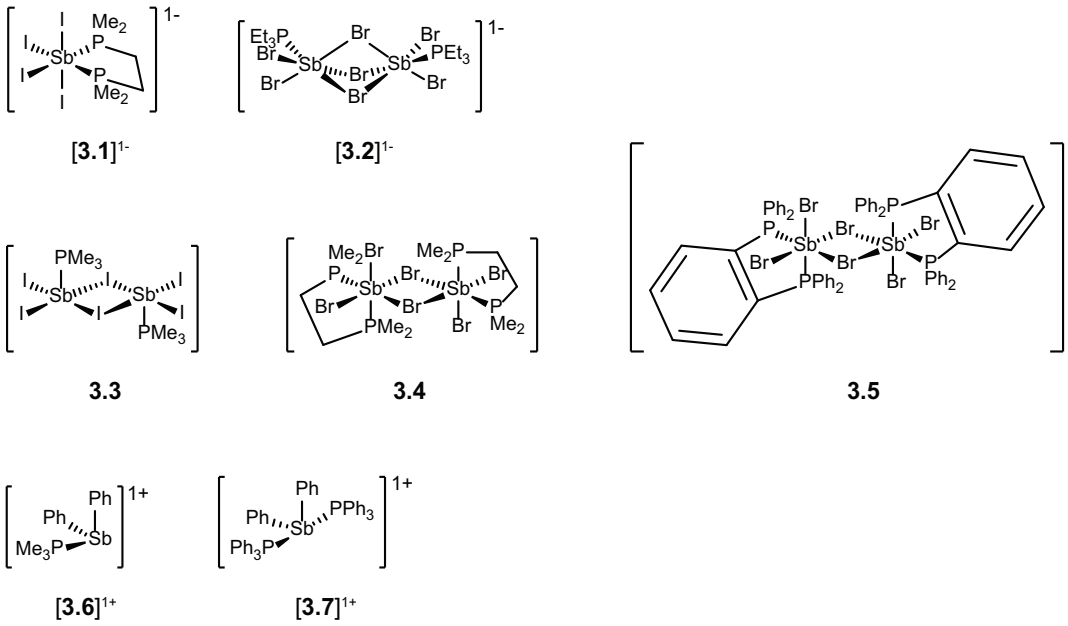

Scheme 3.0.1. Structurally-authenticated P−Sb coordination complexes. See text for references.

A diverse array of phosphine complexes have previously been reported for monoantimony(III) acceptors, but few have been structurally authenticated and no systematic assessment of structural trends has been conducted. As shown in Scheme 3.0.1, known examples include anionic complexes $[\mathbf{3.1}]^{1-}$ and $[\mathbf{3.2}]^{1-}$,[122,123] neutral derivatives **3.3**-**3.5**,[123,124] and cations such as $[\mathbf{3.6}]^{1+}$ and $[\mathbf{3.7}]^{1+}$.[33] The structural diversity exhibited in these cases, in particular with respect to the relative phosphine and halide orientation, prompted a comprehensive assessment of phosphine complexes of chloroantimony acceptors. The broad configurational variety for such compounds is illustrated in Scheme 3.0.2 for the generic formula $[(R_3P)_mSbCl_n]^{(3-n)+}$ (n = 2, 3 or 4 and m = 1 or 2) using an octahedral frame that includes a lone pair at the antimony acceptor site and, in some cases, a vacant coordination site.

As discussed in the following sections, examples have been found for nine of the twelve frameworks listed in Scheme 3.0.2. A careful analysis of the metric parameters has enabled rationalization of configurational preferences, providing a predictive structural model for the coordination chemistry of a lone pair bearing stibine site that can be generalized to other acceptors. In select cases, experimental observations are interpreted in light of dispersion-corrected DFT calculations to

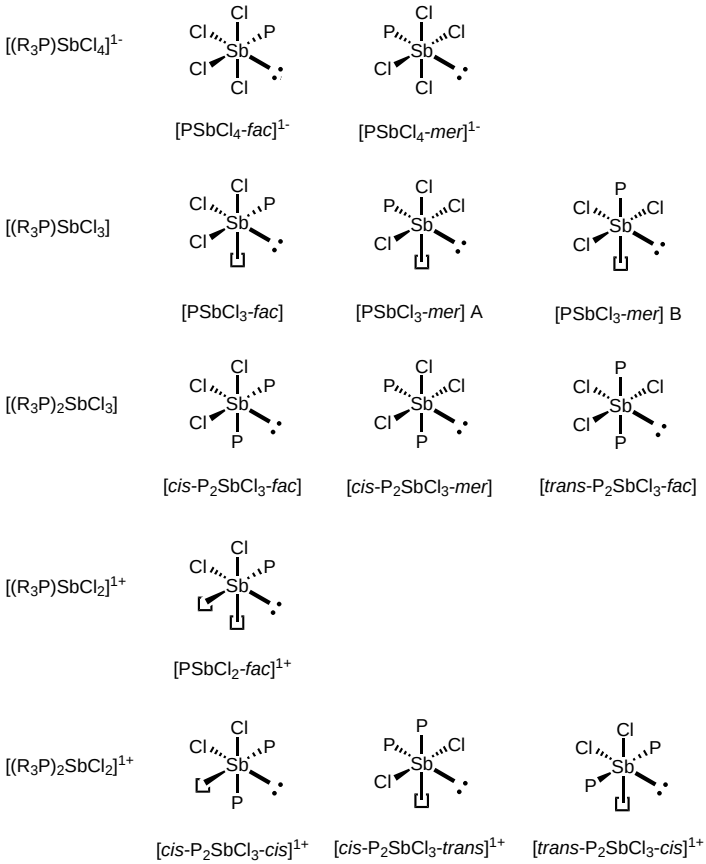

Scheme 3.0.2. Potential structural variety (VSEPR-inconsistent structures not considered) in an octahedral frame for antimony complexes composed of four (anion), three (neutral), or two (monocation) chloride substituents and one or two phosphine ligands (P = R_3P). The labels denote abbreviated generic formulae distinguishing each configuration of the chloride substituents and phosphine ligands. Bold line = lone pair and square = vacant coordination site.

develop an understanding of the bonding interactions and their impact upon the structural arrangements. Together, the results of this chapter debut a systematic study of the phosphine coordination chemistry for antimony, which has the potential to be as extensive and diverse as that of many transition metals.

3.1 Phosphine Complexes of Chloroantimony Acceptors

A series of PR_3 (R = Me, Ph, Cy) complexes bound to $SbCl_3$, $[SbCl_2]^{1+}$, $[SbCl]^{2+}$, or $[SbCl_4]^{1-}$ acceptors have been prepared and characterized crystallographically. As outlined in Scheme 3.1.1*a*, reactions of PR_3 with $SbCl_3$ yield derivatives of $[(R_3P)SbCl_3]$. In the presence of excess phosphine the *bis*-phosphine complexes, $[(R_3P)_2SbCl_3]$, are formed. Analogous reactions of $PhSbCl_2$ with PR_3 (R = Me, Ph) predictably give complexes $[(R_3P)SbPhCl_2]$, but *bis*-phosphine complexes $[(R_3P)_2SbPhCl_2]$ are only accessible for R = Ph when an excess amount of phosphine is employed (Scheme 3.1.1*b*). Presumably, the Lewis acidity of the antimony centre in $[(R_3P)SbPhCl_2]$ is sufficiently quenched by PMe_3, but not by the weaker base PPh_3.

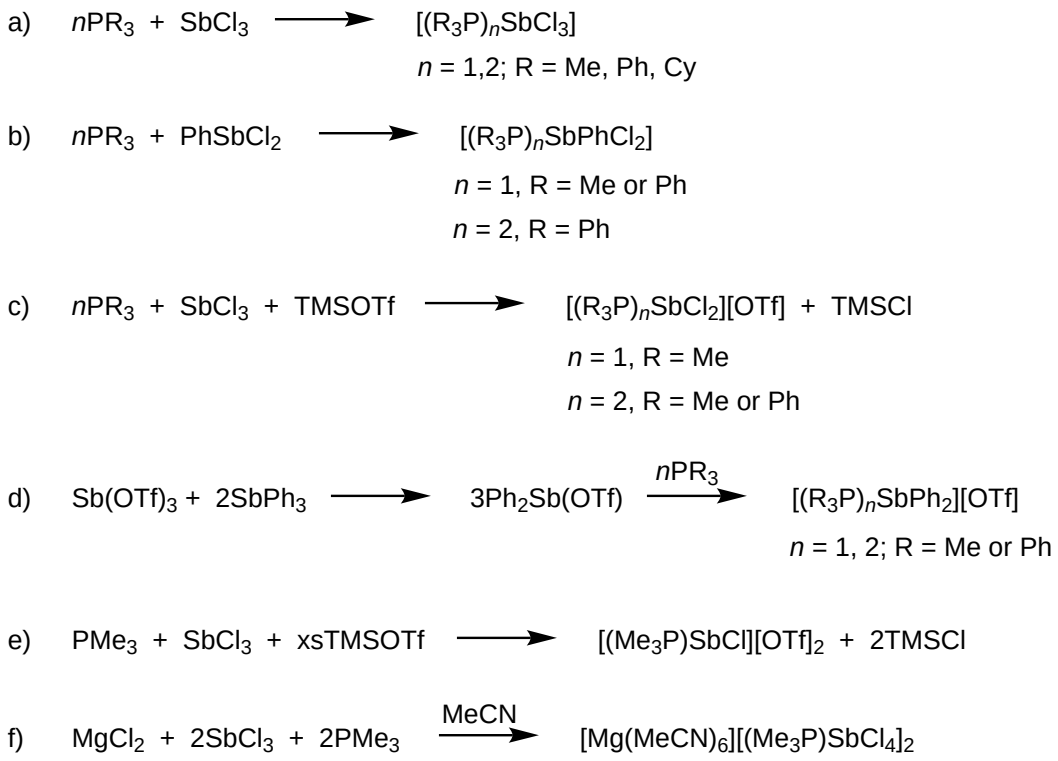

Scheme 3.1.1. Synthetic approaches to prototypical phosphine complexes of antimony(III).

Reaction of PMe_3 with $SbCl_3$ in the presence of one equivalent of TMSOTf gives $[(Me_3P)SbCl_2][OTf]$ with elimination of TMSCl as illustrated in Scheme 3.1.1*c*, while similar attempts to obtain $[(Ph_3P)SbCl_2][OTf]$ were unsuccessful, giving only

$[(Ph_3P)_2SbCl_2][OTf]$. The corresponding $[(Me_3P)_2SbCl_2][OTf]$ is formed in the presence of two equivalents or excess PMe_3. Reactions of PR_3 with $Ph_2Sb(OTf)$, generated *in situ* by substituent exchange between $Sb(OTf)_3$ and $SbPh_3$, yield *mono-* and *bis-*phosphine complexes $[(R_3P)_2SbPh_2][OTf]$ according to Scheme 3.1.1*d*.

When excess TMSOTf is used, mixtures of PMe_3 with $SbCl_3$ yield $[(Me_3P)_2SbCl][OTf]_2$ (Scheme 3.1.1*e*). Attempts to prepare the PPh_3 derivative were unsuccessful, resulting, once again, in formation of $[(Ph_3P)_2SbCl_2][OTf]$ even in the presence of a large excess of TMSOTf. Reaction of PMe_3 with $MgCl_2$ and $SbCl_3$ in MeCN yields $[Mg(MeCN)_6][(Me_3P)SbCl_4]_2$, according to Scheme 3.1.1*f*. The PPh_3 derivative of this anion could not be accessed despite numerous attempts and various reaction conditions.

The isolated complexes are extremely sensitive to moisture and oxygen, resulting in gradual decomposition to protonated phosphonium salts upon exposure to air. Triflate salts undergo more rapid decomposition than neutral or anionic derivatives, consistent with the greater electrophilicity of their cationic metal centres. Under rigorous exclusion of oxygen and water, the compounds are stable as solids or as solutions in organic solvents and it was possible to obtain single crystals suitable for diffraction for all eighteen derivatives in Scheme 3.1.1.

3.1.1 Neutral Complexes

The solid-state structures of the neutral complexes $[(R_3P)_nSbCl_3]$ (n = 1, 2 and R = Me, Ph, Cy) are illustrated in Figure 3.1.1, and selected parameters are listed in Table 3.1.1. In the solid state, $[(Me_3P)SbCl_3]$ adopts a polymeric arrangement in which the metal centres are bridged by chlorides that impose a distorted square-planar $SbCl_4$ frame with a phosphine in the axial position. The Sb−Cl distances involving the bridging chlorides are predictably longer than those involving the terminal chlorides. Considering the shortest Sb−Cl interactions, as explained in Figure 3.1.2, a lone pair of electrons can be envisaged as occupying the site *trans* to the phosphine ligand in the square-based pyramid, representing the configuration $[PSbCl_3{-}mer]$ A, illustrated in Scheme 3.0.2.

Dimeric arrangements are observed for $[(Ph_3P)SbCl_3]$ and $[(Cy_3P)SbCl_3]$ in the solid state, representing configurations $[PSbCl_3{-}fac]$ and $[PSbCl_3{-}mer]$ B, respectively, in Scheme 3.0.2. In each case, two chloride bridges result from edge-sharing,

square-based pyramids with a chlorine atom in the axial position. Interestingly, $[(Ph_3P)SbCl_3]$ adopts a centrosymmetric dimer, while $[(Cy_3P)SbCl_3]$ adopts a dimer with C_2 symmetry. In both cases, the bridging Sb−Cl distances are longer than those involving the terminal chlorides.

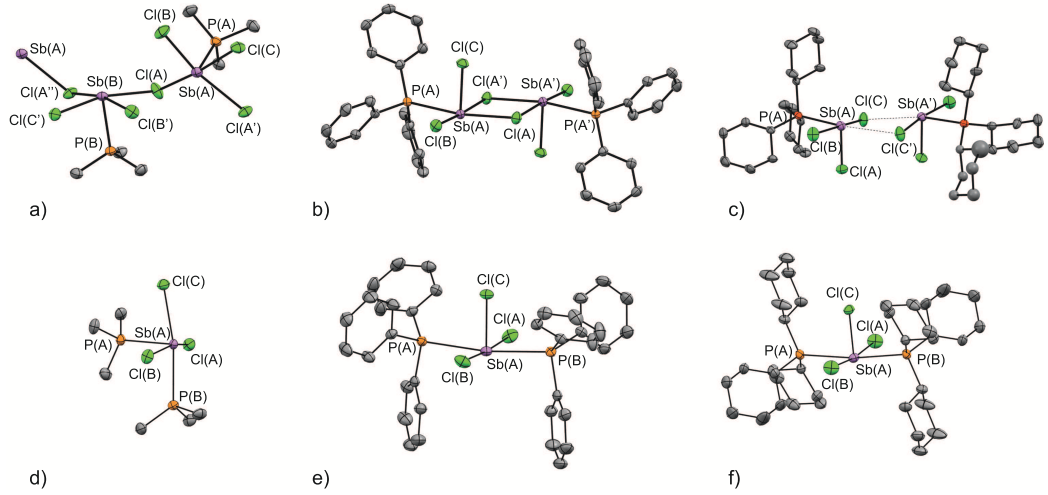

Figure 3.1.1. Solid-state structures for *a*) $[(Me_3P)SbCl_3{-}mer]$, *b*) $[(Ph_3P)SbCl_3{-}fac]$, *c*) $[(Cy_3P)SbCl_3{-}mer]$, *d*) $[cis{-}(Me_3P)_2SbCl_3{-}mer]$, *e*) $[trans{-}(Ph_3P)_2SbCl_3{-}mer]$, and *f*) $[trans{-}(Cy_3P)_2SbCl_3{-}mer]$.

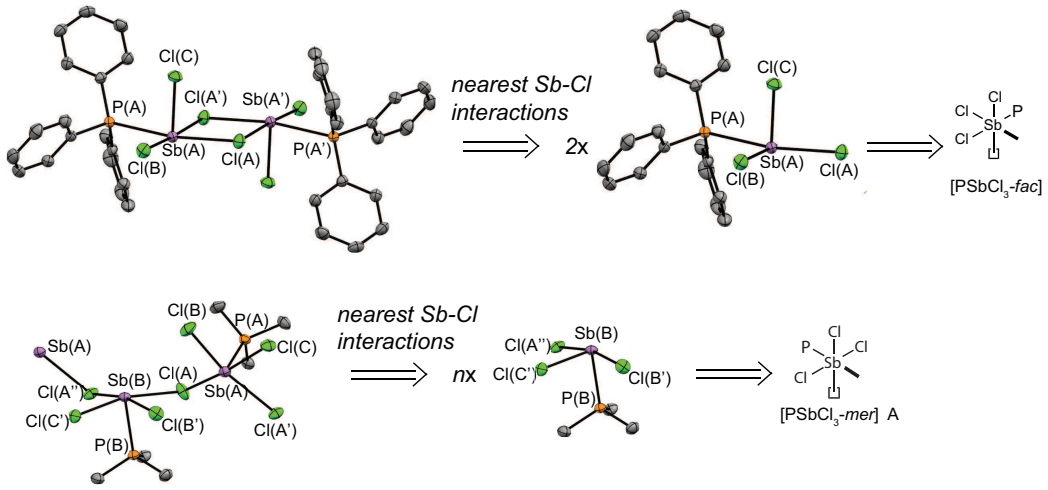

Figure 3.1.2. General procedure for determining the local configuration at antimony as applied to dimeric $[(Ph_3P)SbCl_3{-}fac]$ (top) and polymeric $[(Me_3P)SbCl_3{-}mer]$ (bottom).

The *bis*-phosphine complexes $[(R_3P)_2SbCl_3]$ uniformly adopt monomeric structures in the solid state with meridionally-configured chlorides. The phosphine ligands are

Table 3.1.1. Selected bond lengths (Å) and angles (°) in the solid-state structures of complexes $[(R_3P)SbCl_3]$.

	$[(Me_3P)SbCl_3]$	$[(Ph_3P)SbCl_3]$	$[(Cy_3P)SbCl_3]$
P−Sb	2.5951(9) Sb_A	2.7576(5)	2.6516(14)
	2.5962(9) Sb_B		
Sb−Cl	2.7656(9) Sb_A-Cl_A	2.7562(5) Cl_A	2.3362(14)
	2.8204(9) Sb_B-Cl_A	2.8949(5) Cl_A,	
	2.9504(9) Sb_A-Cl_A,		
	2.7083(9) Sb_B-Cl_A"		
	2.4062(9) Sb_A-Cl_B	2.4037(5)	2.5773(15)
	2.5093(9) Sb_B-Cl_B,		
	2.4783(9) Sb_A-Cl_C	2.3569(5)	2.5939(14) Sb_A-Cl_C
	2.4688(9) Sb_B-Cl_C,		3.269(2) Sb_A-Cl_C,
P_A-Sb−Cl	77.55(3) Cl_A	170.59(2)	94.96(4)
	76.68(3) Cl_A,		
	90.32(3) Cl_B	91.73(2)	86.64(5)
	87.67(3) Cl_C	86.52(2)	86.43(5)
P_B-Sb−Cl	87.73(3) Cl_B,		
	79.65(3) Cl_A"		
	87.73(3) Cl_B,		
	88.54(3) Cl_C,		
Cl−Sb−Cl	88.91(3)	94.56(2)	89.15(5)
	Cl_A-Sb_A-Cl_B		
	89.62(3) Sb_B	176.65(2)	
	Cl_A-Sb_B-Cl_B,		
	165.22(3) Sb_A	86.24(2)	87.68(5)
	Cl_A-Sb_A-Cl_C		
	165.58(3) Sb_B		
	Cl_A-Sb_B-Cl_C,		
	90.77(4) Sb_A	92.41(2)	171.90(5)
	Cl_B-Sb_A-Cl_C		
	89.85(3) Sb_B		
	Cl_B,-Sb_B-Cl_C,		

Table 3.1.2. Selected bond lengths (Å) and angles (°) in the solid-state structures of complexes $[(R_3P)_2SbCl_3]$.

	$[(Me_3P)_2SbCl_3]$	$[(Ph_3P)_2SbCl_3]$	$[(Cy_3P)_2SbCl_3]$
P−Sb	2.5757(4) P_A	2.7934(4) P_A	2.848(2) $_A$
	2.7278(4) P_B	2.7934(4) P_B	2.871(2) $_B$
Sb−Cl	2.6046(4) Cl_A	2.5571(5) Cl_A	2.568(2) Cl_A
	2.5653(4) Cl_B	2.5572(5) Cl_B	2.556(2) Cl_B
	2.7096(4) Cl_C	2.3849(6) Cl_C	2.377(2) Cl $_C$
P−Sb−P	93.08(2)	171.86(2)	172.95(4)
P_A−Sb−Cl	82.19(2) Cl_A	85.94(2) Cl_A	90.60(6) Cl_A
	86.85(2) Cl_B	93.73(2) Cl_B	89.42(6) Cl_C
	78.33(2) Cl_C	85.93(2) Cl_C	86.41(5) Cl_C
P_B−Sb−Cl	86.81(2) Cl_A	93.73(2) Cl_A	89.17(6) Cl_A
	80.24(2) Cl_B	85.94(2) Cl_B	89.85(6) Cl_B
	170.33(2) Cl_C	85.93(2) Cl_C	86.56(5) Cl_C
Cl_A−Sb−Cl	162.55(2) Cl_B	175.27(2) Cl_B	172.12(4) Cl_B
	96.30(2) Cl_C	87.64(2) Cl_C	84.45(6) Cl_C
Cl_B−Sb−Cl_C	94.73(2)	87.64(2)	87.68(6)

cis-configured in [*cis*−$(Me_3P)_2SbCl_3$−*mer*] while a *trans* configuration is observed for [*trans*−$(Ph_3P)_2SbCl_3$−*mer*] and [*trans*−$(Cy_3P)_2SbCl_3$−*mer*]. Since the two trialkylphosphine ligands are of comparable basicity,[125] the divergent configurational outcomes are presumably due to a preference for *cis*-phosphine configuration, *unless* sterically demanding ligand such as PCy_3 and PPh_3 are employed. The remaining coordination site at antimony accommodates a lone pair of electrons in each case. Notably, the alternative VSEPR-consistent configuration, [*cis*−$(R_3P)_2SbCl_3$−*fac*], is not observed.

The P−Sb and Sb−Cl bond lengths in derivatives of [$(R_3P)SbCl_3$] and [$(R_3P)_2SbCl_3$] are compared graphically in Figure 3.1.3, which is coded according to the substituent (or lone pair) that is *trans* to the P−Sb and Sb−Cl bonds, respectively. Derivatives of [$(R_3P)SbCl_3$] exhibit average P−Sb lengths (horizontal lines in Figure 3.1.3, left) that are consistent with the relative Lewis basicity of the phosphine and the presence or absence of a halide *trans* to the P−Sb bond being considered.

Longer P−Sb bonds are observed in derivatives of [$(R_3P)_2SbCl_3$] than in *mono*-phosphine complexes, imposed in the PPh_3 and PCy_3 derivatives by the mutually-*trans* arrangement of the phosphines. Unlike [*trans*−$(Cy_3P)_2SbCl_3$−*mer*], where a *cis* configuration is sterically disfavourable and a *trans* configuration unavoidable, in [*cis*−$(Me_3P)_2SbCl_3$−*mer*] a *cis*-configuration of the phosphines is observed, which avoids an arrangement placing the ligands in mutually *trans*-labilizing positions around the metal. As a result the *bis*-PMe_3 complex has the shortest average P−Sb bonds within the [$(R_3P)_2SbCl_3$] series. The P−Sb bonds in [*trans*−$(Cy_3P)_2SbCl_3$−*mer*] are longer than in the PPh_3 derivative, illustrating a modulation of the *trans*-labilizing effect by donor strength, since both phosphines have comparable steric properties but very different basicities. Thus, the magnitude of the proposed *trans* influence of the phosphines follows the trend: $PPh_3 < PCy_3 \approx PMe_3$.

As shown in Figure 3.1.3, the P−Sb or Sb−Cl bonds *trans* to a chlorine atom (∘) are observed with intermediate length between those *trans* to a phosphine and those *trans* to a lone pair (◇). Consequently, *trans* Cl−Sb−Cl arrangements are preferred over *trans* P−Sb−Cl and *trans* P−Sb−P arrangements. The *trans* P−Sb−Cl arrangement is tolerated by the relatively low basicity of PPh_3 in [$(Ph_3P)SbCl_3$−*fac*], and is enforced in [*cis*−$(Me_3P)_2SbCl_3$−*mer*] to avoid the *trans* placement of the more basic PMe_3 ligands. The *trans* P−Sb−P arrangements in [*trans*−$(Ph_3P)_2SbCl_3$−*mer*]

and [*trans*−$(Cy_3P)_2SbCl_3$−*mer*] are unavoidable due to the greater steric presence of PPh_3 and PCy_3, compared to PMe_3. Based on these structural comparisons the *trans* influence series in neutral P−Sb complexes can be appended as follows: lone pair < $PPh_3 \approx [Cl]^{1-} < PCy_3 \approx PMe_3$. In Figure 3.1.3, this trend is broadly illustrated by the observation that bonds *trans* to phosphines tend to be longer than those *trans* to chlorides, which tend to be longer than than those *trans* to a lone pair.

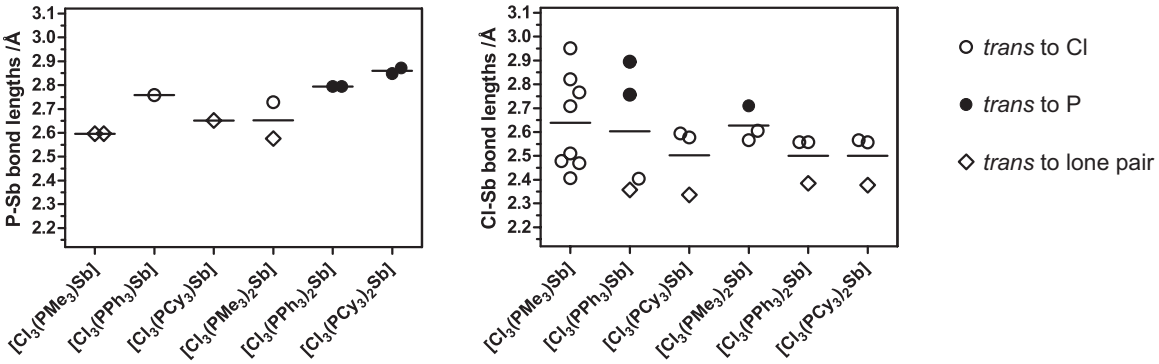

Figure 3.1.3. P−Sb (left) and Sb−Cl (right) bond lengths in derivatives of $[(R_3P)SbCl_3]$ and $[(R_3P)_2SbCl_3]$, coded according to the substituent *trans* to the considered bond. Horizontal bars indicate the average value within a compound.

Table 3.1.3. Calculated (B3LYP-D3 with Counterpoise correction) reaction enthalpies/Gibbs energies for the formation of $[(R_3P)SbCl_3]$ according to Scheme 3.1.1*a*. All values are given in kJ mol^{-1}.

	R = Me	R = Ph
$[(R_3P)SbCl_3$−*fac*$]$	−18.0/+21.8	+105.9/+151.9
$[(R_3P)SbCl_3$−*mer*$]$	−9.2/+33.1	+140.6/+192.9
$[(R_3P)SbCl_3$−*pyr*$]$	−93.7/−11.8	−49.4/+10.5

Calculations on gas-phase models using dispersion-corrected DFT (B3LYP-D3)* were carried out to determine the reaction enthalpies and Gibbs energies for the formation of $[(R_3P)SbCl_3]$ (R = Me, Ph) according to Scheme 3.1.1*a*, under standard conditions (see Table 3.1.3). Interestingly, geometry optimizations revealed the global minimum in each case to be the trigonal pyramidal arrangement, *pyr*-$[(R_3P)SbCl_3]$, with the phosphine in the apical position and the antimony slightly below the basal plane, consistent with previous theoretical investigations (Scheme 3.1.2).[126] However,

*The B3LYP functional was used with Grimme's empirical dispersion correction (S_6 = 1.05).

there are no experimental data for such a non-VSEPR geometry, and the observed [$(Me_3P)SbCl_3$−*mer*] is calculated as a shallow minimum, observed only when using the strictest convergence criterion and when the angle between two chlorine substituents is restricted to greater than 175°. It is therefore likely that the *fac*- and *mer*-configurations observed for [$(R_3P)SbCl_3$] result from intermolecular interactions that are evident for these compounds in the solid state. These results highlight the importance of gas-phase structural studies for monomers of such configurationally-ambiguous complexes.

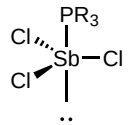

pyr-[$(R_3P)SbCl_3$]

Scheme 3.1.2. Trigonal pyramidal geometry calculated as the minimum energy configuration for [$(Me_3P)SbCl_3$] in the gas phase across a variety of theoretical methods and basis sets.

As shown in Table 3.1.3, the reaction enthalpies for complexes of PMe_3 are negative (exothermic) and small, as expected for closed-shell interactions. However, the entropic costs of complexation are sufficiently high that the overall Gibbs energy changes for the observed *mer* and *fac* isomers are positive (non-spontaneous). The gas-phase reaction Gibbs energies predict that all three configurations of [$(Ph_3P)SbCl_3$] are unstable with respect to the starting reagents, consistent with the importance of the experimentally-observed intermolecular lattice interactions in the stability of the complex.

The calculated gas-phase structures for derivatives of [$(R_3P)_2SbCl_3$] failed to reproduce the experimental geometric parameters. For instance, the calculated gas-phase structure of [*cis*−$(Me_3P)_2SbCl_3$−*mer*] shows good agreement with the experimentally observed (see top half of Figure 3.1.4 for labelling scheme) Sb_A-P_A (Δ = 0.01 Å; Δ = calcd. expt.), Sb_A-Cl_A (Δ = 0.01 Å) and Sb_A-Cl_B (Δ = 0.05 Å) distances, but the calculations overestimate the Sb_A-P_B distance by 0.19 Å and underestimate the Sb_A-Cl_C distance by 0.17 Å. In the gas phase, one ligand is bound only weakly, effecting a relatively short Sb_A-Cl_C bond *trans* to the long P_B-Sb_A bond. One calculated imaginary frequency is associated with S_N2-type displacement of Cl_C from the metal centre by P_B. Calculations in a simulated solvent field (PCM) of pentane

(dielectric constant, $\epsilon = 1.84$), acetonitrile ($\epsilon = 37.5$), or water ($\epsilon = 80.1$) show that greater solvent field polarity fully recovers the experimentally observed structural parameters (Figure 3.1.4, bottom half). The calculated gas-phase Sb_A-P_B and Sb_A-Cl_C distances for $[cis{-}(Me_3P)_2SbCl_3{-}mer]$ model the initial steps of an S_N2-type nucleophilic displacement of a chloride anion by a phosphine ligand at the antimony centre. In solvents of greater polarity, the minimum energy structure is farther along the reaction coordinate towards $[Cl_2(PMe_3)_2Sb]^{1+}$ and a free chloride ion.

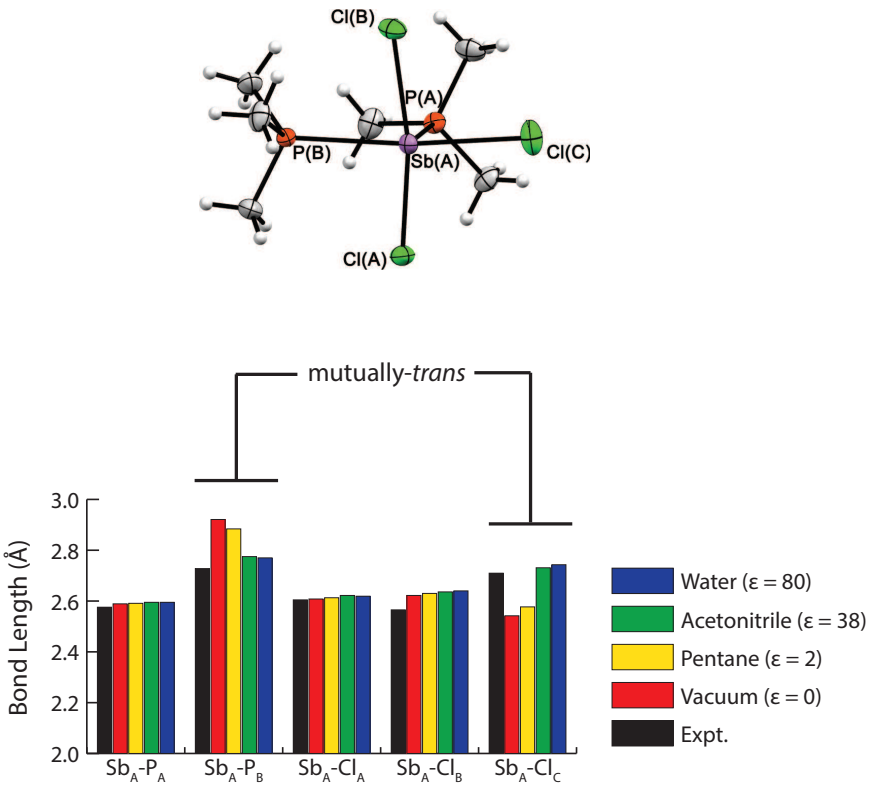

Figure 3.1.4. Variations in calculated bond lengths of $[cis{-}(Me_3P)_2SbCl_3{-}mer]$ as a function of the dielectric constant (ϵ) of the applied PCM solvent field.

3.1.2 Mono- and Dicationic Complexes

The solid-state structures of cations $[(Me_3P)SbCl_2]^{1+}$, $[cis{-}(Me_3P)_2SbCl_2{-}trans]^{1+}$, $[trans{-}(Ph_3P)_2SbCl_2{-}cis]^{1+}$, $[(Me_3P)SbPh_2]^{1+}$ and $[trans{-}(Me_3P)_2SbPh_2{-}cis]^{1+}$ in their triflate salts are illustrated in Figure 3.1.5, alongside those in the previously reported[33] salts $[(Ph_3P)SbPh_2][PF_6]$ and $[trans{-}(Ph_3P)_2SbPh_2{-}cis][PF_6]$. Key structural parameters for these compounds are listed in Table 3.1.4. The triflate derivatives

in Table 3 are considered to be ionic, exhibiting Sb−O contacts that are substantially greater than the sum of the covalent radii for the two elements ($\Sigma_{r,cov}$ = 2.05 Å).[127] The cation in $[(Me_3P)SbCl_2][OTf]$ (Figure 3.1.5*a*) involves two interion Sb−O contacts imposing a square pyramidal geometry at antimony. Similar structures are observed for the cations in $[(Me_3P)SbPh_2][OTf]$ (Figure 3.1.5*d*) and the ternary salt $[(Me_3P)SbPh_2]_4[Cl][PF_6]_3$.[128]

The *bis*-phosphine cations in $[cis{-}(Me_3P)_2SbCl_2{-}trans][OTf]$ (Figure 3.1.5*b*) and $[trans{-}(Ph_3P)_2SbCl_2{-}cis][OTf]$ (Figure 3.1.5*c*) illustrate different configurational preferences for the phosphines. The *cis*-configuration of the more basic ligands in the former is consistent with that of $[cis{-}(Me_3P)_2SbCl_3{-}mer]$ and contrasts the *trans*-configuration of the phosphines in the PPh_3 derivative, made possible by the lower basicity of the arylphosphine ligand. A *trans* configuration of two PMe_3 ligands is uniquely present in $[trans{-}(Me_3P)_2SbPh_2{-}cis]^{1+}$ (Figure 3.1.5*e*), suggesting that phenyl substituents are the most strongly *trans*-labilizing of the groups discussed here, and a mutually *trans* arrangement for them is energetically unfavourable. The trend in the magnitude of *trans* influence is therefore further appended by inclusion of the phenyl group to give lone pair < PPh_3 ≈ $[Cl]^{1-}$ < PCy_3 ≈ PMe_3 < $[Ph]^{1-}$.

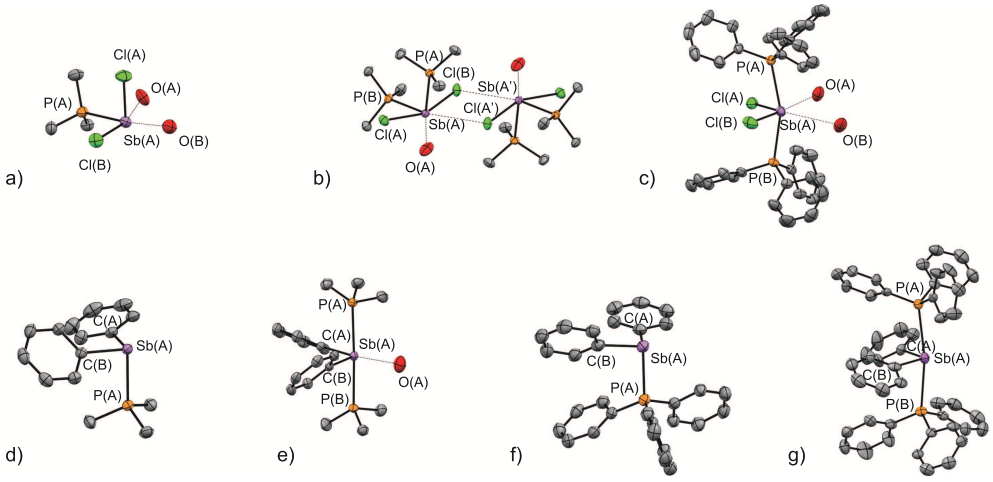

Figure 3.1.5. Solid-state structures of the cations in *a*) $[(Me_3P)SbCl_2][OTf]$, *b*) $[cis{-}(Me_3P)_2SbCl_2{-}trans][OTf]$, *c*) $[trans{-}(Ph_3P)_2SbCl_2{-}cis][OTf]$, *d*) $[(Me_3P)SbPh_2][OTf]$, *e*) $[trans{-}(Me_3P)_2SbPh_2{-}cis][OTf]$, *f*) $[(Ph_3P)SbPh_2][PF_6]$, and *g*) $[trans{-}(Ph_3P)_2SbPh_2{-}cis][PF_6]$. Hydrogen atoms and non-essential portions of anions have been omitted for clarity.

Table 3.1.4. Selected bond lengths (Å) and angles (°) in the solid-state structures of some monocationic P−Sb complexes.

	$[(Me_3P)SbCl_2][OTf]$	$[(Me_3P)SbPh_2][OTf]$	$[(Ph_3P)SbPh_2][PF_6]$ [33]	$[(Me_3P)SbPh_2][Cl][PF_6]_3$ [128]
P_A-Sb	2.6043(9)	2.5584(4)	2.595(2)	2.591(2)
Sb−X_A	2.3719(9)	2.149(2)	2.152(5)	2.153(4)
Sb−X_B	2.3926(8)	2.155(2)	2.153(5)	2.153(3)
Sb−O_A	2.705(2)	3.548(2)		
Sb−O_B	2.755(2)	3.688(2)		
P_A-Sb−X_A	90.71(3)	89.55(4)	93.7(2)	89.08(9)
P_A-Sb−X_B	90.62(3)	94.74(4)	97.6(2)	89.08(9)
X_A-Sb−X_A	92.78(3)	96.35(6)	100.2(2)	107.6(2)

	$[(Me_3P)_2SbCl_2][OTf]$	$[(Ph_3P)_2SbCl_2][OTf]$	$[(Me_3P)_2SbPh_2][OTf]$	$[(Ph_3P)_2SbPh_2][PF_6]$ [33]
P_A-Sb	2.5890(4)	2.8621(5)	2.8034(4)	2.8694(8)
P_B-Sb	2.5805(4)	2.8042(5)	2.7559(4)	2.8426(9)
Sb−X_A	2.6707(4)	2.3643(6)	2.159(2)	2.157(2)
Sb−X_B	2.5079(4)	2.4083(6)	2.156(2)	2.157(2)
Sb−O_A	2.996(1)	2.679(2)	3.495(2)	
Sb−O_B		3.233(2)		
P−Sb−P	101.75(2)	160.90(2)	177.14(2)	170.11(8)
P_A-Sb−X_A	79.28(2)	81.52(2)	86.64(4)	87.9(2)
P_A-Sb−X_B	87.03(2)	84.40(2)	89.90(4)	86.9(3)
P_B-Sb−X_A	79.63(2)	82.14(2)	90.51(4)	86.5(2)
P_B-Sb−X_B	87.12(2)	88.23(2)	90.90(4)	86.2(3)
X_A-Sb−X_B	158.50(2)	98.27(3)	95.06(6)	101.1(3)

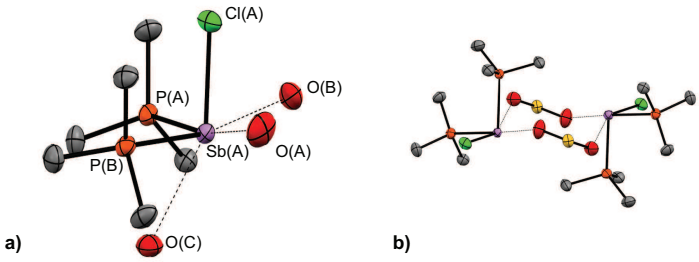

Figure 3.1.6. Solid-state structure of *a*) the cation in $[(Me_3P)_2SbCl][OTf]_2$ and *b*) its triflate anion bridged dimeric structure. Hydrogen atoms and non-interacting portions of the triflate anions have been omitted for clarity. Key experimental/calculated (free cation, MP2/def2-TZVPP) bond lengths (Å) and angles (°) are as follows: P_A-Sb = 2.5950(4)/2.5612, P_B-Sb = 2.5834(4)/2.5612, Sb−Cl = 2.3511(4)/2.3167, Sb-O_A = 2.792(2), Sb-O_B = 2.855(2), Sb-O_C = 2.711(2), P_A-Sb-P_B = 102.03(2)/102.45, Cl-Sb-P_A = 90.11(2)/89.93, Cl-Sb-P_B = 92.81(2)/89.93, O_A-Sb-O_B = 103.36(5), Cl-Sb-O_C = 153.19(3).

Derivatives of $[(R_3P)_2SbPh_2]^{1+}$ (R = Me, Ph) adopt P−Sb distances that are shorter by approximately 0.08 Å when R = Me (see Table 3.1.4). The Sb−Cl distances are more sensitive (range of 0.21 Å) to the substitution pattern around the metal. Complexes with shorter P−Sb distances show longer Sb−Cl bond lengths. By comparison, in complexes featuring $[SbPh_2]^{1+}$ centres, the Sb−C_{phenyl} distances are relatively unperturbed by variation of the number or type of phosphine ligand (range of 0.01 Å), consistent with the greater elasticity in the more polarized (more ionic) Sb−Cl bond than in the less polarized (more covalent) Sb−C bond.

Two views of the dication in the solid-state structure of $[(Me_3P)_2SbCl][OTf]_2$ are shown in Figure 3.1.6, one illustrating the three closest contacts to oxygen atoms of anions (Figure 3.1.6*a*), and the other showing the dimeric association of the formula units through bridging O−S−O units of the anions (Figure 3.1.6*b*). The P−Sb bond lengths in the dication are predictably short, but in the range that is observed for neutral and cationic phosphine complexes of antimony. The very short Sb−Cl bond [2.3511(4) Å] is within the sum of the covalent radii for the two elements ($\Sigma_{r,cov}$ = 2.38 Å).[127] The facial configuration of the chlorine substituent and two phosphine ligands, together with the oxygen centres of three separate triflate units impose a distorted octahedral environment for antimony. The Sb−O contacts are comparable in length to the shorter contacts in the monocationic salts (Table 3.1.4), and are substantially greater than the sum of the covalent radii ($\Sigma_{r,cov}$ = 2.07 Å).[127] The close

match between the experimental and calculated (MP2/def2-TZVPP) bond lengths (± 0.04 Å) and angles (± 3°) for anion-free $[(Me_3P)_2SbCl]^{2+}$ in the gas phase, suggests minimal structural distortion of the cation due to interion contacts, supporting the ionic formulation.

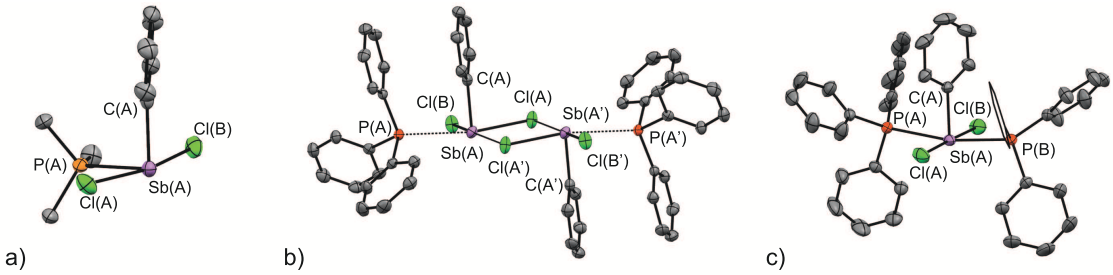

Figure 3.1.7. Solid-state structures of *a*) $[(Me_3P)SbPhCl_2]$, *b*) $[(Ph_3P)SbPhCl_2]$, and *c*) $[(Ph_3P)_2SbPhCl_2]$.

Table 3.1.5. Selected bond lengths (Å) and angles (°) in the solid-state structures of complexes $[(R_3P)SbPhCl_2]$ and $[(R_3P)_2SbPhCl_2]$.

	$[(Me_3P)SbPhCl_2]$	$[(Ph_3P)SbPhCl_2]$	$[(Ph_3P)_2SbPhCl_2]$
P−Sb	2.5612(4)	2.9656(5)	2.8741(4)
Sb−Cl_A	2.6286(5)	2.3965(6)	2.5989(4)
		3.3152(6)Cl_A,	
Sb−Cl_B	2.5566(5)	2.5463(6)	2.5989(4)
Sb−C	2.164(2)	2.146(2)	2.163(2)
P−Sb−P			169.10(2)
P−Sb-C	95.85(4) P_A	84.04(6) P_A	84.549(8) P_A
			84.548(8) P_B
P_A−Sb−Cl	78.95(2) Cl_A	169.44(2) Cl_A	85.72(2) Cl_A
		100.92(2) Cl_A,	
	87.30(2) Cl_B	83.23(2) Cl_B	94.42(2) Cl_B
P_B−Sb−Cl			94.42(2) Cl_A
			85.72(2) Cl_B
Cl−Sb−Cl	165.79(2)	90.09(2)	178.53(2)

The trend in the magnitude of *trans* influence at the antimony acceptor site (lone

pair < PPh_3 ≈ $[Cl]^{1-}$ < PCy_3 ≈ PMe_3 < $[Ph]^{1-}$) is further demonstrated in the neutral complexes featuring multiple substituents on the same antimony centre. The solid-state structures of $[(Me_3P)SbPhCl_2]$, $[(Ph_3P)SbPhCl_2]$ and $[(Ph_3P)_2SbPhCl_2]$ are shown in Figure 3.1.7, and selected structural parameters are listed in Table 3.1.5. The weakly *trans*-labilizing chlorine substituents in the three compounds account for the observed *trans* Cl−Sb−Cl configurations in all three structures. Consistently, the more *trans*-labilizing PMe_3 ligand and $[Ph]^{1-}$ substituent are *cis*-configured. In this context, the series defined above, enables rationalization and prediction of the configurations even with the variety of VSEPR-consistent configurational options available for derivatives with multiple substituents at the central atom.

3.1.3 An Anionic Complex

Hypervalent centres such as those in pnictogen pentafluorides are powerful Lewis acids and react with halides to give weakly-coordinating hexahalopnictogenate anions. Indeed anionic $[SbCl_4]^{1-}$ is sufficiently Lewis acidic to form the square-based pyramidal (AX_5E) dianion $[SbCl_5]^{2-}$ in the presence of excess chloride anions. The anions $[\mathbf{3.1}]^{1-}$ and $[\mathbf{3.2}]^{1-}$ (Scheme 3.0.1) have also been reported as serendipitous products of a hydrolysis reaction.[122] The preparation of $[Mg(MeCN)_6][(Me_3P)SbCl_4]_2$ according to Scheme 3.1.1*f* therefore represents the first reported rational synthesis of a phosphine-stibine anion. Formation of $[(Ph_3P)SbCl_4]^{1-}$ is precluded by the relatively low basicity of PPh_3.

The molecular structure of the $[(Me_3P)SbCl_4]^{1-}$ anion is derived from $[SbCl_5]^{2-}$ by replacing the apical anionic chloride substituent with a neutral PMe_3 ligand (Figure 3.1.8). The Sb−Cl bonds [2.555(2) − 2.634(2) Å, average 2.593 Å] are shorter than the basal ones in $[SbCl_5]^{2-}$ [2.478(2) − 2.885(2) Å, average 2.646 Å][129], and those in $[SbCl_4]^{1-}$ [2.4317(7) − 2.640(2) Å, average 2.536 Å].[130] The hard $[Mg]^{2+}$ centre, being encapsulated with hard MeCN ligands (solvent), does not engage the soft phosphine donor resulting in coordination of PMe_3 to the soft $[SbCl_4]^{1-}$ anion.

Coordination of a Lewis base to cationic or neutral haloantimony centres is understood as donor occupation of vacant *p*-orbitals or low-lying σ^* Sb−X antibonding orbitals at antimony. As shown in Figure 3.1.8, phosphine coordination to anionic $[SbCl_4]^{1-}$ also involves overlap of the PMe_3 lone pair and a vacant *p*-orbital perpendicular to the $SbCl_4$ plane (HOMO−1). Bonding within the $SbCl_4$ plane involves

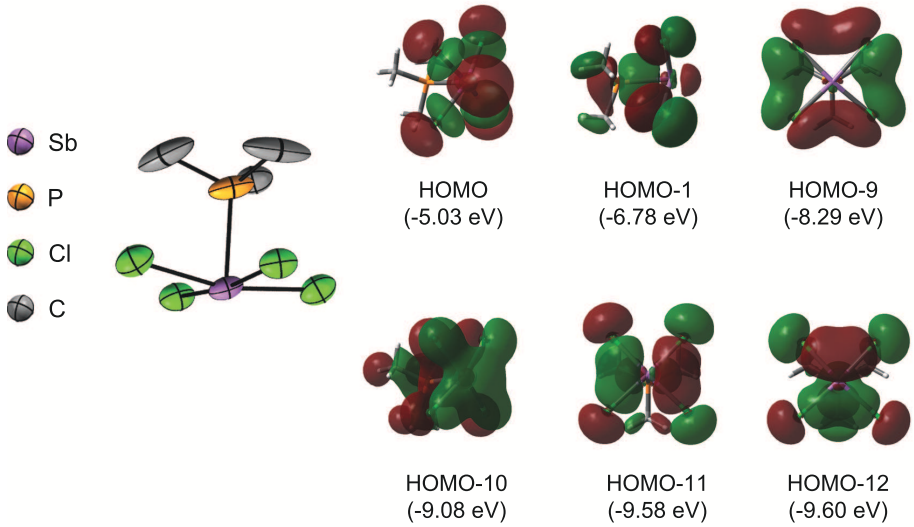

Figure 3.1.8. Left: Molecular structure of the anion in $[Mg(MeCN)_6][(Me_3P)SbCl_4]_2$. Only one of two nonequivalent molecules in the unit cell is shown and hydrogen atoms have been omitted for clarity. Key experimental/calculated (free anion, MP2/def2-TZVPP) bond lengths (Å) and angles (°) are as follows: P−Sb = 2.582(2)/2.5578, Sb−Cl Sb−Cl Sb−Cl = 2.580(2)/2.5354, 2.555(2)/2.5354, 2.634(2)/2.6335, 2.601(2)/2.6335, P−Sb−Cl = 82.10(7)/76.42, 81.05(8)/76.42, 85.53(8)/85.95, 88.89(7)/85.95, Cl−Sb−Cl = 90.98(8)/93.42, 170.93(7)/161.64, 90.91(7)/87.27, 89.45(8)/87.27, 155.08(7)/161.64, 86.58(7)/86.42. Right: Calculated (MP2/def2-TZVPP) molecular orbitals relevant to key bonding interactions in the $[(Me_3P)SbCl_4]^{1-}$ anion.

overlap between the chlorine lone pairs and the two remaining *p*-orbitals (HOMO−11, HOMO−12), a small degree of Cl−Cl bonding *via* in-phase overlap of the chlorine *p*-orbitals in a ring around Sb (HOMO−9), and delocalized π-bonding involving the chlorine lone pairs and the *p*-orbital that is used for P−Sb bonding (HOMO−10). A non-bonding lone pair is evident as the HOMO, thereby accounting for the five bonding pairs and one non-bonding pair of electrons around Sb in six molecular orbitals.

3.2 Accessing Tricationic Antimony Acceptors

While stepwise removal of halides from Sb^{III} centres readily yields mono- and dicationic phosphine complexes, the use of this strategy to access tricationic centres was not straightforward. The Lewis acidity of the metal centre increases as its charge is augmented with successive halide abstraction. Consequently, removal of the final halide is thermodynamically challenging and reactions of $SbCl_3$ with donors in the presence of three equivalents of TMSOTf, $TMSNTf_2$, $AlCl_3$, $GaCl_3$, or LiOTf yielded only monocations and dications. When neat Lewis acids were used as solvents (*e.g.* boiling TMSOTf or molten $GaCl_3$), side products from reactions of the donors with the Lewis acid were obtained. For instance, the equimolar mixture of *bipy* and $SbCl_3$ in molten $GaCl_3$ gave $[(bipy)GaCl_2][Ga_2Cl_7]$ as the only isolable product. The solid-state structure of the salt is shown in Figure 3.2.1*a*, confirming an ionic formulation with four-coordinate gallium atoms. Similarly, reactions involving PMe_3 and *dppe* with excess TMSOTf or $GaCl_3$, respectively, gave the corresponding adducts which were identified crystallographically (Figure 3.2.1).

Finally, a strategy analogous to the synthesis of antimony triazide by fluoride abstraction from SbF_3 with $TMSN_3$,[131] was attempted. Reaction mixtures of SbF_3 and TMSOTf in a 1:3 stoichiometry in MeCN were assessed and found to yield $Sb(OTf)_3$ as a quantitative product. Formation of gaseous TMSF (b.p. 16.5°C)[16] is detected in the form of bubbles and as a trace component dissolved in MeCN by ^{19}F NMR assay, which also shows disappearance of the broad resonance due to SbF_3 and evolution of a sharp peak due to the triflate anion. Removal of all volatiles under high vacuum at *ca.* 100 °C yields solvent-free $Sb(OTf)_3$ as a light yellow, extremely air-sensitive powder. Variation of the reaction stoichiometry gives $F_2Sb(OTf)$ and $FSb(OTf)_2$, both as air-sensitive white powders. The three antimony

triflates are indefinitely stable under inert atmosphere and can be prepared and isolated as anhydrous solids on a 80-100 mmol scale with excellent reproducibility.

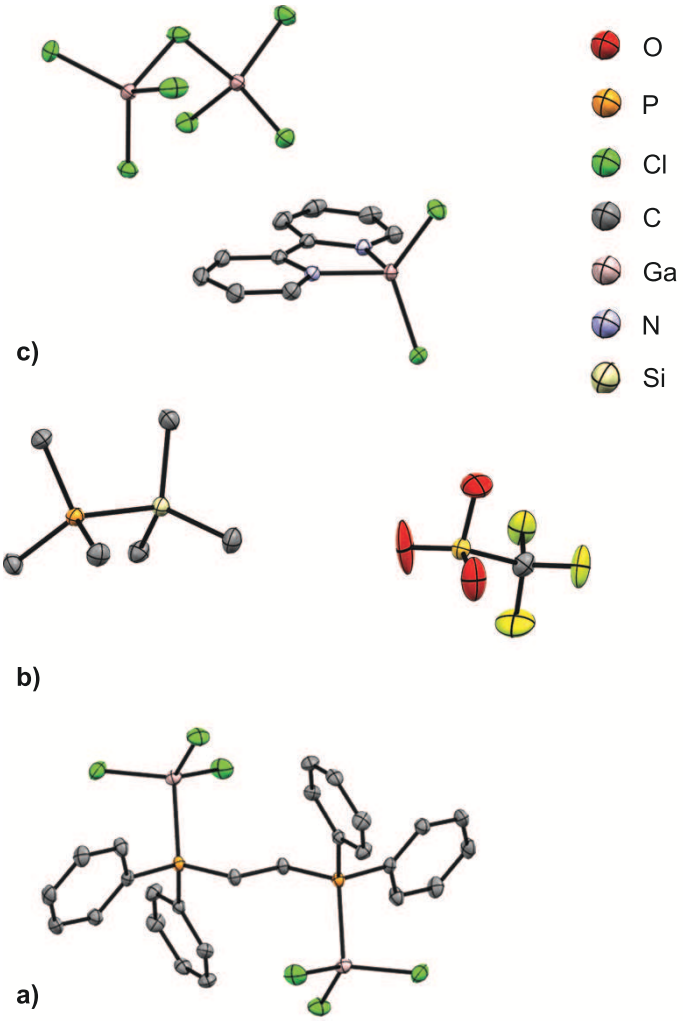

Figure 3.2.1. Solid-states structure of *a*) [*dppe*($GaCl_3$)$_2$], *b*) [Me_3PSiMe_3][OTf], and *c*) [(*bipy*)$GaCl_2$][Ga_2Cl_7]. Hydrogen atoms have been omitted for clarity.

3.2.1 *bipy* Complexes of $F_nSb(OTf)_{(3-n)}$

Addition of *bipy* to solutions of antimony or fluoroantimony triflates led to the formation of stable adducts, which were isolated as pure substances. The structures of [(*bipy*)SbF_2][OTf] and [(*bipy*)$_2$Sb][OTf]$_3$ are shown in Figure 3.2.2 and key structural parameters are collected in Table 3.2.1. The *bis*-triflate derivative [(*bipy*)$_2$SbF][OTf]$_2$ was isolated as a pure compound but could not be characterized by crystallography.

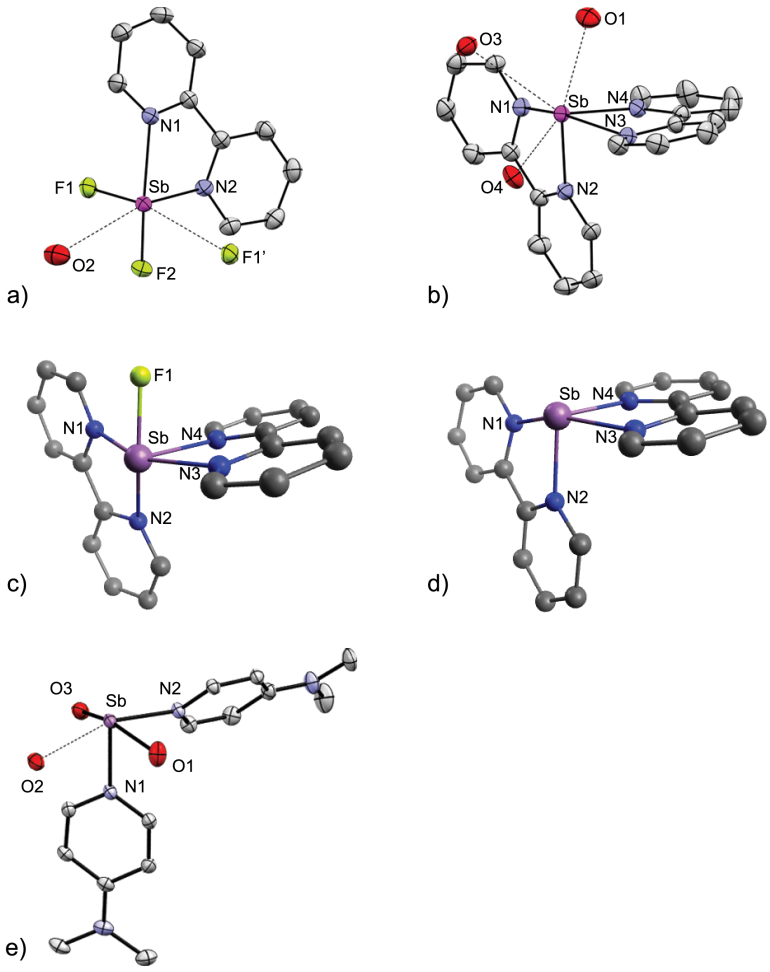

Figure 3.2.2. Solid states structure of *a*) [(*bipy*)SbF_2][OTf], *b*) [(*bipy*)$_2$Sb][OTf]$_3$ and *e*) [(*dmap*)$_2$Sb][OTf]$_3$. Hydrogen atoms and non-interacting portions of the triflate anions have been omitted. Calculated (B3LYP/def2-TZVPP) structures of *c*) [(*bipy*)$_2$SbF]$^{2+}$ and *d*) [(*bipy*)$_2$Sb]$^{3+}$.

The solid-state structure of [(*bipy*)SbF_2][OTf] is best described as a triflate salt of a difluorostibenium cation, $[SbF_2]^{1+}$, which is asymmetrically chelated at antimony by a *bipy* ligand. The antimony centre also engages in weak interactions with one oxygen atom of the anion and a fluorine atom of a neighbouring $[SbF_2]^{1+}$ unit, imposing an overall distorted octahedral geometry at antimony. The structure of [(*bipy*)$_2$Sb][OTf]$_3$ is best described as a *tris*-triflate salt of an $[Sb]^{3+}$ cation chelated by two bidentate *bipy* ligands. The antimony centre shows weak contacts with three oxygen atoms of the triflate anions. The ^{19}F NMR spectra of the *mono*- and *bis*-triflate salts show signals for the $[SbF_2]^{1+}$ and $[SbF]^{2+}$ fragments at $\delta = -90.1$ ppm and $\delta = -93.3$ ppm, respectively, that are severely broadened by the quadrupolar spins of the antimony nuclides. The ^{19}F NMR signals corresponding to the triflate anions in all three cases are characteristically sharp at $\delta = -79.5$ ppm, suggestive of dissociated $[OTf]^{1-}$ ions in MeCN.

The Sb−N bond distances in [(*bipy*)SbF_2][OTf] and [(*bipy*)$_2$Sb][OTf]$_3$ are slightly longer (0.13-0.23 Å) than the sum of the covalent radii for the two elements ($\Sigma_{r,cov}$ = 2.10 Å),[127] while the Sb-O_{OTf} distances are substantially longer (0.55-1.02 Å) than the sum of the covalent radii for the elements ($\Sigma_{r,cov}$ = 2.05 Å),[127] implicating a high degree of ionicity. The Sb−F bond lengths in the *mono*-triflate derivative [1.933(2) Å and 1.939(2) Å] are substantially shorter than the interion Sb−F contact [2.757(2) Å] between adjacent $[SbF_2]^{1+}$ units. Within the respective sums of the van der Waals radii [$\Sigma_{r,vdW}$ = 3.55 Å (Sb−N), 3.52 Å (Sb−O), 3.47 Å (Sb−F)],[111] the antimony centres adopt a six or seven coordinate geometry. While the distortions from ideal octahedral or pentagonal bipyramidal geometry are due to the influence of a stereochemically-active lone pair and the steric strain of the rigid *bipy* ligand, there may also be contributions due to packing of the ions. This is particularly relevant for [(*bipy*)$_2$Sb][OTf]$_3$, where three interion contacts persist.

Atoms O1, O3, and O4 lie 37° below, 38° above, and 32° above, respectively, the plane defined by N4, Sb,and N2. The average Sb−N distance [2.317(4) Å][132] in the neutral complex [(*bipy*)SbF_3] is slightly longer than in its *mono*-triflate counterpart [2.301(4) Å] and substantially longer than in [(*bipy*)$_2$Sb][OTf]$_3$ [2.273(5) Å], despite the steric restrictions imposed by the presence of a second *bipy* ligand in the latter. The trend in Sb−N distances correlates with an increase in the charge at the Sb centre going from [(*bipy*)SbF_3] to [(*bipy*)$_2$Sb][OTf]$_3$. The C−C bond length between

Table 3.2.1. Selected bond lengths (Å) and angles (°) in nitrogen donor complexes of antimony triflates and fluorotriflates. Square brackets denote values calculated for anion-free cations in the gas phase at the B3LYP/def2-TZVPP level.

	$[(bipy)SbF_2]$ $[OTf]$•MeCN	$[(bipy)_2SbF]^{2+}$	$[(bipy)_2Sb]$ $[OTf]_3$•MeCN	$[(dmap)_2Sb]$ $[OTf]_3$
Sb−N1	2.372(2)[2.429]	[2.342]	2.284(2)[2.286]	2.126(3)
Sb−N2	2.230(2)[2.258]	[2.502]	2.233(2)[2.192]	2.158(3)
Sb−N3		[2.502]	2.332(2)[2.286]	
Sb−N4		[2.502]	2.243(2)[2.192]	
Sb−O1			2.598(2)	2.221(3)
Sb−O2	2.942(2)		2.650(2)	2.233(3)
Sb−O3			3.077(1)	2.608(3)
Sb−F1	1.933(2)[1.900]	[1.942]		
Sb−F2	1.939(2)[1.938]			
Sb−F1’	2.757(2)			
N1−Sb−N2	69.70(6)[69.4]	[67.6]	72.09(4)[73.6]	87.66(10)
N1−Sb−N3		[159.1]	156.02(4)[157.9]	
N1−Sb−N4		[91.7]	87.87(4)[91.4]	
N2−Sb−N3		[117.6]	91.42(4)[91.4]	
N2−Sb−N4		[80.2]	78.66(4)[95.5]	
N3−Sb−N4		[70.4]	71.53(4)[73.6]	
N1−Sb−F2	143.26(6)[150.0]			
N2−Sb−F1	95.78(6)[94.8]	[145.2]		
N2−Sb−F2	83.13(6)[83.2]			
F1−Sb−F2	83.92(6)[73.6]			

the pyridine rings of the *bipy* ligand in both triflate salts (*ca.* 1.47 Å) is consistent with a single C−C bond (1.50 Å in free *bipy*)[133] discounting oxidation of the ligand upon interaction with the antimony cation.

The $[SbF_2]^{1+}$ moiety in $[(bipy)SbF_2]^{1+}$ can be compared with the only structurally characterized examples of difluoropnictenium ions in $[AsF_2][SbF_6]$[134] and $[K/NH_4][SbF_2][HAsO_4]$.[135] The Sb−F bond lengths [1.933(2) Å and 1.939(2) Å] in the *bipy* complex are significantly shorter than the sum of the covalent radii for the elements ($\Sigma_{r,cov}$ = 2.03 Å),[127] and are slightly shorter than those in $[K/NH_4][SbF_2][HAsO_4]$ [1.959(2) Å and 1.995(2) Å for K; 1.953(4) Å and 1.999(4) Å for NH_4]. Consistent with the trends observed in the Sb−N distances, the Sb−F bonds in are *ca.* 0.1 Å shorter than those in neutral $[(bipy)SbF_3]$ and are comparable to those observed in compounds featuring $[SbF]^{2+}$ centres with strongly interacting anions: 1.934(4) Å in $[Na][SbF][PO_4]$ and 1.923(4) Å in $[NH_4][SbF][PO_4]$.[136]

The optimized DFT (B3LYP/def2-TZVPP) structures for anion-free $[(bipy)_2SbF]^{2+}$ and $[(bipy)_2Sb]^{3+}$ in the gas phase (see Figures 3.2.2*c* and 3.2.2*d*) show five- and four-coordinate geometries, respectively. The calculated structure for the anion-free trication shows similar bond lengths (within 0.05 Å) to the experimentally observed values for its triflate salt and a disphenoidal (AB_4E) VSEPR geometry for Sb. The hypothetical C_{2v} (square-based pyramid), D_{2h} (square-planar N_4) and S_4 (tetrahedral N4) structures for $[(bipy)_2Sb]^{3+}$ are not global minima and are all higher in energy than the disphenoidal structure. Table 3.2.1 lists the calculated metric parameters for the three cations. The calculated Sb−N bonds in $[(bipy)SbF_2]^{1+}$ and $[(bipy)_2Sb]^{3+}$ are on average 0.069 Å longer and 0.034 Å shorter, respectively, than those observed in the solid-state structures. There is no significant variation between the observed and calculated bond angles for $[(bipy)SbF_2]^{1+}$. On the other hand, comparison of the bond angles for $[(bipy)_2Sb]^{3+}$ clearly shows that the presence of three anion contacts in the plane of N2 and N4 in the solid-state causes a compression of the angle between the two *bipy* ligands [calcd.: 95.55°, expt.: 78.66(4)°]. The distorted trigonal-bipyramidal geometry at antimony arises from the presence of a stereochemically-active lone pair.

The calculated Sb−F bond length in $[(bipy)_2SbF]^{2+}$ is essentially the same as the observed and calculated Sb−F bonds in $[(bipy)SbF_2][OTf]$, suggesting that the increased charge in the dication is effectively offset by the introductions of a second *bipy* ligand. Consistently, the calculated Sb−N bond lengths in $[(bipy)_2SbF]^{2+}$ are on

average 0.130 Å longer than those calculated for $[(bipy)_2Sb]^{3+}$, indicating accommodation of molecular charge in the Sb−N bonds. The alternate VSEPR C_{2v} square-based pyramid (AB_4CE) geometry for $[(bipy)_2SbF]^{2+}$ was calculated to be 22 kJ mol^{-1} higher than the minimum energy structure in Figure 3.2.2*c*.

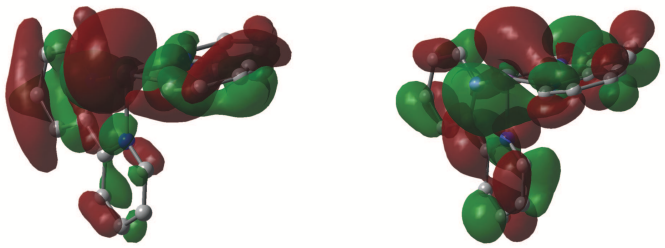

Figure 3.2.3. Calculated (B3LYP/def2-TZVPP) HOMO−2 (left) and LUMO (right) for the $[(bipy)_2Sb]^{3+}$ cation in the gas phase. Hydrogen atoms omitted for clarity.

NBO analysis for $[(bipy)_2Sb]^{3+}$ gives a residual charge of $+1.77e$ at the Sb atom, indicating a substantial Lewis acidity. Furthermore, the LUMO (Figure 3.2.3, right) shows two large lobes at Sb *trans* to the N_2−Sb and N_4−Sb bonds, inviting interaction from a third chelate. Consistently, the optimized structure for $[(bipy)_3Sb]^{3+}$ in the gas phase is *ca.* 250 kJ mol^{-1} lower in energy than $[(bipy)_2Sb]^{3+}$ and dissociated *bipy*. However, a 1:1 mixture of $[(bipy)_2Sb][OTf]_3$ with *bipy* showed no evidence for the formation of the *tris-bipy* complex and the starting materials were recovered. While *tris-bipy* complexes are commonplace in transition metal chemistry,[137,138] their formation is presumably precluded for antimony(III) due to the presence of a stereochemically-active 5*s* lone pair, identified as HOMO−2 (see Figure 3.2.3, left), as well as triflate anion contacts in $[(bipy)_2Sb]^{3+}$, both of which impose a significant kinetic barrier to association of the third ligand molecule.

Consideration of the bond angles in $[(bipy)SbF_2][OTf]$ and $[(bipy)_2Sb][OTf]_3$ reveals the acceptor orbitals at the antimony centre. In the former, the F1−Sb−N2 and F_2−Sb−N_2 angles [95.78(6)° and 83.13(6)°, respectively] indicate that N2 interacts with the vacant *p*-orbital that is orthogonal to the F−Sb−F plane. The slightly longer Sb−N_1 interaction is due to the *trans* influence of the Sb−F2 bond. In the *tris*-triflate, where four N-donors are present, two sets involving three approximately orthogonal N−Sb interactions (corresponding to three vacant *p*-orbitals of $[Sb]^{3+}$) are evident,

with deviation from the idealized 90° angle due to restrictions imposed by the chelate interaction and possibly due to the presence of a stereochemically-active $5s$ lone pair. Thus, the average N−Sb−N angle involving Sb−N1, Sb−N4 and Sb−N2 bonds is 79.54° and the average N−Sb−N angle involving Sb−N2, Sb−N3 and Sb−N4 bonds is 80.57°. For comparison, the gas-phase[139] and solid-state[140] structures of SbF_3 show F−Sb−F angles of 94.8(2)° and 87.3(3)°, respectively.

The structure of $[(dmap)_2Sb][OTf]_3$ was also obtained to provide an example where bond angles are not determined by steric restrictions in the ligands. In line with the orbital discussion above, the N_1−Sb−N_2 angle in this compound is 87.66(10)°, and two strong triflate interactions subtend an average angle of 81.11° with respect to the N1-Sb-N2 plane. The deviation in this value from 90° is attributed to the lone pair at Sb as well as the presence of a third triflate anion contact. The Sb−N lengths are shortest amongst the compounds discussed here [2.126(3) and 2.158(3) Å] due to the greater donor strength and lesser steric constraints of *dmap* relative to *bipy*.

The chelate *bipy* complexation of $[SbF_2]^{1+}$ is analogous to that observed for the interaction of *dppm* with $[SbCl_2]^{1+}$ in $[(dppm)SbCl_2][AlCl_4]$ (*vide infra*), illustrating retention of a pyramidal geometry at antimony and asymmetric chelation. In contrast to $[(bipy)_2SbF][OTf]_2$, where the $[SbF]^{2+}$ fragment accommodates two *bipy* ligands, $[SbCl]^{2+}$ engages only one *dppm* in $[(dppm)SbCl][Al_2Cl_7]_2$ (*vide infra*). Mixtures of the latter with excess *dppm* and a variety of Lewis acids show no evidence of a $[(dppm)_2Sb]^{3+}$ complex. Similarly, mixtures of $SbCl_3$, TMSOTf and *bipy* initially show ^{1}H NMR signals assigned to chloride derivatives $[(bipy)SbCl_2][OTf]$ and $[(bipy)_2SbCl][OTf]_2$, while $[(bipy)_2Sb][OTf]_3$ is only observed in trace amounts when the reaction mixtures are subjected to removal (under vacuum) of TMSCl followed by addition of excess TMSOTf. This observation suggests a very low equilibrium constant for abstraction of a chloride anion from $[SbCl]^{2+}$ by TMSOTf.

To understand the thermodynamic factors that enable fluoride ion abstraction from $[SbF]^{2+}$ and preclude the chloride ion abstraction from $[SbCl]^{2+}$, the reaction enthalpy for halide transfer from antimony to silicon was calculated according to the equation 3.3 below.

$$SbX_3 \longrightarrow [Sb]^{3+} + 3\,[X]^{1-} \tag{3.1}$$

$$3\,[Me_3Si]^{1+} + 3\,[X]^{1-} \longrightarrow 3\,Me_3SiX \tag{3.2}$$

$$SbX_3 + 3\,[Me_3Si]^{1+} \longrightarrow [Sb]^{3+} + 3\,Me_3SiX \qquad (3.3)$$

To assess their relative thermodynamic contributions, the E−X heterolytic bond strengths (half-reactions 3.1 and 3.2) were also estimated by using an isodesmic scheme that incorporates experimentally known halide-ion-affinities for $AlCl_3$[114] as reference reactions. The enthalpies of reactions 3.1−3.3 (see Table 3.2.2) show that halide transfer from antimony to silicon is substantially more favourable for SbF_3 than for $SbCl_3$, because the heterolytic association of three Si−F bonds is 607 kJ mol^{-1} more exothermic than the heterolytic association of three Si−Cl bonds whereas the heterolytic cleavage of three fluoride ions from SbF_3 is only 463 kJ mol^{-1} more endothermic than the heterolytic cleavage of three chloride ions from $SbCl_3$. Consequently, the fluoride ion affinity of the hypothetical $[TMS]^+$ cation (950 kJ mol^{-1} calculated here; *cf.* 965 kJ mol^{-1} calculated at the MP2 level[53]), more than compensates for the increased Sb−X bond strength going from chlorine to fluorine, rendering equation 3.3 more favourable by 144 kJ mol^{-1} for X = F, consistent with the experimental observations.

Table 3.2.2. Calculated (B3LYP/def2-TZVPP) reaction enthalpies (kJ mol^{-1}) for complete dissociation of $[X]^{1-}$ ions from SbX_3 (eq. 3.1), for association of $[X]^{1-}$ ions with $[Me_3Si]^{11+}$ (eq. 3.2), and for halide transfer from SbX_3 to $3[Me_3Si]^{1+}$ (eq. 3.3).

Reaction	ΔH_{rxn}(X=F)	ΔH_{rxn}(X=Cl)	$\Delta\Delta H_{rxn}$
3.1	+5275	+4812	+463
3.2	−2850	−2243	−607
3.3	+2425	+2569	−144

Reaction enthalpies calculated from isodesmic reactions using experimentally known halide-ion-affinities of $AlCl_3$ and calculated halide-ion-affinities of $[SbX_n]^{(3-n)+}$ and $[Me_3Si]^{1+}$. Definition of $\Delta\Delta H_{rxn} = \Delta H_{rxn}$(X=F) $-\Delta H_{rxn}$ (X=Cl).

Thus, by exploiting the thermodynamically favourable elimination of gaseous TMSF from the rapid reaction of SbF_3 with the highly fluoro-acidic TMSOTf reagent,[138] antimony triflates are easily accessed in high yields and isolated as *bipy* complexes. With a synthetic route to $Sb(OTf)_3$ in hand, it was subsequently possible to prepare and isolate phosphine complexes of this strong acceptor, and these are described in Sections 3.2.2 and 3.2.3 as well as Chapters 5 and 6.

3.2.2 Charge-variant Series of P−Sb Complexes

Unlike hard pyridinoid donors, soft phosphine donors are expected to behave quite differently with very hard acceptors like the $[Sb]^{3+}$ cation. To assess the potential for novel reaction chemistry arising from such a soft/hard donor/acceptor combination, reactions of $Sb(OTf)_3$ were attempted with a variety of phosphines. In brief, *tris*-trialkylphosphine complexes of the form $[(R_3P)_3Sb][OTf]_3$ are accessible but only as transients that undergo unprecedented redox chemistry to give *catena*-antimony compounds. For example, the solid-state structure of the $[(Me_3P)_3Sb]^{3+}$ cation has been obtained from a low-temperature preparation but this compound spontaneously eliminates $[Me_3PPMe_3]^{2+}$ at room temperature. A detailed study of this reaction pathway has been conducted and results are given in Chapter 5.

This redox chemistry aside, the solid-state structure of $[(Me_3P)_3Sb]^{3+}$ is also significant because it completes the structural characterization for an extensive charge-variant series consisting of the complexes $[(Me_3P)SbCl_4]^{1-}$, $[(Me_3P)SbCl_3]$, $[(Me_3P)SbCl_2]^{1+}$, $[(Me_3P)_2SbCl_3]$, $[(Me_3P)_2SbCl_2]^{1+}$, $[(Me_3P)_2SbCl]^{2+}$ and $[(Me_3P)_3Sb]^{3+}$, for which selected bond lengths are illustrated graphically in Figure 3.2.4. Notwithstanding the outlier long P−Sb bond for $[(Me_3P)_2SbCl_3]$, corresponding to the only P−Sb bond that is *trans* to a chloride substituent, the Sb−Cl bonds adopt a substantially broader range than the P−Sb bonds. A similar effect is evident for phosphine complexes of tin halides.[42]

While a greater positive charge is expected to result in stronger and shorter coordinate bonds, the P−Sb bonds are slightly longer for complexes with greater charge. These results are borne out by calculated (MP2/def2-TZVPP) gas-phase geometry optimizations for select complexes. For example, the calculated gas-phase structure of $[(Me_3P)SbCl_3]$ shows a P−Sb bond (2.542 Å) that is slightly shorter than that calculated for $[(Me_3P)SbCl_2]^{1+}$ (2.561 Å). The corresponding Sb−Cl distances for the neutral (2.491 Å) and cationic (2.315 Å) complexes show the opposite trend. Similarly, the P−Sb distance in the calculated structure of $[(Me_3P)_2SbCl_2]^{1+}$ (2.555 Å) is shorter than in $[(Me_3P)_2SbCl]^{2+}$ (2.561 Å), whereas the Sb−Cl distance is shorter for the greater charge (2.507 Å and 2.317 Å, respectively). These observations are consistent with strengthening of the Sb−Cl bond with increasing charge, predicted by increased electrostatic attraction across the polar Sb−Cl bond. In addition, electronic structure calculations on the model complex $[(Me_3P)SbCl_2]^{1+}$ also show (Figure 3.2.5)

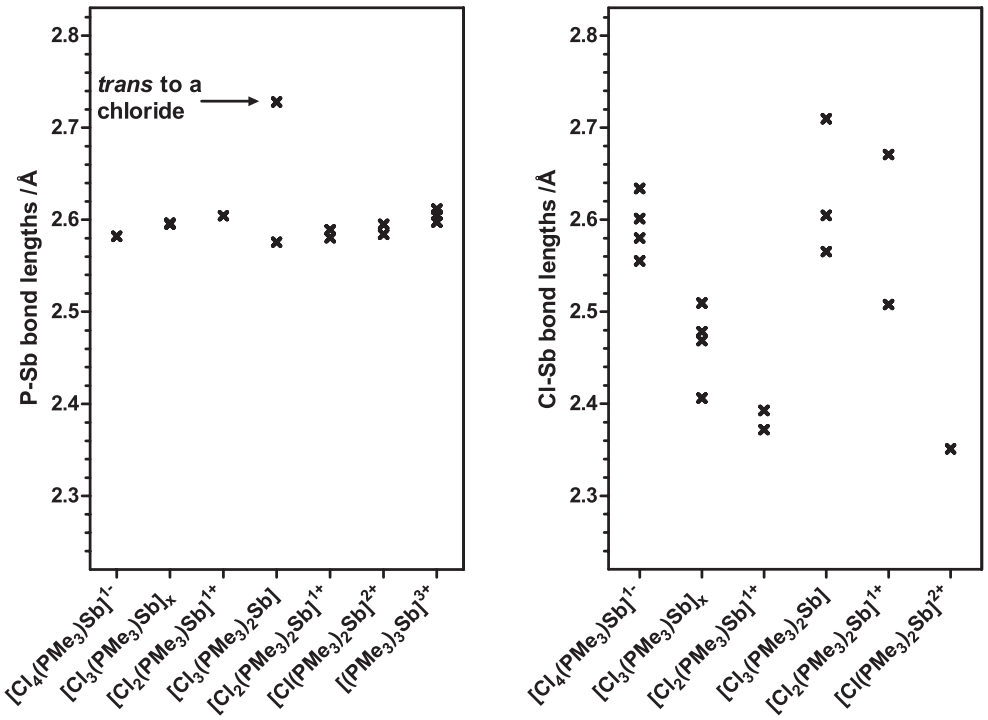

Figure 3.2.4. P−Sb (left) and Sb−Cl (right) bond lengths in PMe_3 complexes of chloroantimony acceptors. Note the identical range of the y-axis in both plots.

increased Sb−Cl covalency via two π-type bonding MOs (HOMO−4, HOMO−5) delocalized over the Cl−Sb−Cl fragment, evidencing competitive occupancy of a *p*-orbital at Sb by the phosphine and chlorine lone pairs. This π-type interaction is in addition to two Sb−Cl σ-bonding MOs (HOMO−6, HOMO−8) and may explain preferential shortening of the Sb−Cl bonds at the cost of elongated P−Sb bonds.

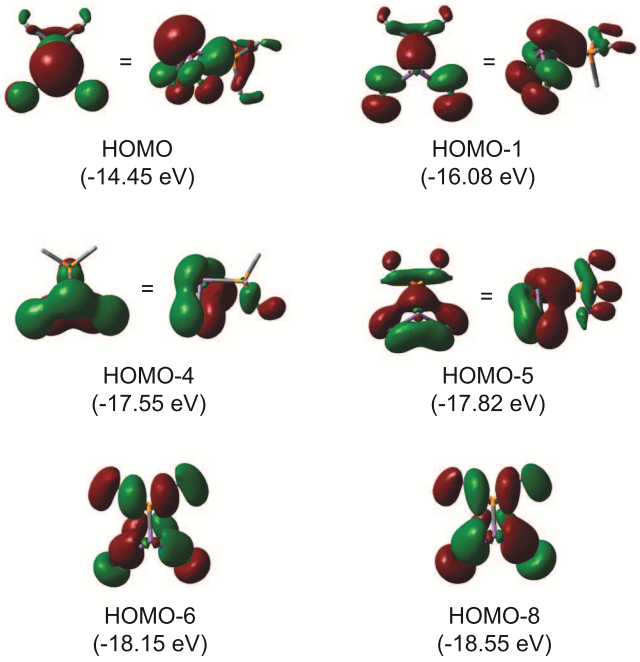

Figure 3.2.5. Calculated (MP2/def2-TZVPP) molecular orbitals relevant to key bonding interactions in the $[(Me_3P)SbCl_2]^{1+}$ cation.

The sum of bond angles around the trigonal pyramidal Sb centres in $[(Me_3P)SbCl_2]^{1+}$ (274.1°), $[(Me_3P)_2SbCl]^{2+}$ (283.9°), and $[(Me_3P)_3Sb]^{3+}$ (305.8°) increase drastically with steric bulk upon stepwise substitution of chlorides with phosphines. For comparison, the sum of the Cl−Sb−Cl bond angle in solid and gaseous $SbCl_3$ is 285.6°[16] and 291.57°,[141] respectively. The extent of pyramidalization around phosphorus decreases only slightly upon successive removal of chlorides in $[(Me_3P)SbCl_4]^{1-}$ (319.1°), $[(Me_3P)SbCl_3]$ (320.5°), and $[(Me_3P)SbCl_2]^{1+}$ (322.2°).

The ^{31}P-NMR spectra of derivatives of $[(Me_3P)_mSbCl_n]^{(3-n)+}$ (n = 1 − 4, m = 1, 2) in CD_3CN at 298 K are plotted in Figure 3.2.6 as a function of the formal charge on the complex. The phosphorus centres in $[(Me_3P)_2SbCl_2]^{1+}$, and $[(Me_3P)_2SbCl]^{2+}$ are isochronous by symmetry and give rise to a single chemical shift value. For [*cis*−$(Me_3P)_2SbCl_3$−*mer*], only one signal is observed, despite the non-equivalence

of the phosphorus centres in its solid-state structure, indicating a dynamic process that exchanges the two phosphines. In a low-temperature NMR experiment, the slow-exchange limit characterized by decoalescence and peak separation was not reached even at −90 °C, preventing a determination of unique chemical shifts for the two environments.

The ^{31}P NMR results are consistent with greater deshielding of the phosphorus nucleus for complexes of higher positive charge. The *mono*-phosphine complexes show chemical shifts that are further downfield than their *bis*-phosphine analogues, indicating a distribution of the charge over two phosphines. The effect is most pronounced in complexes of $[SbPh_2]^+$, which show ^{31}P chemical shifts of −21.2 ppm and −41.3 ppm for the *mono*- and *bis*-PMe_3 complexes, respectively. Similarly, the shift for $[(Cy_3P)SbCl_3]$ (+25.1 ppm) is 10 ppm downfield of $[(Cy_3P)_2SbCl_3]$ (+15.7 ppm). By comparison, the ^{31}P chemical shifts of PPh_3 complexes are essentially independent of charge or geometry, and are almost identical to that of free PPh_3 (−5.6 ppm), suggesting that even in weakly polar solvents (*e.g.* CD_2Cl_2), solutions of the PPh_3 complexes consist of dissociated phosphine ligands and solvated $SbCl_3$, $Cl_2Sb(OTf)$, or $Ph_2Sb(OTf)$. The solvation enthalpies of these individual species therefore match or surpass the strength of the phosphine-stibine interaction, and in the absence of solvent, crystalline products with P−Sb bonds are obtained in the solid-state. Consistently, all observed PPh_3 complexes are soluble in CH_2Cl_2.

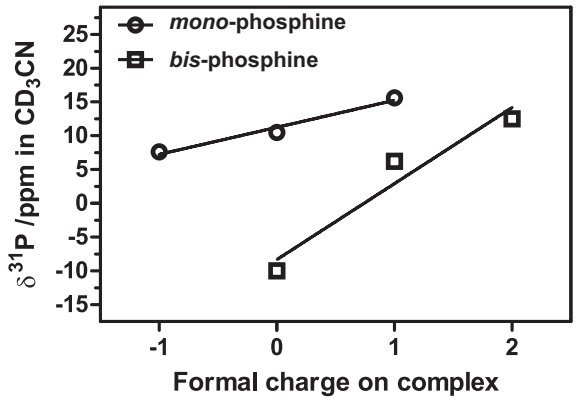

Figure 3.2.6. ^{31}P NMR chemical shifts (CD_3CN) for complexes in the charge-variant series $[(Me_3P)_mSbCl_n]^{(3-n)+}$; $n = 1-4$, $m = 1, 2$, plotted as a function of the formal charge on the complex.

Complexes with chelating donors

Much of the preceding discussion has focused upon monodentate ligands. A fundamentally different class of ligands, bidentate phosphines, were also found to bind antimony acceptors, giving rise to new cyclic structural frameworks. Charge-variant series of complexes with *dppm* and *dppe* have been prepared and structurally characterized as shown in Figure 3.2.7. A detailed analysis of structural parameters and chemical shifts, as performed for the PMe_3 case above, is not given here since an investigation into the structure and reactivity of these interesting inorganic heterocycles, together with their fluorine analogues, is deferred for a later project.

It is worth noting, however, that the structures observed in Figure 3.2.7 are all consistent with trends in the *trans*-labilizing influence of phosphine ligands described in previous sections. In particular, the arylphosphine ligands in $[dppm(SbCl_3)_2]$ and $[dppe(SbCl_3)_2]$ bind to antimony in a position *trans* to a chloride. For cationic complexes, the chelate interaction enforces a *cis* geometry for the ligands, forcing the halides to be *trans* to one another.

Another example of the unique chemical outcomes due to cyclic coordination framework is the dynamic behaviour of $[(dppm)SbCl_2]^{1+}$ in solution. The asymmetric chelation observed in the solid-state structure of the cation in its tetrachloroaluminate salt, with one coordinated and one free phosphine (see Figure 3.2.7*b*), does not give rise to unique ^{31}P resonances but rather an averaged value at room temperature. The broadness of the signal is indicative of a dynamic exchange process and upon cooling to *ca.* -85° the two phosphorus environments are resolved as two doublets with very different chemical shifts. On the basis of the coalescence temperature for the signals (see Figure 3.2.8), an estimate of the activation barrier to transfer of the stibenium cation between the phosphorus centres was estimated to be *ca.* 10 kJ mol^{-1}.

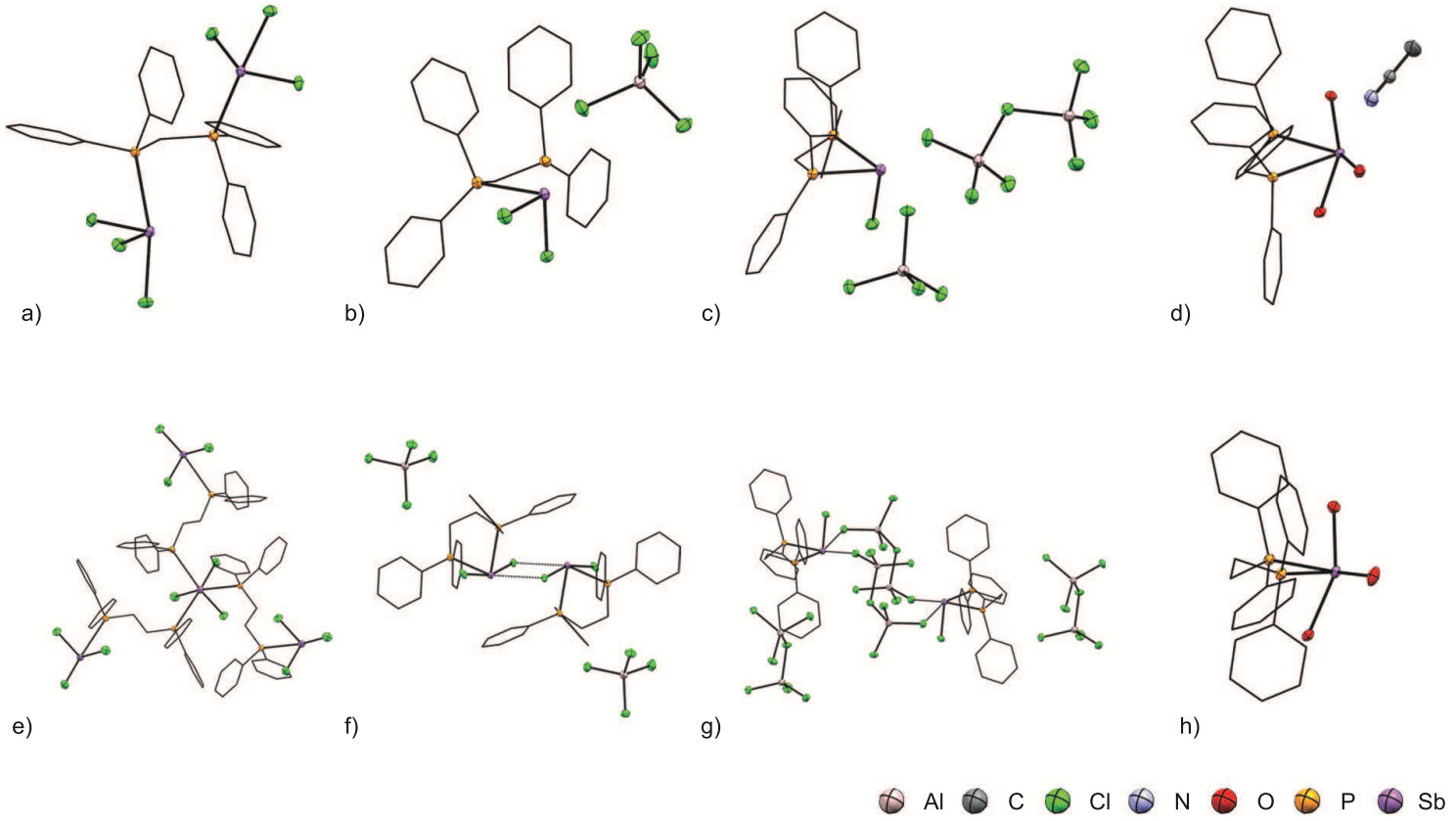

Figure 3.2.7. Solid-state structures of *a*) [(*dppm*)($SbCl_3$)$_2$], *b*) [(*dppm*)$SbCl_2$][$AlCl_4$], *c*) [(*dppm*)SbCl][$AlCl_4$][Al_2Cl_7], *d*) [(*dppm*)Sb($OTf)_3$)]•MeCN , *e*) [(*dppe*)$SbCl_3$], *f*) [(*dppe*)$SbCl_2$)][$AlCl_4$], *g*) [(*dppe*)SbCl][Al_2Cl_7]$_2$.

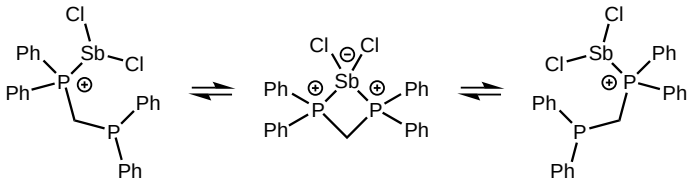

Scheme 3.2.1. Transfer of a $[SbCl_2]^{1+}$ cation between the two phosphine donors of *dppm*.

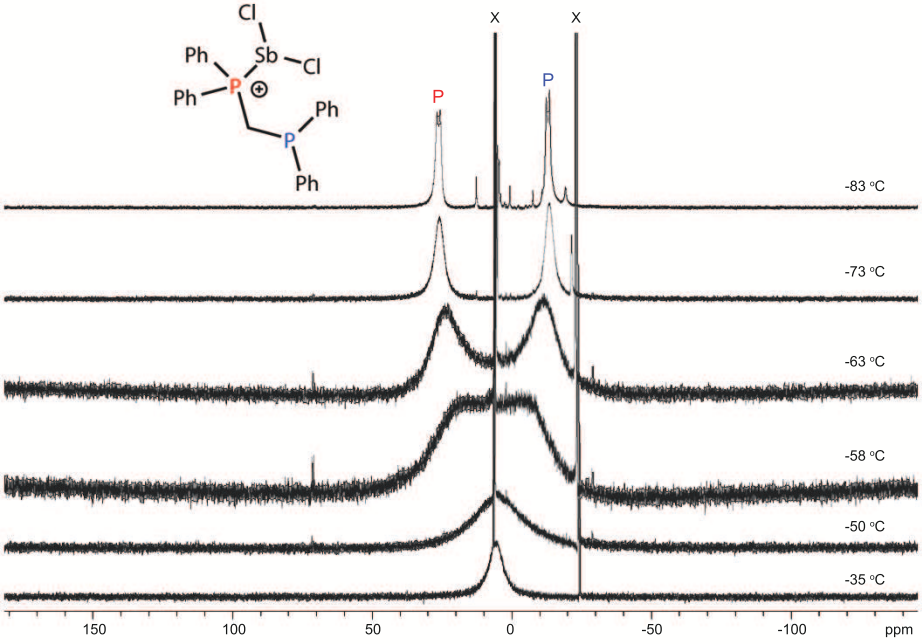

Figure 3.2.8. $^{31}P\{^1H\}$ NMR spectra of $[(dppm)SbCl_2][AlCl_4]$ showing a temperature dependent dynamic process that shuttles the $[SbCl_2]^{1+}$ cation between the two phosphine donors of *dppm*. Signals due to a trace amount of $[(dppm)H]^{1+}$ are denoted with an '×' symbol.

The ability to coordinate multiple metal centres to the same ligand (Figures 3.2.7*a* and 3.2.7*b*) together with the ability to coordinate two phosphines to the same antimony centre sets the stage for preparing heterobimetallic complexes and coordination polymers featuring bidentate phosphine linkers between antimony nodes. Ligands with two phosphine moeities may be coerced into bridging ligation by the use of a rigid backbone as in the case of *trans-dppe*. As a proof of this principle, a complex featuring two $[SbCl_2]^{1+}$ donors bound to *trans*-1,2-*bis*(diphenylphosphino)ethylene (*trans-dppe*) has been isolated and characterized (Figure 3.2.9). Reactions of the

saturated ligand, *dppe*, with half an equivalent of the $[SbCl_2]^{1+}$ ion (generated *in situ*) only yield the chelating phosphine complex $[(dppe)SbCl_2]^{1+}$ and unreacted phosphine, evidencing the apparent need for a restricted backbone to preclude chelation.

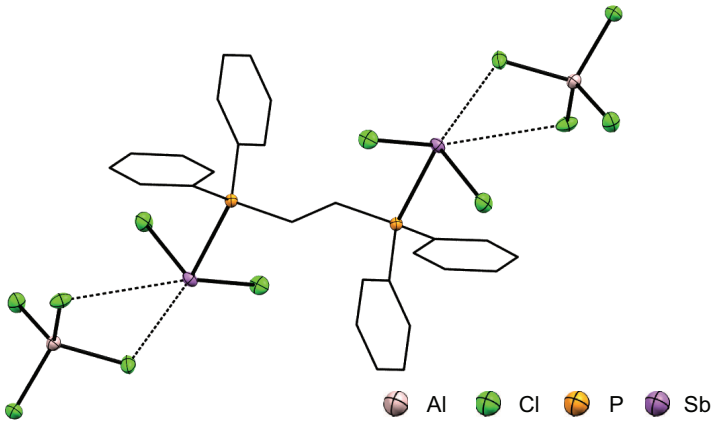

Figure 3.2.9. Molecular structure of $[trans{-}dppe(SbCl_2)_2][AlCl_4]_2$ in the solid state. Select bond lengths (Å) and angles (°) are as follows: P−Sb = 2.6283(4), Sb−Cl = 2.3375(5), 2.3430(5), Cl−Sb−Cl = 95.845(19), P−Sb−Cl = 90.550(15), 87.777(15).

3.3 Summary

Several series of P−Sb complexes featuring anionic, charged and cationic antimony acceptors have been synthesized and structurally characterized. Based on the observed configurations of substituents and ligands at antimony, the relative *trans*-labilizing influence exerted by a lone pair, a substituent or a ligand is concluded to be: lone pair < PPh_3 ≈ $[Cl]^{1-}$ < PCy_3 ≈ PMe_3 < $[Ph]^{1-}$. Consistent with this model, all previously reported adducts of $SbCl_3$ with Lewis bases weaker than PMe_3 adopt a facial configuration of chloride substituents, while complexes with the strong donors like *bipy*, 1,3-dimethyl-2-imidazolethione, tetramethylthiourea, or PCy_3, show the meridional configuration of chloride substituents, and the distinction is also evident in the solid-state structures of other antimony halides. It is expected that relative *trans*-labilizing influence of these fragments will be broadly applicable to analogous complexes of other main group acceptor centers bearing a lone pair. Therefore carbene complexes of the type $[(NHC)SbCl_3]$ are predicted to feature a $[(NHC)SbCl_3{-}mer]$ A configuration (Scheme 3.0.2), since carbenes are stronger donors than the most basic phosphines, and this prediction has recently been borne out by structural reports of

such complexes.[38,142] By corollary, donors weaker than phosphines, such as phosphine sulfides, will adopt a [$LSbCl_3$−*fac*] configuration (Scheme 3.0.2), and this claim has also been verified in a recent structural assessment of such compounds.[40]

Calculations on molecules in the gas-phase suggest that the 1:1 neutral complexes are stable, but the 1:2 stibine:phosphine complexes are unstable with respect to dissociation of one of the phosphine ligands. Nevertheless, they are observed in the solution and solid states due to additional stabilization from intermolecular interactions. These findings advocate for a measure of skepticism when interpreting statements regarding the stability of such weakly-bound complexes in cases when such conclusions are drawn exclusively from gas-phase modelling, and particularly without the use of dispersion corrected theoretical methods.[126] Comparison of the experimental structural data for a charge-variant series of PMe_3 complexes of haloantimony centers reveals counterintuitive differences in the P−Sb and Sb−Cl bond lengths, which are explained with reference to increased ionic and covalent Sb−Cl bonding, as borne out in computational models. For PMe_3 complexes, solution-phase ^{31}P NMR spectroscopy is a sensitive probe of the overall charge on the complex, while PPh_3 complexes dissociate in solution and show only the free ligand.

Access to tricationic (*tris*-triflate) complexes is possible by judicious choice of the antimony halide and Lewis acid. The combination of SbF_3 and TMSOTf in these roles gives facile access to the desired triflates due to the strong Si−F bond strength and by exploiting Le Châtelier's principle in removing the gaseous product of the fluoride abstraction from the reaction mixture. Using this strategy, a number of bipyridine and phosphine complexes of $Sb(OTf)_3$ could be isolated. A novel redox chemistry for tricationic trialkylphosphine complexes has been mentioned briefly and in Chapter 5, full details of this reaction pathway are given along with a study of the resulting products.

There is renewed interest in the development of ligand-stabilized main group halides and pseudohalides, with a view towards using their reduction chemistry to access species featuring multiply-bonded elements. While most efforts have been directed towards carbene-stabilized main group centers, analogous reductive coupling chemistry for phosphine-stabilized cationic halophosphine and halostibine centers has also been demonstrated.[52,78] In addition, a recent theoretical investigation[126] has made specific predictions about the viability of accessing phosphine-stabilized group

15 element dimers (E−E triple bonded molecules) from $[(R_3P)ECl_3]$. The complexes presented in this chapter are ideal precursors to test such predictions.

Chapter 4

Bismuth Complexes

Bismuth bookends the periodic table as the heaviest element with a stable nuclide. From the perspective of coordination chemistry, bismuth is expected to closely mirror features observed for its lighter congener, antimony. Nevertheless its larger covalent radius, greater oxidizing ability and the established importance of relativistic effects in determining its structure and reaction chemistry prompted an extension of phosphine coordination chemistry to this heavy main group metal.

This chapter outlines the synthesis of bismuth coordination complexes with O, and P donors. In broad terms, the structural features of these compounds suggest that due to the large covalent radius of bismuth, they are more accurately formulated as triflate *complexes* (significant ion-pairing in the solid state) rather than triflate *salts* (minimal ion-pairing in the solid state). Their ^{31}P NMR chemical shifts show a marked downfield shift when compared with antimony homologues. The phosphine complexes are difficult to handle, particularly in solution where they undergo decomposition within days to elemental bismuth and unidentified products, even at -30 °C. By comparison, with oxidatively resistant O ligands, indefinitely stable complexes are obtained.

The results of preliminary reactivity studies show that the phosphine complexes are strong and hard Lewis acids which abstract halides from other metal halides but do not coordinate to electron rich metals *via* Z-type interactions. The enhanced Lewis acidity of the complexes described here makes them interesting candidates for the study of Lewis acid-catalyzed organic transformations, an area of research where bismuth-based Lewis acids have already found much utility due to their low

toxicity, low catalyst loadings, and hydrocompatibility.[143] In this context, a significant outcome of this chapter is the preparative scale (*ca.* 10 g) synthesis of the powerful Lewis acid $[(THF)_4Bi_2Br_4(OTf)_2]$.

4.1 Complexes of Bismuth Triflates with THF and *dmpe*

The coordination chemistry of bismuth acceptors is well-established with nitrogen, oxygen and sulfur donors and has been reviewed recently.[144–146] Coordination with phosphine ligands is known to a lesser extent and a comprehensive list of structurally-authenticated complexes is in given in Table 4.1.1. A number of other P−Bi complexes have been studied using vibrational and NMR spectroscopy as well as elemental analysis.[18]

Unlike neutral complexes, charged derivatives remain quite rare. Only one cation is known, featuring a $[BiPh_2]^{1+}$ acceptor with two PPh_3 donors giving a four-coordinate, disphenoidal geometry around Bi with axially-oriented phosphine ligands.[33] To expand the scope of cationic P−Bi complexes, triflate derivatives of bismuth halides were prepared as precursors to cationic phosphine complexes. For comparison with previously reported neutral and anionic examples, the chelating phosphines *dmpe*, and *dppe* were chosen as ligands, with the expectation of observing enhanced Lewis acidity in complexes formulated as having dihalobismuthenium ($[BiX_2]^{1+}$) and halobismuthidenium ($[BiX]^{2+}$) cations as acceptors.

Equimolar combination of $BiBr_3$ and MeOTf in THF results in exothermic elimination of gaseous CH_3Br and formation of $[(THF)_4Bi_2Br_4(OTf)_2]$ (**4.1**). The reaction mixture becomes gelatinous over the course of the reaction due to Lewis acid-catalyzed ring-opening polymerization of THF, which is a well-known mode of reactivity for metal cations in ethereal solvents.[147] Nevertheless, single crystals of the compound were obtained in 78% yield (isolated crystals) upon recrystallization from a 1:1 Et_2O/CH_2Cl_2 solution. The crystalline solid retains THF under vacuum (0.05 mbar) at room temperature as confirmed by NMR spectroscopy and elemental analysis data. When the crystals are heated under vacuum an insoluble dark brown powder is formed.

Reaction of **4.1** with *dmpe* in toluene results in quantitative (as shown by ^{31}P NMR spectra of the reaction mixtures) formation of $[(dmpe)_2Bi_2Br_4(OTf)_2]$ (**4.2**)

demonstrating displacement of the THF groups in **4.1** by the chelating phosphine ligand. Crystals of **4.2**•MeCN were obtained by recrystallization from a concentrated MeCN solution at −30 °C. While room temperature solutions of the compound are unstable with respect to deposition of insoluble elemental bismuth within days, isolated crystals are thermally stable under inert atmosphere at room temperature for weeks.

Table 4.1.1. Structurally-authenticated phosphine complexes of bismuth acceptors.

Compound	Reference
$[(Me_3P)_2Bi_2Br_7]^{1-}$	[148]
$[(PhMe_2P)BiI_4]^{1-}$	[122]
$[(Me_3P)_4Bi_2Br_6]$	[149]
$[(Et_3P)_4Bi_4Br_{12}]$	[123]
$[(dmpe)_2Bi_2Br_6]$	[123]
$[(PhMe_2P)_2(PhMe_2PO)_2Bi_2Br_6]$	[149]
$[(dppm)_2Bi_2Cl_6]$	[150]
$[(dppe)_2Bi_2Cl_6]$	[150]
$[(dppe)_4Bi_2Br_6]$	[123]
$[(dppe)_3Bi_2Cl_6]$	[150]
$[(Ph_3P)_2BiPh_2]^{1+}$	[33]

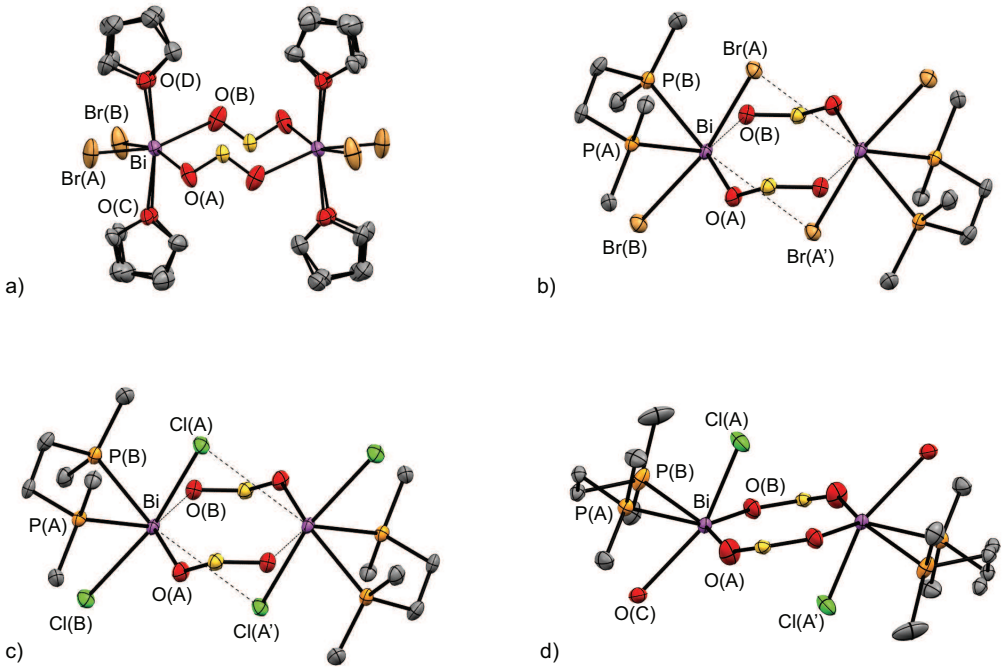

Figure 4.1.1. Molecular structure of compounds **4.1**, **4.2**•MeCN, **4.3**•MeCN, and **4.4**•MeCN in the solid state. Hydrogen atoms, solvent molecules and non-essential portions of triflate ions have been omitted for clarity.

Table 4.1.2. Selected bond lengths (Å) and angles (°) in the solid-state structures of compounds **4.1**, **4.2**•MeCN, **4.3**•MeCN, and **4.4**•MeCN along with gas-phase values for ligand- and anion-free cations $[BiBr_2]^{1+}$, $[BiCl_2]^{1+}$, and $[BiCl]^{1+}$. Calculated values (MP2/Def2-TZVPP) are given in square brackets.

	4.1	**4.2**•MeCN	**4.3**•MeCN	**4.4**•MeCN	$[BiBr_2]^{1+}$	$[BiCl_2]^{1+}$	$[BiCl]^{2+}$
P/O−Bi	2.4059(5) 2.4070(5) [2.382]	2.6883(14) 2.6750(13) [2.690]	2.6754(9) 2.6634(10) [2.680]	2.6730(10) 2.6671(12) [2.709] [2.689]			
P/O−Bi−P/O	158.5(5) [174.1]	77.97(4) [79.9]	77.95(3) [80.5]	77.15(3) [79.3]			
Bi−X	2.6068(17) 2.6073(17) [2.579]	2.8332(6) 2.7871(6) [2.778]	2.6802(10) 2.6348(10), [2.626]	2.4990(22) [2.435]	[2.506]	[2.360]	[2.276]
X−Bi−X	93.73(6) [100.4]	168.09(2) [162.3]	168.77(3) [155.3]		[101.4]	[100.0]	
$Bi-O_{OTf}$	2.7862(5) 2.8299(7)	2.995(4) 2.838(4)	3.010(3) 2.844(2)	2.858(4) 2.645(3) 2.744(4)			

Attempts to isolate $[(THF)_4Bi_2Cl_4(OTf)_2]$ from $BiCl_3$ and MeOTf in THF were consistently foiled by the rapid thickening of the solvent, suggesting that $[BiCl_2]^{1+}$ is a more potent polymerization catalyst than $[BiBr_2]^{1+}$, presumably an inductive effect due to the greater electronegativity of chlorine relative to bromine. Therefore, $[(dmpe)_2Bi_2Cl_4(OTf)_2]$ (**4.3**) was prepared directly from equimolar mixtures of $BiCl_3$, TMSOTf and *dmpe* in toluene and precipitated as an insoluble yellow powder. When $BiCl_3$ was reacted with *dmpe* in the presence of excess TMSOTf, the complex $[(dmpe)_2Bi_2Cl_2(OTf)_4]$ (**4.4**) was obtained. Single crystals of each compound were obtained by recrystallization from MeCN at −30 °C as both compounds exhibit thermal instability in solution at room temperature, as judged by the deposition of elemental bismuth within hours. However, both compounds are thermally stable for weeks in the solid state under inert atmosphere.

The solid-state structures of **4.1**, **4.2**•MeCN, **4.3**•MeCN,* and **4.4**•MeCN (Figure 4.1.1) all involve dimeric arrangements by virtue of Bi−O_{OTf} contacts, which form O−S−O bridges between two bismuth centres. The distorted octahedral environment at bismuth is more regular in **4.1** than in the other structures where the axially-configured halide centres are slanted to additionally accommodate long Bi−X contacts (Figure 4.1.1). Selected structural parameters for each compound are summarized in Table 4.1.2, together with analogous parameters for phosphine free halobismuth cations in the gas phase.

The structure of **4.1** is at low-resolution due to disorder, but is consistent with elemental analysis data and sufficient to illustrate the connectivity as a *cis*-configured dibromobismuth center with two *trans*-configured THF ligands and two *cis*-configured contacts to oxygen atoms of separate triflate groups. In contrast, the solid-state structures of compounds **4.2** and **4.3** involve *trans*-configured halide substituents imposed by the chelating (*cis*-configured) *dmpe* ligand. Compound **4.4** features bismuth centres with a chelating *dmpe* ligand, one chlorine substituent and three *cis*-configured interactions with the oxygen atoms of separate triflate groups.

The range of Bi−O_{OTf} distances in compounds **4.1**-**4.4** [2.645(3)-3.010(3) Å] is significantly longer than the sum of the covalent radii for the two elements [$\Sigma_{r,cov}$ = 2.25 Å][127] but significantly shorter than the sum of the van der Waals radii

*The structure of this compound was obtained by Ahmed Rashid as part of an undergraduate research project.

[$\Sigma_{r,vdW}$ = 3.80 Å].[111] While the structure of $Bi(OTf)_3$ has not been reported, the observed Bi−O_{OTf} distances are generally similar to those reported in $Ph_2Bi(OTf)$ [(2.473(5) − 3.553(6) Å],[151] in $[(THF)_4BiCl(OTf)_2]$ [2.386(11) − 2.879(15) Å],[152] and in the aqua complex $[(H_2O)_4Bi(OTf)_3]$ [2.54(5) − 2.84(3) Å][153] and longer than the Bi−O distances in the covalent oxide α−Bi_2O_2 [2.08(3) − 2.80(2) Å and 3.25(4) Å][154] or alkoxide $Bi(OCPh_3)_3$ [2.070(4) − 2.081(4) Å].[155] Thus, while the Bi−O_{OTf} distances in compounds **4.1**, **4.2**, **4.3** and **4.4** are generally longer than a formal covalent Bi−O bond, the compounds are best formulated as triflate complexes of the type $[L_2BiXn(OTf)_{(3-n)}]_2$ rather than ionic salts of the type $[L_2BiXn]_2[OTf]_{2(3-n)}$.

To further assess the structural influences of the Bi−O_{OTf} contacts, ligation by *dmpe*, and dimer formation, *ab initio* calculations (MP2/def2-TZVPP) were performed to obtain the gas-phase structures of the triflate-free cations $[(THF)_2BiBr_2]^{1+}$, $[(dmpe)_2BiBr_2]^{1+}$, $[(dmpe)_2BiCl_2]^{1+}$, $[(dmpe)_2BiCl]^{2+}$, $[BiBr_2]^{1+}$, $[BiCl_2]^{1+}$, and $[BiCl]^{2+}$ (see Table 4.1.1, values in square brackets). The optimized geometry at the bismuth center in all ligand-bound cations is a distorted see-saw, consistent with a AX_4E VSEPR geometry with a stereochemically active lone pair. Further evidencing lone pair activity in the gas phase structures of the *dmpe* complexes, the halide substituents are bent back towards the phosphines (Br−Bi−Br = 162.3°; Cl−Bi−Cl = 155.3°), and in the the ethereal complex, the axial THF molecules are bent back (O−Bi−O = 174.1°) towards the bromide substituents. The corresponding experimental values for the X−Bi−X bond angle [168.09(2)°for **4.2**, 168.77(3)°for **4.3**] or the O-Bi-O bond angle [158.5(5)°for **4.1**] are significantly larger than those in the gas phase, implying a reduced lone pair stereochemical activity in the solid state. Gas-phase minima for the hypothetical tetrahedral geometries (AX_4 VSEPR arrangement) around four-coordinate bismuth centres could not be located even with the most finely-spaced integration grid for the DFT geometry scan. By comparison, a tetrahedral geometry was readily calculated and experimentally observed[42] in the solid state for the $[(Me_3P)_2SnCl_2]^{2+}$ dication, consistent with an AX_4 VSEPR geometry where no lone pair stereochemistry is possible.

The *trans*-$(THF)_2$ structure observed for the cation in the solid-state structure of **4.1**, is calculated to be a minimum in the gas phase, while there is no minimum evident for the hypothetical *cis*-$(THF)_2$ structure with *trans*-bromine substituents. The calculated P−Bi bond lengths and angles for **4.2**, **4.3**, and **4.4**, are very similar

to those observed in the solid state, while the calculated Bi−X (X = Cl or Br) bonds are significantly shorter than those experimentally. These findings suggest that strong interactions with the triflate groups suppress the lone pair stereochemical activity at bismuth, and attenuate the overall Lewis acidity of the metal centres in the solid state, leading to lengthened Bi−X bonds.

Experimental values for the *cis*-configured [Br−Bi−Br = 93.73(6)°] Bi−Br bonds in **4.1** are shorter than those in $[(12\text{-c-}6)BiBr_2][BiBr_4]$,[156] $[(THF)_3BiBr_3]$,[157] $BiBr_3$,[158] $[(THF)BiPh_2Br]$[159] and $[(THF)BiPhBr_2]_x$,[159] and are similar to those observed in $[Bi_2Br_6][AlBr_4]_2$, all of which feature *cis* Bi−Br bonds. The *trans* configuration of bromine atoms in **4.2** is accompanied by substantially longer Bi−Br bonds, likely due to a *trans* influence, which is also predicted by the MP2-optimized structure of $[(dmpe)BiBr_2]^{1+}$ in the gas-phase. Consistently, the *trans* configured Bi−Cl bonds [Cl−Bi−Cl = 168.77(3)°] in **4.3** are also significantly longer than in related species, including neutral $BiCl_3$ [2.500(18) Å],[16] which features a *cis* configuration of chlorine atoms at the bismuth center. As expected, the Bi−Cl bond in **4.4** [2.4990(22) Å] is markedly shorter than in **4.3** and is only marginally longer than those observed in the related $[(15\text{-c-}5)BiCl][SbCl_6]_2$ [2.479(6) Å][160] and $[BiCl][W_6Cl_{14}]$ [2.489(3) Å].[161] By comparison, the shortest Bi−Cl bond reported in the Cambridge Structural Database (CSD) to date is 2.394 Å in the neutral arene complex $(p\text{−xylene})_2Bi_2Cl_6$, and the MP2-optimized value for the hypothetical gas-phase diatomic $[BiCl]^{2+}$ is 2.276 Å.

The observed and calculated P−Bi bond lengths in **4.2**, **4.3** and **4.4** are essentially equivalent despite the greater electronegativity of the chlorine substituents and the greater charge concentration at the Bi centre in **4.4**, suggesting that these structural features are insensitive to the Lewis acidity of the Bi center. Moreover, the P−Bi bond lengths in **4.2** and **4.3** are similar to those in neutral and anionic compounds containing P−Bi bonds. Therefore, the substantially shorter Bi−Cl and $Bi-O_{OTf}$ distances in **4.4**, compared to those in **4.3**, preferentially compensate for the enhanced Lewis acidity at the metal center. The differing sensitivity of E−X and E−P bonds to the charge at the metal center is consistent with observations for cationic $P-SbX_n$ and $P-SnX_n$ complexes and may be a general feature of phosphine complexes of main group halides.[42] The Lewis basicity and configuration of the phosphine ligands is nevertheless important. Thus, the more basic *dmpe* ligand results in substantially shorter P−Bi distances than those found in $[(Ph_3P)_2BiPh_2][PF_6]$ [2.968(3) Å and

2.937(3) Å], which bears *trans*-configured phosphine ligands.[33]

The Bi−O_{THF} lengths in **4.1** are approximately 0.23 Å shorter than those in the neutral adducts $(THF)_3BiBr_3$,[157] $(THF)BiPh_2Br$,[157] or polymeric $[(THF)BiPhBr_2]_x$[159] reflecting a stronger Bi-O_{THF} interaction in the triflate complex despite the *trans* configuration of the ether ligands. Taken together with the short Bi−Br bonds in **4.1** (*vide supra*), these features demonstrate that the bismuth center in this complex is highly Lewis acidic even in the presence of the triflate contacts.

The structure of **4.3** is consistent with that of the antimony derivative $[(dmpe)SbCl_2][OTf]$ with *trans* configured chlorine substituents imposed by the stereochemical active lone-pair. The average E−Cl and E−P bond lengths when E = Bi [2.6678(20) Å and 2.6694(19) Å, respectively] are predictably longer than observed when E = Sb [2.5625(8) Å and 2.5657(8) Å, due to the larger covalent radius of bismuth (1.48 Å, *cf.* antimony 1.39 Å).[127] Consistently, the average of two contacts to the triflate anions are *ca.* 0.05 Å shorter for **4.3** [2.927(5) Å], due to the lesser steric restriction at the larger bismuth atom, and the lower stereochemical activity of the bismuth 6*s* lone pair compared to the 5*s* lone pair in the antimony derivative. Therefore, the dimeric structure adopted by **4.3** is not observed for antimony, which adopts a complex network structure where the two interacting triflate anions bridge different metal centers in the extended solid state structure.[58]

Recently, it has been shown that due to the combination of low-lying vacant acceptor orbitals and a lone-pair at the central phosphorus atom, ligands of the type $[LPR_2]^{1+}$ and $[L_3P]^{3+}$ (L = Fischer carbene) can coordinate with electron-rich late transition metals, classifying these main group cations as a novel family of π-accepting ligands with demonstrated applications in catalysis.[162,163] Transition metal complexes bearing cationic ligands of the type $[(R_3P)_2P]^{1+}$ have also emerged recently as a fundamentally new class of transition metal coordination compounds.[164] However, despite the well-established use of neutral stibine and bismuthine ligands in transition metal chemistry,[165–167] investigations of their Z-type ligand abilities are limited. Few instances of well-established bismuth-metal coordinate bonds have been reported, both employing P−Bi−P type pincer ligands to bind Au^I in a tridentate fashion, such that the P−Au interaction enforces the Au−Bi interaction.[168,169] Analysis of the bonding situation showed that in both cases the Au−Bi bonding was driven by transfer of electron density from the Au atom to the Bi−Cl σ^* antibonding orbital. Fernandez

et al. have also reported a long Bi−Au [3.7284(5) Å] interaction between the cation $[Bi(C_6H_4CH_2NMe_2{-}2)_2]^{1+}$ and the $[Au(C_6F_5)_2]^{1-}$ anion, without the need for a pincer framework or other structure-directing features to enforce the Bi−Au contact.[170]

Following an analysis of the electronic structure of **4.4** at the MP2 level, it was envisioned that analogous to the cases above, the low-lying vacant *p*-orbitals centered at the bismuth atom in **4.4** may also serve as π-acceptor orbitals with electron-rich, late transition metal donors. The Bi−metal interaction may also be enhanced by the localization of the HOMO on the Bi atom, prompting an assessment of its σ-donor/π-acceptor ligand capabilities.

Addition of a MeCN solution of **4.4** to one equivalent of K_2PdCl_4 results in the formation of a clear orange solution, which shows a single peak at +38.9 ppm in the ^{31}P-NMR spectrum of the reaction mixture, consistent with formation of the known $[(dmpe)_2Pd]^{2+}$ cation.[171] Concentration of the solution under vacuum yields a large quantity of light grey powder and crystalline blocks. The identity of the crystalline material was confirmed by X-ray crystallography to contain the square planar $[(dmpe)_2Pd]^{2+}$ cation and $[(CH_3CN)_2Bi_2Cl_6(OTf)_2]^{2-}$ dianion (Figure 4.1.2). The grey powder showed no signals in its ^{1}H-NMR or ^{31}P-NMR spectrum, consistent with its formulation as a mixture of KOTf and unreacted K_2PdCl_4, implying that the overall reaction is:

$$[(dmpe)BiCl(OTf)_2] + K_2PdCl_4 \xrightarrow{2MeCN} [(dmpe)_2Pd][(MeCN)_2Bi_2Cl_6(OTf)_2] + 2\,KOTf \tag{4.1}$$

The $[Bi_2Cl_8]^{2-}$ dianion is a well-known formulation that is observed as dimers,[172] a polymer[173] and as ligand supported dimers.[174] The last of these is the most accurate classification for $[(CH_3CN)_2Bi_2Cl_6(OTf)_2]^{2-}$, which crystallizes as a centrosymmetric edge-sharing bioctahedron *via* two O−S−O linkages between adjacent bismuth centers. The preference for phosphine/halide exchange (metathesis) over Bi−Pd Z-type coordination evidences a substantially higher Lewis acidity at the bismuth center in **4.4** (*p*-orbitals as acceptor MOs) than in the formally more highly-charged phosphorus-centered cations (*p*-orbital derived acceptor MOs) or in the neutral halobismuthines (Bi−X σ^* acceptor MOs). Moreover, whereas the $3s$ lone pair in cationic phosphines readily engages the transition metal leading to synergistic σ-donation and π-back donation, the contracted $6s$ lone-pair at the bismuth center in **4.4** is a much weaker

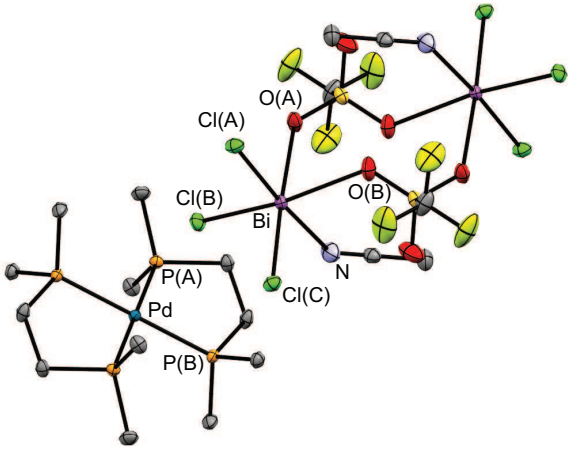

Figure 4.1.2. Molecular structure of compounds **4.5** in the solid state. Hydrogen atoms have been omitted for clarity. Select bond lengths (Å) and angles (°) are as follows: P(A)−Pd = 2.3154(5), P(B)−Pd = 2.3138(5) , Bi−Cl(A) = 2.5171(6), Bi−Cl(B) = 2.5074(6), Bi−Cl(C) = 2.5192(6), Bi−O(A) = 2.6617(18), Bi−O(B) = 2.6724(18), Bi−N = 2.757(2), Cl(A)−Bi−Cl(B/C) = 91.940(19), Cl(B)−Bi−Cl(C) = 94.400(19), Cl(B)−Bi−O(B) = 172.114(5), Cl(A)−Bi−N = 171.49(6), O(A)−Bi−O(B) = 84.30(6).

Lewis base and likely does not benefit from such an interaction. It is therefore unlikely that such bismuth complexes can be used as ligands in the absence of additional structure-enforcing factors such as pincer chelation.

4.2 Summary

In summary, the synthesis and characterization of compounds featuring bismuth acceptors stabilized by THF or *dmpe* ligands are described. In the solid state, the triflate compounds **4.1**-**4.4** crystallize as dimers involving significant Bi-O_{OTf} interactions. The Bi−X bond lengths exhibit a greater sensitivity to the formal Lewis acidity of the bismuth center than do the Bi−P bond lengths. The strong *trans* influence of the halide ligands is also documented. A comparison of homologous Sb/Bi structures **4.3** and [(*dmpe*)$SbCl_2$][OTf] nicely illustrates the structural consequences of relative lone-pair stereochemical activity. In solution, the triflate complexes behave as classic coordination complexes as illustrated by the ligand substitution reaction that yields **4.2** from a solution of **4.1** and *dmpe*. An assessment of the electronic structure of **4.4** suggested that it may behave as a Z-type ligand due to the presence of both a lone-pair and vacant *p*-orbitals at the bismuth center. However, experimental attempts to realize such reactivity were unsuccessful and led instead to the discovery of a metathesis reaction highlighting an important distinction between the chemistry of phosphorus and bismuth cations, with the latter showing a substantially greater Lewis acidity even with lower formal charges and more strongly interacting counterions. These insights provide direction for further developing and diversifying the coordination chemistry of bismuth.

Chapter 5

Cyclo-tetra(stibinophosphonium) Tetracations

The preceding chapters on the coordination chemistry of antimony and bismuth have featured single metal centres embedded within varying ligand environments, yielding monometallic coordination complexes. This chapter is devoted to polymetallic frameworks as found within catenated antimony ring systems.

Inorganic homoatomic rings are a fundamentally interesting class of molecules and represent a significant portion of main group catenation chemistry. Besides boron, carbon, silicon, sulfur and phosphorus, few elements in the periodic table exhibit well-defined catenation,[175] and this is particularly true of *d*-block metals and *p*-block metalloids, where clusters are more prevalent than rings as a structural motif in catenated systems. Moreover, while the structures of homopolynuclear rings and clusters are predictable using semiempirical concepts such as Wade's Rules, the mechanisms of their formation and their reactivity patterns are generally poorly-understood compared to those of their mononuclear counterparts. It is essential to bridge this knowledge gap in order to prepare catenated *p*-block metalloid systems in a controlled fashion so that potential applications for emergent behaviours such as σ-bond conjugation and cooperative catalysis in these species may be assessed.

Neutral or anionic homocycles are now known for most *p*-block metalloids but structurally-authenticated cationic cycles remain rare, as highlighted in reviews on the topic.[176,177] Examples are limited to unsupported selenium and tellurium dications[177] and heavily-substituted silicon[178,179] or germanium[180] monocations. By comparison,

while catenation in the group 15 metals antimony and bismuth is well-established in neutral rings and cationic clusters,[181] cationic rings featuring homoatomic Sb−Sb or Bi−Bi bonding have not been reported. For antimony, in particular, a number of linear monocations ($[\mathbf{5.1}]^{1+}$ and $[\mathbf{5.2}]^{1+}$)[182–184] and dications ($[\mathbf{5.3}]^{2+}$, $[\mathbf{5.4}]^{2+}$, $[\mathbf{5.5}]^{2+}$ and $[\mathbf{5.6}]^{2+}$)[184–187] have been isolated recently. However, the yields of these compounds, where reported, are consistently low as they are either formed unexpectedly or crystallized from small scale reactions, precluding further study of their properties. Nevertheless, the existence of these linear cations as stable species prompts the search for cyclic analogues.

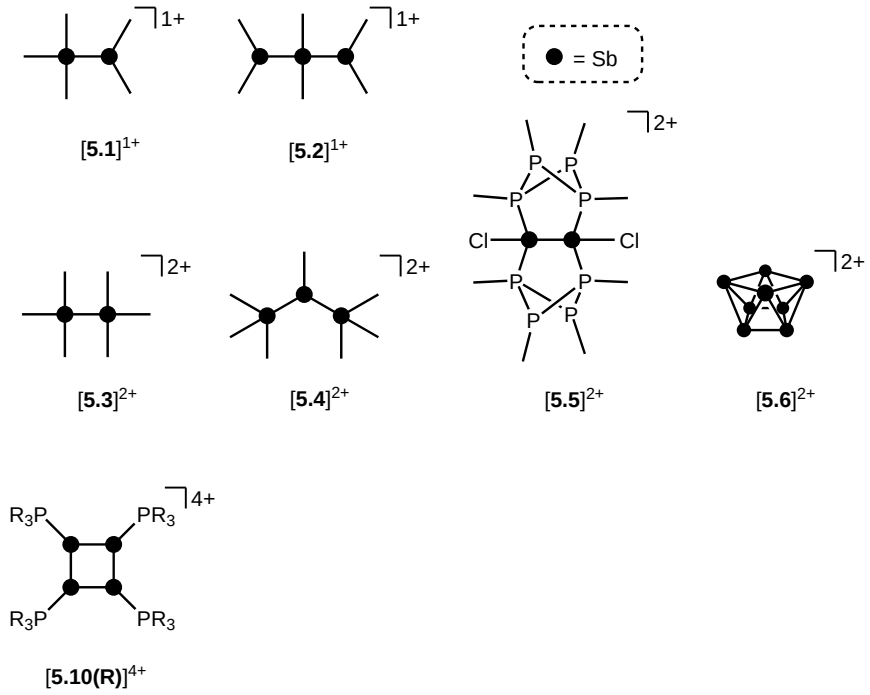

Scheme 5.0.1. Structurally confirmed cations featuring Sb−Sb bonds.

The first derivative, $[(Me_3P)_4Sb_4][OTf]_4$,[**5.10(Me)**][OTf]$_4$, of the title compound class was discovered by Dr. Y. Carpenter in 2007 as one crystalline product amongst several formed in the 1:2:2 reaction between $PhSbCl_2$, TMSOTf, and PMe_3.[188] Due to the presence of inseparable impurities, it was not possible at the time to obtain definitive spectroscopic data for the compound and its crystal structure remained as the only datum of information about this interesting species for several years.

It was not until mid-2012 that, in an attempt to demonstrate ligand substitution, the reaction of $[(bipy)_2Sb][OTf]_3$ with excess PMe_3 was attempted, and from

the reaction mixture a significant amount of yellow crystalline material, identified as [**5.10(Me)**][OTf]$_4$, was isolated. Co-crystallized with this material was copious amounts of [Me_3PPMe_3][OTf]$_2$. No other phosphorus containing products were detected and the substantial amount of material isolated implied that formation of [**5.10(Me)**][OTf]$_4$ was, for the first time, occurring as a major reaction outcome, rather than as a trace byproduct. Furthermore the formation of the two products was reproducible and independent of the presence of *bipy* in the reaction mixture, the compounds being formed even when uncomplexed Sb(OTf)$_3$ was employed as the antimony source.

Formation of a *catena*-Sb compound suggests that PMe_3 can act as both a ligand and a reducing agent in these reactions. Indeed, although phosphines are prototypical two-electron ligands in the coordination chemistry of *d*-block metals, they also exhibit redox reactivity within the coordination sphere of an acceptor. For example, reductive elimination of tetraorgano- or halotriorganophosphonium cations (Scheme 5.0.2*a*),[189–192] and oxidative addition of PR−X bonds (Scheme 5.0.2*b*),[193–195] or P−R bonds (Scheme 5.0.2*c*)[196,197] are all known pathways of tertiary phosphine activation in transition metal chemistry. One report hints at the reductive elimination of a diphosphonium dication from a phosphine-metal complex (Scheme 5.0.2*d*).[198] In this instance, spectroscopic studies indicated that the reaction of excess PMe_3 with [Cu(MeCN)$_x$][PF_6]$_2$ or [Tl(MeCN)$_x$][UF_6]$_3$ yields [Me_3PPMe_3]$^{2+}$, and the reduced metal complexes [Cu(PMe_3)$_4$][PF_6] and [Tl(PMe_3)$_2$][UF_6], respectively. However, neither the high oxidation state reactants nor the reduced products were structurally verified and three different ^{31}P NMR chemical shifts were ascribed to [Me_3PPMe_3]$^{2+}$ (depending upon the counterion: +65.0 ppm, +46.3 ppm, or +27.8 ppm). The collective weight of these ambiguities is perhaps the reason why a fundamental and potentially widespread phosphine activation pathway in coordination chemistry has remained unrecognized.

As reductive elimination is observed in high oxidation state complexes of both a transition metal (Cu^{II}) and a main group (Tl^{III}) acceptor, phosphine activation may be broadly applicable to complexes exhibiting a mismatch between hard acceptors (high oxidation state/charge) and soft phosphine donors (low oxidation state/charge). Indeed phosphines are considered poor donors for hard acceptors and coordination to such centres generally requires enforcement by chelate or pincer ligands.[199,200]

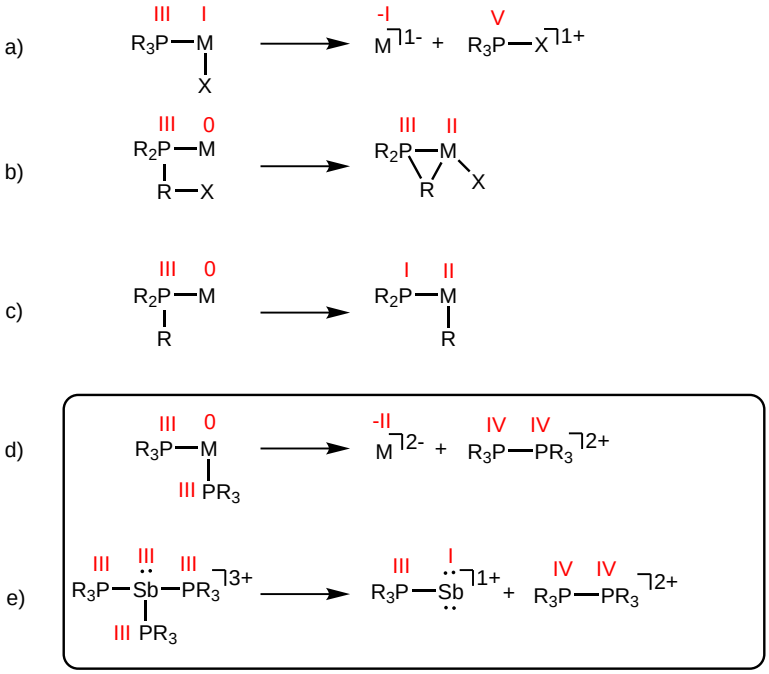

Scheme 5.0.2. Activation of phosphine ligands in the coordination sphere of Lewis acceptors. Roman numerals indicate formal oxidation states.

5.1 Reaction of $FSb(OTf)_2$ and $Sb(OTf)_3$ with PR_3

Combinations of $FSb(OTf)_2$ or $Sb(OTf)_3$ with PR_3 (R = Me, Et, Pr, or Bu) in MeCN solvent at the optimized stoichiometries given in Scheme 5.1.1 have been investigated. The ^{31}P, ^{13}C, ^{19}F and ^{1}H NMR spectra of reaction mixtures indicate quantitative formation of *cyclo*-tetra(stibinophosphonium) triflate salts, [**5.10(R)**][$OTf]_4$ (R = Me, Et, Pr, Bu), together with diphosphoniums, [**5.11(R)**][$OTf]_2$ (Scheme 5.1.1*a*), or fluorophosphoniums, [**5.12(R)**][OTf] (Scheme 5.1.1*b*). Large lattice enthalpy differences permit separation of the monocationic salts [**5.12(R)**][OTf] from the tetracationic salts [**5.10(R)**][$OTf]_4$ by fractional crystallization, whereas pure salts cannot be isolated from mixtures of dicationic [**5.11(R)**][$OTf]_2$ and [**5.10(R)**][$OTf]_4$.

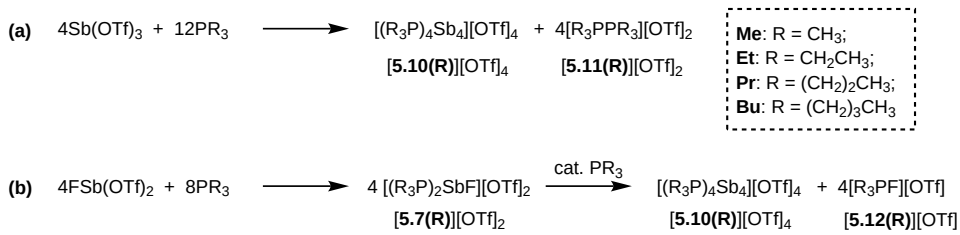

Scheme 5.1.1. Formation of cations $[\mathbf{5.10(R)}]^{4+}$, $[\mathbf{5.11(R)}]^{2+}$, and $[\mathbf{5.12(R)}]^{1+}$ as triflate salts in reaction mixtures containing trialkylphosphines and *a*) $Sb(OTf)_3$ and *b*) $FSb(OTf)_2$.

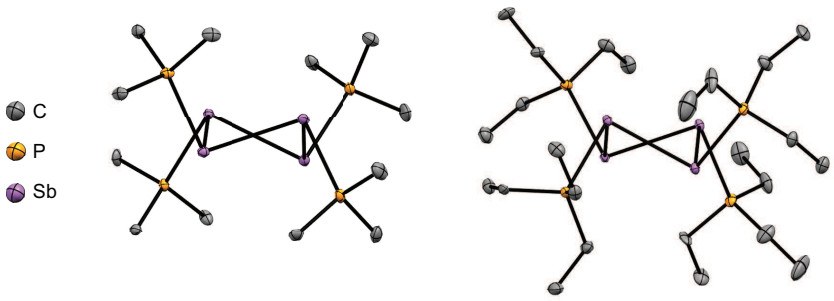

Figure 5.1.1. Molecular structure of the cations in [**5.10(Me)**][$OTf]_4$ (left) and [**5.10(Et)**][$OTf]_4$ (right) in the solid state. Hydrogen atoms, anions and solvent molecules have been omitted for clarity. Metric parameters are given in Table 5.1.1.

Four derivatives of [**5.10(R)**][$OTf]_4$ (R = Me, Et, Pr, Bu) have been characterized spectroscopically by solution NMR spectroscopy, and two salts, [**5.10(Me)**][$OTf]_4$ and [**5.10(Et)**][$OTf]_4$, comprehensively characterized. The solid-state structures of these

Table 5.1.1. Selected bond lengths (Å) and angles (°) in the solid-state structures of [**5.10(Me)**][OTf]$_4$•(MeCN)$_3$ and [**5.10(Et)**][OTf]$_4$•MeCN. Calculated (MP2/6-311g//def2-TZVPP) values for anion-free [**5.10(Me)**]$^{4+}$ are given in square brackets.

	[**5.10(Me)**]	[**5.10(Et)**]
Parameter	[OTf]$_4$•(MeCN)$_3$	[OTf]$_4$•MeCN
Sb−Sb	2.8354(6)-2.8797(5) [2.853]	2.838(2)-2.884(2)
Sb_n−Sb_{n+2}	3.7471(5)-3.7792(5) [3.662]	3.646(2)-3.804(2)
P−Sb	2.552(2)-2.564(2) [2.555]	2.553(3)-2.578(2)
Sb−O	3.210(4)	2.871(8)
Sb−Sb−Sb	82.09(2)-83.36(2) [79.84]	78.62(3)-82.88(4)
P−Sb−Sb	93.74(4)-99.60(4) [97.59]	91.91(7)-98.69(7)
Sb−Sb−Sb−Sb	38.85(2)-39.27(2) [45.55]	43.30(2)-44.56(3)

salts have been determined by X-ray crystallography to confirm formulae involving a tetracation with a folded Sb_4-cyclic core with four exocyclic PR_3 units and four triflate anions (Figure 5.1.1, Table 5.1.1). The Sb−Sb bond lengths are very similar for $[\mathbf{5.10(Me)}]^{4+}$ [2.8354(6)−2.8797(5) Å] and $[\mathbf{5.10(Et)}]^{4+}$ [2.838(2)−2.884(2) Å] and their values are marginally longer than those observed in rare examples of *catena*-antimony cations [*cf.* $[\mathbf{5.1}]^{1+}$ = 2.8205(12) Å,[182] 2.8278(3) Å,[184] $[\mathbf{5.2}]^{1+}$ = 2.8203(4) Å,[183] $[\mathbf{5.3}]^{2+}$ = 2.7624(11) Å and 2.7867(12) Å,[185] $[\mathbf{5.4}]^{2+}$ = 2.811(1) Å and 2.830(1) Å,[184] and $[\mathbf{5.5}]^{2+}$ = 2.8484(12) Å and 2.8353(12) Å[186]]. Consistent with the high Lewis acidity of the Sb_4 core, the P−Sb distances [2.552(2)−2.578(2) Å] are similar to those observed in other triflate salts such as $[(Me_3P)_2SbCl][OTf]_2$ [2.5950(4) Å and 2.5834(4) Å] and $[(Me_3P)SbPh_2][OTf]$ [2.5584(4) Å].

A number of Sb−O contacts are also observed, the shortest of which measures 3.210(4) Å for $[\mathbf{5.10(Me)}]^{4+}$ and 2.871(8) Å for $[\mathbf{5.10(Et)}]^{4+}$. Given the high molecular charge, these values are expectedly smaller than the sum of the van der Waals radii ($\Sigma_{r,vdW}$ = 3.61 Å)[111] but nevertheless significantly longer than the sum of the single bond covalent radii ($\Sigma_{r,cov}$ = 2.05 Å)[127] for the two elements.

For $[\mathbf{5.10(Me)}]^{4+}$, a gas-phase optimization of the cation at the MP2 level in the absence of the triflate anions produced a geometry that is essentially identically to that observed experimentally (see Table 5.1.1), suggesting that the anion contacts do not distort the structural features to a measurable extent. The cation can be viewed as having a $[Sb]_4^{4+}$ core with four phosphine ligands (coordinate model) or as a cyclotetrastibine with exocyclic phosphonium cations (Lewis model). Within the latter context, the electronic structure and MO framework of $[\mathbf{5.10(Me)}]^{4+}$ should closely resemble that of the the isoelectronic neutral compound $(Me_3C)_4Sb_4$.

Figure 5.1.2 compares the relative shapes and energies of the eight highest occupied MOs for the two species. While the phosphorus derivative has significantly lower orbital energies, as expected from its high cationic charge, the topological similarity between the bonding MOs for two compounds nicely illustrates their isolobality and implies the presence of Sb−Sb and P−Sb single bonds. Consistently, the Wiberg Bond Index (WBI) for the two interactions are 0.98 and 0.89, respectively. By comparison, the WBI for the transannular Sb_n−Sb_{n+2} interaction is only 0.02, showing negligible bonding and implying that the sub-van der Waals transannular interaction is a result rather than the cause of the observed folded-square geometry.

The calculated net natural population analysis (NPA) charges for the Sb_4 fragment is 0.81e, and the remainder of the cationic charge is borne by the exocyclic PMe_3 fragments, classifying them as phosphoniums within the Lewis model. Consistently, the P−C bond lengths in [**5.10(Me)**]$^{4+}$ [calcd.: 1.801 Å, expt.: 1.770(7)-1.802(7) Å] are typical for trimethylphosphonium fragments [*e.g.* 1.783(3) Å, as found in [Me_3PPMe_3]$^{2+}$], and are significantly shorter than those in PMe_3 [1.8464(3) Å].[16]

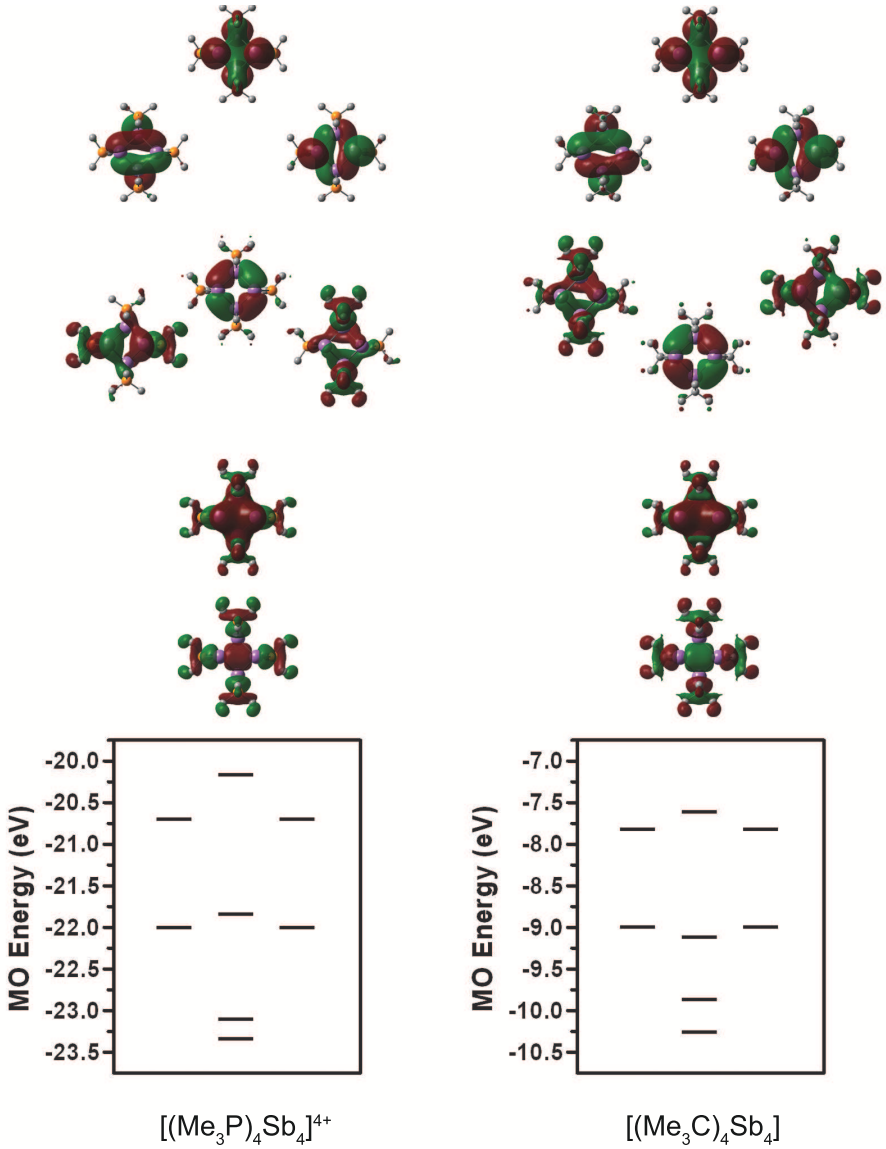

Figure 5.1.2. Surface plots and energies of the eight highest-energy occupied MOs in the gas-phase structure of [**5.10(Me)**]$^{4+}$ (left) and [$(Me_3C)_4Sb$] (right) at the MP2/6-311g/def2-TZVPP level of theory.

The reactions in Scheme 5.1.1 represent a two electron reduction of each anti-

mony(III) centre and collectively, an eight electron reductive coupling of four antimony centres to form derivatives of $[\mathbf{5.10(R)}]^{4+}$. In Scheme 5.1.1*a*, eight of the twelve equivalents of phosphine are involved in the redox process, being oxidatively coupled to give four diphosphonium cations, $[\mathbf{5.11(R)}]^{2+}$,[7,100,101] and the remaining four equivalents represent ligands on the reduced antimony(I) centres of $[\mathbf{5.10(R)}]^{4+}$. Scheme 5.1.1*b* describes a similar redox process that involves formation of $[\mathbf{5.11(R)}]^{2+}$ as transients, which are converted to the corresponding fluorophosphonium cations, $[\mathbf{5.12(R)}]^{1+}$, in the presence of the fluoride ion. The key feature in both processes is reductive elimination of a diphosphonium unit from a hard, tricationic Sb^{III} centre to give a soft, monocationic Sb^{I} centre, representing a novel mode of phosphine ligand activation in the coordination sphere of metals (Scheme 5.0.2*e*).

^{31}P NMR spectra (Figure 5.1.3) of reaction mixtures containing PR_3 and $FSb(OTf)_2$ in a 2:1 stoichiometry show a broad doublet in the +20 to +40 ppm range and the signal due to the free phosphine (−60 to −20 ppm) is not observed. The ^{19}F NMR spectra of these mixtures show a broad triplet in the −170 to −175 ppm range and no evidence of $FSb(OTf)_2$. The broadness of peaks in the ^{31}P and ^{19}F NMR spectra is consistent with the connectivity of these nuclides to a quadrupolar antimony centre [I = ⅝ for ^{121}Sb (57 %), ⅞ for ^{123}Sb (43 %)],[201] and they are assigned to the dicationic *bis*-phosphine cations $[\mathbf{5.7(R)}]^{2+}$, which are stable in MeCN solutions at room temperature (Scheme 5.1.2*a*). Upon addition of *ca.* 5 mol % of phosphine to these solutions, the ^{31}P NMR signals due to cations $[\mathbf{5.7(R)}]^{2+}$ are replaced over 16 hours by doublets corresponding to $[\mathbf{5.12(R)}]^{1+}$ (δ^{31}P: $+140$ to $+150$ ppm, $^{1}J_{PF}$ = 950-1000 Hz) and a singlet in the −25 to 0 ppm range, corresponding to $[\mathbf{5.10(R)}]^{4+}$. Addition of *ca.* 15 mol % of phosphine increases the rate of the reaction and effects complete conversion of $[\mathbf{5.7(R)}]^{2+}$ to $[\mathbf{5.12(R)}]^{1+}$ and $[\mathbf{5.10(R)}]^{4+}$ within an hour.

The results suggest that displacement of fluoride from $[\mathbf{5.7(R)}]^{2+}$ by added phosphine yields the highly-charged trications $[\mathbf{5.8(R)}]^{3+}$ (Scheme 5.1.2*b*), which undergo reductive elimination of $[\mathbf{5.11(R)}]^{2+}$ and $[\mathbf{5.9(R)}]^{1+}$ (Scheme 5.1.2*c*). Subsequent tetramerization of the six-valence electron cations $[\mathbf{5.9(R)}]^{1+}$ to $[\mathbf{5.10(R)}]^{4+}$ (Scheme 5.1.2*d*), and displacement of PR_3 from $[\mathbf{5.11(R)}]^{2+}$ by fluoride gives the $[\mathbf{5.12(R)}]^{1+}$ regenerating the phosphine catalyst (Scheme 5.1.2*e*). Cyclization of transients $[\mathbf{5.9(R)}]^{1+}$ is analogous to the formation of tetrameric $(Mes{-}E)_4$ (Mes = 2,4,6-trimethylphenyl, E = As or Sb) *via* catalytic extrusion of $Mes{-}As^{I}$ from a

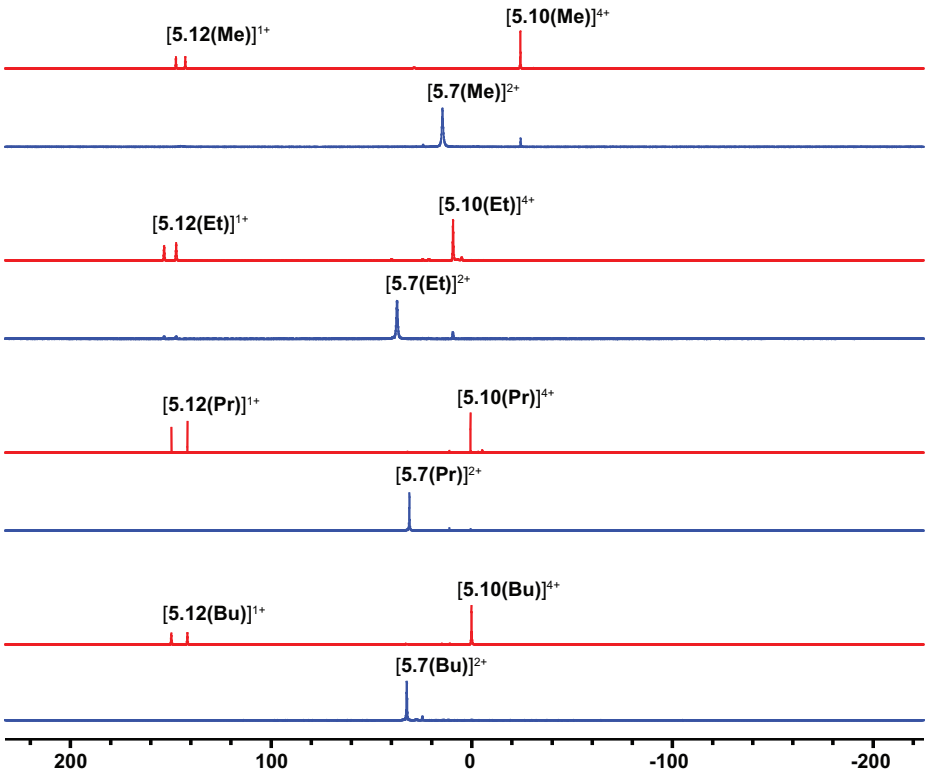

Figure 5.1.3. $^{31}P\{^{1}H\}$ NMR spectra (202.5 MHz, 298 K, CD_3CN) of reaction mixtures containing $FSb(OTf)_2$ and PR_3 leading to the formation of $[\mathbf{5.7(R)}]^{2+}$ (blue) and, upon addition of 15 mol % PR_3, to $[\mathbf{5.12(R)}]^{1+}$, and $[\mathbf{5.10(R)}]^{4+}$ (red). See Table 5.2.1 for chemical shift and coupling constants data.

zirconium complex[202] or Mes−Sb^{I} from a hafnium complex.[203] Nucleophilic displacement of PMe_3 has been reported in reaction mixtures of [**5.11(Me)**][ClO_4]$_2$ and [NEt_4][F],[101] and a control experiment further confirmed that the equimolar reaction of [**5.11(Me)**][OTf]$_2$ with CsF yields a 1:1 mixture of PMe_3 and [**5.12(Me)**]$^{1+}$. Trications [**5.8(R)**]$^{3+}$ are also implicated in the formation of [**5.10(R)**]$^{4+}$ from Sb(OTf)$_3$ (Scheme 5.1.2*f*) and the ternary salt [**5.8(Me)**][**5.11(Me)**][OTf]$_5$ was crystallized from a 1:3 mixture of Sb(OTf)$_3$ and PMe_3 at −30 °C (*vide infra*). Consistent with the role of [**5.8(Me)**]$^{3+}$ as a metastable intermediate, the same reaction stoichiometry yields only [**5.10(Me)**][OTf]$_4$ and [**5.11(Me)**][OTf]$_2$ at ambient temperature.

The ^{31}P NMR spectra of reaction mixtures containing [$(Me_3P)_2SbCl$]$^{2+}$ and 20 mol % PMe_3 show only partial conversion to [**5.10(Me)**][OTf]$_4$ and [**5.11(Me)**][OTf]$_2$ after 48 hours. Additionally, a broad signal at +10.4 ppm is also observed, which is close to the average for the values in [$(Me_3P)_2SbCl$]$^{2+}$ (+15.8 ppm) and [$(Me_3P)_2SbCl_2$]$^{1+}$ (+6.2 ppm), suggesting that the free chloride ion is sequestered in an equilibrium between the starting material and [$(Me_3P)_2SbCl_2$]$^{1+}$. Consequently, nucleophilic attack by chloride to liberate free phosphine from [**5.11(Me)**]$^{2+}$ is precluded in these reaction mixtures and neither [Me_3PCl]$^{1+}$ nor free phosphine are detected by ^{31}P NMR spectroscopy.

Signifying the role of free phosphine as a catalyst, formation of [**5.10(Me)**]$^{4+}$ does not occur catalytically in the chloride system because the reaction is arrested upon formation of [**5.11(Me)**]$^{2+}$, which is the sole detected oxidation product. Generation of free phosphine from diphosphonium, the turnover limiting step, does not take place (Scheme 5.1.2, right). In contrast, no diphosphonium is detected in reactions involving the fluoroantimony complexes [**5.7(R)**]$^{2+}$ (Scheme 5.1.2, left), where, due to nucleophilic attack by fluoride anions on [**5.11(R)**]$^{2+}$, only the fluorophosphoniums [**5.12(R)**]$^{1+}$ are detected as the oxidation product and the formation of [**5.10(R)**]$^{4+}$ occurs catalytically in the presence of free PR_3. Differences in the reactivity of homologous Sb−X (X = Cl, F) complexes towards Lewis acids have also been noted in Chapter 3.

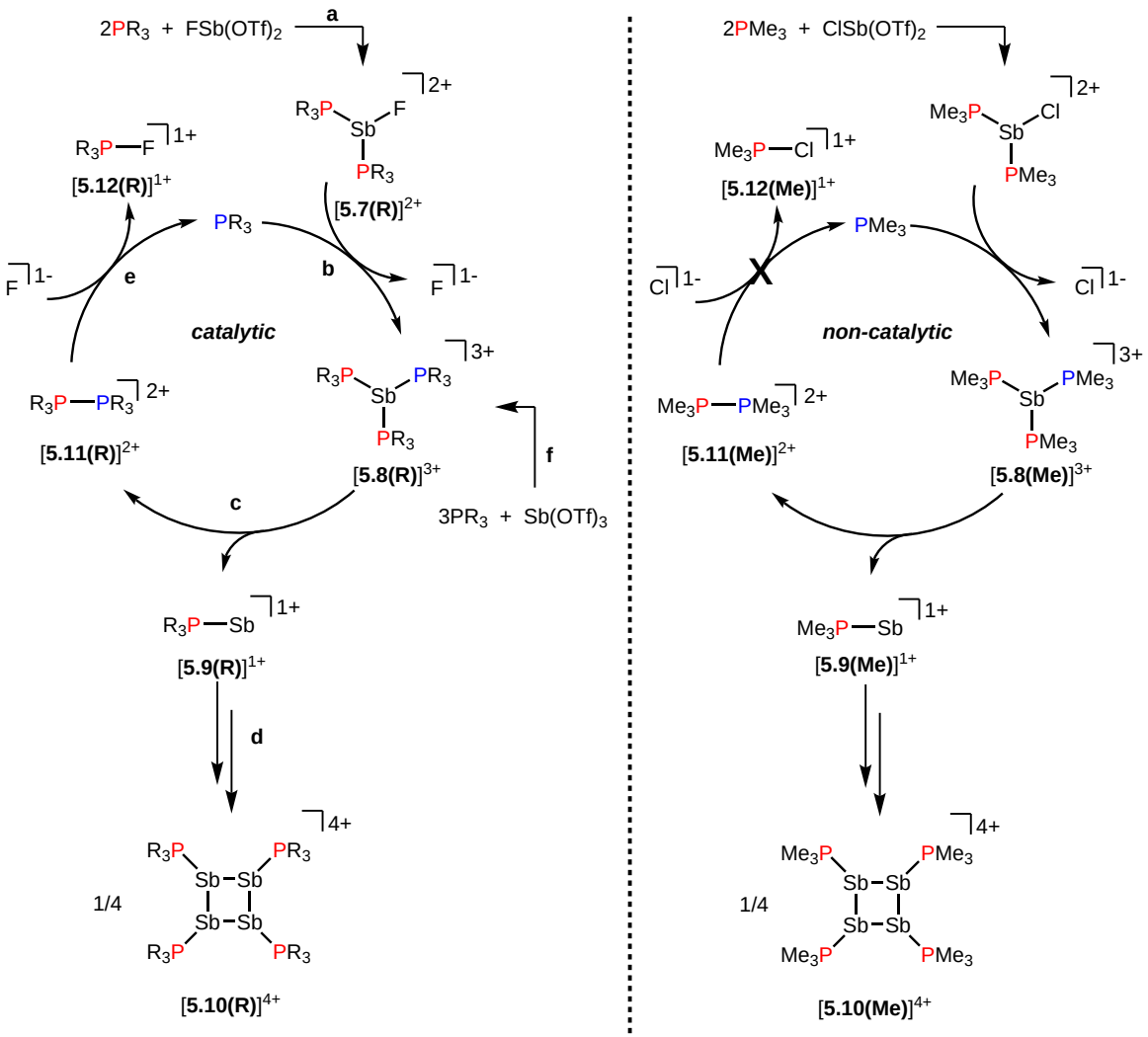

Scheme 5.1.2. Left: Proposed catalytic mechanism for the formation of cations $[\mathbf{5.7(R)}]^{2+}$, $[\mathbf{5.8(R)}]^{3+}$, $[\mathbf{5.9(R)}]^{1+}$, $[\mathbf{5.10(R)}]^{4+}$, $[\mathbf{5.11(R)}]^{2+}$, and $[\mathbf{5.12(R)}]^{1+}$. See text for descriptions of a-f. Right: Non-catalytic formation of $[\mathbf{5.10(Me)}]^{4+}$ from the reaction of $[(Me_3P)_2SbCl]^{2+}$ with PMe_3.

5.2 Isolation of Intermediates and Byproducts

Solution NMR data for derivatives of $[\mathbf{5.7(R)}]^{2+}$, $[\mathbf{5.8(R)}]^{3+}$, $[\mathbf{5.10(R)}]^{4+}$, $[\mathbf{5.11(R)}]^{2+}$, and $[\mathbf{5.12(R)}]^{1+}$ are summarized in Table 5.2.1, with evidence for the assignments discussed below. It has not been possible to detect or isolate derivatives of $[\mathbf{5.9(R)}]^{1+}$. Attempts to trap these cations and other radical intermediates in the presence of a twenty-fold excess of 2,3-dimethyl-1,3-butadiene were unsuccessful, and upon removal of the diene under vacuum no new products were identified.

Derivatives of $[\mathbf{5.7(R)}]^{2+}$ represent the first examples of soft donor complexes of fluoroantimony acceptors although numerous fluoroantimony complexes with hard, oxidatively-resistant donors such as pyridines,[132] ethers,[135,204–207] and pnictogen oxides,[208] have been reported. The $^{2}J_{\mathrm{PF}}$ couplings for $[\mathbf{5.7(Me)}]^{2+}$ and $[\mathbf{5.7(Pr)}]^{2+}$ are resolved as a doublet in the ^{31}P NMR spectra and as a triplet in the ^{19}F NMR spectra, consistent with an AX_2 spin system. Fine structure could not be resolved for $[\mathbf{5.7(Et)}]^{2+}$ and $[\mathbf{5.7(Bu)}]^{2+}$ even under the dilute conditions and low temperatures (-30°C) employed to mitigate exchange related broadening.

Although $[\mathbf{5.7(Me)}][\mathrm{OTf}]_2$ and $[\mathbf{5.7(Et)}][\mathrm{OTf}]_2$ have both been isolated as analytically pure substances and spectroscopically characterized, it was not possible to obtain X-ray quality crystals. Moreover, there are no known examples of $^{2}J_{\mathrm{PF}}$ coupling constants through an antimony centre for direct comparison with the assigned NMR data. For this reason, the close analogue $[(\textit{dmpe})\mathrm{SbF}][\mathrm{OTf}]_2$, $[\mathbf{5.13}][\mathrm{OTf}]_2$, was prepared from an equimolar mixture of *dmpe* and $\mathrm{FSb(OTf)_2}$ in MeCN. Aided by the rigidity of the chelating donor, which is also resistant towards ligand exchange in solution, the salt could be readily crystallized and the solid-state structure of $[\mathbf{5.13}][\mathrm{OTf}]_2$ was determined. A dimeric arrangement is observed with the cations bridged by O−S−O contacts from the triflate anions, and additional interactions with two non-bridging triflate anions, as shown in Figure 5.2.1. The pyramidal geometry at Sb in the cation is retained in solution, as demonstrated by the two non-equivalent methyl group resonances in the ^{13}C (+6.1 and +7.2 ppm) and ^{1}H NMR (+1.86 and +2.10 ppm) spectra. Crucially, the expected $^{2}J_{\mathrm{PF}}$ coupling was unambiguously observed (Figure 5.2.2) for $[\mathbf{5.13}]^{2+}$, and the chemical shift and coupling constants are comparable to those assigned to derivatives of $[\mathbf{5.7(R)}]^{2+}$ (Table 5.2.1).

It was not possible to isolate salts of $[\mathbf{5.8(R)}]^{3+}$ at room temperature due to their high reactivity, consistent with their disproportionation to $[\mathbf{5.11(R)}]^{2+}$ and

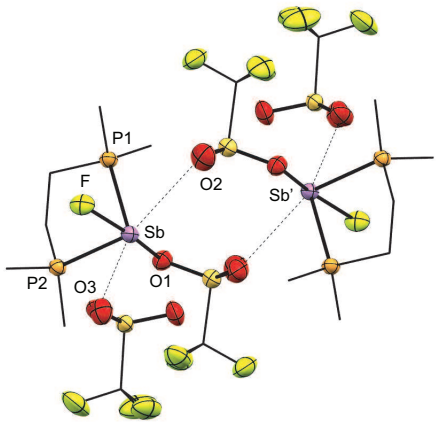

Figure 5.2.1. Molecular structure of [**5.13**][OTf]$_2$ in the solid state. Hydrogen atoms have been omitted for clarity. Bond lengths (Å) and angles (°) are as follows: Sb−F = 1.952(1), Sb−P1 = 2.5575(6), Sb−P2 = 2.5846(6), Sb−O1 = 2.575(2), Sb−O3 = 2.956(3), Sb−Sb' = 5.1812(6), P1−Sb−P2 = 80.08(2), F−Sb−P1 = 85.92(5), F−Sb−P2 = 81.02(4), F−Sb−O1 = 153.58 (6).

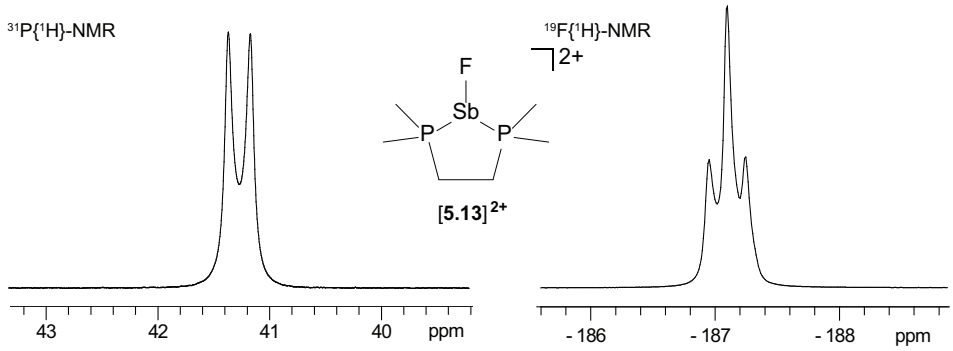

Figure 5.2.2. $^{31}P\{^1H\}$ (left) and $^{19}F\{^1H\}$ (right) NMR resonances for [**5.13**][OTf]$_2$ in CD_3CN at 298 K.

Table 5.2.1. Solution NMR data (CD_3CN, 298 K) for derivatives of $[\mathbf{5.7(R)}]^{2+}$, $[\mathbf{5.8(R)}]^{3+}$, $[\mathbf{5.10(R)}]^{4+}$, $[\mathbf{5.11(R)}]^{2+}$, and $[\mathbf{5.13}]^{2+}$. Values in parentheses indicate literature values for chemical shifts of known compounds. Values in curly brackets denote peak width at half-maximum where the expected $^2J_{PF}$ coupling was not observed (n.o.).

Cation	δ^{31}P (ppm)	δ^{19}F (ppm)	$^1J_{PF}$ (Hz)
$[\mathbf{5.7(Me)}]^{2+}$	+15.9	−178.2	44
$[\mathbf{5.7(Et)}]^{2+}$	+38.0{23}	−174.2{73}	n.o.
$[\mathbf{5.7(Pr)}]^{2+}$	+29.3	−173.4	41
$[\mathbf{5.7(Bu)}]^{2+}$	+32.4{62}	−173.9{52}	n.o.
$[\mathbf{5.13}]^{2+}$	+41.3	−187.1	39
$[\mathbf{5.8(Me)}]^{3+}$	+21.3		
$[\mathbf{5.8(Et)}]^{3+}$	+27.8		
$[\mathbf{5.8(Pr)}]^{3+}$	+22.1		
$[\mathbf{5.8(Bu)}]^{3+}$	+22.4		
$[\mathbf{5.10(Me)}]^{4+}$	−24.4		
$[\mathbf{5.10(Et)}]^{4+}$	+9.3		
$[\mathbf{5.10(Pr)}]^{4+}$	+0.6		
$[\mathbf{5.10(Bu)}]^{4+}$	+0.5		
$[\mathbf{5.11(Me)}]^{2+}$	+28.5(+28.4)		
$[\mathbf{5.11(Et)}]^{2+}$	+38.5(21)		
$[\mathbf{5.11(Pr)}]^{2+}$	+31.4(32)		
$[\mathbf{5.11(Bu)}]^{2+}$	+31.0(32)		
$[\mathbf{5.12(Me)}]^{1+}$	+148.0	−138.0	948
$[\mathbf{5.12(Et)}]^{1+}$	+150.2	−159.3	973
$[\mathbf{5.12(Pr)}]^{1+}$	+145.6	−154.7	971
$[\mathbf{5.12(Bu)}]^{1+}$	+145.6	−155.4	971

[**5.10(R)**]$^{4+}$ in solution as proposed in Scheme 5.1.2. The ^{31}P NMR signals assigned to derivatives of [**5.8(R)**]$^{3+}$ are singlets and broadened ($\Delta\nu_{1/2} = 90-500$ Hz), presumably due to a combination of the quadrupolar antimony nuclides and dynamic ligand exchange. However, upon combining $Sb(OTf)_3$ and PMe_3 in a 1:3 stoichiometry at −30°C, [**5.8(Me)**][OTf]$_3$ was isolated as a co-crystallate with [**5.11(Me)**][OTf]$_2$. The molecular structure of [**5.8(Me)**][**5.11(Me)**][OTf]$_5$ (Figure 5.2.3) shows a pyramidal geometry at Sb with three P−Sb lengths in the 2.5974(8)−2.6115(7) Å range and P−Sb−P angles in the $101.33(3) - 102.40(2)°$ range. In addition, three interion Sb−O contacts are observed in the $2.791(2) - 2.960(2)$ Å range (*cf.* $\Sigma_{r,vdW} = 3.61$ Å),[111] with each contact appearing *trans* to a P−Sb bond, intimating a triple displacement of triflate anions from $Sb(OTf)_3$ by three PMe_3 ligands.

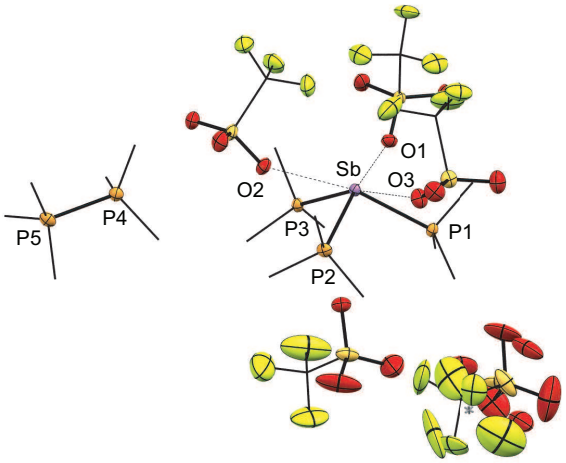

Figure 5.2.3. Solid-state structure of [**5.8(Me)**][OTf]$_3$ co-crystallized with [Me_3PPMe_3][OTf]$_2$. Hydrogen atoms have been omitted for clarity. Bond distances (Å) and angles (°) are follows: Sb−P1: 2.6050(7), Sb−P2: 2.5974(8), Sb−P3: 2.6115(7), Sb−O11: 2.960(2), Sb−O21: 2.791(2), Sb−O31: 2.844(2), P1−Sb−P2: 102.05(3), P2−Sb−P3: 11.33(3), P1−Sb−P3: 102.40(2), P4−P5: 2.2235(12), P1−Sb−P2: 102.05(3), P1−Sb−P3: 102.40(2), P2−Sb−P3: 101.33(3).

Signals attributed to derivatives of [**5.11(R)**]$^{2+}$ are assigned by comparison with previously reported ^{31}P chemical shifts for their triflate or perchlorate salts in MeCN for [**5.11(Me)**]$^{2+}$, [**5.11(Pr)**]$^{2+}$, and [**5.11(Bu)**]$^{2+}$.[101] Isolation of [**5.11(Pr)**][OTf]$_2$ enabled comprehensive characterization, including by crystallography. The identity of [**5.11(Et)**][OTf]$_2$ could not be established directly from solution NMR data since a previously assigned ^{31}P NMR chemical shift for the cation (+21 ppm) in

[**5.11(Et)**][ClO_4]$_2$* could not be reproduced for the triflate salt, which shows a single peak in its ^{31}P NMR specturm at +38.5 ppm. In order to resolve this discrepancy, [**11(Et)**][OTf]$_2$ was independently synthesized from a 2:1 reaction of PEt_3 with *in situ* generated $Ph_3Sb(OTf)_2$, according to Scheme 5.2.1,[79] and the molecular structure of the cation (Figure 5.2.4) now definitively establishes its identity and the associated ^{31}P NMR chemical shift.

The P−P bond length [2.2209(8) Å] is comparable to that in rare examples of acyclic diphosphonium dications such as [**5.11(Me)**]$^{2+}$ [2.198(2) Å] or [Me_3PPEt_3]$^{2+}$ [2.216(1) Å], and a partially eclipsed conformation is observed between the six ethyl groups. The relative arrangement of alkyl groups in hexaalkyl diphosphoniums appears to be determined mainly by packing effects. For instance, the [**5.11(Me)**]$^{2+}$ cation in [**5.8(Me)**][**5.11(Me)**][OTf]$_5$ shows a fully eclipsed configuration, which is in contrast to the staggered arrangement observed in [**5.11(Me)**][OTf]$_2$.[7]

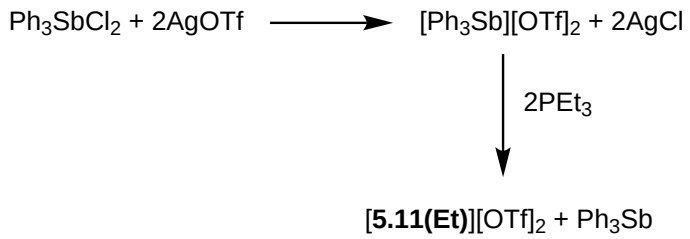

Scheme 5.2.1. Synthesis of [**5.11(Et)**][OTf]$_2$ *via* oxidative coupling of PEt_3 with $Ph_3Sb(OTf)_2$.

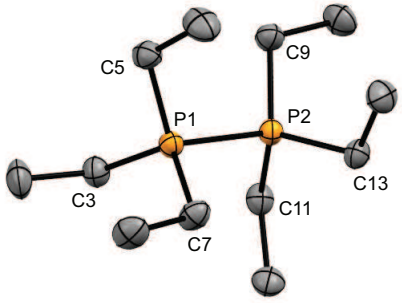

Figure 5.2.4. Solid-state molecular structure of the cation in [**5.11(Et)**][OTf]$_2$. Hydrogen atoms and triflate anions have been omitted for clarity.

*This salt was not structurally authenticated and its identity was based only upon elemental analysis. It is likely that the composition determined from elemental analysis corresponds to a different atomic connectivity.

The ^{31}P and ^{19}F NMR assignments for fluorophosphonium cations [**5.12(R)**]$^{1+}$ were confirmed by comparison to literature values or independent synthesis of triflate salts from small-scale equimolar mixtures of the appropriate phosphine and XeF_2 followed by treatment with one equivalent of TMSOTf. The solid-state structure of [**5.12(Me)**][OTf] (Figure 5.2.5) represents the first structural characterization of a trialkylfluorophosphonium salt, and involves three hydrogen bonds with the triflate anion in addition to one weak contact [3.297(3) Å] between a triflate oxygen atom and the phosphorus atom, which is marginally shorter than $\Sigma_{r,vdW}$ for the two elements (3.320 Å).[111] The O−P−F angle generated by this contact is 177.34(8)°, representing adjustment of the D_{3h} structure of Me_3PF_2.[209]

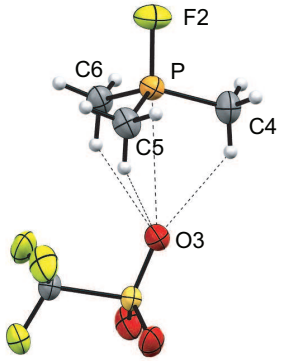

Figure 5.2.5. Molecular structure of [**5.12(Me)**][OTf] in the solid state. Bond lengths (Å) and angles (°) are as follows: P−F2 = 1.551 (1), P−C = 1.757(2), 1.755 (2), 1.755 (2), P−O3 = 3.301(2), F2−P−O3 = 177.34(8), F2−P−C = 106.38(6), 105.2(1), 106.38(6).

The ^{31}P NMR chemical shifts for species in Table 5.2.1 vary over a 150 ppm range but within each class of cations, generally decrease in the order δ(R = Et) > δ(R = Pr) ≈ δ(R = Bu) > δ(R = Me). Notably, the chemical shifts of the free phosphines (range of 30 ppm) also show the same order, providing additional support for the proposed assignments (Figure 5.2.6).

Attempts to isolate cations [**5.7(R)**]$^{2+}$ or [**5.10(R)**]$^{4+}$ with bulky phosphines such as P^{i}Pr$_3$ were unsuccessful. A ^{31}P NMR assay of the reaction mixture containing P^{i}Pr$_3$ and FSb(OTf)$_2$ in a 2:1 ratio displayed numerous fluorine containing products as indicated by the observation of spin systems with P−F couplings but no pure compounds could be isolated. A 3:1 mixture of P^{i}Pr$_3$ with Sb(OTf)$_3$ also gave a complex mixture of products at room temperature which could not be separated. Deprotonation of MeCN solvent was observed upon refluxing the reaction mixture for short

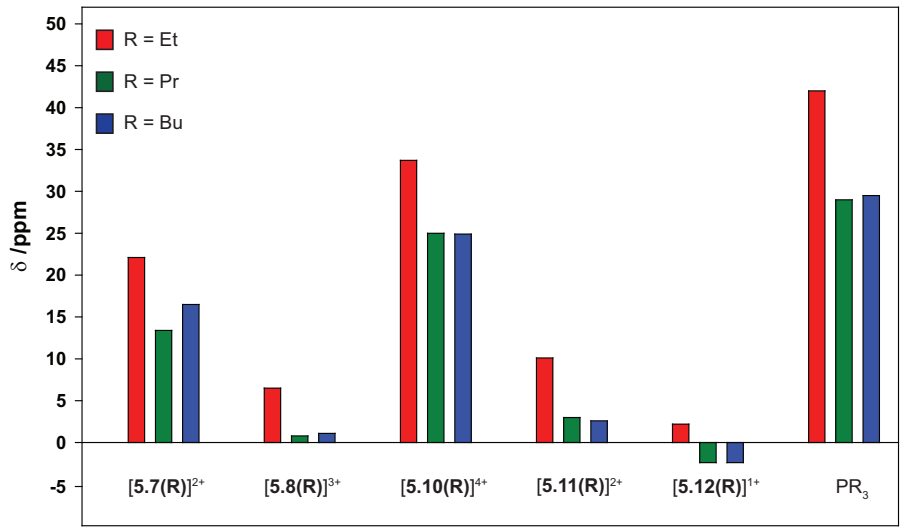

Figure 5.2.6. ^{31}P NMR chemical shifts of derivatives of $[\mathbf{5.7(R)}]^{2+}$, $[\mathbf{5.8(R)}]^{3+}$, $[\mathbf{5.10(R)}]^{4+}$, $[\mathbf{5.11(R)}]^{2+}$, $[\mathbf{5.12(R)}]^{1+}$, and PR_3 relative to the PMe_3 containing derivative of each species (Δ, in ppm).

periods or stirring at room temperature for 16 hours. Presumably, steric bulk at the α-carbon of the phosphine hinders the coordination required for clean transformation of *bis*-phosphine cations $[\mathbf{5.7(R)}]^{2+}$ to *tris*-phosphine cations $[\mathbf{5.8(R)}]^{3+}$.

5.3 Reactions of $[\mathbf{5.10(Me)}][OTf]_4$

While the initial isolation of $[\mathbf{5.10(Me)}][OTf]_4$ as a pure substance was achieved on a paltry 150 mg scale (*ca.* 0.1 mmol), impractical for further reactivity studies, reaction conditions have now been optimized for a one-pot, three-step reaction to give reproducible yields of analytically pure $[\mathbf{5.10(Me)}][OTf]_4$ and $[\mathbf{5.10(Et)}][OTf]_4$ on a scale up to 10 g. Consistent with the *exquisite* sensitivity of these compounds towards hydrolysis and oxidation, particularly in solution, the key determinants of purity and reactions yields are the rigorous drying and deoxygenation of the inert gas atmosphere and solvent,[†] the use of freshly sublimed (SbF_3) or distilled (TMSOTf, PMe_3) reagents and careful application of dynamic vacuum (*ca.* 10^{-1} mbar) in the latter stages of the reaction to avoid free phosphine-catalyzed decomposition (*vide infra*).

5.3.1 Thermolysis and Photolysis

The four-membered ring of $[\mathbf{5.10(Me)}]^{4+}$ contains four of the six Sb−Sb bonds required to make neutral, tetrahedral Sb_4, which is directly analogous to P_4 and As_4. Moreover, $[\mathbf{5.10(Me)}]^{4+}$ also contains four phosphine ligands which may be susceptible to further reductive elimination of two diphosphonium dications, $[\mathbf{5.11(Me)}]^{2+}$, to yield neutral Sb_4. While P_4 and As_4 are well-characterized, the antimony analogue has not been isolated as a bulk solid, and only one solid-state structural determination has been made using a scanning tunnelling microscope to characterize a thin film of the material under ultra-high-vacuum conditions.[210][‡] In this context, the thermal or photochemical decomposition of $[\mathbf{5.10(Me)}][OTf]_4$ was envisioned as a route to bulk

[†]Water content, as determined by Karl-Fischer titrations, was maintained below 1 ppm and solvent was stored in the glovebox in a Strauss flask over carefully activated 3 Å molecular sieves until needed.

[‡]The authors of this report appropriately use the phrase '*a somewhat provocative description of the fact that nanocrystalline structures of Sb_4 tetrahedrons exist on the substrates $AuSb_2(100)$ and $MoS_2(0001)$*' to summarize their results in the abstract section.

solid Sb_4.

A sample of [**5.10(Me)**][OTf]$_4$ (yellow solid) heated under argon at 120 °C for 16 hours turned black, consistent with the formation of elemental antimony. A CD_3CN extract of the black product showed ^{31}P, ^{1}H and ^{13}C NMR signals corresponding exclusively to [**5.11(Me)**]$^{2+}$ as the sole oxidation product. A Raman spectrum of the black solid matched that of the amorphous α-phase (110 cm^{-1}, 150 cm^{-1})[211] of antimony rather than the reported Raman spectrum of tetrahedral Sb_4 in argon matrix (138 cm^{-1}, 179 cm^{-1}, 242 cm^{-1}).[212] Identical results were obtained when heating was carried out in the dark, under vacuum, or in solution (toluene). Irradiating solid [**5.10(Me)**][OTf]$_4$ or as a solution in MeCN at 256 nm for 3 hours at room temperature had no measurable effect. It should be noted that in the gas phase tetrahedral Sb_4 is the preferred allotrope of the element up to 1050 K.[213] It is possible that despite its gaseous stability, tetrahedral Sb_4 is thermodynamically unstable with respect to its amorphous phases in the condensed state, preventing its isolation as a solid and is, in this context, analogous to tetrahedral As_4 (yellow arsenic) which spontaneously decomposes to a hexagonal allotrope (grey arsenic, α-As) at room temperature.[214]

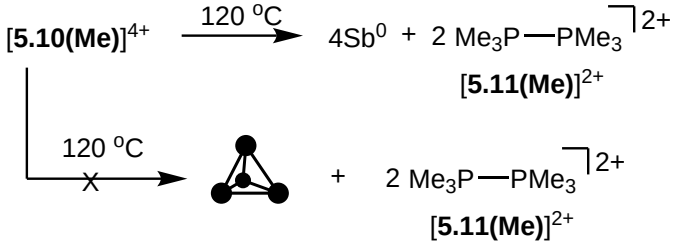

Scheme 5.3.1. Thermolysis of [**5.10(Me)**][OTf]$_4$ to yield [**5.11(Me)**][OTf]$_2$ and elemental antimony.

The thermolysis described above must be carried out in rigorously dried glassware, the surface of which has been treated with TMSCl to silanize terminal −OH groups. Samples heated without prior passivation of glassware produced elemental antimony and [**5.11(Me)**][OTf]$_2$, but also showed resonances due to [Me_3PH]$^{1+}$ and a singlet at +115.6 ppm in the $^{31}P\{^{1}H\}$ NMR spectrum (CD_3CN) of the reaction mixture, tentatively assigned to the Hendrickson's reagent derivative, [Me_3POPMe_3]$^{2+}$. This assignment is supported by an independent synthesis of the cation from a 2:1 mixture of Me_3PO and triflic anhydride, using the standard synthetic protocol for these reagents.[215] The formation of these by-products is interpreted as being due to the

reaction of the extremely moisture sensitive [**5.10(Me)**][OTf]$_4$ with surface hydroxyl groups in nonsilanized glassware.

5.3.2 Reactions with R_2PH, RPH_2, R_2PCl, and $RPCl_2$

Addition of a solution of R_2PH (R = C_6H_{11} (Cy), Ph) to a clear yellow-coloured solution of [**5.10(Me)**][OTf]$_4$ in MeCN results in immediate deposition of a fine black precipitate and loss of the yellow coloration. The $^{31}P\{^1H\}$ NMR spectra of reaction supernatant show a singlet due to $[Me_3PH]^{1+}$ and two doublets characteristic of phosphinophosphonium cations $[Me_3PPR_2]^{1+}$ (R = Cy, Ph) with typical $^1J_{PP}$ values in the 300-350 Hz range (Scheme 5.3.2).[91] Cation $[Me_3PPPh_2]^{1+}$ is known[216] and the assignment of $[Me_3PPCy_2]^{1+}$ was confirmed by comparison of chemical shifts and coupling constants with literature values[91] for phosphinophosphonium salts and by elemental analysis.

Analogously, addition of a solution of RPH_2 (R = Cy, ^{t}Bu) to a solution of [**5.10(Me)**][OTf]$_4$ results in immediate precipitation of elemental antimony. The ^{31}P NMR spectra of these reaction mixtures show complete consumption of RPH_2 and [**5.10(Me)**][OTf]$_4$, and formation of a singlet due to $[Me_3PH]^{1+}$ and a pair of doublets assigned to $[Me_3PP(H)R]^{1+}$ (Scheme 5.3.3). Consistent with this formulation, the $^{31}P\{^1H\}$ coupled NMR spectrum of the reaction involving $CyPH_2$ shows (Figure 5.3.1*a*) both $^1J_{PP}$ and $^1J_{HP}$ couplings for the phosphinic signal centred at −83.6 ppm. The Pα-Pβ(Hβ)Cy connectivity is also confirmed in the ^1H NMR spectrum of the reaction mixture, where Hβ resonates at +3.65 ppm exhibiting $^1J_{H\beta P\beta}$, $^2J_{H\beta P\alpha}$, and $^3J_{H\beta H\gamma}$ couplings, the last of these arising from coupling to the *ipso* proton (Hγ) of the cyclohexyl ring. The methyl protons (Hα) around Pα also show the expected $^2J_{H\alpha P\alpha}$ and $^3J_{H\alpha P\beta}$ couplings indicating a P−P bond. Finally, a two-dimensional $^{31}P/^1H$ HSQC (Figure 5.3.1*b*) spectrum, which was optimized to show one-bond couplings, shows coupling between Hβ and Pβ but no coupling involving Hβ and Pα. The corollary two-dimensional HMBC experiment (Figure 5.3.1*c*), optimized to exclude one-bond couplings, shows coupling between Hβ and Pα, but no coupling involving Hβ and Pβ. Despite numerous attempts, it was not possible to separate $[Me_3PP(H)Cy][OTf]$ from $[Me_3PH][OTf]$, precluding elemental analysis or structural determination by X-ray diffraction. Nevertheless, this study represents the first spectroscopic detection of an H-phosphinophosphonium cation.

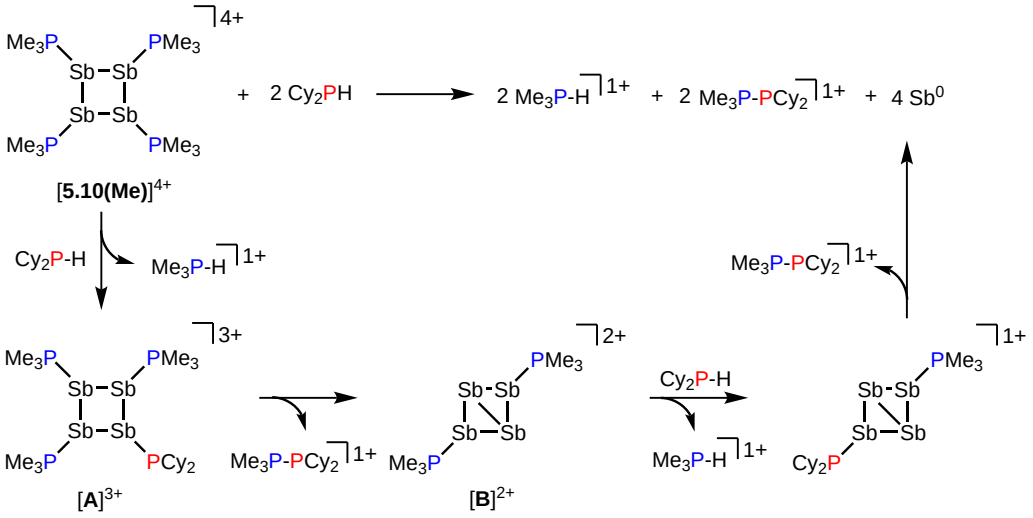

Scheme 5.3.2. Formation of $[Me_3PH]^{1+}$ and $[Me_3PPCy_2]^{1+}$ from the reaction of [**5.10(Me)**] $[OTf]_4$ with Cy_2PH.

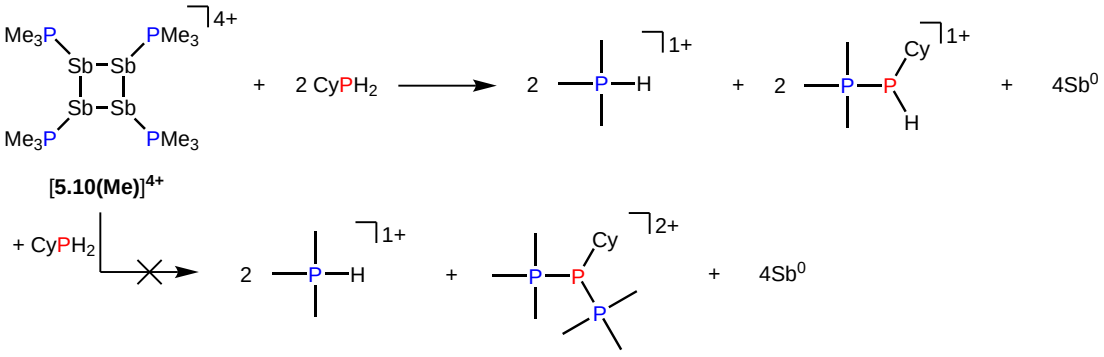

Scheme 5.3.3. Reaction of [**5.10(Me)**][$OTf]_4$ with $CyPH_2$.

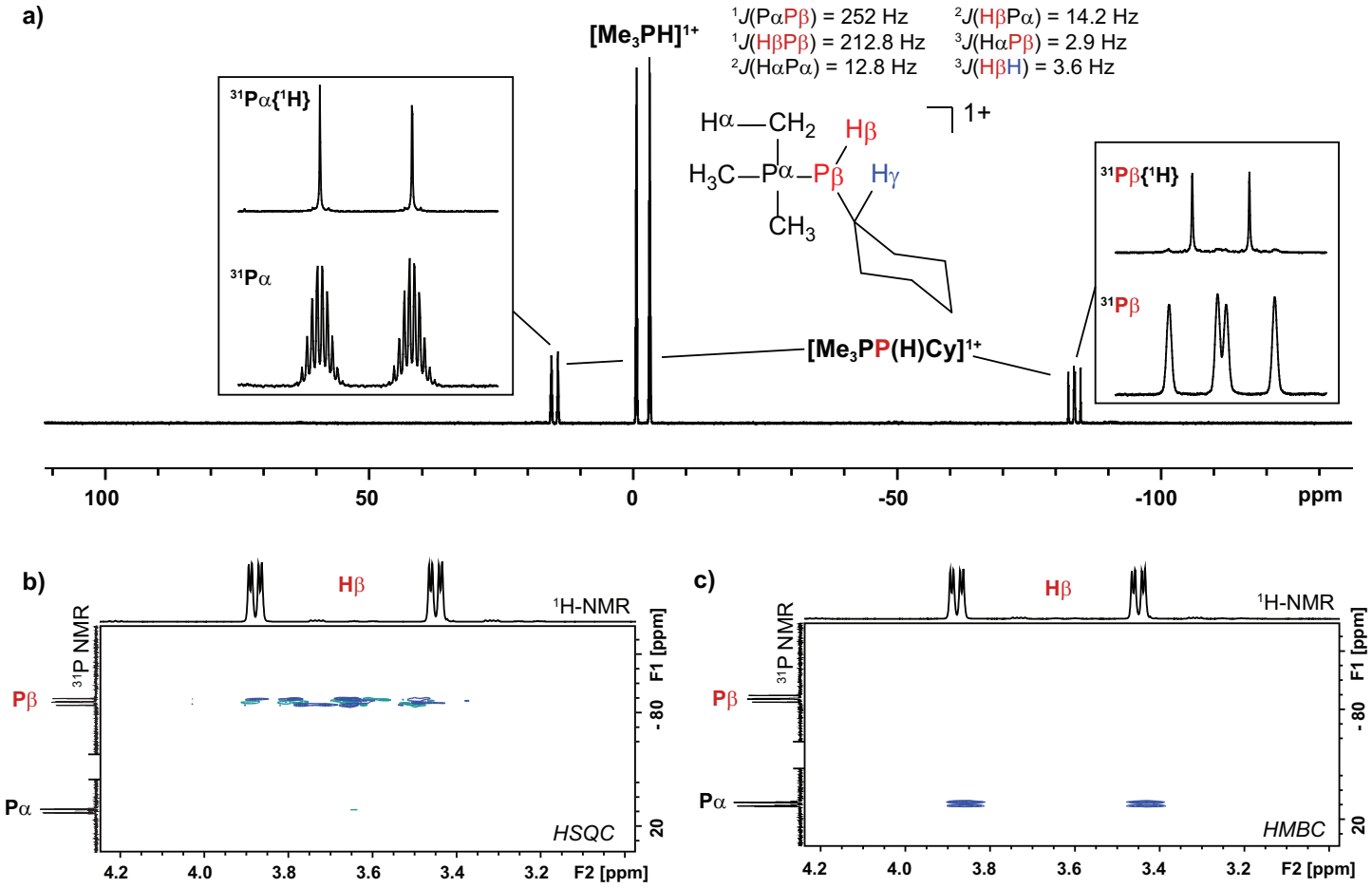

Figure 5.3.1. *a)* ^{31}P NMR spectrum of the crude reaction mixture containing $CyPH_2$ and **[5.10(Me)]**[OTf]$_4$ in a 2:1 ratio. Insets show detailed views of the $^{31}P\{^1H\}$ and ^{31}P NMR resonances assigned to the Me_3P- (left) and $-P(H)Cy$ (right) fragments in $[Me_3PP(H)Cy]^{1+}$. *b)* Sections of the $^{31}P/^1H$ HSQC spectrum showing a $^1J_{PH}$ coupling. *c)* Sections of the $^{31}P/^1H$ HMBC spectrum showing a $^2J_{PH}$ coupling.

The formation of $[Me_3PH]^{1+}$ and the phosphinophosphonium salts is understood in broad terms as a metathesis step followed by a reductive elimination step as outlined in Scheme 5.3.2. Coordination of Cy_2PH to one of the antimony centres in [**5.10(Me)**][OTf]$_4$ is followed by intramolecular deprotonation by PMe_3 to yield the observed $[Me_3PH]^{1+}$ cation and a tricationic intermediate, $[\mathbf{A}]^{3+}$. This trication can undergo rapid intramolecular reductive elimination of the first equivalent of the phosphinophosphonium cation to give dication $[\mathbf{B}]^{2+}$. A second round of coordination, deprotonation and reductive elimination completes the reduction of antimony to its elemental form and furnishes the observed distribution of products. Unfortunately, the partially reduced species were not observed and appear to be fleeting intermediates. Nevertheless, formation of $[Me_3PP(H)R]^{1+}$ from reactions involving primary phosphines (Scheme 5.3.3) is consistent with the proposed mechanism, although it is unclear why the second deprotonation does not occur to yield the corresponding dication $[(Me_3P)_2PR]^{2+}$. As before, Raman analysis of the black precipitate matches the amorphous α-phase of metallic antimony rather than tetrahedral Sb_4.

The observation that [**5.10(Me)**][OTf]$_4$ serves as a source of PMe_3, which deprotonates added primary and secondary phosphines, implies a labile and polarized P−Sb bond that undergoes facile heterolytic cleavage. Consistently, addition of Cy_2PCl or $CyPCl_2$ to a solution of [**5.10(Me)**][OTf]$_4$ results in quantitative formation of $[Me_3PPCy_2]^{1+}$ or $[(Me_3P)_2PCy]^{2+}$,[188] respectively, concomitant with deposition of elemental antimony (Scheme 5.3.4). In these cases, $[\mathbf{5.10(Me)}]^{4+}$ behaves overall as a chloride abstractor and phosphine donor. Formation of chloroantimony species is proposed as transients that undergo loss of chlorine gas to yield elemental antimony as there is no evidence of Sb−Cl bond stretching modes in the Raman spectra of the insoluble black solid isolated from these reactions. However, since no products expected from reactions of dissolved Cl_2 could be detected, the fate of the chlorine atoms cannot yet be definitively described. When intermediate stoichiometries of $CyPCl_2$ are employed, formation of the known $[Me_3PP(Cl)Cy]^{1+}$ cation is also observed, indicating a single chloride abstraction event, that is analogous to the formation of $[Me_3PP(H)Cy]^{1+}$ in reactions with $CyPH_2$. ^{31}P NMR data for $[Me_3PPCy_2]$[OTf], $[Me_3PP(H)Cy]$[OTf], $[(Me_3P)_2PCy]$[OTf]$_2$, and $[Me_3PP(Cl)Cy]$[OTf] are given in Table 5.3.1.

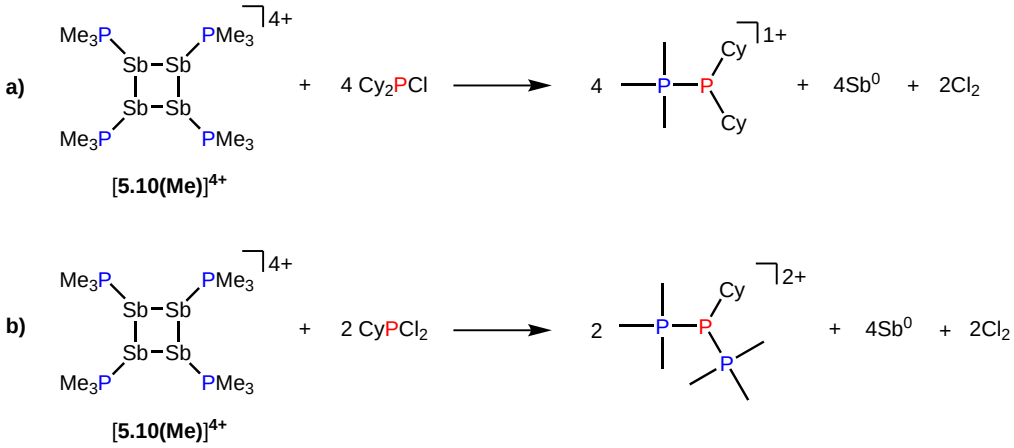

Scheme 5.3.4. Formation of $[Me_3PPCy_2]^{1+}$, $[Me_3PP(Cl)Cy]^{1+}$, and $[(Me_3P)_2PCy]^{2+}$ from the reaction of [**5.10(Me)**][OTf]$_4$ with Cy_2PCl or $CyPCl_2$.

Table 5.3.1. ^{31}P NMR (CD_3CN, 298 K) chemical shifts and coupling constants for products obtained from the reaction of Cy_2PH, $CyPH_2$, Cy_2PCl, and $CyPCl_2$ with [**5.10(Me)**][OTf]$_4$.

	δ^{31}P	$^1J_{PP}$
$[Me_3PPCy_2][OTf]$	+12.8, −5.1	327
$[Me_3PP(H)Cy][OTf]^a$	+14.8, −83.6	252
$[(Me_3P)_2PCy][OTf]_2$	+22.7, −30.8	307, 326
$[Me_3PP(Cl)Cy][OTf]$	+23.0, +78.4	326

^{a} $^1J_{PH}$ = 214 Hz

5.3.3 Reaction with PMe_3

The ^{31}P NMR spectrum of a reaction mixture containing 15 mol % of PMe_3 and [**5.10(Me)**][OTf]$_4$ shows slow disappearance of the signal due to the latter and evolution of broadened signals due to [**5.11(Me)**]$^{2+}$ and free PMe_3. Concomitantly, a mirror of metallic antimony is deposited in the reaction vessel. Within 12 hours at 298 K, there is no evidence of [**5.10(Me)**]$^{4+}$, while signals due to [**5.11(Me)**]$^{2+}$ and free PMe_3 persist, consistent with complete decomposition of the tetracation, catalyzed by PMe_3. The proposed mechanisms (Scheme 5.3.5) involve nucleophilic attack by the added phosphine at either the antimony or the phosphorus centres. Attack at a stibine should yield intermediate [**A**]$^{4+}$ (Scheme 5.3.5), featuring a hypercoordinate antimony centre. Several examples of such hypervalent P−Sb complexes have been reported. Due to its high charge concentration, this complex is predicted to be strongly oxidizing, and, in a process analogous to reductive elimination from [**5.8(Me)**]$^{3+}$, an equivalent each of [**5.11(Me)**]$^{2+}$ and intermediate [**B**]$^{2+}$ (Scheme 5.3.5) can be generated, enabling dissociation of PMe_3. Alternatively, attack at one of the phosphorus centres of [**5.10(Me)**]$^{4+}$ directly generates intermediate [**B**]$^{2+}$ together with [**5.11(Me)**]$^{2+}$ and PMe_3. The liberated phosphine can further reduce [**B**]$^{2+}$ by a second nucleophilic attack either at Sb or at P to evolve the second equivalent of [**5.11(Me)**]$^{2+}$ and yield fully reduced antimony. Nucleophilic attack by a neutral two-electron ligand at tetracoordinate trimethylchlorophosphonium, trimethylphosphonium and dimethylthiophosphonium cations has been demonstrated previously.[84,217] The broadness of signals for [**5.11(Me)**]$^{2+}$ and PMe_3 in these reaction mixtures is attributed to an exchange process that is also detected when free PMe_3 is added to a solution of [**5.11(Me)**][OTf]$_2$.

The catalytic decomposition of [**5.10(Me)**][OTf]$_4$ in the presence of PMe_3 explains the difficulties encountered during synthesis of this salt. For instance, if the addition rate of PMe_3 to FSb(OTf)$_2$ is too high, a dark orange solution is obtained which rapidly deposits elemental antimony. However, if a dynamic vacuum is applied to the dark orange solution to remove the volatile PMe_3 (b.p. = 38 °C), the solution maintains a yellow colour, leading to the formation of [**5.10(Me)**][OTf]$_4$. Moreover reactions with Lewis bases that displace PMe_3 must be carried out with explicit steps to remove the liberated phosphine in order to avoid decomposition (*vide infra*).

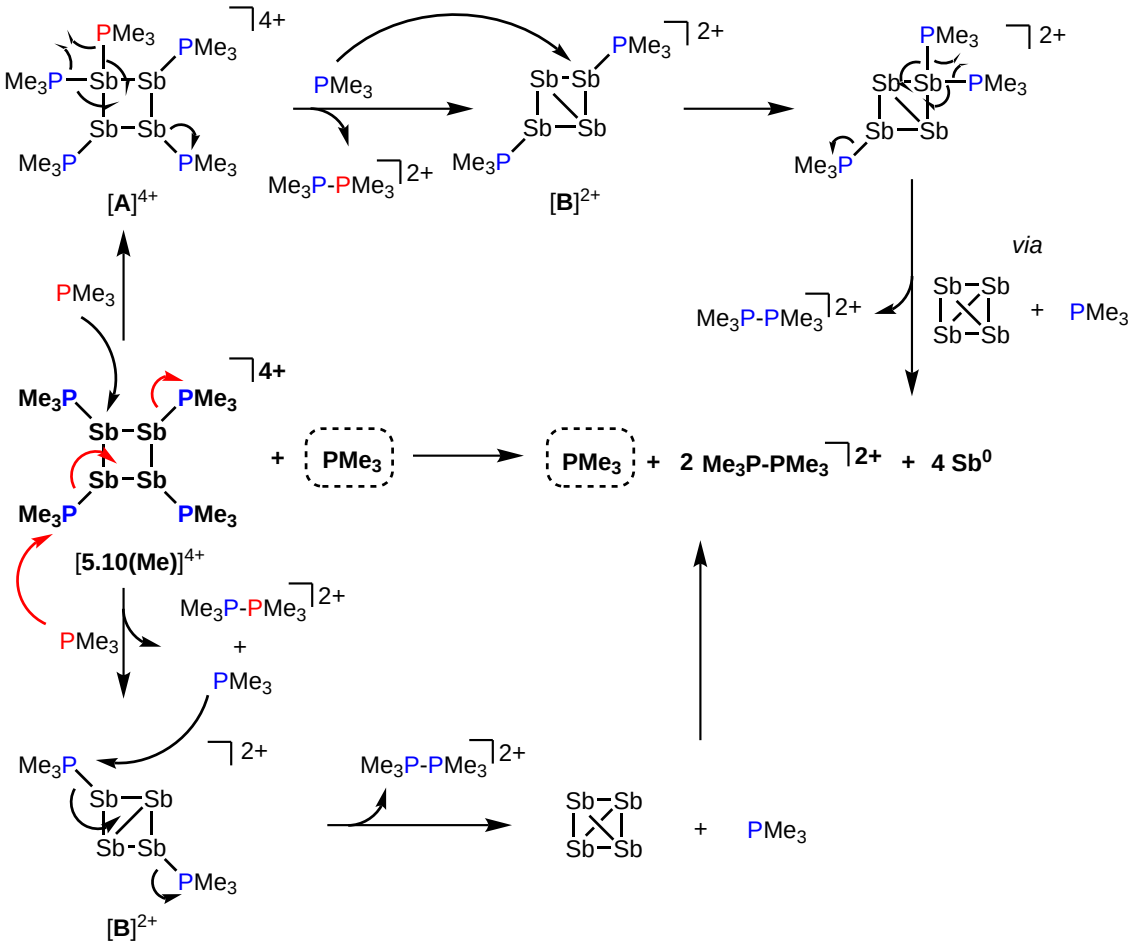

Scheme 5.3.5. Catalytic decomposition of [**5.10(Me)**][OTf]$_4$ by PMe$_3$ *via* nucleophilic attack at Sb (upper half) or P (lower half).

5.3.4 Reaction with [Li][*nacnac*^{dipp}]

In contrast to the sterically unhindered and neutral base PMe_3, a bulky and anionic base is expected to yield products arising from ligand substitution rather than from addition. Consistently, the $^{31}P\{^1H\}$ NMR spectra of equimolar reaction mixtures of [**5.10(Me)**][OTf]$_4$ and [Li][*nacnac*$^{(dipp)}$] (*dipp* = 2,6-diisopropylphenyl), indicate quantitative formation of [**5.15(Me)**][OTf]$_3$ (Scheme 5.3.6). The 1,3-diketiminate anion [*nacnac*$^{(dipp)}$]$^{1-}$, abbreviated as *nacnac*, displaces one PMe_3 ligand from [**5.10(Me)**]$^{4+}$ to give [$(Me_3P)_3Sb_4$(*nacnac*)]$^{3+}$, which is an analogue of [$(Me_3P)_3Sb_4(PCy_2)$]$^{3+}$ (intermediate [**A**]$^{3+}$ in Scheme 5.3.2). The $^{31}P\{^1H\}$ NMR spectrum of [**5.15(Me)**][OTf]$_3$ shows the expected AX_2 spin system [−26.6 ppm (triplet), −33.6 ppm (doublet), $^3J_{PP}$ = 32 Hz] and a corresponding AX_2 spin system [−6.3 ppm (triplet), −2.5 ppm (doublet), $^3J_{PP}$ = 23 Hz] is also observed for [**5.15(Et)**]$^{3+}$, prepared from the reaction of [**5.10(Et)**]$^{4+}$ with [Li][*nacnac*$^{(dipp)}$]. Isolation of [**5.15(Me)**] [OTf]$_3$ is only possible when the reaction is performed under a mild dynamic vacuum to remove the displaced phosphine, which effects redox decomposition at high concentrations, presumably *via* similar mechanisms as described for [**5.10(Me)**]$^{4+}$ in Scheme 5.3.5.

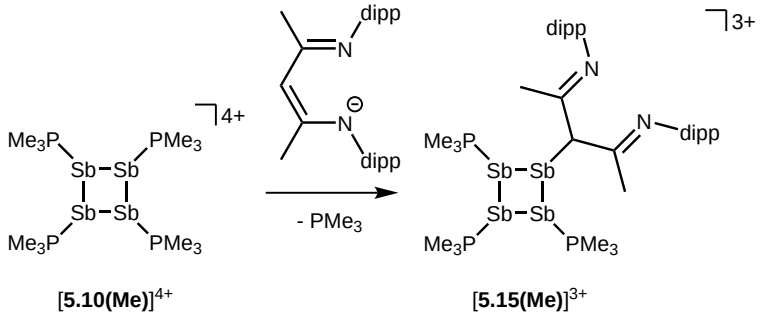

Scheme 5.3.6. Formation of [**5.15(Me)**]$^{3+}$ by nucleophilic displacement of PMe_3 from [**5.10(Me)**]$^{4+}$.

The solid-state structure of the cation in [**5.15(Me)**][OTf]$_3$•MeCN (Figure 5.3.2) shows three phosphine ligands and the rare γ-coordination mode for the *nacnac* substituent,[218] which has not been observed previously for haloantimony centres bound to this substituent.[219] Heteroleptic substitution is very rare in antimony homocycles[220–223] and examples for cationic systems have not been reported. The range of Sb−Sb [2.8209(5)−2.8612(5) Å] and Sb−P [2.538(5)−2.604(9) Å] distances are similar to those in [**5.10(Me)**]$^{4+}$ indicating minimal distortion of the Sb_4 ring

upon displacement of PMe_3 with *nacnac*. While [**5.15(Me)**][$OTf]_3$ is stable in the solid state under inert atmosphere, $^{31}P\{^1H\}$ NMR spectra of MeCN solutions show decomposition over five days at 20 °C to elemental antimony, [**5.10(Me)**][$OTf]_4$ and [**5.11(Me)**][$OTf]_2$.

To assess whether or not bonding *via* the γ carbon of *nacnac* is a general feature of antimony compounds and because *nacnac*-functionalized antimony centres are rare in the literature,[219] the synthesis of (*nacnac*)$Sb(OTf)_2$ by salt metathesis between an equimolar mixture of *in situ* generated $Sb(OTf)_3$ and [Li][$nacnac^{(dipp)}$] was attempted. Upon separation from LiOTf, the compound was isolated as a pure substance and comprehensively characterized. The molecular structure of (*nacnac*)$Sb(OTf)_2$, determined by X-ray diffraction, shows a see-saw geometry around antimony with two strongly interacting triflate anions in axial positions (Figure 5.3.3). In contrast to γ-coordination observed for [**5.15(Me)**]$^{3+}$, N,N'-chelation by *nacnac* is observed for (*nacnac*)$Sb(OTf)_2$, and the difference in bonding modes is attributed to the different steric environments around antimony in the two compounds, rather than intrinsic features of the *nacnac*-Sb interaction.

Interestingly, the ^{19}F resonances for the two triflate CF_3 groups are different (−78.3 and −78.4 ppm), implying a rigid ring system with non-equivalent positions above and below the plane of the ring. Consistently, the isopropyl substituents show two unique resonances for the C_{ipso} protons. Furthermore, there is restricted rotation around the $C_{ipso}-C_{phenyl}$ bond giving rise to four unique signals for the methyl groups in the ^1H NMR spectrum of the compound. These results evidence the solution-phase persistence of the weak hydrogen bonding interactions between N1, N2 and the isopropyl C_{ipso} protons, detected as short contacts in the solid-state molecular structure.

5.3.5 Reaction with *dmap*

The reaction of [**5.10(Me)**][$OTf]_4$ with *dmap* has been examined by ^{31}P NMR (Figure 5.3.4) and shows substitution of one phosphine ligand (Scheme 5.3.7) but it was not possible to isolate the resulting products. Following filtration of the reaction mixture (black suspension), the yellow-green filtrate shows the expected AX_2 spin system (triplet at +66.9 ppm, doublet at +42.5 ppm, $^3J_{PP}$ = 24 Hz), tentatively assigned to [$(Me_3P)_3Sb_4$(*dmap*)]$^{4+}$ ([**5.16**]$^{4+}$), and broad signals due to PMe_3 (−62 ppm), [(*dmap*)$PMe_3]^{2+}$ ([**5.17**]$^{2+}$, +89.0 ppm) and [**5.11(Me)**]$^{2+}$. Within hours, signals due

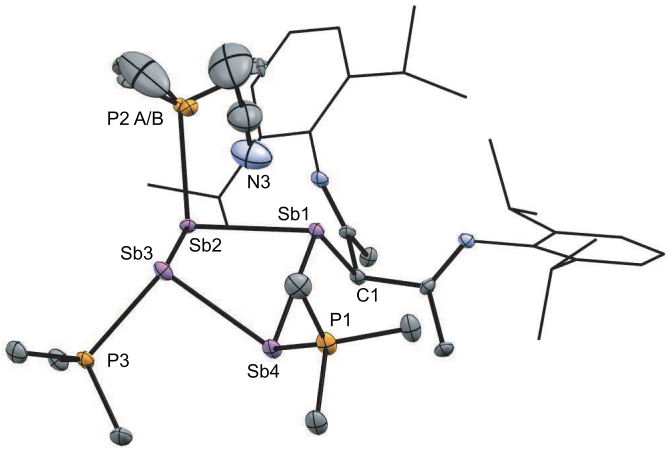

Figure 5.3.2. Molecular structure of the cation in [**5.15(Me)**][OTf]$_3$•MeCN in the solid state. Hydrogen atoms and triflate anions have been omitted for clarity. Thermal ellipsoids are drawn at 30 % probability level. Bond lengths (Å) and angles (°) are as follows: Sb1−Sb2 = 2.8209(5), Sb2−Sb3 = 2.8457(5), Sb3−Sb$_4$ = 2.8501(5), Sb1−Sb$_4$ = 2.8612(5), P1−Sb$_4$ = 2.538(2), P2A−Sb2 = 2.548(5), P2B−Sb2 = 2.604(9), P3−Sb3 = 2.541(1), C1−Sb1 = 2.209(5), Sb1−Sb3 = 3.7344(5), Sb2−Sb$_4$ = 3.7003(5), Sb1−N3 = 3.42(1), Sb3−N3 = 3.19(1), Sb1−Sb2−Sb3 = 82.45(1), Sb2−Sb3−Sb$_4$ = 81.03(1), Sb3−Sb$_4$−Sb1 = 81.67(2), Sb$_4$−Sb1−Sb2 = 81.26(1), Sb1−Sb2−Sb3−Sb$_4$ = −42.10(2).

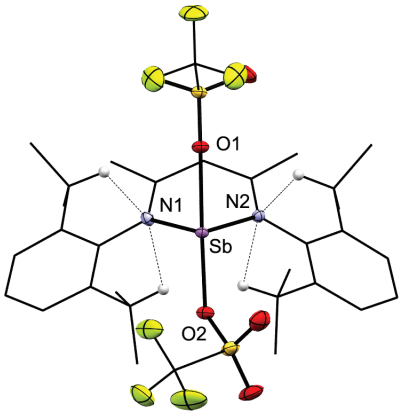

Figure 5.3.3. Molecular structure of [(*nacnac*)Sb(OTf)$_2$] in the solid state. Non-essential hydrogen atoms have been omitted for clarity. Bond lengths (Å) and angles (°) are as follows: N1−Sb = 2.071(2), N2−Sb = 2.075 (2), O1−Sb = 2.287(1), O2−Sb = 2.196(1), N1−Sb−N2 = 89.11(6), O1−Sb−O2 = 174.33(5), O1−Sb−N1 = 88.86(6), O1−Sb-N2 = 89.46(6), O2−Sb−N1 = 86.31(6), O2−Sb−N2 = 87.51(6).

to $[Me_3PCH_2PMe_2]^{1+}$ ($[\mathbf{5.18}]^{1+}$, doublet at −53.9 ppm, doublet at +26.0 ppm, $^2J_{PP}$ = 58 Hz)[224] appear in the ^{31}P NMR spectrum and a significant amount of $[dmap\text{H}]^{1+}$ is observed by ^{1}H NMR spectroscopy. The latter two species are proposed to arise from deprotonation of the slightly acidic protons of $[\mathbf{5.11(Me)}]^{2+}$ by *dmap* and the subsequent rearrangement of $[Me_3PPMe_2CH_2]^{1+}$ (Scheme 5.3.7). Consistently, a 1:1 control reaction of *dmap* and $[\mathbf{5.11(Me)}]^{2+}$ initially shows broad signals for $[\mathbf{5.17}]^{2+}$ and free PMe_3 as the kinetic products, but within 4 hours signals due to $[\mathbf{5.18}]^{1+}$ and $[dmap\text{H}]^{1+}$ are observed, revealing them to be the thermodynamic products (Scheme 5.3.8). In addition to $[\mathbf{5.18}]^{1+}$, four unique and mutually coupled phosphorus environments (by ^{31}P NMR spectroscopy) are also observed which could not been assigned definitively.

The $^3J_{PP}$ coupling constant for the signal assigned to $[\mathbf{5.16}]^{4+}$ (24 Hz) is comparable to the values in $[\mathbf{5.15(Me)}]^{3+}$ (32 Hz) and $[\mathbf{5.15(Et)}]^{3+}$ (23 Hz). However, the ^{31}P NMR chemical shifts observed for $[\mathbf{5.16}]^{4+}$ (A: +66.9, X_2: +42.5) are significantly downfield from those of $[\mathbf{5.15(Me)}]^{3+}$ and $[\mathbf{5.15(Et)}]^{3+}$ (Table 5.3.2), and this cannot be attributed solely to the different formal charges in the species as the PMe_3 groups in tetracationic $[\mathbf{5.10(Me)}]^{4+}$ resonate at −24.5 ppm. A survey of reported spectroscopic data indicates that *dmap*-stabilized main group cations generally show ^{31}P NMR chemical shifts that are substantially downfield from their PMe_3-stabilized homologues (Table 5.3.2), presumably due to the greater electronegativity of nitrogen relative to phosphorus, bolstering the assignment for $[\mathbf{5.16}]^{4+}$.

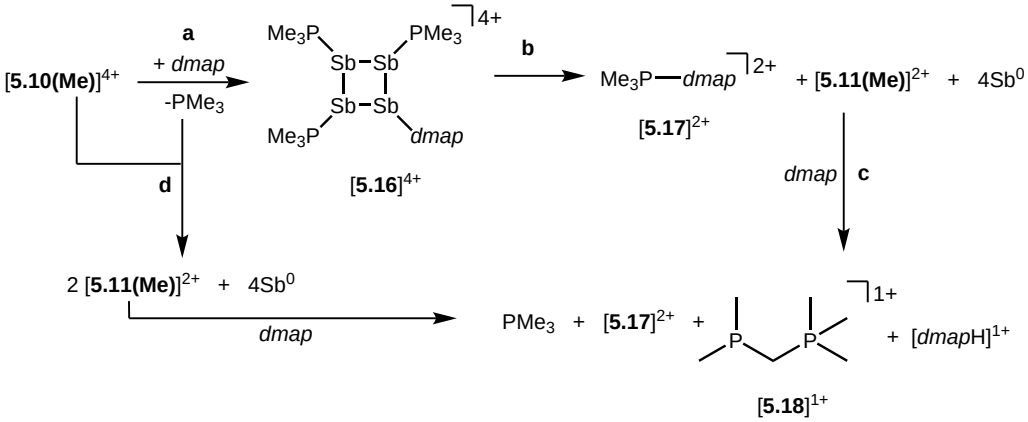

Scheme 5.3.7. Proposed pathways to formation of $[\mathbf{5.16}]^{4+}$ (a), $[\mathbf{5.17}]^{2+}$, $[\mathbf{5.11(Me)}]^{2+}$, and elemental antimony (b, d), and $[\mathbf{5.18}]^{1+}$ (c) in reaction mixtures containing $[\mathbf{5.10(Me)}][OTf]_4$ and *dmap* in a 1:1 stoichiometry.

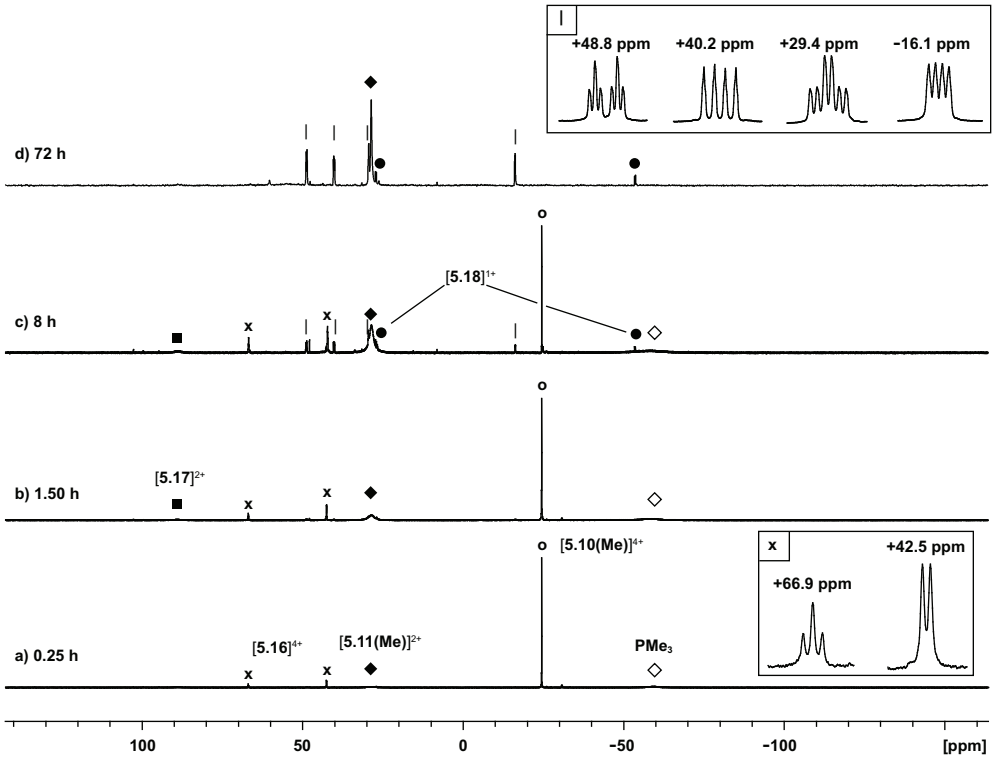

Figure 5.3.4. Formation of $[\mathbf{5.11(Me)}]^{2+}$ (⧫), $[\mathbf{5.16}]^{4+}$ (×), $[\mathbf{5.17}]^{2+}$ (■), $[\mathbf{5.18}]^{1+}$ (•), and PMe_3 (◇) in the equimolar reaction of *dmap* with $[\mathbf{5.10(Me)}][OTf]_4$ (○). Peaks labelled with a vertical line (|) correspond to an unidentified product. Insets show the spin systems observed for $[\mathbf{5.16}]^{4+}$ (×) and the unidentified product (|).

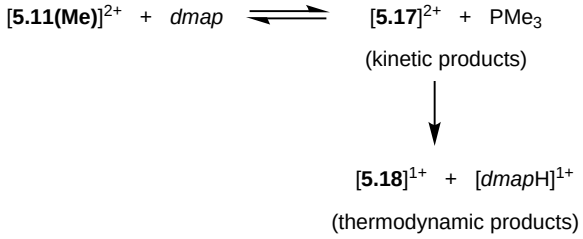

Scheme 5.3.8. Kinetic and thermodynamic outcomes in the reaction between $[\mathbf{5.11(Me)}]^{2+}$ and *dmap*.

Table 5.3.2. Comparison of ^{31}P NMR chemical shifts for some phosphorus containing main group cations stabilized by PMe_3 or *dmap*. Values for tetracoordinate phosphorus centres are given in parentheses, where applicable.

Cation	δ ^{31}P
$[Me_3PPMe_2]^{1+}$	(-59), $+18$ [7]
$[(dmap)PMe_2]^{1+}$	$+91$ [217]
$[Me_3PPh_2]^{1+}$	$(+15)$, -23 [216]
$[(dmap)PPh_2]^{1+}$	$+88$ [225]
$[Me_3PP(S)Me_2]^{1+}$	$(+38)$, $(+16)$ [84]
$[(dmap)P(S)Me_2]^{1+}$	$(+88)$ [84]
$[\mathbf{5.11(Me)}]^{2+}$	$(+28.4)$ [7]
$[\mathbf{5.17}]^{2+}$	$(+89.0)$ [217]
$[\mathbf{5.10(Me)}]^{4+}$	(-24.5)
$[\mathbf{5.15(Me)}]^{3+}$	(-26.6), (-33.6)
$[\mathbf{5.15(Et)}]^{3+}$	(-2.5), (-6.3)
$[\mathbf{5.16}]^{4+}$	$(+66.9)$, $(+42.5)$
$[\mathbf{5.18}]^{1+}$	$(+26.0)$, (-23.9) [224]

5.3.6 Reaction with [5.10(Et)][OTf]$_4$

Neutral *catena*-antimony rings are known to participate in ring-ring equilibria unless bulky substituents or dilute solutions are employed. For instance, solutions of hexaphenylcyclohexastibine (Ph_6Sb_6) equilibrate to give a mixture of four-, five-, and six-membered rings suggesting labile Sb−Sb bonds.[226]

To assess the possibility of preparing heteroleptic derivatives of [**5.10(R)**][OTf]$_4$, pure samples of [**5.10(Me)**][OTf]$_4$and [**5.10(Et)**][OTf]$_4$ were combined in a 1:1 stoichiometry. The $^{31}P\{^1H\}$ NMR spectrum (Figure 5.3.5*c*) of the resulting mixture suggests formation of multiple constitutional isomers of $[(PMe_3)_x(PEt_3)_{(4-x)}Sb_4]^{4+}$, implicating scrambling in the two ring systems *via* Sb−Sb or P−Sb bond cleavage. A scrambling process involving Sb−Sb cleavage has been described previously for distibines.[220] However, a control experiment, where free PEt_3 was added to [**5.10(Me)**][OTf]$_4$, also showed (Figure 5.3.5*d*) formation of these isomers. Therefore a nucleophilic displacement pathway, where a bound PR_3 ligand is displaced by an added ligand, cannot be precluded. Notably this displacement route to heteroleptically substituted derivatives also yields significant amounts of [**5.11(Me)**]$^{2+}$ and elemental antimony, presumably due to free PMe_3 catalyzed decomposition of [**5.10(Me)**][OTf]$_4$ as described earlier. Although it has not yet been possible to purify these reaction mixtures and isolate the first examples of heteroleptically substituted catena-antimony rings, signal multiplicities consistent with AM_2X, A_2X_2, and AA'XX' spin systems are observed, as expected from a mixture of [**5.10(Me)$_3$(Et)**]$^{4+}$, *cis*/*trans*-[**5.10(Me)$_2$(Et)$_2$**]$^{4+}$, and [**5.10(Me)(Et)$_3$**]$^{4+}$ (Scheme 5.3.9). The coupling constants also lie in the $21 - 26$ Hz range and are comparable to $^3J_{PP}$ coupling constants detected in [**5.15(Me)**]$^{3+}$ (32 Hz), [**5.15(Et)**]$^{3+}$ (23 Hz), and [**5.16**]$^{4+}$ (24 Hz). Collectively, these data enable a tentative assignment of the spectral features observed in Figure 5.3.5.

5.4 The Bicyclo[3.1.0]hexastibinotetraphosphonium Tetracation

The four-membered rings discussed in the preceding examples constitute rare examples of main group cationic homocycles. Even more sparse in the chemical literature are

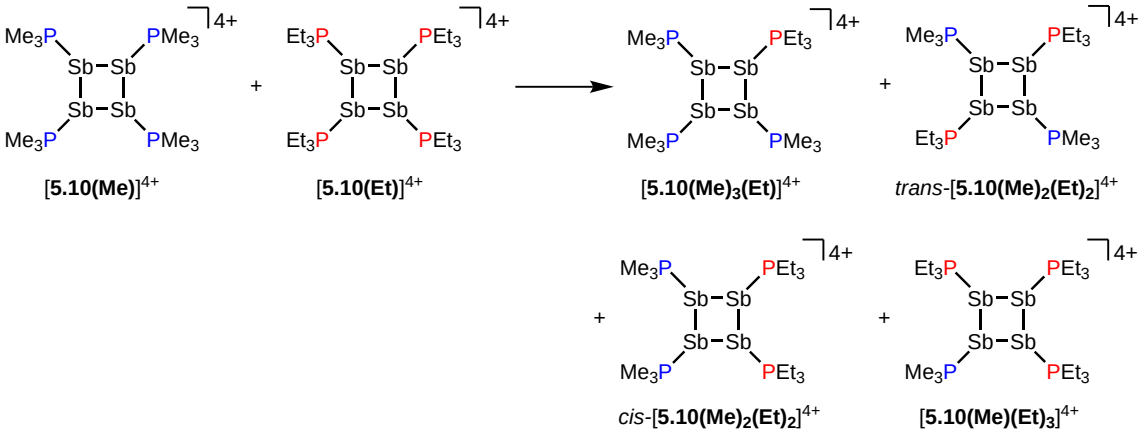

Scheme 5.3.9. Proposed formation of constitutional isomers from the equimolar reaction of $[\mathbf{5.10(Me)}]^{4+}$ and $[\mathbf{5.10(Et)}]^{4+}$.

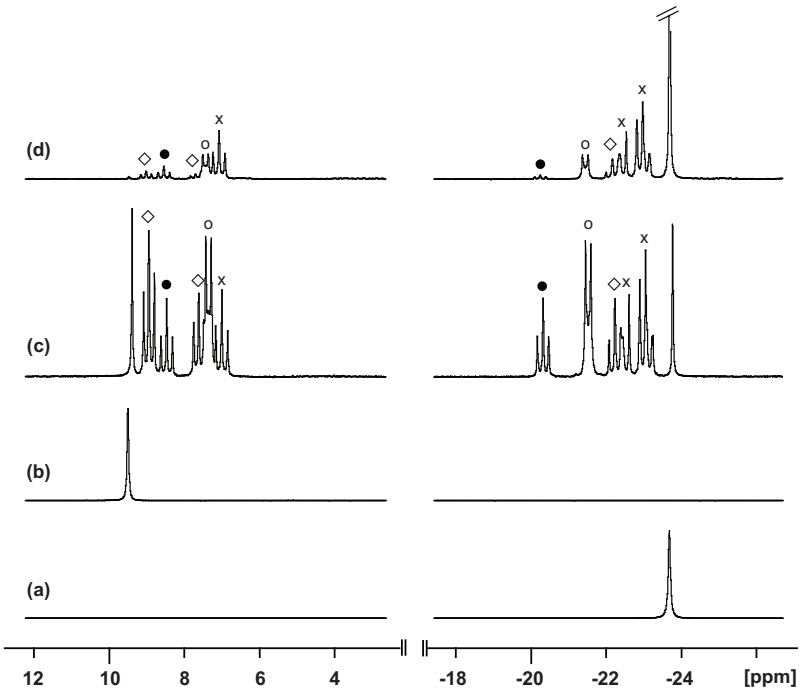

Figure 5.3.5. $^{31}P\{^{1}H\}$ NMR spectra (CD_3CN, 298 K) of a) $[\mathbf{5.10(Me)}]^{4+}$, b) $[\mathbf{5.10(Et)}]^{4+}$, c) 1:1 mixture of $[\mathbf{5.10(Me)}]^{4+}$ and $[\mathbf{5.10(Et)}]^{4+}$, and d) 1:1 mixture of $[\mathbf{5.10(Me)}]^{4+}$ and PEt_3. Symbols denote tentative assignments for $[\mathbf{5.10(Me)_3(Et)}]^{4+}$ (x), *cis*-$[\mathbf{5.10(Me)_2(Et)_2}]^{4+}$ (○), *trans*-$[\mathbf{5.10(Me)_2(Et)_2}]^{4+}$ (•), and $[\mathbf{5.10(Me)(Et)_3}]^{4+}$ (◇).

main group polycycles, as represented by the title compound. Polycycles are a basic elemental architecture that, in the case of antimony, is only known in neutral[220,223] or anionic derivatives[227,228] (Scheme 5.4.1) and therefore, the discovery of a cationic *catena*-antimony bicycle reveals a new intersection of structural complexity and electronic properties for this element.

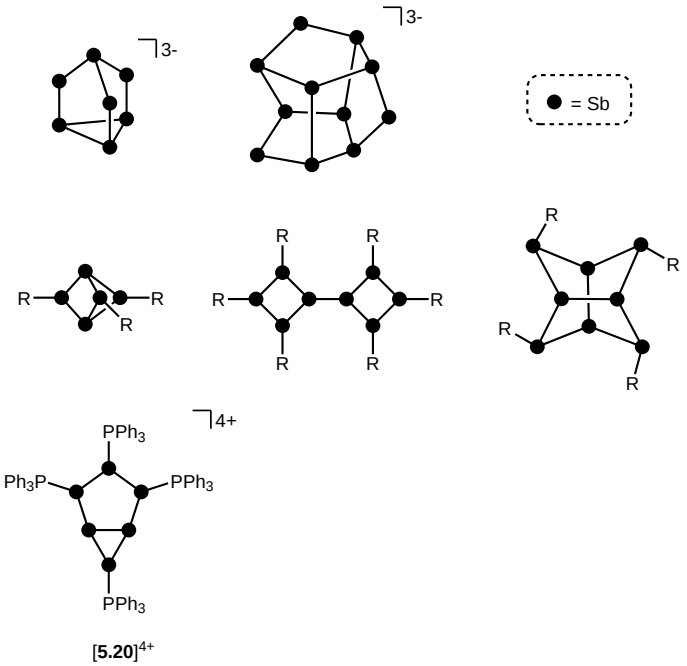

Scheme 5.4.1. Known anionic and neutral *catena*-antimony polycycles and the novel $[\mathbf{5.20}]^{4+}$ bicycle.

The reaction of $FSb(OTf)_2$ with PPh_3 was studied and a ^{31}P NMR spectrum of a 1:2 mixture in MeCN (yellow solution) initially shows a broad peak centred at +28 ppm, assigned to $[(Ph_3P)_2SbF]^{2+}$, $[\mathbf{5.7(Ph)}]^{2+}$ (Figure 5.4.1*a*). The corresponding peak in the ^{19}F NMR spectrum appears at −117.5 ppm, indicating a significantly deshielded fluorine centre compared to trialkylphosphine derivatives of $[\mathbf{5.7(R)}]^{2+}$ (R = Me, Et, Pr, Bu; $\delta = -173.4$ to −187.1 ppm) due to the poor donor ability of the weaker triarylphosphine ligand, which leaves significant residual positive charge at antimony. For comparison, the *mono*-phosphine derivative, $[(Ph_3P)SbF][OTf]_2$, was also prepared *in situ* from an equimolar mixture of $FSb(OTf)_2$ and PPh_3, and its ^{31}P and ^{19}F NMR resonances (+30.2 and −102 ppm, respectively) were both found to be even further deshielded relative to derivatives of $[\mathbf{5.7(R)}]^{2+}$. These findings are consistent with trends in relative chemical shifts for *mono*- and *bis*-phosphine

complexes of the same acceptor detailed in Chapter 3.

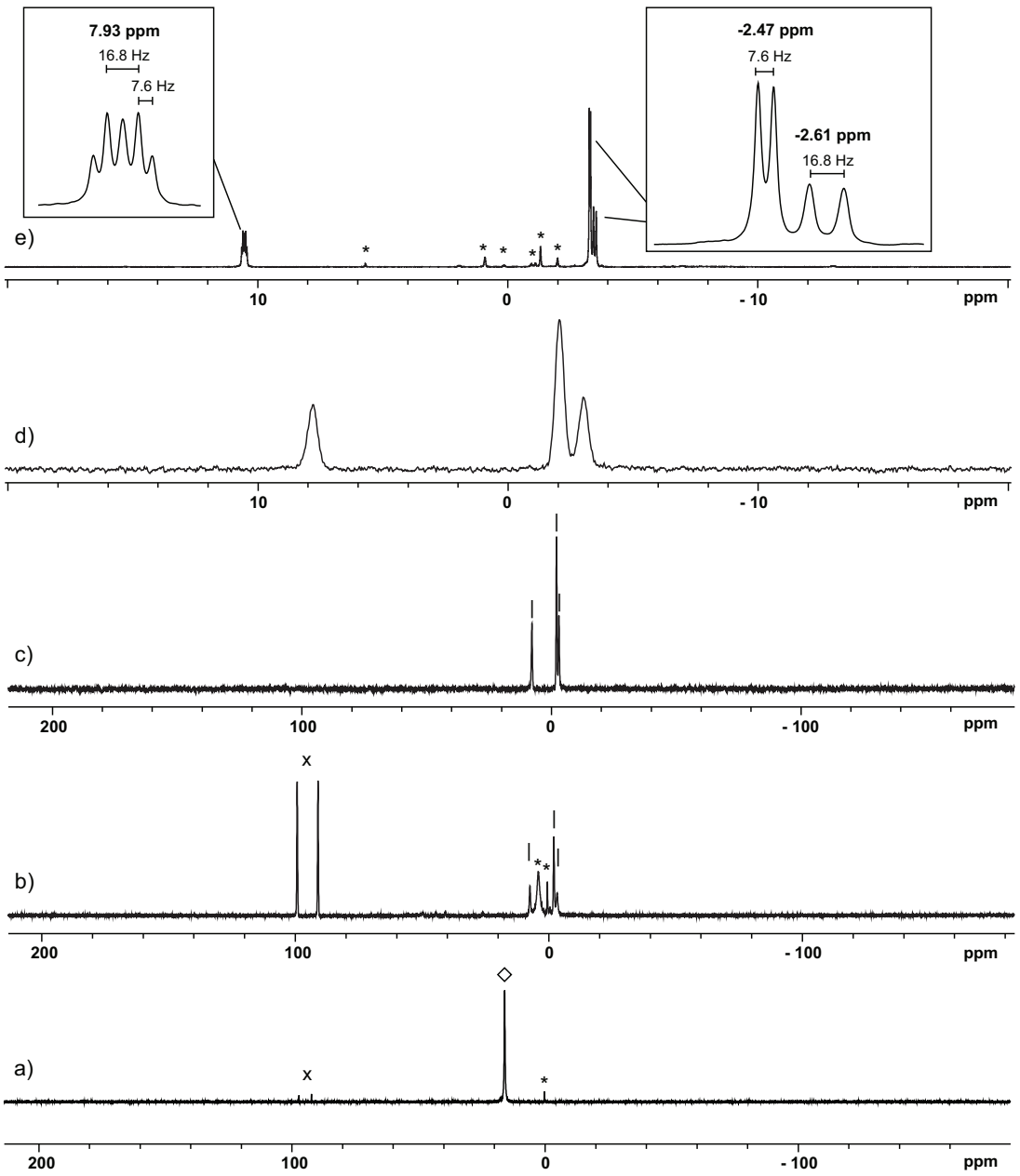

Figure 5.4.1. $^{31}P\{^{1}H\}$ NMR spectrum (CD_3CN, 298 K unless otherwise specified) of *a*) the 1:2 reaction mixture of $FSb(OTf)_2$ and PPh_3 immediately upon mixing, *b*) upon heating to 80 °C for 90 minutes, *c*) purified $[\mathbf{5.20}]^{4+}$ following workup of the reaction mixture, *d*) purified $[\mathbf{5.20}]^{4+}$ showing detail at 298 K, and *e*) showing detail upon cooling to 248 K. Insets show fine structure for indicated resonances. Symbols denote $[\mathbf{5.7(Ph)}]^{2+}$ ($\diamond$) $[\mathbf{5.12(Ph)}]^{1+}$ ($\times$), $[\mathbf{5.20}]^{4+}$ (|), and unidentified products (*).

The ^{31}P NMR spectrum of the 1:2 reaction mixture after refluxing for 3 hours is

shown in Figure 5.4.1*b*. The signal due to [**5.7(Ph)**]$^{2+}$ disappears and an intensely orange solution is obtained, which shows the unambiguous presence of $[Ph_3PF]^{1+}$, [**5.12(Ph)**]$^{1+}$, by ^{31}P NMR as a characteristic doublet at +94.7 ppm ($^1J_{PF}$ = 995 Hz) and by ^{19}F NMR as a doublet at −128.7 ppm ($^1J_{PF}$ = 994 Hz). [§] One of the broad signals in the ^{31}P NMR may be due to $[Ph_3PPPh_3]^{2+}$, [**5.11(Ph)**]$^{2+}$, but the chemical shift for this species has not been definitively assigned. Finally, three broad resonances are observed in a 1:2:1 ratio and assigned to the novel bicyclo[3.1.0]hexastibinotetraphosphonium tetracation, $[(Ph_3P)_4Sb_6][OTf]_4$, [**5.20**][OTf]$_4$, the identity of which was established by X-Ray crystallography and elemental analysis.

The molecular structure of [**5.20**][OTf]$_4$ (Figure 5.4.2) shows a chair conformation for the *catena*-antimony framework with phosphine ligands at the formally cationic antimony centres. The Sb−Sb distances in the ring [2.8200(3)−2.8642(2) Å] are typical for a single bond and comparable to those found in cations $[(R_3P)_4Sb_4]^{4+}$ as well as those in neutral derivatives Ar_6Sb_6 [Ar = *o*-tolyl, 2.818(1)−2.836(1) Å; *m*-tolyl = 2.828(1)−2.834(1) Å],[226] indicating substantial delocalization of the cationic charge over the phosphonium ligands. The P-Sb lengths, however, are slightly longer [2.5875(7)−2.6254(7) Å] than in derivatives of $[(R_3P)_4Sb_4]^{4+}$ [2.552(2)−2.578(2) Å for R = Me, Et] due to the lower basicity and greater steric bulk of PPh_3 compared to PMe_3 or PEt_3. The bridging Sb2−Sb3 distance [2.8200(3) Å] is substantially shorter than the transannular distance between Sb4-Sb6 [4.0444(7) Å], resulting in more acute bond angles around the bridgehead antimony atoms [Σ_{Sb2} = 208.6°, Σ_{Sb3} = 194.4°] than at non-bridging ones [Σ_{Sb5} = 279.5°]. The distortion induced by the bridging interactions results in a C_s point group for the antimony skeleton, which is a reduction of symmetry from an idealized D_{3d} point group observed in cyclohexane (chair conformer). Interion Sb−O contacts are observed in the 2.887(6)−3.335(3) Å range, consistent with the high molecular charge, but these are significantly longer than the sum of the covalent radii for the two elements ($\Sigma_{r,cov}$ = 2.05 Å).[127]

The ^{31}P NMR spectrum of [**5.12(Ph)**]$^{4+}$ shows broad resonances at room temperature (Figure 5.4.1*d*), which narrow upon cooling to 248 K (Figure 5.4.1*e*). The signal at −2.47 ppm can be assigned straightforwardly on the basis of its intensity to P2/P4 and appears as a doublet (7.6 Hz). Assignment of the remaining two signals cannot

[§]This assignment was further confirmed by an independent synthesis of [Ph$_3$PF][OTf] from an equimolar mixture of PPh_3, XeF_2, and TMSOTf.

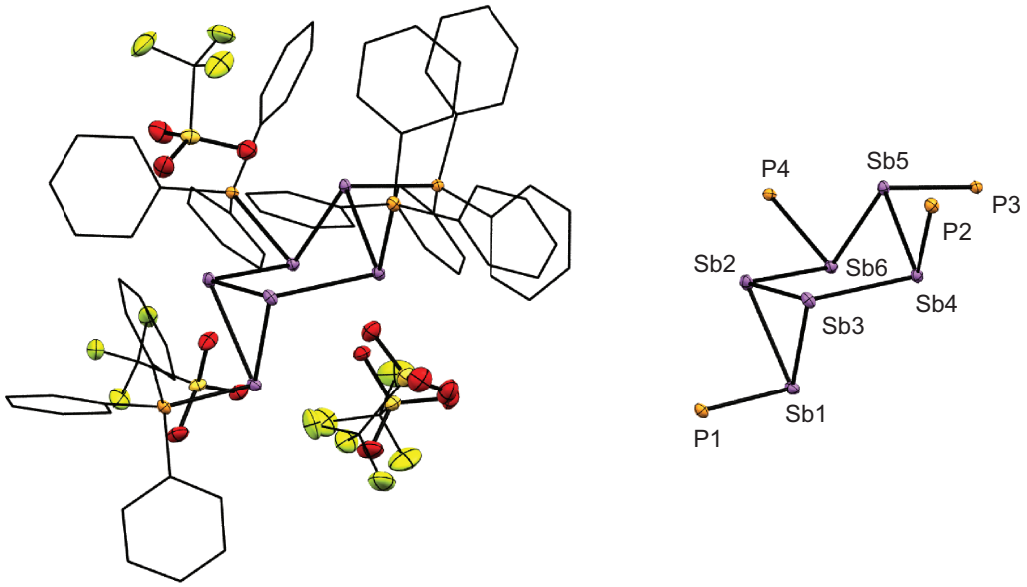

Figure 5.4.2. Left: Molecular structure of [**5.20**][OTf]$_4$•(MeCN)$_2$•(EtCN)$_2$ in the solid state. Solvent molecules and hydrogen atoms have been omitted for clarity. Right: Bicyclic core of the [**5.20**]$^{4+}$ cation with exocyclic P atoms. All other atoms have been omitted for clarity. Key bond lengths (Å) and angles (°) are as follows: Sb1−Sb2 = 2.8289(3), Sb1−Sb3 = 2.8479(5), Sb2−Sb3 = 2.8200(3), Sb3−Sb4 = 2.8310(3), Sb4−Sb5 = 2.8642(2), Sb5−Sb6 = 2.8598(3), Sb6−Sb2 = 2.8443(5), Sb4−Sb6 = 4.0444(7), P1−Sb1 = 2.5875(7), P2−Sb4 = 2.6254(7), P3−Sb5 = 2.6049(7), P4−Sb6 = 2.6377(7), Sb1−O8 = 3.335(3), Sb1−O7 = 2.960(2), Sb4−O7 = 2.928(2), Sb4−O11A/B = 2.98(3), 2.887(6), Sb5−O4 = 3.036(2), Sb6−O7 = 3.0422(18), Sb6−O1 = 3.035(3),Sb1−Sb2−Sb3 = 60.551(13), Sb2−Sb1−Sb3 = 59.568(13), Sb2−Sb3−Sb1 = 59.880(13), Sb1−Sb2−Sb6 = 88.043(12), Sb2−Sb6−Sb5 = 89.727(15), Sb6−Sb5−Sb4 = 89.912(13), Sb5−Sb4−Sb3 = 94.082(15), Sb4−Sb3−Sb1 = 94.901(14), P1−Sb1−Sb2 = 87.253(17), P2−Sb4−Sb5 = 91.304(18), P2−Sb4−Sb3 = 91.96(2), P3−Sb5−Sb4 = 93.606(18), P3−Sb5−Sb6 = 94.97(2), P4−Sb6−Sb5 = 96.24(2), P4−Sb6−Sb2 = 91.679(19).

be made definitively without assuming the presence of additional unresolved coupling. For example, assignment of the signal at +7.93 ppm to P1 would suggest detection of $^{4}J_{\mathrm{PP}}$ and $^{5}J_{\mathrm{PP}}$ couplings (to P2/P4 and P3, respectively), but no $^{3}J_{\mathrm{PP}}$ coupling between P2/4 and P3. On the other hand, assignment of the signal at −2.61 ppm to P1 implies detection of a $^{5}J_{\mathrm{PP}}$ coupling between P1 and P3 but no $^{4}J_{\mathrm{PP}}$ coupling between P1 and P2/P4. Detection of long range coupling spanning $6-10$ bonds through rigid ring systems is known for phosphorus compounds[229] and absence of short range coupling in the presence of long range coupling is typically due to dihedral angle dependence of coupling constants (Karplus relationship). However, Karplus curves for coupling between a P−Sb−Sb−P arrangement are unknown and there are no examples in the literature of a comparable framework where such couplings might be possible due to non-equivalent phosphorus centres. Low temperature measurements in other solvents such as CH_2Cl_2 and EtCN were also performed but failed to reveal additional coupling. Attempts to conduct measurements at temperatures lower than 248 K were frustrated by precipitation of the salt from solution and loss of signal. A solid-state NMR experiment has not yet been attempted.

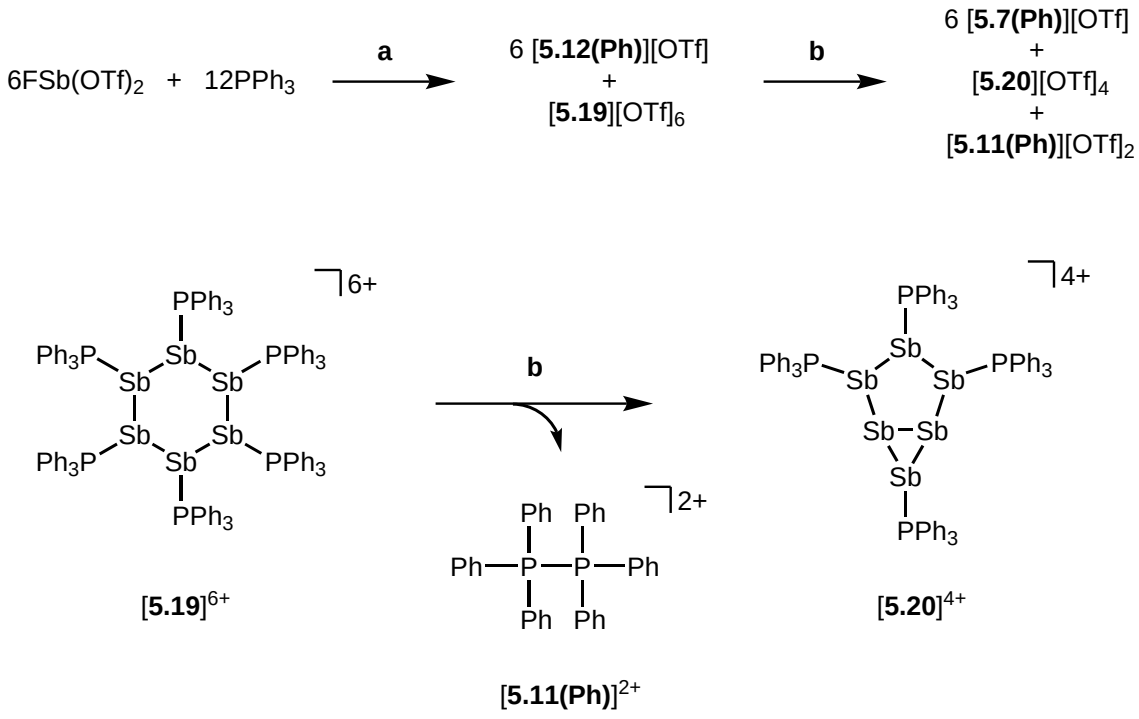

Scheme 5.4.2. Formation of $[\mathbf{5.20}][\mathrm{OTf}]_4$ from the reaction of $\mathrm{FSb(OTf)_2}$ and $\mathrm{PPh_3}$.

Formation of cation $[\mathbf{5.20}]^{4+}$ is understood as involving a two-step process outlined

in Scheme 5.4.2. The intermediate proposed to result from 5.4.2*a*, $[(Ph_3P)_6Sb_6][OTf]_6$, [**5.19**][OTf]$_6$, is likely formed by a 12-electron reductive assembly akin to the 8-electron reduction proposed for the formation of cations $[(R_3P)_4Sb_4]^{4+}$ (see Scheme 5.1.2) but could not be detected spectroscopically or isolated. The inability to observe this species suggests a short lifetime and rapid conversion of the hexacation to the tetracation, consistent with [**5.19**]$^{6+}$ being a powerful oxidizer due to its formidable molecular charge. While relief of this coulombic instability in the hexacation by a 2-electron reductive elimination of [**5.11(Ph)**]$^{2+}$ (Scheme 5.4.2*b*) is a parsimonious explanation for the observed final products, and consistent with the reactivity observed for very electron deficient P-Sb complexes (Chapter 5), it has not yet been possible to isolate and definitively characterize [**5.11(Ph)**][OTf]$_2$ as a product from this reaction mixture.

Several attempts were made to prepare [**5.11(Ph)**]$^{2+}$ independently and obtain its ^{31}P NMR spectrum. First, a halide abstraction/coordination strategy was employed, analogous to the synthesis of $[(dmap)PMe_3]^{2+}$ from equimolar mixtures of $[Me_3PCl]^{1+}$, TMSOTf and *dmap*. Thus, equimolar mixtures of the fluorophosphonium salt, [**5.12(Ph)**][OTf], TMSOTf, and PPh_3 were assessed by ^{31}P and ^{19}F NMR spectroscopy, but under all applied conditions, including reflux in neat TMSOTf, no reaction was observed. Similarly, refluxing a 1:1 mixture of Ph_3PO and PPh_3 under various conditions including in neat TMSOTf failed to induce the expected deoxygenation (in the form of TMS−O−TMS) and P−P coupling to give [**5.11(Ph)**]$^{2+}$. Presumably, in both cases, the lower basicity and greater steric bulk of the triarylphosphine hamper the P−P coordination required to weaken and break the P−F or P−O bond in [**5.12(Ph)**]$^{1+}$ or Ph_3PO, even when the powerful fluoro- and oxoacidic reagent TMSOTf is present as a solvent. The second strategy involved using a strong oxidizer to oxidatively couple two equivalents of PPh_3. The Sb^{V} compound $Ph_3Sb(OTf)_2$ was chosen as the oxidizer following reports that it readily couples trialkylphosphines to give derivatives of [**5.11(R)**][OTf]$_2$.[79] However, only $[Ph_3POPPh_3]^{2+}$ could be isolated from the 1:2 reaction of $Ph_3Sb(OTf)_2$ and PPh_3, indicating anion activation. Finally, attempts to phenylate $Ph_2P{-}PPh_2$ with PhOTf were also unsuccessful.

The 1:3 reaction of $Sb(OTf)_3$ and PPh_3 was also assessed by ^{31}P NMR and initially shows evidence of the *tris*-phosphine complex $[(Ph_3P)_3Sb]^{3+}$, [**5.8(Ph)**]$^{3+}$, as a very broad peak centred at +12.6 ppm (Figure 5.4.3*a*). After 16 hours at

room temperature, the yellow reaction mixture turns orange showing a multitude of products (Figure 5.4.3*b*). Crucially, a small amount of $[\mathbf{5.20}]^{4+}$ is also observed in the ^{31}P NMR spectrum of the reaction mixture along with broad peaks in the same region as observed previously. There is no evidence of the fluorophosphonium $[\mathbf{5.12(Ph)}]^{1+}$ indicating that formation of $[\mathbf{5.20}]^{4+}$ is not due to the unintentional presence of $FSb(OTf)_2$ as an impurity in the sample of $Sb(OTf)_3$ employed. These results are consistent with formation of $[\mathbf{5.20}][OTf]_4$ from both $FSb(OTf)_2$ as well as $Sb(OTf)_3$, and strongly reminiscent of results obtained for trialkylphosphines, where the same reduction products, cations $[(R_3P)_4Sb_4]^{4+}$, are obtained but the observed oxidation products, either $[\mathbf{5.11(R)}]^{2+}$ or $[\mathbf{5.12(R)}]^{1+}$, depend upon the choice of antimony precursor employed. The main difference in the case of PPh_3 is that the reaction involving $Sb(OTf)_3$ shows poor selectivity and a number of competing reaction pathways exist such that $[\mathbf{5.20}][OTf]_4$ is only formed in trace amounts.

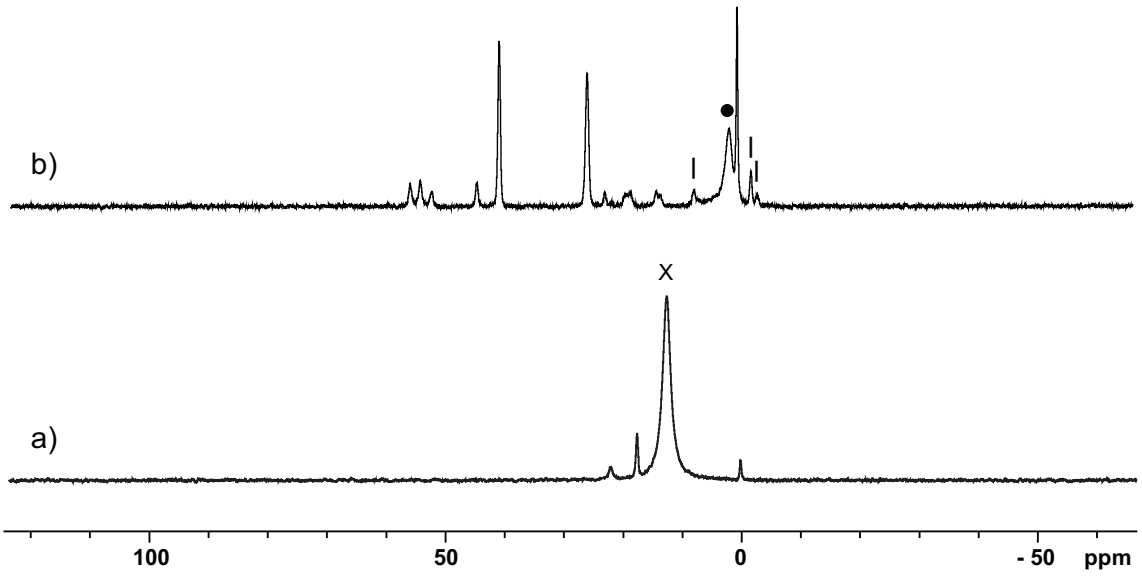

Figure 5.4.3. ^{31}P NMR spectrum (CD_3CN, 298 K) of *a*) the 1:3 reaction mixture of $Sb(OTf)_3$ and PPh_3 immediately upon mixing, *b*) after 16 hours at room temperature. Symbols denote $[\mathbf{5.8(Ph)}]^{3+}$ (×), and $[\mathbf{5.20}]^{4+}$ (|). No signals corresponding to $[\mathbf{5.12(Ph)}]^{1+}$ are observed ($\delta^{31}P = +94.7$ ppm).

In summary, attempts to generate PPh_3 derivatives of cations $[(R_3P)_4Sb_4]^{4+}$ yielded the first cationic bicycle for antimony, $[\mathbf{5.20}]^{4+}$, which is understood as being the result of an unprecedented 14-electron reductive coupling *via* a postulated hexacationic intermediate, $[\mathbf{5.19}]^{6+}$. Of the two proposed oxidation products, the fluorophosphonium

[**5.12(Ph)**]$^{1+}$ and diphosphonium [**5.11(Ph)**]$^{2+}$, only the former could be definitively characterized whereas numerous attempts to isolate or independently prepare the latter were unsuccessful. The precise reason behind the formation of a more extensively catenated framework when PPh_3 is employed compared to when trialkylphosphines are employed, remains to be studied.

5.5 Phosphino-fluorophosphonium Cations

Reductive coupling of P-chlorine functionalized phosphino-chlorophosphonium cations, $[R_2ClPPR_2]^{1+}$, by dehalogenation has been demonstrated previously as a means of achieving highly catenated polyphosphorus compounds.[52,78] With an eye towards accessing P-chlorine functionalized derivatives, $[(R_2ClP)_4Sb_4][OTf]_4$, reactions of $FSb(OTf)_2$ with a range of chlorophosphines R_2PCl were attempted. These reactions, however, did not yield the desired salts, but rather species formulated as phosphino-fluorophosphonium cations, $[R_2(F)PPR_2]^{1+}$, [**5.21(R)**]$^{1+}$ (R = Me, Ph, Mes, Tol, Cy, and ^{i}Pr), as the only phosphorus containing product, presumably following chloride/fluoride substituent exchange (equations 5.1 and 5.2). In all but the most sterically-encumbered cases (R = Mes, Cy), the cations are unstable in solution and undergo decomposition to difluorophosphoranes, R_3PF_2, and other fluorinated phosphines over 24 hours. Although, it was not possible to isolate salts of even the stable derivatives of these cations from the reaction mixture, their identity is strongly supported by the detection of all of the expected spin systems and coupling constants in the solution NMR spectra for all derivatives (Table 5.5.1, Figure 5.5.1).

$$2\,R_2PCl + FSb(OTf)_2 \longrightarrow [R_2(Cl)PPR_2][OTf] + FSbCl(OTf) \qquad (5.1)$$

$$[R_2(Cl)PPR_2][OTf] + FSbCl(OTf) \longrightarrow [R_2(F)PPR_2][OTf] + Cl_2Sb(OTf) \qquad (5.2)$$

Phosphinofluorophosphonium cations have not been prepared to-date due to the difficulty of handling fluorophosphines, which tend to be volatile and exhibit low basicity. Moreover small alkyl or aryl fluorophosphines spontaneously disproportionate into diphosphines and difluorophosphoranes (equation 5.3).[230] Accessing phosphinofluorophosphine cations therefore depends upon pre-assembly of the P−P bond in the form of phosphinochlorophosphonium cations, which are known and stable

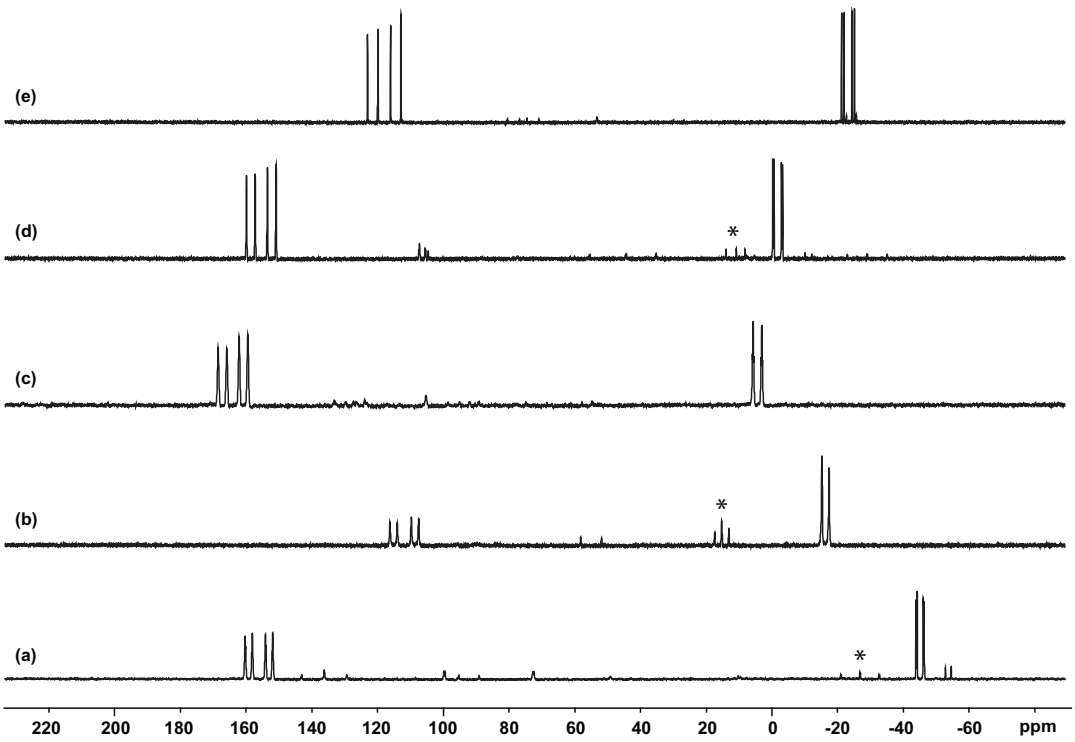

Figure 5.5.1. ^{31}P NMR spectra of crude reactions mixtures containing cations *a)* [**5.21(Me)**]$^{1+}$, b) [**5.21(Ph)**]$^{1+}$, *c)* [**5.21(Mes)**]$^{1+}$, *d)* [**5.21(Tol)**]$^{1+}$, *e)* [**5.21(Cy)**]$^{1+}$, and *f)* [**5.21(**^{i}**Pr)**]$^{1+}$. Asterisks denote signals due to $[R_2PF_2]^{1+}$.

Table 5.5.1. ^{31}P and ^{19}F NMR data for derivatives of [**5.21(R)**]$^{1+}$.

	δ ^{31}**P**		δ ^{19}**F**	$^{1}\boldsymbol{J}_{\mathbf{PP}}$	$^{1}\boldsymbol{J}_{\mathbf{PF}}$	$^{2}\boldsymbol{J}_{\mathbf{PF}}$	$^{3}\boldsymbol{J}_{\mathbf{FH}}$
R	$R_2(F)P$	PR_2					
Me	−45.8	−161.1	−153.5	356.5	1032.9	49.9	13.9
Ph	−15.8	+114.9	−146.1	373.9	1095.8	70.3	n.a.
Mes	−25.4	+114.9	−103.6	523.6	1175.8	125.7	n.a.
Tol	−18.5	+113.2	−143.4	377.1	1084.3	56.9	n.a.
Cy	−3.6	+157.9	−165.2	438.7	1059.3	55.8	6.9
^{i}Pr	+2.8	+166.6	−165.8	438.7	1060.8	48.4	7.5

species, followed by halide exchange. The reaction mixtures solidify into a gelatinous mass over several days when CH_2Cl_2 or MeCN are used as solvents posing a barrier to isolation. Nevertheless, stabilization of fluorophosphines in the form of precursor cations $[\mathbf{5.21(R)}]^{1+}$ may prove valuable in the context of their transition metal coordination chemistry. Addition of a transition metal fluoride (MF) to solutions of phosphinofluorophosphonium cations may lead to trapping of the *in situ* generated fluorophosphines as ligands in the coordination sphere of the metal (equation 5.4), thereby enabling access to this potentially interesting family of poor σ-donating ligands, whose conspicuous absence in the literature has recently been highlighted.[230]

$$3\,R_2PF \longrightarrow R_2PPR_2 + R_2PF_3 \tag{5.3}$$

$$[R_2(F)PPR_2]^{1+} + MF \longrightarrow [M(P(F)R_2)_2] \tag{5.4}$$

5.6 Summary

The reductive elimination of fluorophosphonium monocations $[\mathbf{5.12(R)}]^{1+}$ and diphosphonium dications $[\mathbf{5.11(R)}]^{2+}$ from trialkylphosphine complexes of highly electrophilic antimony(III) centres has been discovered. The reduced antimony(I) fragments cyclize into frameworks identified as the unique *cyclo*-tetra(stibinophosphonium) tetracations, $[\mathbf{5.10(R)}]^{4+}$. As outlined in Scheme 5.1.2, a phosphine catalyzed mechanism is proposed for fluoroantimony complexes, and isolation or spectroscopic characterization of key mechanistic intermediates is presented. The scope of this reductive assembly is dependent upon the steric bulk of the phosphine employed as demonstrated by non-productive reactions involving P^iPr_3. Formation of cyclic $(R\text{-}Pn)_n$ or $[L\text{-}Pn]_n{}^{(n+)}$ species (R = aryl group, L = alkylphosphine ligand, E = heavy pnictogen) appears to be the general fate of low-valent (R-Pn) or $[L{-}Pn]^{1+}$ monomers, respectively. A multi-gram scale synthesis for the triflate salt of a prototypical *cyclo*-tetra(stibinophosphonium) tetracation, $[\mathbf{5.10(Me)}][OTf]_4$, has enabled reactivity studies that are summarized in Scheme 5.6.1.

The reactivity of *catena*-antimony(I) tetracation $[\mathbf{5.10(Me)}]^{4+}$ is directed by two features: *i)* high charge concentration, and *ii)* the presence of strongly polarized P−Sb bonds. The former explains the electrophilicity of cation $[\mathbf{5.10(Me)}]^{4+}$, its thermolysis to extrude $[\mathbf{5.11(Me)}]^{2+}$, and the observed facility for reductive elimination to yield

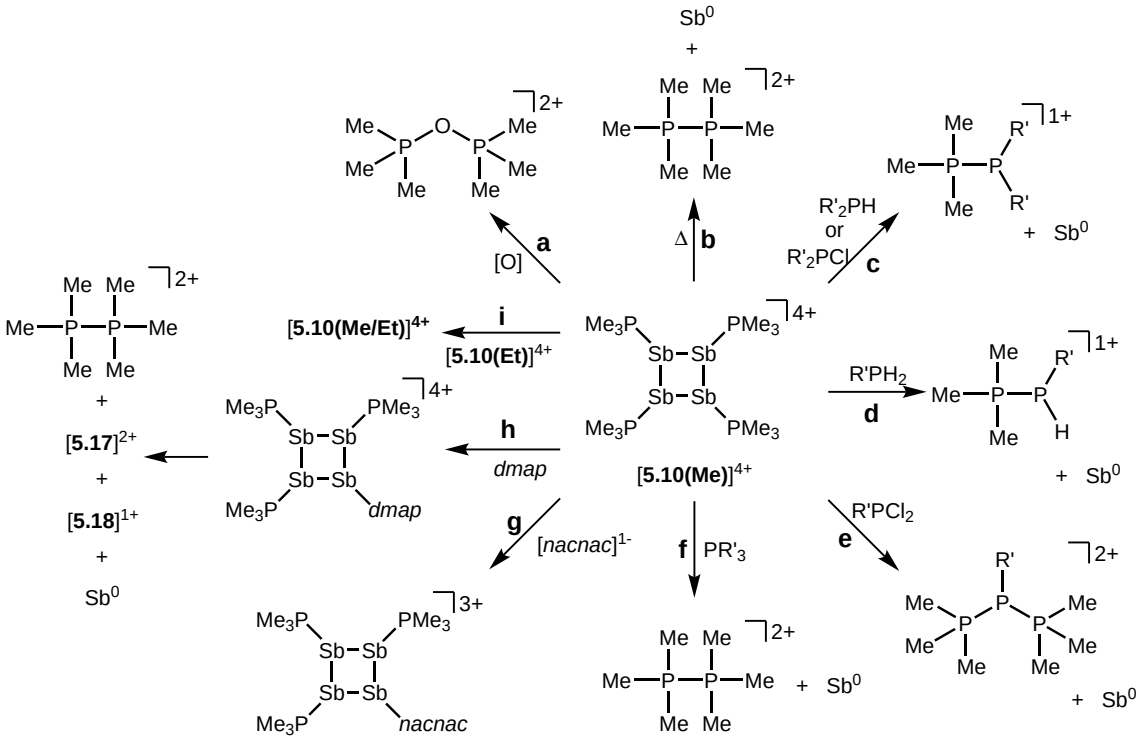

Scheme 5.6.1. Reactivity of a prototypical *cyclo*-tetra(stibinophosphonium) tetracation, [**5.10(Me)**]$^{4+}$. See text for descriptions of **a-i**.

elemental antimony (Scheme 5.6.1, reactions **a-f**). The significant polarization of the P−Sb bonds enables activation of a wide spectrum of bonds with the unusual outcome of yielding the same products *via* reaction with oppositely polarized substrates (*e.g.* P−Cl and P−H containing reagents) (Scheme 5.6.1, reactions **c-f**). This unique feature has led to the spectroscopic detection of the an *H*-phosphino-phosphonium cation, $[Me_3PP(H)Cy]^{1+}$, examples of which have not been reported previously. The high P−Sb bond polarization also supports a coordinate bonding model, consistent with ligand displacement reactivity demonstrated for cation $[\mathbf{5.10(Me)}]^{4+}$ (Scheme 5.6.1, reactions **g-i**). Ligand displacement has permitted functionalization of the four-membered Sb ring with substituents such as $[nacnac]^{1-}$ or *dmap* (transiently). A heteroleptic phosphine substitution pattern around the Sb_4 is feasible, but multiple isomers are observed on a relatively shallow potential energy surface hindering the isolation of a single derivative.

Attempts to generate triarylphosphine derivatives of cations $[\mathbf{5.10(R)}]^{4+}$ yielded the first cationic bicycle for antimony, $[\mathbf{5.20(Ph)}]^{4+}$, from an unprecedented 14-electron reductive coupling *via* a postulated hexacationic intermediate, $[\mathbf{5.19}]^{6+}$. Of the two proposed oxidation products, the fluorophosphonium $[\mathbf{5.12(Ph)}]^{1+}$ and diphosphonium $[\mathbf{5.11(Ph)}]^{2+}$, only the former could be definitively characterized. The unexpected discovery of a new class of phosphinophosphonium cations, $[\mathbf{5.21}]^{1+}$, featuring fluorophosphines as donors for the first time is described together with spectroscopic data for seven derivatives.

Within the broader context of phosphines as ubiquitous ligands in coordination chemistry, evidence of a novel ligand activation pathway has been presented and the associated reactants and products characterized. Taken together with previous, albeit less definitive, detection of such reactivity,[79,198] the observation of this reductive elimination (metal-centred) or oxidative coupling (ligand-centred) pathway confirms that these prototypical ligands can behave simultaneously as reducing agents and stabilizing ligands, a feature that may be generally applicable for phosphine complexes of highly electrophilic acceptors across the periodic table. Diversification of this synthetic protocol may therefore provide access to more heavily catenated systems for antimony as well as other elements. As demonstrated for $[\mathbf{5.10(Me)}]^{4+}$, a unique and rich reaction chemistry can be expected, in addition to the potential for valuable emergent properties such as σ-bond conjugation and cooperative catalysis.

Chapter 6

Coordination Complexes of $E(OTf)_3$, E = P, As, Sb, Bi

As noted in Chapter 1, few *tris*-phosphine complexes are known for main group acceptors, examples being limited to thallium, indium, gallium and antimony.[231] The tripodal ligation mode of *bis*(diphenylphosphinoethyl)phenylphosphine, *triphos*, is ideally suited for expanding the known range of *tris*-phosphine complexes in the *p*-block. To generate a series of such complexes the reaction of this tridentate ligand with $E(OTf)_3$ (E = P, As, Sb, Bi) was attempted. Whereas $Sb(OTf)_3$ and $Bi(OTf)_3$ are readily accessible, the phosphorus and arsenic triflates are unknown as isolated compounds. Complexes [(*triphos*)$E(OTf)_3$] (E = Sb, Bi) could be successfully prepared and structurally characterized. Attempts to generate the lighter congeners from mixtures of ECl_3, halide abstractor and *triphos* were frustrated by the hitherto unreported intramolecular redox chemistry of *triphos*. This novel reactivity gave access to cations featuring both reduced P^I or As^I centres and P^V halophosphonium centres within the same molecule.

To circumvent the formation of halophosphonium cations, access to a source of pre-made $E(OTf)_3$ (E = P, As) was sought and successfully achieved in the form of the bipyridine derivatives $[(bipy)_2P][OTf]_3$ and $[(tbbipy)_2As][OTf]_3$ (*tbbipy* = 4,4'-^{t}Bu$_2$-2,2'-*bipy*). The reactivity of the phosphorus derivative was studied towards a variety of substrates. With these $E(OTf)_3$-equivalents, a ligand substitution reaction between excess *triphos* and the $[(bipy)_2P]^{3+}$ cation (as its triflate salt) was attempted to yield the *tris*-phosphine complex $[(triphos)P]^{3+}$. However, this reaction failed to

yield the desired product, the reaction outcome, once again, being determined by a redox process.

6.1 Synthesis and Structures of [(*triphos*)E(OTf)$_3$] E = Sb, Bi

The antimony derivative of the title compound could be prepared and isolated nearly quantitatively from the equimolar reaction mixture of *triphos* and Sb(OTf)$_3$ in CH_2Cl_2. A ^{31}P NMR assay of the reaction mixture shows two signals in a 1:2 ratio that are shifted nearly 40 ppm downfield of the free ligand. Crystals were obtained from a concentrated solution and the salt has been comprehensively characterized. The analogous reaction with Bi(OTf)$_3$ in MeCN shows two products in a 80:20 ratio and the major component could be separated by fractional crystallization and identified as [(*triphos*)Bi(OTf)$_3$] by X-ray crystallography. The ^{31}P NMR spectrum of this salt exhibits a much greater downfield shift of nearly 80 ppm with respect to the free ligand.

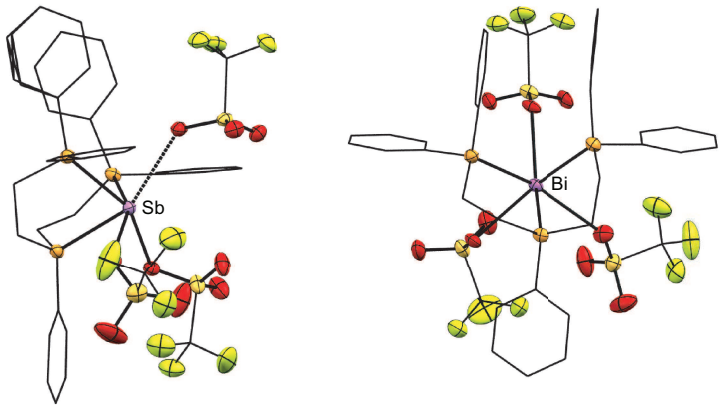

Figure 6.1.1. Molecular structure of [(*triphos*)Sb(OTf)$_3$] (left) and [(*triphos*)Bi(OTf)$_3$] in the solid state. Solvent molecules and hydrogen atoms have been omitted for clarity.

The solid-state structure of both complexes are given in Figure 6.1.1 and confirm the proposed tridentate binding mode. Short triflate contacts impose a six-coordinate geometry in each case and the length of these contacts is significantly shorter than the sum of the van der Waals radii for the elements involved. Both compounds are extremely moisture sensitive and crystals decompose within minutes of exposure to

ambient atmosphere. For antimony, the only *tris*-phosphine complex in the literature is the metastable $[(Me_3P)_3Sb]^{3+}$ cation while for bismuth no *tris*-phosphine complexes have been reported.

6.1.1 Reactions of *triphos* with ECl_3 (E = P, As) and AgOTf

Addition of *triphos* to a 1:2 mixture of PCl_3 and AgOTf yields a white suspension. Upon stirring for 2 hours, filtration of AgCl, and removal of volatiles, a white powder is obtained and spectroscopically identified as $[(triphos{-}Cl)P][OTf]_2$. The ^{31}P NMR spectrum of this compound shows a highly shielded triplet at −249.6 ppm, consistent with the established body of NMR data for cyclic triphosphenium cations. The remaining signals confirm the connectivity by displaying all the expected coupling constants (Figure 6.1.2). When excess AgOTf is employed, the same redox chemistry is observed, in addition to which coordination of the P^I centre to the silver cation is observed as a significant downfield shift for its resonance to *ca.* −150 ppm.

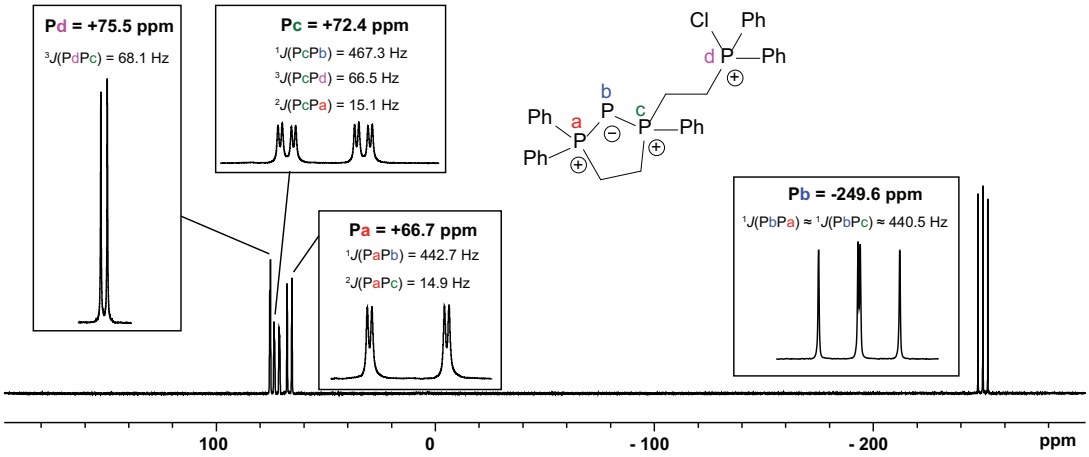

Figure 6.1.2. ^{31}P NMR spectrum (CD_2Cl_2, 298 K) of $[(triphos{-}Cl)P][OTf]_2$. Insets show fine structure, chemical shifts and coupling constants for the various phosphorus environments.

The proposed mechanism for the formation of $[(triphos{-}Cl)P][OTf]_2$ is given in Scheme 6.1.1. Stepwise halide abstraction and coordination is thought to produce cations $[(triphos)PCl_2]^{1+}$ and $[(triphos)PCl]^{2+}$, analogous to established halide abstraction/phosphine coordination chemistry for interpnictogen cations. Removal of the third chlorine as a chloronium cation is more favourable than as a chloride anion, presumably due to the high charge concentration within the P−P(Cl)−P framework

of the dication. An alternative, though not mutually exclusive, explanation is that elimination of chloronium is favoured because the *tris*-phosphine coordination resulting from chloride elimination may produce excessive steric clash.

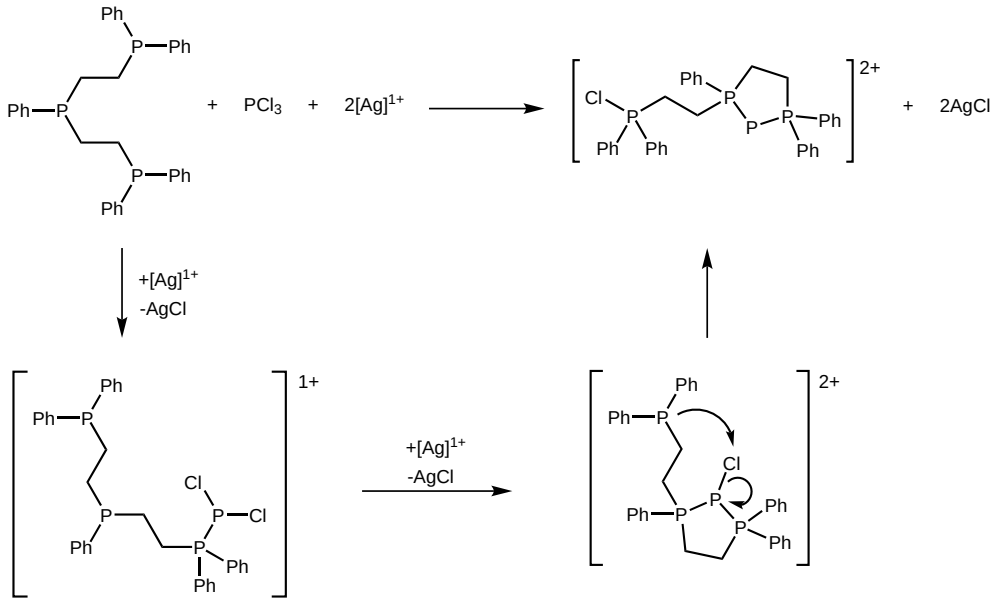

Scheme 6.1.1. Formation of a triphosphenium-chlorophosphonium cation from the reaction of *triphos* with PCl_3 and AgOTf.

6.1.2 Bipyridine Complexes of $E(OTf)_3$

Despite being one of the most common ligands in transition metal chemistry, the coordination chemistry of *bipy* in the *p*-block context has only been explored to a perfunctory level. For instance, the first *bipy* complexes of Se and Te were only reported in 2009 in the form of $[(bipy)SeCl_2]$ and $[(bipy)TeCl_2]$, and serve as bottleable sources of these otherwise unstable chalcogen dihalides. Complexes featuring pnictogen acceptors are limited to As, Sb, and Bi and of these, only in the case of Sb has a 'naked' pnictogen atom been sequestered in a *bipy* complex to give $[(bipy)_2Sb(OTf)_3]$ (Section 3.2.1). Since $P(OTf)_3$ and $As(OTf)_3$ remain unknown as isolated species, their *bipy* adducts, if isolable, would be valuable as stable sources of these highly Lewis acidic element centres.

Unlike *triphos*, *bipy* is expected to be stable towards oxidation due to the relative hardness of the more electronegative nitrogen centres. Consistently, reactions of ECl_3 (E = P, As, Sb, or Bi) with AgOTf and *bipy* in a 1:3:2 ratio do not yield P^I or As^I

centres as in the *triphos* case but rather the corresponding pnictogen *tris*-triflates as *bipy* adducts. The compounds exhibit very poor solubility in organic solvents, a challenge that is partially overcome by using *tbbipy*. The complete series of salts $[(bipy)_2E][OTf]_3$ and $[(tbbipy)_2E][OTf]_3$ (E = P, As, Sb, Bi) has been prepared (Scheme 6.1.2) and the compounds isolated as analytically pure substances, representing rare examples of *p*-block element centres surrounded by L-type ligands in their primary coordination sphere. The solid-state structures of $[(bipy)_2P)][OTf]_3$, $[tbbipy)_2As][OTf]_3$, and $[(bipy)_2Sb][OTf]_3$ were determined by X-Ray crystallography and the cations are shown in Figure 6.1.3.*

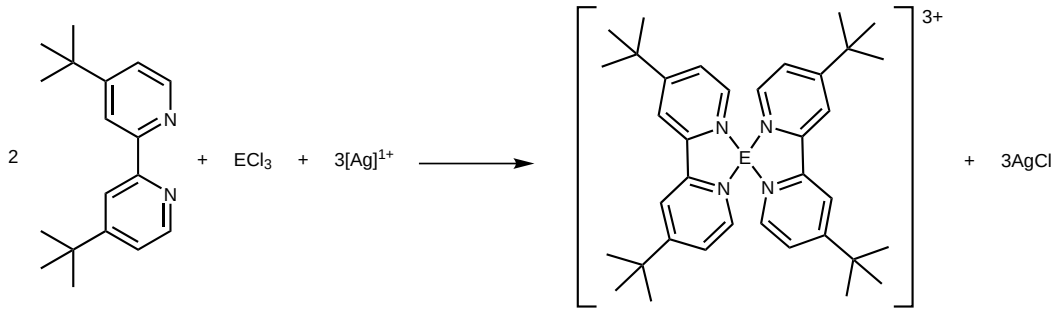

Scheme 6.1.2. Formation of triflate salts $[(tbbipy)_2E][OTf]_3$ (E = P, As, Sb, and Bi) from the reaction of *tbbipy* with ECl_3 and AgOTf.

Selected metric parameters for the three species are collated in Table 6.1.1. The E−N bond lengths follow trends in the element radii and are consistently close to the $\Sigma_{r,cov}$ for the elements involved. By comparison the P−O interion contacts lie close to the $\Sigma_{r,vdW}$ for the two elements and the E−O distances (E = As, Sb) lie midway between $\Sigma_{r,cov}$ and $\Sigma_{r,vdW}$ for the elements. In MeCN, a single ^{19}F NMR chemical shift is observed for the three species at −79.2 ppm, indicative of dissociated triflate anions, supporting the ionic description implied by formulation as triflate salts.

The structure of $[(bipy)_2P]^{3+}$ features an extremely rare example of a hypervalent P^{III} centre, previous examples being limited to a small number of complexes with NHC donors[232,233] and the newly reported $[(NHC)(aNHC)PCl_2]^{1+}$ (*a*NHC = abnormal NHC).[234] Moreover, phosphorus complexes bound by *bipy* (or substituted derivatives thereof) have not been structurally authenticated although spectroscopic evidence for their formation has been presented for some P^V acceptors.[235] Similarly, very few *bipy*

*The synthesis of $[(bipy)_2P][OTf]_3$ was performed by Dr. Alasdair P. M. Robertson who also provided its molecular structure.

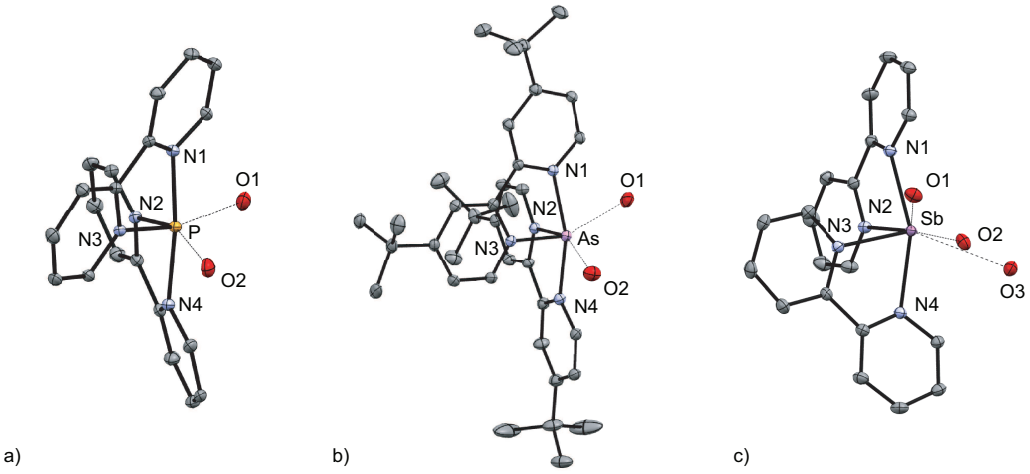

Figure 6.1.3. Molecular structures of the cations in *a*) $[(bipy_2P)][OTf]_3$, *b*) $[(tbbipy)_2As][OTf]_3$, and *c*) $[(bipy)_2Sb][OTf]_3$ in the solid state. Solvent molecules, hydrogen atoms, and non-interacting portions of the triflate anions have been omitted for clarity.

Table 6.1.1. Selected bond lengths (Å) and angles (°) in the solid-state structures of $[(bipy)_2P][OTf]_3$, $[(tbbipy)_2As][OTf]_3$•3MeCN, and $[(bipy)_2Sb][OTf]_3$•MeCN.

	$[(bipy)_2P][OTf]_3$	$[(tbbipy)_2P][OTf]_3$	$[(bipy)_2Sb][OTf]_3$
E−N1	1.9389(16)	2.136	2.3322(12)
E−N2	1.8157(18)	1.995	2.2434(12)
E−N3	1.8111(18)	1.994	2.3333(12)
E−N4	1.9735(17)	2.118	2.2843(12)
$\Sigma_{r,cov}$	1.78	1.90	2.10
$\Sigma_{r,vdW}$	3.35	3.40	3.64
E−O1	3.006	2.736	2.6499(12)
E−O2	3.109	2.683	2.5978(12)
E−O3			3.077
$\Sigma_{r,cov}$	1.73	1.85	2.05
$\Sigma_{r,vdW}$	3.32	3.37	3.61
N1−E−N2	82.80(7)	77.71	71.53(4)
N2−E−N3	99.57(8)	91.79	78.66(4)
N3−E−N4	93.36(7)	77.86	72.09(4)
N1−E−N4	173.09(8)	163.01	156.02(4)

complexes of arsenic are known. Hypervalency is more common for antimony and a number of *bipy* complexes of antimony halides have been reported previously.[132,236]

Variations in bond lengths and angles around the three acceptors elegantly demonstrate the influence of increasing atomic radii upon an AX_2Y_2E VSEPR frame where X and Y represent chelating donors and these variations should presumably be transferable to other chelating complexes. A systematic decrease is observed in the bond angle formed between the axial donor interactions, N1−E−N4, which subtends 173.09(8)° when E = P to 156.02(4)° when E = Sb. Similarly, the angle between the two ligands (N2−E−N3) also decreases from its value of 99.57(8) °in the phosphorus case to 91.79° in arsenic and, more drastically, to 78.66(4)° for antimony. The sharp decrease for antimony is due to the intrusion of a third triflate anion contact within the coordination sphere of the metal and, consistently, the angle relaxes to a value of 95.5° when the cation is modelled in the gas phase without anion interactions (Section 3.2.1). The reduction of the inter-ligand angle between phosphorus and arsenic is also noteworthy since the latter structure was obtained for the bulkier *tbbipy* ligand, evidencing minimal influence due to steric repulsion. Indeed the quaternary carbons of the ^{t}butyl groups in the ligands are nearly 10 Å apart, implying that $[(tbbipy)_2As][OTf]_3$ is likely to be a good structural model for $[(bipy)_2As][OTf]_3$, for which X-Ray quality crystals could not be obtained despite ardent efforts. Similarly, it has not yet been possible to crystallographically characterize the bismuth analogues of these salts and thereby complete the heavy pnictogen series.

The reactivity of $[(tbbipy)_2P][OTf]_3$ as a $P(OTf)_3$-equivalent, was studied towards a variety of substrates. Upon treatment of a yellow-coloured solution of $[(tbbipy)_2P][OTf]_3$ with excess PMe_3 in acetonitrile, a colourless solution is immediately obtained. Following removal of unreacted PMe_3 under vacuum, a ^{31}P NMR assay of the white residue shows no major signals besides those due to $[Me_3PPMe_3]^{2+}$ and $[(Me_3P)_2P]^{1+}$ (Figure 6.1.4), indicative of a redox reaction as outlined in Scheme 6.1.3. The proposed mechanism involves nucleophilic displacement of one or both of the *tbbipy* ligands by excess PMe_3 to give a tricationic *bis*-phosphine complex. In a process analogous to that described for $[(Me_3P)_3Sb]^{3+}$, an oxidative coupling of the phosphine ligands is implicated as being the pathway leading to detection of $[Me_3PPMe_3]^{2+}$. In the presence of excess PMe_3, the reduction product, a P^I monocation, is evidently sequestered as a phosphine complex in $[(Me_3P)_2P]^{1+}$ following ligand displacement

from the proposed intermediate $[(tbbipy)P]^{1+}$. Seeking to detect this intermediate, a dilute solution of PMe_3 was slowly added to a suspension of $[(tbbipy)_2P][OTf]_3$ in MeCN until a final stoichiometry of 2:1 was achieved. After stirring for 20 minutes a yellow-orange suspension was obtained and analysis of the supernatant by ^{31}P NMR analysis showing unreacted starting material, $[Me_3PPMe_3]^{2+}$, and $[(Me_3P)_2P]^{1+}$ as the main species. A small and broad signal is also observed at +233.6 ppm together with a sharp singlet at +115.3 ppm. The identity of these species has not yet been established nor has the reaction been performed at reduced temperatures to detect the proposed or additional intermediates. The precipitate was dissolved in fresh MeCN and assayed as unreacted $[(tbbipy)_2P][OTf]_3$ by NMR spectroscopy.

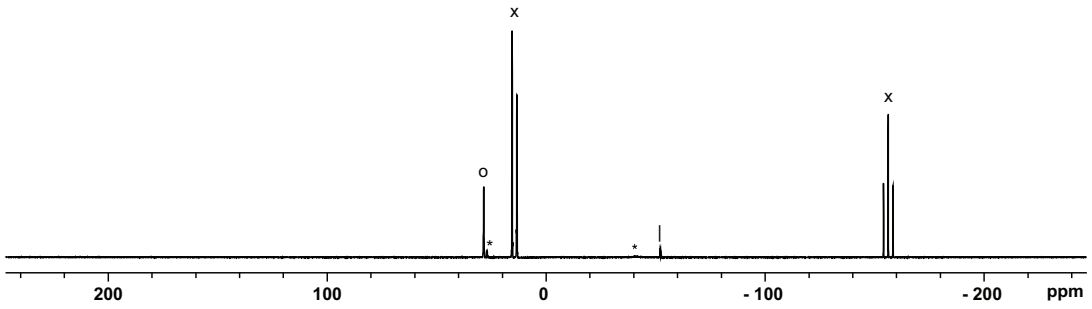

Figure 6.1.4. ^{31}P NMR (298 K, MeCN) of the residue after removal of volatiles from a reaction mixture containing $[(bipy)_2P][OTf]_3$ and PMe_3 in a 1:6 ratio in MeCN.

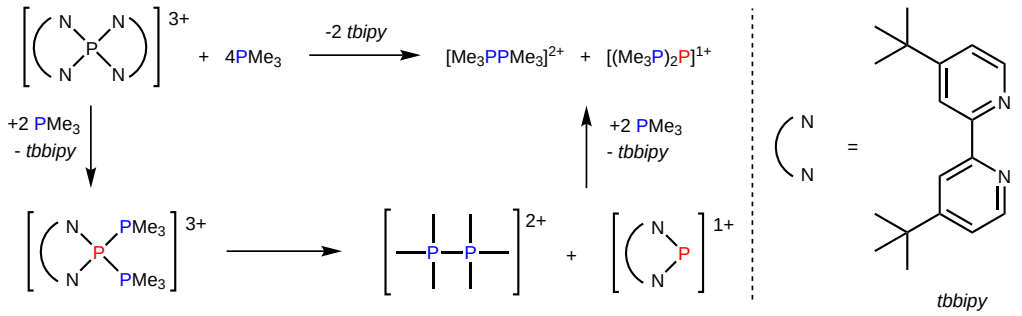

Scheme 6.1.3. Proposed mechanism for the formation of $[Me_3PPMe_3]^{2+}$ (o) and $[(Me_3P)_2P]^{1+}$ (×) from the reaction of $[(bipy)_2P][OTf]_3$ with excess PMe_3 (|). Asterisks denote a small amount of unidentified products.

Addition of neat MeOTf to a solution of $[(tbbipy)_2P][OTf]_3$ results in no immediate reaction. After stirring for an hour a ^{31}P NMR assay shows no evidence of reaction, although a small amount of methylated ligand, $[(tbbipy)Me][OTf]$ is observed by ^1H NMR spectroscopy. The absence of P−C bond formation indicates a very low

basicity for the P^{III} centre, in line with its high molecular charge, and the detection of [(*tbbipy*)Me][OTf] suggests that the most basic site in the cation is one of the pyridinoid nitrogen centres. Recently, there has been much interest in the use of phosphorus polycations as ligands due to the combination of σ-donating and π-accepting properties some of them exhibit.[162,163] The results presented here suggest that $[(tbbipy)_2P][OTf]_3$ is likely not a suitable ligand in this context for onward coordination to Lewis acids *via* the phosphorus centre.

Exposure of the salt to moist air results in instanteneous loss of the bright yellow colouration to leave behind a white solid. The transformation quantitatively (by NMR) converts the starting material to a single product which resonates in the ^{31}P NMR at +5.9 ppm and in the ^{1}H NMR at 6.85 ppm (Figure 6.1.5). It definitively contains a P−H bond, detected by NMR spectroscopy as having a $^{1}J_{PH}$ coupling constant of 692.3 Hz. The ^{1}H NMR spectrum also shows very clean conversion to a single *tbbipy*-containing product, where a single chemical shift is observed for the 18 methyl-group protons and three resonances for the remaining 6 aromatic protons of *tbbipy*, indicating C_2 symmetry. An additional signal integrating to 3 protons is observed at 12.0 ppm, indicating a highly deshielded proton. These spectroscopic features are consistent with a mixture of protonated *tbbipy* and H_3PO_3.

6.1.3 Reactions of *triphos* with E(OTf)$_3$-equivalents

As described previously, the attempted synthesis of *tris*-phosphine and -arsine complexes using *triphos*, ECl_3 and Lewis acids failed due to the redox activity of the ligand giving tripnictenium-chlorophosphonium cations. Reactions of $[(tbbipy)E][OTf]_3$ (E = P, As) with *triphos* seemed a reasonable route to *tris*-phosphine complexes, while avoiding the formation of redox products due to the absence of chlorine atoms in the $E(OTf)_3$-equivalents. Thus, access to the $[(triphos)P]^{3+}$ and $[(triphos)As]^{3+}$ cations, analogous to complexes of *triphos* with Sb and Bi, was sought *via* displacement of the *tbbipy* ligands.

The reaction of excess *triphos* with $[(tbbipy)P][OTf]_3$ yielded [(*triphos*)P][OTf] as the major identified product by ^{31}P NMR spectroscopy. Although it has not yet been possible to isolate this compound as a pure substance, an attempt to confirm its identity spectroscopically was made by reductive dechlorination of $[(triphos{-}Cl)P][OTf]_2$ with elemental magnesium. Following removal of insoluble magnesium salts, the ^{31}P NMR

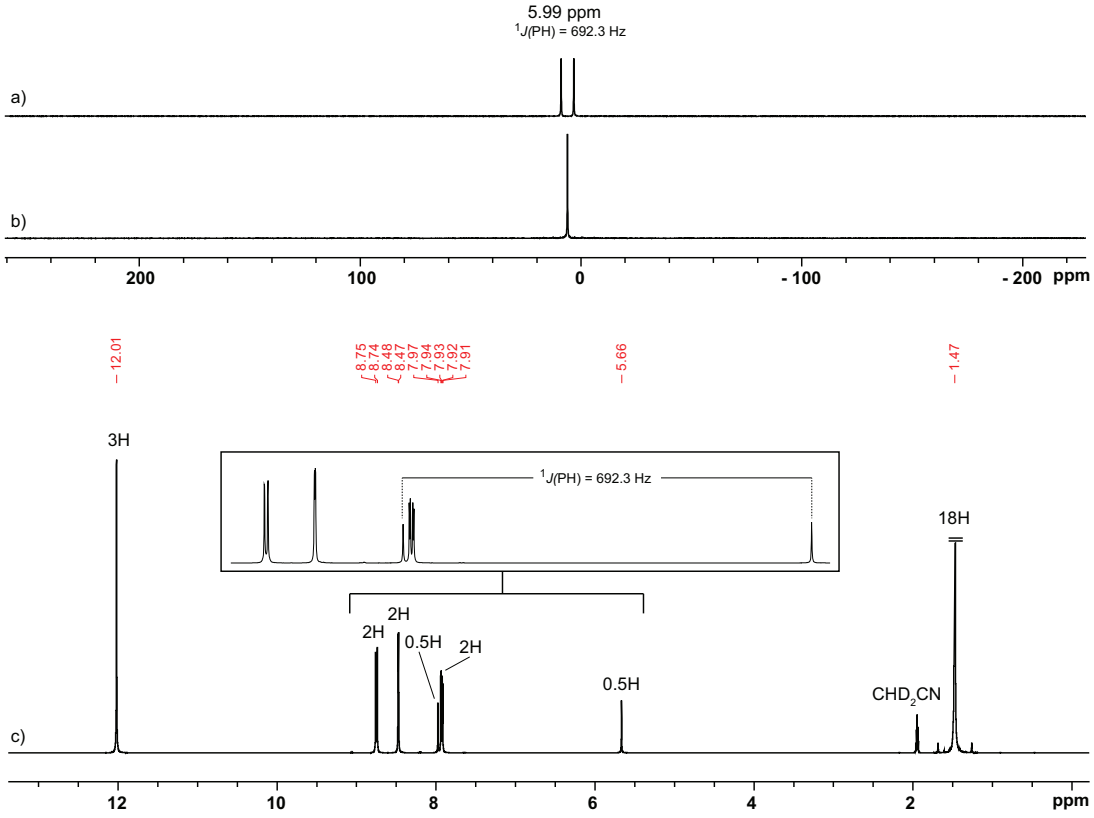

Figure 6.1.5. *a*) ^{31}P, *b*) ^{31}P{^{1}H}, and *c*) ^{1}H NMR spectra (CD_3CN, 298 K) of the white residue obtained upon exposure of a yellow sample of $[(tbbipy)_2P][OTf]_3$ to air for five minutes. Inset shows fine structure for the indicated region in the ^{1}H NMR spectrum.

spectrum of the crude product from this reaction (Figure 6.1.6) matches that of the reaction mixture containing $[(tbbipy)_2P][OTf]_3$ and *triphos*, and showing all the expected coupling for the $[(triphos)P]^{1+}$ cation (Figure 6.1.6). In addition an unusual $^4J_{PP}$ and an even more unusual $^5J_{PP}$ coupling is also observed, assigned to through-space interactions due to a dynamic process tentatively understood as involving exchange of a phosphonium donor of the triphosphenium moiety with the pendant neutral phosphine. Consistently, these couplings are only detected at temperatures below −65 °C and disappear completely at room temperature concomitant with severe line broadening. The ^{31}P NMR spectrum of $[(triphos{-}Cl)P][OTf]_2$ (Figure 6.1.2) does not show such broadening since the pendant phosphine is oxidized and unavailable to participate in ligand exchange. Formation of monocationic $[(triphos)P][OTf]$ from the reaction of tricationic $[(tbbipy)P]^{3+}$ and neutral *triphos* necessarily requires coevolution of other cationic oxidation products, but these have not yet been isolated. Nevertheless, the evidence suggests that the *triphos* complex of $P(OTf)_3$ may be inherently unstable, in line with results obtained for reactions involving PMe_3.

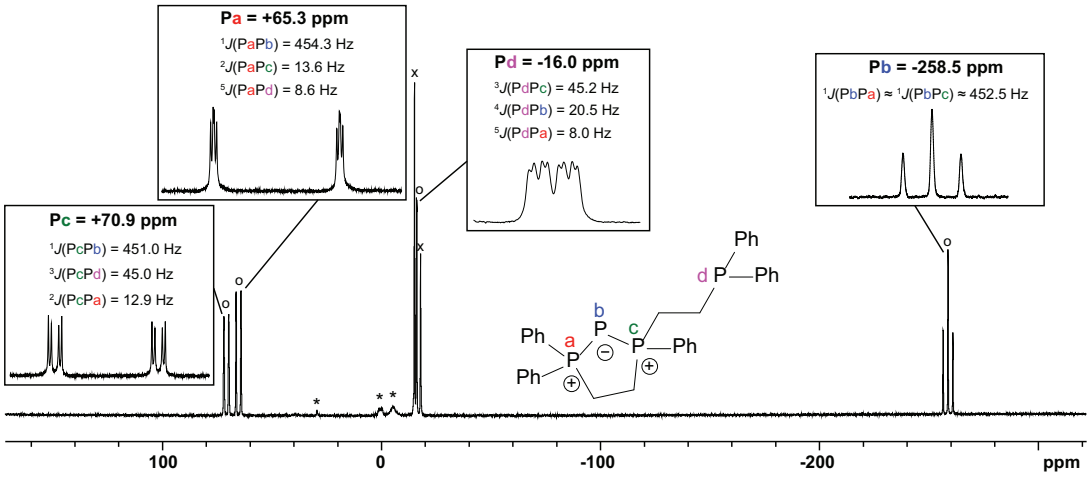

Figure 6.1.6. ^{31}P NMR spectrum (208 K, CD_2Cl_2) of the crude product obtained from the equimolar mixture of $[(triphos{-}Cl)P][OTf]_2$ and elemental magnesium. Insets denote fine structure for indicated peaks and symbols denote *triphos* (×) and $[(triphos)P][OTf]$ (o). Unidentified products are denoted with asterisks.

These preliminary experiments indicate that $[(tbbipy)_2P][OTf]_3$ is a strong oxidizing agent that is capable of effecting oxidative coupling of trialkylphosphines concomittant with transfer of the resultant P atom, as observed by formation of $[Me_3PPMe_3]^{2+}$ and $[(Me_3P)_2P]^{1+}$ cations from the reaction with PMe_3. Moreover, even though it serves

as a $P(OTf)_3$-equivalent, it is too potent an oxidizer to make stable *triphos* complexes, as judged from the formation of the reduced $[(triphos)P]^{1+}$. It may be possible to detect the *triphos* complex at low temperatures but these experiments have yet to be performed.

The demonstrated oxidizing ability of $[(tbbipy)_2P][OTf]_3$ bodes well for its application in *catena*-phosphorus chemistry as a reagent that may couple a broad variety of phosphorus substrates (*e.g.* neutral polyphosphines or phosphorus anions) to give novel polyphosphorus frameworks as both the oxidation and the reduction products. The reaction of $[(tbbipy)_2P][OTf]_3$ with excess PPh_3 is of great interest since it may give the elusive $[\mathbf{6.5(Ph)}]^{2+}$ dication, which has been postulated as an oxidation product in Section 6.1.3. On the other hand, given the extreme steric bulk around the P−P bond in this compound and the lower oxidation potential of triarylphosphines compared to alkylphosphines, formation of the diphosphonium may be disfavoured and the first *tris*-phosphine complex of phosphorus, $[(Ph_3P)_3P]^{3+}$, may become accessible. Both of these outcomes would be valuable contributions to *catena*-phosphorus chemistry. Given the similar electronegativities and covalent radii of phosphorus and arsenic, the analogous reaction chemistry with the heavier analogue is also likely to be rich and remains to be explored. It may yield novel *catena*-arsenic species which have largely been ignored due to the toxicity associated with this element.

6.2 Summary

In summary, *tris*-phosphine complexes of antimony and bismuth are readily accessed but those of phosphorus and arsenic are difficult to form due to the presence of competing redox reactions. Synthesis of *tris*-triflate equivalents for phosphorus and arsenic has been achieved but their conversion to *triphos* complexes continues to be challenged by the strong oxidizing abilities of the formally $[E]^{3+}$ cations.[†] Partially fluorinated aromatic phosphines may prove to be a suitable class of ligands for making *tris*-phosphine complexes of $P(OTf)_3$ due to their higher ionization energies, but these may also be poor donors that fail to displace the *tbbipy* ligands from the $E(OTf)_3$-equivalents used to avoid chlorophosphonium formation.

[†]The reduction of $[(triphos{-}Cl)P][OTf]_2$ with magnesium and some of the reactions involving $[(tbbipy)_2P][OTf]_3$ were performed by Kevin Vos as part of an undergraduate Honours project.

Chapter 7

Summary

Phosphine complexes of lone pair bearing acceptors are known for almost all *p*-block elements, except boron, aluminum, oxygen, and some halogens. There is a particular scarcity of *bis*- and *tris*-phosphine complexes, however, and in the latter class examples are only known for four elements. In some cases, such as the group 14 tetrylones, interpretation of compounds as phosphine coordination complexes has only recently been made and there is ongoing debate about the nature of the chemical bond in these species, highlighting the need for a flexible understanding of the bonding phenomenon in coordination compounds.

As a contribution to this evolving understanding, Chapter 2 provided a case study where oft-assumed correlations between theoretical bonding models and experimental observables were evaluated. Specifically, a comprehensive experimental and computational assessment of the P−P bond in some prototypical organophosphorus compounds was presented, constituting a rare, complete catalogue of experimental bond length and stretching frequency data for a series of known molecules. Isotopic enrichment methods were used to obtain definitive assignments for vibrational spectroscopy data. Additionaly, gas- and solid-phase bond strengths were calculated or estimated semi-empirically, answering some fundamental questions regarding homoatomic bonding (see Scheme 2.1.1*c* and *d*) and inspiring the most atom-economical route possible to phosphinophosphonium salts, namely the P−P Menschutkin reaction.

In Chapter 3, several series of P−Sb complexes featuring were synthesized and structurally characterized to determine the relative *trans*-labilizing influence exerted by a lone pair, a substituent or a ligand. A structural model was derived that

expands the scope of existing VSEPR concepts and is consistent with all previously reported adducts of antimony acceptors. It is expected that relative *trans*-labilizing influence of these fragments will be broadly applicable to analogous complexes of other main group acceptor centers bearing a lone pair. A comparison of the experimental structural data for a charge-variant series of PMe_3 complexes of haloantimony centers revealed counterintuitive differences in the P−Sb and Sb−Cl bond lengths, which were explained with reference to increased ionic and covalent Sb−Cl bonding by means of sophisticated quantum chemical computational models. Access to *tris*-triflate complexes of antimony is possible by judicious choice of the antimony halide and Lewis acid. The combination of SbF_3 and TMSOTf in these roles gave facile access to the desired triflates due to the strong Si−F bond strength. This route, for the first time, provides access to anhydrous triflates of antimony and bismuth, which are used as Lewis acid catalysts, on a *ca.* 100 g scale. Since the Lewis acidity of these species is likely to be partially quenched by hydration, the anhydrous formulations reported here may prove to be more potent catalysts.

Chapter 4 described the synthesis and characterization of compounds featuring bismuth acceptors stabilized by THF or *dmpe* ligands. In the solid state, the triflate complexes crystallize as dimers involving significant Bi-O_{OTf} interactions. The strong *trans* influence of the halide ligands is also documented. Experimental attempts to realize potential Z-ligand type reactivity from some P−Bi complexes were unsuccessful and led instead to the discovery of a metathesis reaction highlighting an important distinction between the chemistry of phosphorus and bismuth cations.

The most significant findings in Chapter 5 pertain to the discovery of reductive elimination of diphosphonium dications $[R_3PPR_3]^{2+}$ from trialkylphosphine complexes of highly electrophilic antimony(III) centres. The reduced antimony(I) fragments cyclize into frameworks identified as *cyclo*-tetra(stibinophosphonium) tetracations, $[(R_3P)_4Sb_4]^{4+}$. A phosphine catalyzed mechanism was proposed on the basis of comprehensive studies involving isolation of the key intermediates. A multi-gram scale synthesis for the triflate salt of a prototypical derivative, $[(Me_3P)_4Sb_4][OTf]_4$, enabled a range of reactivity studies, which are characterized by two key features: *i)* high charge concentration, and *ii)* the presence of strongly polarized P−Sb bonds. The reactions studied yielded new *catena*-antimony frameworks as well as the first spectroscopic evidence of an *H*-phosphinophosphonium cation. Attempts to generate

triarylphosphine derivatives of cations $[(R_3P)_4Sb_4]^{4+}$ yielded the first cationic bicycle for antimony, $[\mathbf{5.20(Ph)}]^{4+}$, from an unprecedented 14-electron reductive coupling *via* a postulated hexacationic intermediate, $[\mathbf{5.19}]^{6+}$. Of the two proposed oxidation products, the fluorophosphonium $[\mathbf{5.12(Ph)}]^{1+}$ and diphosphonium $[\mathbf{5.11)}]^{2+}$, only the former could be definitively characterized.

Chapter 6 described synthetic efforts to access and structurally characterize rare *tris*-phosphine complexes $[(triphos)E][OTf]_3$. While the antimony and bismuth derivatives could be accessed straightforwardly, numerous challenges were encountered in making the phosphorus and arsenic derivatives due to oxidative halogenation of the the phosphine ligand by the E-X bonds in the ECl_3 substrates employed. In an attempt to circumvent this reactivity, a series of *bipy* and 4,4'-^{t}Bu$_2$-2,2'-bipyridine *tbbipy* complexes of $E(OTf)_3$ (E = P, As, Sb, Bi) were prepared as stable and soluble $E(OTf)_3$-equivalents. However, attempts to make *triphos* complexes of phosphorus from these derivatives once again only yielded products due to oxidation of the ligand, implying that tricationic *tris*-phosphine complexes of these elements are inherently unstable with respect to oxidation due to the high electrophilicity of the acceptor centres. The range of reactivity traversed from stable $E(OTf)_3$ coordination by *triphos* (E = Sb, Bi) to oxidation by $E(OTf)_3$ (E = P, As) defines a breadth of coordination chemistry outcomes that may apply broadly to other groups of the periodic table.

Within the context of phosphines as ubiquitous ligands in coordination chemistry, the discovery of a strutural *trans*-influence effect for lone pair bearing complexes and the study of a novel ligand activation pathway are the most significant findings of the research presented in this thesis. The former fills a gap in VSEPR theory, which does not have predictions for complex substitution patterns and the latter has important implications as a new P−P bond forming reaction, which also gives access to low-oxidation state compounds. The phosphine ligand activation pathway highlighted here is predicted to be widely applicable across the periodic table in electron deficient complexes and its strategic use will undoubtedly yield new classes *catena*-element compounds. Reagents such as $[(tbbipy)E][OTf]_3$ (E = P, As) have been revealed and these might find applications in a variety of contexts as transfer reagents for the highly-reactive and as-yet unisolated $E(OTf)_3$ functionality.

Chapter 8

Future Work

A number of ongoing research projects are summarized in this section. A combined experimental and theoretical study of the P−P bond is presented that closely complements the analysis summarized in Chapter 2 by looking at P−P bond strengths in phosphinophosphonium cations, $[Me_3PPR_2]^{1+}$ as a function of the substituent R. Finally, the potentially broad phenomenon of P−P oxidative coupling in the coordination sphere of metals is discussed, with a special emphasis on activation of small molecules such as P_4.

8.1 The P−P Bond

The assessment of the P−P bond in Chapter 2 focused primarily upon variations as a function of charge and coordination number. An orthogonal study has now been initiated which considers the influence of steric and electronic features at a given intersection of charge and coordination number. Thus, a series of phosphinophosphonium cations, $[Me_3PPR_2]^{1+}$, $[\mathbf{8.1(R)}]^{1+}$, have been prepared with R = Me, ^{i}Pr, ^{t}Bu, Ph, and N^iPr_2 to model a diverse array of phosphenium moieties. The fundamental bond dissociation processes for these cations in the gas phase have been assessed by means of ESI-MS/MS experiments.

In these experiments, salts are introduced into an evacuated chamber following desolvation and, using a quadrupole assembly, only the ion of interest is filtered to advance into a second collision chamber. The isolated ion is then accelerated with a controllable voltage and collided with argon atoms. The m/z ratio detected for the

resulting fragments and the isotopic abundances of their constituent elements yields empirical formulae, which are subsequently assigned atomic connectivities. Crucially, by precisely varying the kinetic energy of the colliding ions, fragmentation processes in different energy regimes can be selectively probed, providing a qualitative estimate of the relative energetic requirements of the bond rupture processes generating the fragments.

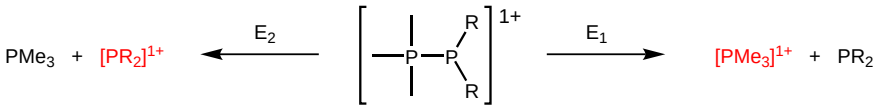

Scheme 8.1.1. Homolytic and heterolytic dissociation of [**8.1(R)**]$^{1+}$. Red colour indicates species detected experimentally and E_1 and E_2 represent the energies of homolytic and heterolytic cleavage, respectively.

Homolytic and heterolytic P−P bond cleavage can be differentiated on the basis of the collision fragments generated from the initial phosphinophosphonium (Scheme 8.1.1). Detection of a m/z ratio corresponding to the $[PMe_3]^{1+}$ radical cation indicates a homolytic fission process whereas detection of a $[PR_2]^{1+}$ cation signals a heterolytic fission pathway. Neutral fragments are not detected. As shown in Figure 8.1.1*a*, when R = Me, both bond rupture pathways are observed experimentally. In addition, the protonated phosphine $[Me_3PH]^{1+}$ is also detected, presumably through hydrogen abstraction by $[PMe_3]^{1+}$.* By comparison, as shown in Figure 8.1.1*b*, the results for [**8.1(Ph)**]$^{1+}$ evidence only the heterolytic P−P dissociation pathway and there is no evidence of the $[PMe_3]^{1+}$ radical cation generated by homolytic fission. Consistently, calculations at the PBE1PBE/6-311G++(d,p) level show that heterolytic cleavage is preferred by *ca.* 65 kJ mol^{-1} for R = Ph and homolytic by *ca.* 45 kJ mol^{-1} for R = Me. The relative preferences calculated for gas-phase species are plotted in Figure 8.1.2.

The data can be used to qualitatively assess calculated trends in the energies required for a given process as a function of substitution. For instance, the calculated values for heterolytic cleavage is *ca.* 120 kJ mol^{-1} higher for R = Me than R = Ph. This is experimentally verified by comparing the values of the apparent x-intercept for the

*The presence of impurities or adventitious moisture can be ruled out since all collisions occur under high vacuum conditions *after* mass selection to filter out all but the [**8.1(R)**]$^{1+}$ ions has been conducted. Therefore, all fragments detected in this experiments arise through one or more fragmentation processes beginning with cations [**8.1(R)**]$^{1+}$.

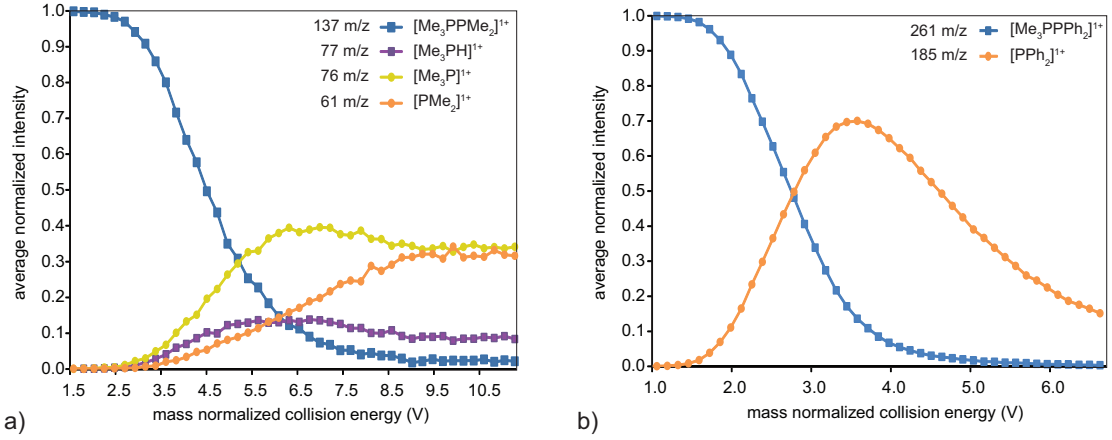

Figure 8.1.1. P−P bond cleavage pathways observed for *a*) [**8.1(Me)**]$^{1+}$ and *b)* [**8.1(Ph)**]$^{1+}$ in the gas phase.

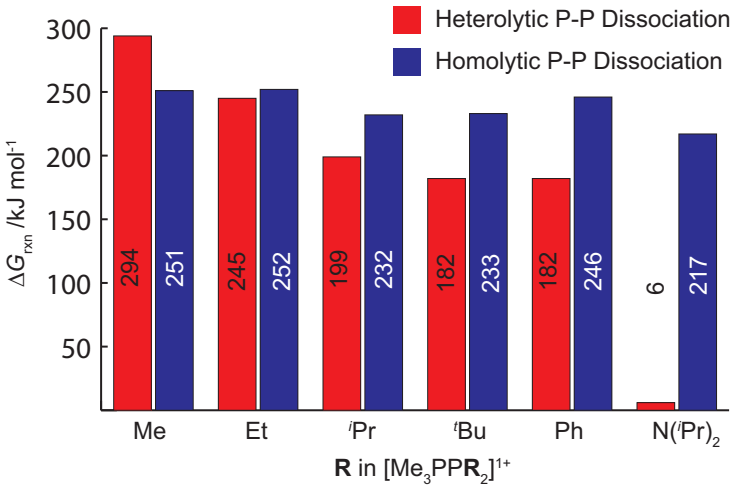

Figure 8.1.2. Calculated P−P bond cleavage energies for cations [**8.1(R)**]$^{1+}$ in the gas phase.

curves corresponding to phosphenium cations $[PR_2]^{1+}$ (*ca.* 2.6 V for R = Me, and *ca.* 1.5 V for R = Ph), which are interpreted as being proportional to the threshold energies required for the formation of these ions from the parent phosphinophosphonium. The dominance of the heterolytic pathway in the phenyl-substituted cation is interpreted as resonance stabilization of the diphenylphosphenium cation by partial transfer of the π electron density from the aromatic rings into the vacant *p*-orbital at phosphorus. Consistently, when the excellent π-donating substituent N^iPr_2 is considered, homolytic cleavage is overwhelmingly operative, requiring nearly 200 kJ mol^{-1} less energy than the alternative. Analysis of the electronic structure of diphenylphosphenium has also

been carried out at the MP2/6-311G++(d,p) level, revealing (Figure 8.1.3) a vacant p-orbital as the LUMO and a delocalized HOMO−3 that features a contiguous electron density region of π symmetry over the C−P−C framework. A low energy orbital (HOMO−4) is also apparent and identified as a lone pair centred at phosphorus.

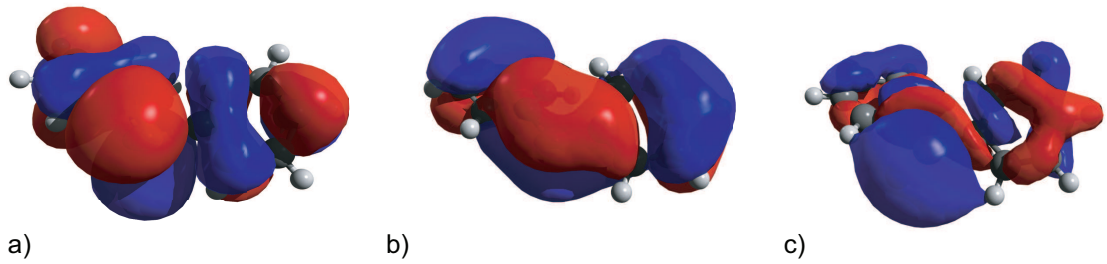

Figure 8.1.3. Surface plots of the *a*) LUMO (−5.07 eV), *b*) HOMO−3 (−14.49 eV), and *c*) HOMO−4 (−15.67 eV) for the $[PPh_2]^{1+}$ cation at the MP2/6-311G++(d,p) level.

The energy values plotted in Figure 8.1.2 predict that the apparent appearance potentials for cations $[PR_2]^{1+}$ should increase in the order R = Me > Et > ^{i}Pr > ^{t}Bu > Ph > N(^{i}Pr)$_2$. Experimental heterolytic cleavage data has been obtained for all but R = Et and N(^{i}Pr)$_2$ and shown in Figure 8.1.4*a*. The asymptotic nature of the curves in their appearance voltage regime necessitates an arbitrary scheme for determining exact x-intercepts for the intensity of the phosphenium fragments, which should be proportional to the threshold energy required for heterolytic cleavage. Black vertical lines indicate x-intercepts calculated at 0.5 % intensity and red lines at 1.5 % intensity. Due to the systematic error introduced by this arbitrary scheme, only relative values for a particular dissociation pathway can be discussed. Nevertheless, as the red lines illustrate, the *trends* are not sensitive to slight variations in the intensity cutoffs employed. The experimental values for heterolytic P−P cleavage energies show the order: Me > ^{t}Bu ≈ ^{i}Pr >> Ph. Given the non-trivial change in the values for the ^{t}Bu derivative as a function of the intensity cutoff employed (compare red and black lines), the most judicious interpretation of these results is that they evidence a more facile P−P bond heterolysis in $[\mathbf{8.1(R)}]^{1+}$ when R = aromatic than when R = aliphatic, and variations within a series of R substituents need to be reproduced before they can be scrutinized in greater detail.

The calculated values for homolytic cleavage are very similar across all derivatives

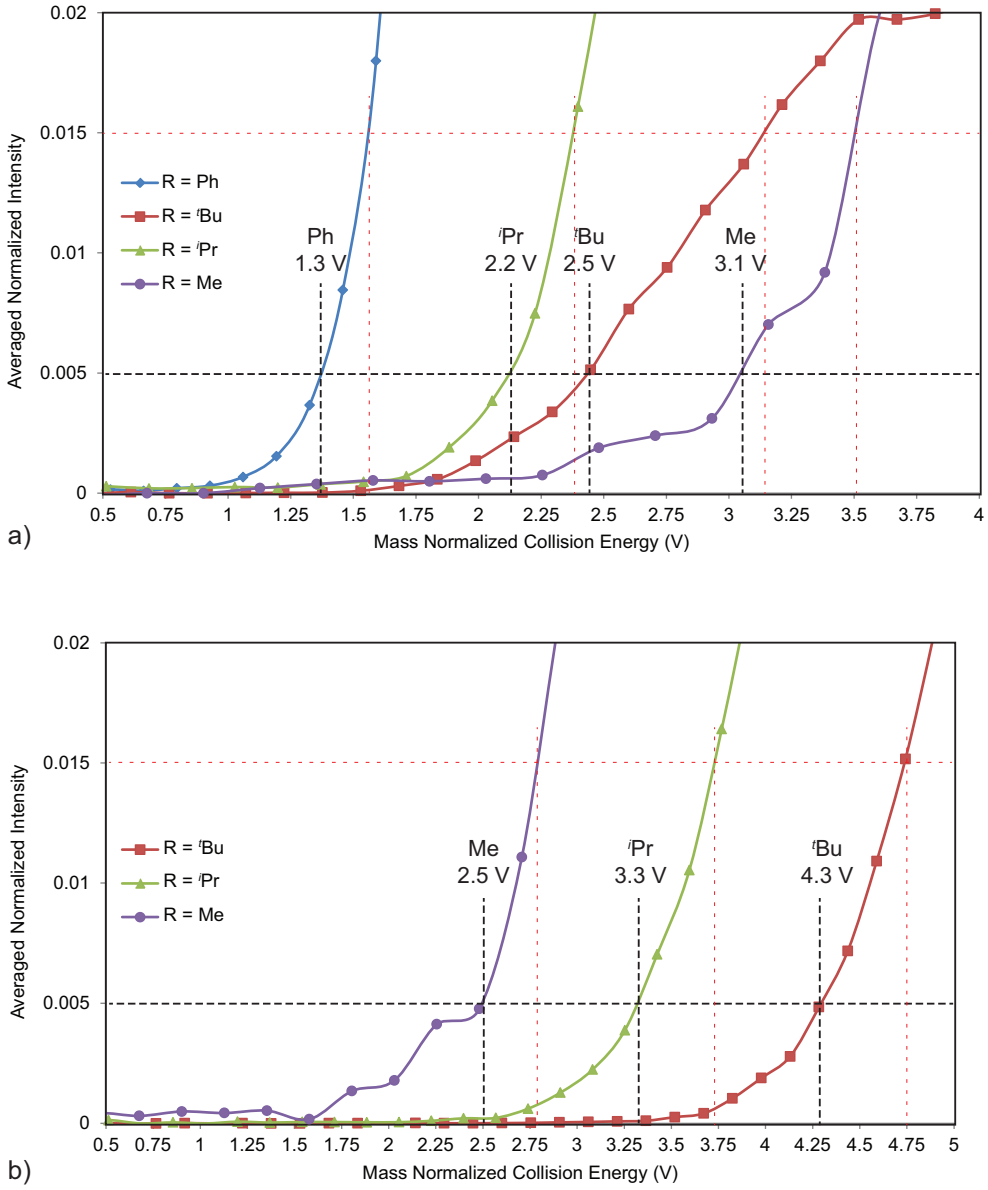

Figure 8.1.4. Normalized intensities of cations *a*) $[PR_2]^{1+}$ and *b*) $[PMe_3]^{1+}$ as a function of kinetic energies transferred to cations $[\mathbf{8.1(R)}]^{1+}$ upon collision with an argon atom. Dashed lines indicate x-intercepts at $y = 0.005$ (black) and 0.015 (red).

considered and lie in a small 35 kJ mol^{-1} range. If the outlier value for the N(^{i}Pr)$_2$ substituent is ignored, the range is even narrower (20 kJ mol^{-1}). For comparison the range for heterolytic dissociation with and without the outlier value for R = N(^{i}Pr)$_2$ is 290 kJ mol^{-1} and 105 kJ mol^{-1}, respectively. The experimental results for homolytic P−P cleavage are illustrated in Figure 8.1.4*b*, where the phenyl derivative is not

included since there was no evidence of this pathway being operative for $[\mathbf{8.1(Ph)}]^{1+}$. The data for the three remaining derivatives show very little sensitivity to the intensity cutoffs and the apparent threshold energies for homolytic P−P bond cleavage increase in the order: ^{t}Bu > ^{i}Pr > Me. However, further discussion of this data would not be justified, since the significance of the observed trend cannot yet be properly assessed without additional control experiments. Specifically the source of the $[Me_3PH]^{1+}$ cation, which is observed in all systems (except R = Ph) to varying extent, must be determined since its formation by hydrogen atom abstraction might be responsible for reducing the apparent intensity of the signal due to the primary homolysis product being monitored ($[PMe_3]^{1+}$).

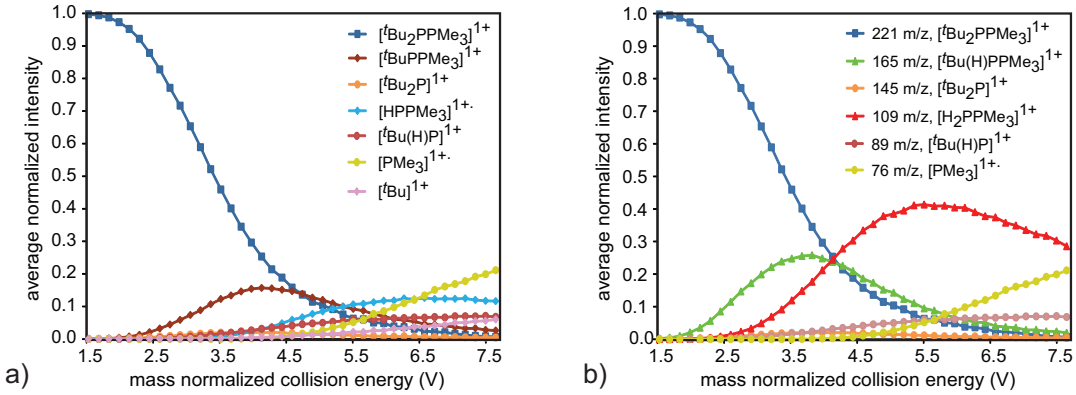

Figure 8.1.5. P−C bond cleavage pathways detected for $[Me_3PP^tBu_2]^{1+}$ involving *a*) loss of ^{t}Bu or $[^{t}Bu]^{1+}$ groups and *b*) β -hydride elimination.

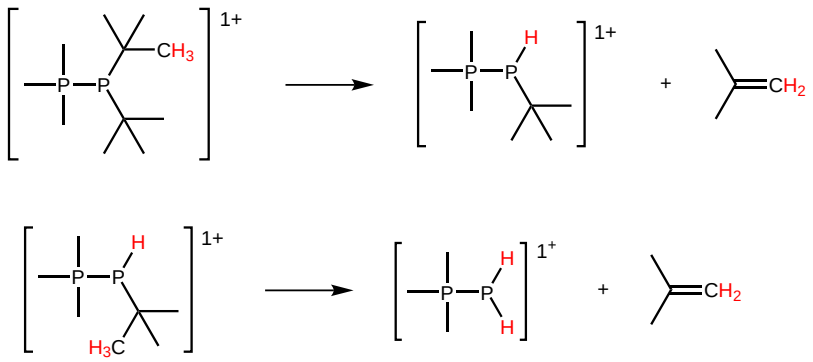

Scheme 8.1.2. Stepwise β-hydride elimination from $[Me_3PP^tBu_2]^{1+}$ to give $[Me_3PP(H)^tBu]^{1+}$ and $[Me_3PPH_2]^{1+}$.

The experimental data also provide evidence for a number of additional pathways, including two that involve P−C bond cleavage. For R = ^{t}Bu, homolytic P−C cleavage

yields $[Me_3PP^tBu]^{1+}$ and heterolytic cleavage yields $[^tBu]^{1+}$ as the charged species and both of these have been observed. Remarkably, as shown in Figure 8.1.5*a*, these pathways are significantly more prevalent compared to P−P cleavage of $[\mathbf{8.1(^tBu)}]^{1+}$. Another major P−C cleavage pathway involves stepwise β-hydride eliminations to release one and two isobutene molecules from the phosphenium fragment to give $[Me_3PP(H)^tBu]^{1+}$ and $[Me_3PPH_2]^{1+}$, respectively, according to Scheme 8.1.2, as evidenced in the experimental data shown in Figure 8.1.5*b*. This unusual elimination, which is also operative in the case of R = $[^iPr]^{1+}$ (releasing propene), is extremely rare for *p*-block complexes and particularly so for non-metals. Attempts to induce thermal elimination of alkenes from bulk solutions containing phosphinophosphonium cations have not yet been successful under the conditions applied. Nevertheless, it is gratifying to note that the product from the first isobutene elimination, $[Me_3PP(H)^tBu]^{1+}$, is a direct analogue of the *H*-phosphinophosphonium cation, $[Me_3PP(H)Cy]^{1+}$, spectroscopically characterized in Chapter 5. Consistently, this ion is also observed as a major product by collision-induced fragmentation of $[\mathbf{8.1(Cy)}]^{1+}$ in the gas phase.

In summary, a number of competing bond dissociation pathways have been detected for phosphinophosphonium cations including P−P and P−C bond cleavage and trends in their energetic thresholds have been compared with calculated values. Bond dissociation energies are notoriously challenging to calculate for all molecules except diatomics, and the ability to obtain even a qualitative estimate for the major pathways in the complex cations studied here is remarkable. Therefore, even though the current experimental data do not enable quantitative discussion, the discovery of diverse and hitherto unimagined dissociation pathways makes an extremely compelling argument for vigorously pursuing the development of ESI-MS/MS techniques as a tool for obtaining experimental analogues for computationally obtained bond strengths. As just one example, a similar study for diphosphoniums $[R_3PPR_3]^{2+}$ would be extremely valuable in clarifying the stability of these species in the gas phase, where lattice enthalpy considerations do not apply.[†]

[†]The experiments and quantum chemical calculations presented here have been carried out by Karlee Bamford as part of an undergraduate Honours project.

8.2 Oxidative Coupling of Phosphorus Centres

Oxidative coupling of phosphines to give diphosphonium cations has been established as a novel P−P bond forming reaction. Both alkyl and arylphosphines participate in this reactivity, and it may therefore be applicable to a wide swathe of phosphorus substrates. Application of this strategy to activate small molecules such as P_4 (Scheme 8.2.1, top) may provide a unique route to homopolyatomic cations of phosphorus (*i.e.* $[P_n]^{m+}$), of which there are currently no structurally authenticated examples, although some ligand-stabilized derivatives (*i.e.* $[LP_n]^{m+}$) are known.[142,237]

Extensively catenated organopolyphosphorus cations may also be accessible by changing the substrate from P_4 to phosphinophosphonium cations, for which coordination and oxidation of the acceptor-centred lone pair has been amply evidenced (Section 1.2.2). For instance the phosphorus analogue of butane may be accessible by oxidative coupling of two units of the pentamethyl phosphinophosphonium cation (Scheme 8.2.1, bottom). Even longer polyphosphorus cations, containing P^I centres, are expected from the use of $[(tbbipy)_2P][OTf]_3$ as the oxidizing reagent.

The use of Sb^{III} reagents as oxidizers is expected to additionally give new *catena*-antimony frameworks as the reduction products. The factors influencing catenation patterns in these cations remain poorly understood as illustrated by the isolation of monocycles when trialkylphosphines are employed and a bicycle when a triarylphosphine is employed (Section 5.4). A comprehensive assessment of catenation outcomes as a function of phosphine steric bulk and Lewis basicity is required to understand the divergent behaviour and exert control over the frameworks obtained. Together with the large-scale synthesis of $FSb(OTf)_2$ and $Sb(OTf)_3$ described in Chapter 3, the ready commercial availability of a vast array of electronically and sterically diverse triarylphosphines bodes well for initiating such an assessment.

8.3 P−P Bond Activation in Diphosphoniums

High level *ab initio* calculations have suggested that the P−P bond in diphosphonium cations is susceptible to homolysis under certain conditions (Section 2.1). The bond may be weakened further by introduction of steric bulk around the phosphorus centres, either *via* alkylation of diphosphines with very bulky electrophiles such as the $[^tBu]^{1+}$ cation or *via* oxidative coupling of bulky trialkylphosphines using, for

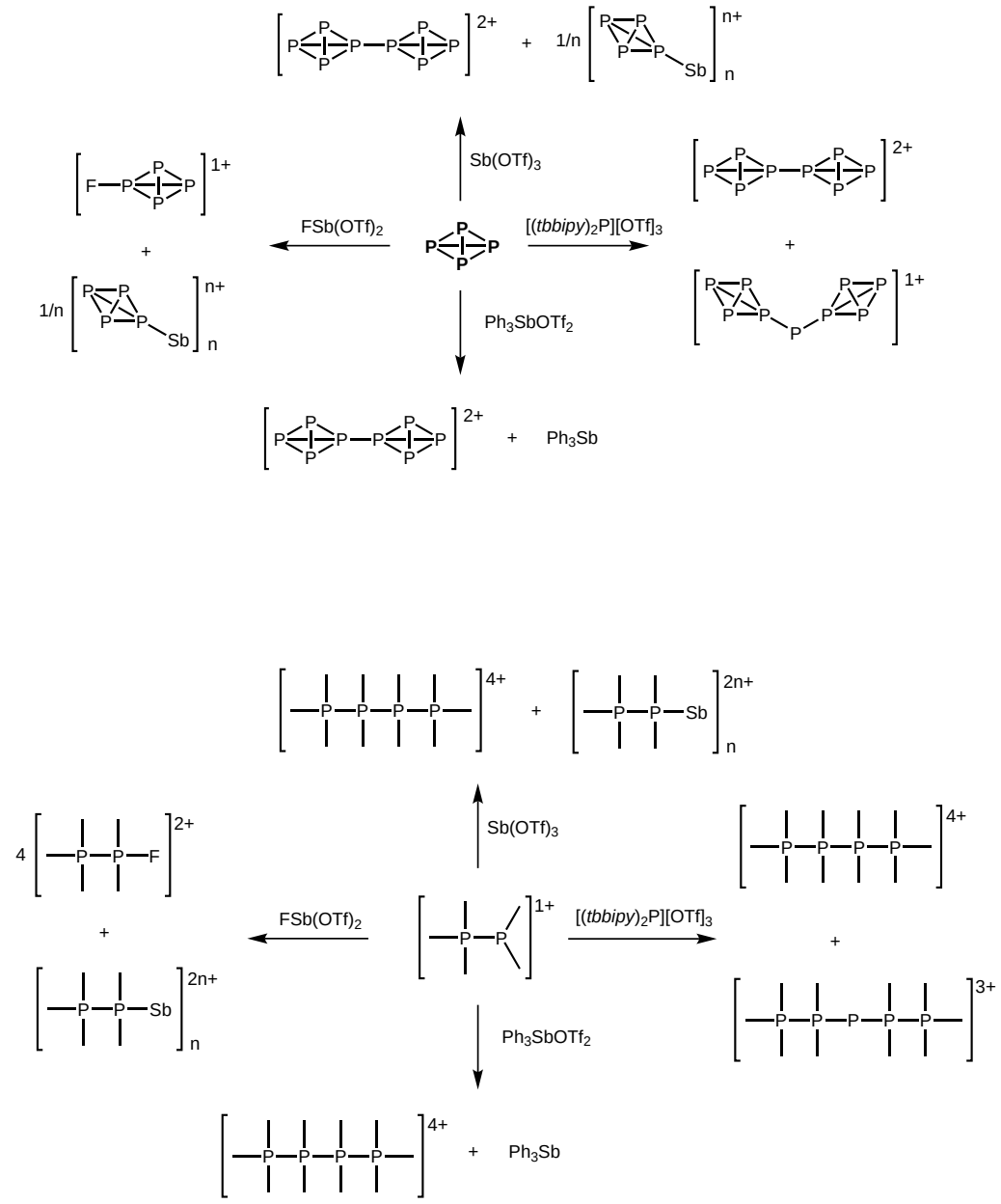

Scheme 8.2.1. Application of oxidative P−P coupling as a novel strategy to make *catena*-phosphorus cations.

example, $Ph_3Sb(OTf)_2$. The diphosphonium with the longest reported P−P bond is $[(Et_2N)_3PP(NEt_2)_3]^{2+}$ (2.364 Å[101], *cf.* 2.198 Å[7] in $[Me_3PPMe_3]^{2+}$), and reactivity studies for this cation have not yet been reported. It is possible that heavily substituted disphosphoniums exist in equilibrium with dissociated radical cations and consistent with this hypothesis a redistribution reaction between two homoleptically substituted

diphosphoniums to give a heteroleptically substituted derivative has been evidenced recently.[238]

As shown in Scheme 8.3.1, a number of interesting reactions leveraging facile P−P bond cleavage may be envisioned from such an activated species. The process outlined in Scheme 8.3.1*a* is an oxidative addition of the P−P bond to a metal centre, which represents a reversal of the diphosphonium reductive elimination described in Chapter 5 and in the previous section. Electron rich, late transition metals may be particularly susceptible to such oxidative additions, providing an alternative route to phosphine complexes of platinum group metals in the +2 oxidation state. Scheme 8.3.1*b*,*c* represent activation of σ and π bonds with diphosphoniums. Activation of substrates containing the C=O group may be particularly favourable since the resultant P−C and P−O bonds are both quite robust. Scheme 8.3.1*d* represents an unusual $4 + 2$ addition reaction between a diphosphonium and a diene, which has also not been reported previously and constitutes a unique way of functionalizing hydrocarbon substrates with a phosphorus centre.

As diphosphoniums are an isolable but metastable species, all of these reaction can in principle exhibit reversibility and a study of reaction and reagent conditions necessary to achieve the targeted directionality of reaction outcomes offers a promising framework for further study of these fundamentally new transformations.

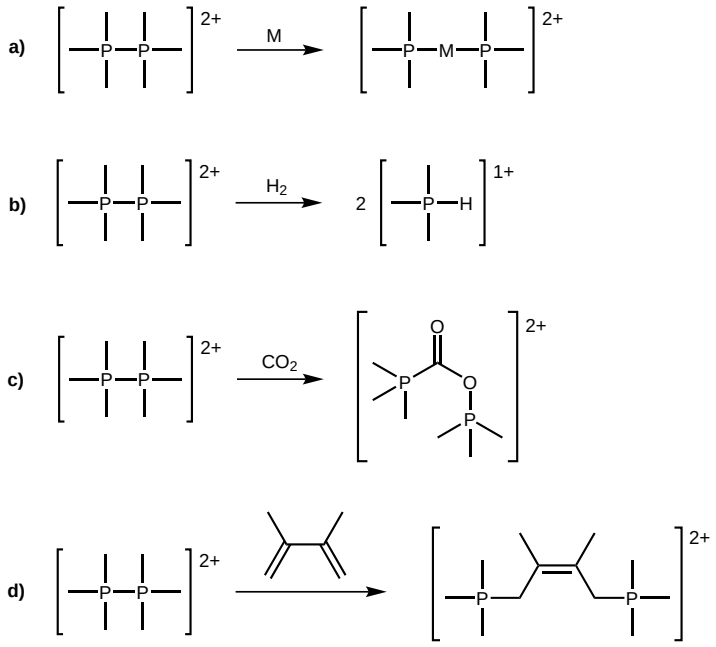

Scheme 8.3.1. Application of oxidative P−P coupling as a novel strategy to make *catena*-phosphorus cations.

Chapter 9

Experimental

9.1 General Procedures

As the majority of compounds studied in this dissertation are sensitive to oxygen and water, their handling requires an inert atmosphere of dried nitrogen or argon gas. All preparative work was therefore carried out under strictly anhydrous and oxygen-free conditions using Schlenk/vacuum-line techniques or within the inert atmosphere of a glovebox.

Schlenk Line: A dual-manifold vacuum-gas line was used for all synthesis conducted outside the glovebox. The base vacuum of the vacuum manifold was always maintained in the 10^{-2} to 10^{-3} mbar range as measured dynamically with a Welch or Vacuubrand digital vacuum gauge and as maintained by an Edwards RV8 or Vacuubrand RV5 pump. A double nitrogen trap was used to avoid contamination of the vacuum pumps. For the inert-gas manifold, the highest available purity of nitrogen and argon were employed, but only after these had been additionally passed either through a column of P_2O_5 supported upon silica or activated molecular sieves for further purification. Standard organometallic reagent transfer techniques were employed.

Glovebox: Experimental work conducted in gloveboxes was done in one of the following gloveboxes: Innovative Technologies (nitrogen working gas, titanocene chemical test for atmosphere quality), MBraun LabMaster 110 (nitrogen working gas, H_2O and O_2 levels < 0.5 ppm) MBraun Labmaster 130 (argon working gas, H_2P and O_2 levels < 0.5 ppm). Small scale reactions were carried out in glass vials with Teflon coated caps using dry and deoxygenated solvents that were stored in the glovebox

over activated molecular sieves. Samples for NMR analyses were prepared either in Teflon-valved J. Young tubes or in standard plastic-capped tubes where a sleeve of Teflon was created using Teflon tape between the plastic cap and the glass surface. Additionally, Teflon tape was also wrapped around the seam of the plastic cap to create a Teflon-Teflon seal and a final layer of Parafilm was wrapped around the seam. Samples prepared in this manner showed no evidence of atmospheric contamination for at least 16-24 hours outside the glovebox environment. The atmosphere of the box was maintained by a twenty-minute purge at the end of each working day and overnight circulation over a catalyst column consisting of copper and activated molecular sieves. Upon use of volatile reactive substances such as PMe_3, a 10-minute purge was carried out.

All solvents were distilled in an argon or nitrogen atmosphere from the appropriate drying agent directly into Teflon-valved Strauss flasks containing freshly-activated molecular sieves of the appropriate porosity (3 Å for MeCN, 4 Å otherwise). Molecular sieves were activated by heating to 300 °C under dynamic vacuum for 24 hours and stored under an atmosphere of inert gas. Solvents were stored in these flasks for a minimum of 48 hours prior to use. Ethereal (Et_2O and THF)and hydrocarbon (C_6H_6, pentane, hexane, toluene) solvents were distilled from potassium. MeCN and CH_2Cl_2 were distilled from CaH_2. Deuterated solvents were dried by storage over activated molecular sieves for 48 hours prior to use.

NMR spectra were obtained on a number of instruments and therefore the field strength is given explicitly with the characterization data for the compounds. In all cases the chemical shifts for ^1H, ^{31}P, and ^{19}F NMR chemical shifts were referenced to $SiMe_4$, 85 % H_3PO_4, and $CFCl_3$, respectively.

Raman spectra were obtained on a Bruker RFS 100 instrument equipped with an Nd-YAG laser (1064 nm excitation). A custom built low-temperature module was used to cool samples with liquid nitrogen-boiloff. Infrared spectra were obtained at room temperature on a Bruker Vector FT-IR spectrometer using CsI plates, or a Bruker Vertex 70 instrument equipped with a RAM II module and an Nd-Yag laser (1064 nm). Selected IR spectra were recorded on a Perkin Elmer Frontier instrument using an ATR unit (diamond).

Quantum chemical calculations were performed using the Gaussian-09 suite[239] of programs as implemented on the Grex cluster within the WestGrid high-performance

computing environment.

9.2 Compounds in Chapter 2

9.2.1 $[Me_3PPMe_2][Cl]$

Me_2PCl (0.483 g, 5.00 mmol) was added to a glass bulb equipped with a Teflon stir bar and frozen at 196 °C. Trimethylphosphine (0.381 g, 5.00 mmol) was condensed and frozen onto the walls of the bulb at −196 °C and any non-condensed material was removed under dynamic vacuum. The bulb was allowed to warm to room temperature with stirring for 5 minutes to yield a fine white powder, which was subjected to dynamic vacuum for 12 hours to remove any volatiles (crude yield = 0.859 g, 99%). A portion of the crude powder was removed for solid-state NMR Analysis and the remainder (0.349 g) was sublimed under dynamic vacuum at approximately 60°C to yield the title product as a fine white powder (0.276 g, 77 %). Due to the low solubility of the powder, a high-resolution solution NMR could not be obtained. For the same reason only a small amount of crystals (< 2 % yield) were isolated from a saturated MeCN solution over 1 week at 30 °C and identified as $[Me_3PPMe_2][Cl]$ using X-ray crystallography. The sublimation range and the elemental composition of the crystals was found to match that of the bulk powder. Yield (fractional yield of sublimation extended to bulk): 0.661 g (77%); Melting Point: 190 − 197 °C sublimes; Elemental Analysis (calcd./expt.): C (34.80/34.54), H (8.76/8.15); Raman (normalized intensities): 83.9 (16), 245.2 (33), 259.9 (15), 268.4 (27), 280.6 (12), 292.8 (9), 329.5 (15), 449.2 (66), 537.2 (14), 666.7 (32), 672.8 (12), 691.1 (72), 713.1 (30), 774.2 (25), 1391.1 (15), 1416.7 (8), 1433.6 (29), 1460.7 (27), 2082.5 (10), 2474.7 (12), 2800.9 (8), 2808.2 (8), 2830.2 (11), 2858.3 (55), 2865.6 (32), 2879.0 (32), 2897. 4 (96), 2914.5 (45), 2948.7 (91), 2957.2 (92), 2964.6 (100), 2980.4 (43), 3001.2 (31); ^{31}P CP-MAS NMR (12 kHz): −65.9 (*d*, $^1J_{PP}$ = 249 Hz), 20.0 (*d*, $^1J_{PP}$ = 249 Hz). Crystallgraphic details for $[Me_3PPMe_2][Cl]$: formula = $C_5H_{15}ClP_2$, mw = 172.56, $Pmn2_1$, a = 9.4581(6) Å, b = 6.5601(4) Å, c = 7.3060 (5), V = 453.31(5) Å^3, Z = 2, ρ = 1.264, μ = 0.690, λ = 0.71073, T = 173.15 K, 3886 reflections collected, 1106 unique ($R_{int.}$ = 0.0167), g.o.f. = 1.110 (all data), R_1 = 0.0177, wR_2 = 0.0465.

9.2.2 $[(Me_3P)_2PMe][Cl]_2$

$MePCl_2$ (0.059 g, 0.50 mmol) and PMe_3 (0.076 g, 1.00 mmol) were combined in 2 mL MeCN and stirred for 5 minutes to yield a white suspension. The solvent was removed under dynamic vacuum and white powder, obtained in essentially quantitative yield, was characterized using ^{31}P CP-MAS NMR. Melting Point: $205 - 220$ °C sublimes; ^{31}P CP-MAS NMR(12 kHz): -63 (broad t), 20.0 (broad d).

9.2.3 $[(Me_3P)PPh_2][Cl]$

Ph_2PCl (0.110 g, 0.50 mmol) and PMe_3 (0.038 g, 0.50 mmol) were combined in CD_3CN (2 mL) and the reaction mixture was stirred for 5 minutes to yield a clear and colourless solution. The crude reaction mixture was analyzed using ^{31}P and ^{1}H NMR spectroscopy. $^{31}P\{^{1}H\}$ NMR (CD_3CN, 122 MHz, 298 K): -24 (broad s), 15 (broad s).

9.2.4 $[(Me_3P)_2PPh][Cl]_2$

$PhPCl_2$ (0.089 g, 0.50 mmol) and PMe_3 (0.076 g, 1.0 mmol) were combined in 2 mL MeCN and stirred for 5 minutes to yield a white suspension. The solvent was removed under vacuum and solids characterized using ^{31}P CP-MAS NMR and elemental Analysis. Melting Point: $212 - 225$ °C sublimes; ^{31}P CP-MAS NMR(11 kHz): -51 (broad s), 2.0 (broad s), 33.0 (broad s, *cyclo*-Ph_4P_4), 20.0 (broad d), +96 (broad s, Me_3PCl_2).

9.2.5 $[Me_2P(dmpe)PMe_2][Cl]_2$

Me_2PCl (0.291 g, 3.00 mmol) was added to a glass bulb equipped with a Teflon stir bar and frozen at -196 °C. Neat *dmpe* (0.450 g, 3.00 mmol) was condensed and frozen onto the walls of the bulb at 196 °C and any non-condensed material was removed under dynamic vacuum. The bulb was allowed to warm to room temperature with stirring for 5 minutes to yield a fine white powder, which was subjected to dynamic vacuum for 12 hours to remove any volatiles (crude yield = 0.487 g, 95%). A portion of the crude powder was removed for solid-state NMR Analysis and the remained (0.113 g) was sealed in a glass tube and sublimed under static vacuum at 80 °C to

yield a fine white powder (0.106 g, 94%). Repeated attempts to grow crystals from a saturated MeCN solution failed to produce crystalline material. Yield (fractional yield of sublimation extended to bulk): 0.458 g, 94%; Melting Point: 185 − 200 °C sublimes; Elemental Analysis (calcd./expt.): C (35.00/34.68), H (8.22/7.78); ^{31}P CP-MAS NMR(12 kHz): −75.1 (*d*, $^{1}J_{PP}$ = 273 Hz), 29.5 (*d*, $^{1}J_{PP}$ = 273 Hz).

9.2.6 [(*dmpe*)PMe][Cl]$_2$

$MePCl_2$ (0.148 g, 1.27 mmol) in 3 mL CH_2Cl_2 was added to a glass bulb equipped with a Teflon stir bar and cooled to −30 °C. Neat *dmpe* (0.191 g, 1.27 mmol) was dissolved in CH_2Cl_2 and added at once to the stirring solution to immediately yield a large amount of white precipitate. The suspension was stirred for an additional 5 minutes and then placed under vacuum to remove all volatiles to yield a fine white powder (crude yield = 0.330 g, 97%). The powder was washed with 5 mL MeCN and placed under dynamic vacuum for 12 hours to remove any volatiles. The resulting fluffy white powder (0.317 g), which is difficult to handle as it easily develops static charge, was found to be analytically pure. Yield: 0.227 g, 94%; Melting Point: 197 − 205 °C sublimes; Elemental Analysis (calcd./expt.): C (31.48/31.25), H (7.17/7.17); ^{31}P CP-MAS NMR (9 kHz): −86.4 (*t*, $^{1}J_{PP}$ = 271 Hz), 49.8 (*dd*, $^{1}J_{PP}$ = 296 Hz).

9.2.7 [Ph_2P(*dmpe*)PPh_2][Cl]$_2$

Ph_2PCl (0.220 g, 1.00 mmol) and *dmpe* (0.075 g, 0.50 mmol) were combined in 2 mL CD_2Cl_2 and stirred for 5 minutes to yield a clear, light pink solution. The crude reaction mixture was analyzed using ^{31}P and ^{1}H NMR spectroscopy. $^{31}P\{^{1}H\}$ NMR (CD_3CN, 122 MHz, 298 K): −13 (broad *s*), 20 (broad *s*).

9.2.8 [(*dmpe*)PPh][Cl]$_2$

$PhPCl_2$ (0.180 g, 1.00 mmol) and *dmpe* (0.150 g, 1.00 mmol) were combined in 2 mL MeCN and stirred for 5 minutes to yield a white suspension. The solvent was removed under dynamic vacuum and solids characterized using ^{31}P CP-MAS NMR. Melting Point: 176 − 193 °C sublimes; ^{31}P SS NMR (8 kHz): −77 (broad *s*), 48 (broad *s*).

9.2.9 $[(dmpe)PPh][OTf]_2$

$PhPCl_2$ (0.180 g, 1.00 mmol), *dmpe* (0.150 g, 1.00 mmol) and TMSOTf (0.222 g, 2.00 mmol) were combined in 2 mL CD_3CN and stirred for 5 minutes to yield a clear, colourless solution. The reaction mixture was analyzed by solution ^{31}P NMR and ^{1}H NMR. $^{31}P\{^{1}H\}$ NMR (CD_3CN, 120 MHz, 298 K): -68.4 (*dd*, $^{1}J_{PP} = 275$ Hz), 53.9 (*dd*, $^{1}J_{PP} = 277$ Hz)

9.2.10 $[(Me_3P)_2P][Cl]$

PMe_3 (1.140 g, 15 mmol) was added to PCl_3 (0.686 g, 5 mmol) in 7 mL dichloromethane to immediately obtain a white precipitate, which became yellow by the end of the addition (1 minute). The reaction mixture was allowed to stir for 1 hour at room temperature to obtain a yellow suspension. Removal of volatiles yielded a fine yellow powder with some orange flecks (yield = 1.826 g, no loss of material). A small amount of the powder was washed with CD_3CN (low solubility) and analyzed by ^{31}PNMR spectroscopy. The insoluble portion was analyzed by ^{31}P CP-MAS NMR spectroscopy. ^{31}P NMR(CD_3CN, 298 K): -156.5 (*dd*, $^{1}J_{PP} = 439$, 438 Hz), 14.7 (*dd*, $^{1}J_{PP} = 439$, 438 Hz); ^{31}P CP-MAS NMR(12 kHz): -146 (*t*, $^{1}J_{PP} = 432$ Hz), 18 (*d*, $^{1}J_{PP} = 436$ Hz), 26 (broad *s*), 96 (broad *s*, Me_3PCl_2).

9.3 Compounds in Chapter 3

9.3.1 $[(Me_3P)SbCl_3]_x$

Trimethylphosphine (0.080 g, 1.00 mmol) and $SbCl_3$ (0.23 g, 1.00 mmol) were combined in MeCN. The resulting white suspension was stirred for 1 h and then allowed to settle. Crystals were obtained from the supernatant by slow evaporation. Yield: 0.270 g, 88 %; Melting point: 188-190 °C; Elemental Analysis (calcd./expt.): C (11.85/11.87), H (2.98/3.22); Raman (normalized intensities): 66.46 (25), 77.0 (36), 85.7 (43), 91.5 (32), 119.5 (36), 127.2 (68), 139.7 (45), 144.6 (57), 158.1 (23), 159.0 (23), 161.9 (23), 193.7 (25), 211.1 (68), 229.4 (18), 243.9 (54), 255.5 (30), 266.1 (52), 277.6 (63), 310.4 (102), 346.1 (27), 1406.8 (9), 1415.4 (11), 2911.0 (100), 2977.5 (20), 2983.3 (27), 2986.2 (18), 3003.6 (18), 3007.4 (7); NMR (CD_3CN, 298 K, 300.3 MHz field strength): ^{1}H: 1.98

ppm (*d*, $^{2}J_{\mathrm{PH}}$ = 14.3 Hz), ^{13}C{^{1}H}: 10.1 ppm, (*d*, $^{1}J_{\mathrm{CP}}$ = 35 Hz), ^{31}P{^{1}H}: 9.6 ppm (*s*).

9.3.2 $[(Me_3P)_2SbCl_3]$

A solution of PMe_3 (0.46 g, 6.0 mmol) in 4 mL MeCN was added to $SbCl_3$ (0.68 g, 3.0 mmol) dissolved in 4 mL MeCN. Midway through the addition a large amount of white precipitate appeared. By the end of addition a clear, pale yellow solution was obtained which was allowed to stir for 30 minutes, concentrated under vacuum to *ca.* 2 mL and filtered through glass wool. Colourless blocks were obtained by diffusion of Et_2O into the concentrated MeCN solution. The crystals were washed with cold MeCN and dried under vacuum. Yield: 1.10 g, 97 %. Melting point: 110-113°C (dec). Elemental Analysis (calcd./expt.): C (18.95/18.84), H (4.77/4.59); Raman (normalized intensities): 116 (17), 130 (11), 149 (16), 173 (6), 187 (2), 206 (3), 223 (12), 257 (38), 265 (23), 328 (2), 352 (6), 668 (35), 747 (6), 754 (8), 757 (7), 758 (6), 947 (2), 1303 (3), 1307 (3), 1402 (6), 1411 (7), 1420 (7), 2794 (2), 2899 (100), 2904 (69), 2909 (42), 2972 (33), 2982 (20), 3000 (11), 3015 (3); NMR (CD_3CN, 298 K, 8.45 T field strength): ^{1}H: 1.76 ppm (*d*, $^{2}J_{\mathrm{PH}}$ = 11.33 Hz), ^{13}C{^{1}H}: 11.9 ppm (*d*, $^{1}J_{\mathrm{CP}}$ = 25.0 Hz), ^{31}P: −10.2 ppm (*m*, $^{2}J_{\mathrm{PH}}$ = 11.2 Hz).

9.3.3 $[(Ph_3P)SbCl_3]_2$

$SbCl_3$ (0.23 g, 1.0 mmol) and PPh_3 (0.26 g, 1.0 mmol) were combined in CH_2Cl_2 (4 mL) to obtain a clear, golden yellow solution, which was stirred for 1 h. The reaction mixture was filtered and concentrated under vacuum to *ca.* 2 mL and stored at room temperature for 24 h, which led to the formation of small yellow crystals. The reaction mixture was removed from vacuum and allowed to sit at room temperature for 24 h which led to the formation of yellow block-shaped crystals that were washed with 0.5 mL cold CH_2Cl_2 and dried under vacuum. Yield: 0.41 g, 84 %. Melting point: 120-122 °C; Elemental Analysis (calcd./expt.): C (44.09/44.97), H (3.08/3.23); I.R. (Nujol mull, KBr plates, cm^{-1}): 499, 516, 615, 664, 668, 691, 712, 743, 845, 853, 925, 967, 994, 1022, 1036, 1070, 1093, 1167, 1180, 1306, 1377, 1395, 1405, 1436, 1457, 1718, 2321, 2854, 2926; NMR (CD_2Cl_2, 298 K, 7.0 T field strength): ^{1}H: 7.1-7.9 (*m*, PPh_3), ^{13}C{^{1}H}: 128.4 ppm (*d*, $^{1}J_{\mathrm{CP}}$ = 25.0 Hz), ^{31}P{^{1}H}: 5.6 ppm (*s*).

9.3.4 $[(Ph_3P)_2SbCl_3]$

PPh_3 (0.52 g, 2.0 mmol) and $SbCl_3$ (0.23 g, 1.0 mmol) were combined in 5 mL CH_2Cl_2. The resulting clear yellow solution was stirred for 1 h, filtered through glass wool, concentrated under vacuum to 2 mL, and recrystallized at −30°C to obtain light yellow translucent crystals. The crystals were isolated by decantation, washed with 0.5 mL cold CH_2Cl_2 and dried under vacuum. Yield: 0.65 g 86%. Melting point: 115-118 °C. Elemental Analysis (calcd./expt.): C (57.45/57.75), H (4.02/4.39); I.R. (Nujol mull, KBr plates, cm^{-1}): 441, 489, 498, 516, 545, 616, 668, 691, 713, 723, 742, 774, 845, 853, 893, 926, 966, 994, 1022, 1026, 1070, 1092, 1157, 1169, 1305, 1377, 1399, 1437, 1457, 1463, 1718, 2345, 2363, 2669, 2724, 2924, 3421; NMR (CD_2Cl_2, 298 K, 7.0 T field strength): ^{1}H: 7.1-7.9 (*m*, PPh_3), $^{13}C\{^1H\}$: 128.4 ppm (*d*, $^1J_{CP}$ = 25.0 Hz), $^{31}P\{^1H\}$: 5.6 ppm (*s*).

9.3.5 $[(Cy_3P)SbCl_3]_2$

$SbCl_3$ (0.11 g, 0.50 mmol) and PCy_3 (0.14 g, 0.50 mmol) were combined in 3 mL of CH_2Cl_2 to obtain a light yellow solution. The reaction mixture was stirred for 20 minutes, filtered through glass wool and concentrated under vacuum to 1 mL. Very pale yellow block-like crystals were obtained over 48 hours at −30°C, isolated by decantation, washed with 0.5 mL cold CH_2Cl_2 and dried under vacuum. Yield: 0.21 g, 82 %. Melting point: 142-145 °C (dec). Elemental Analysis (calcd./expt.): C (42.51/42.73), H (6.54/6.63). NMR (CD_2Cl_2, 298 K, 8.45 T field strength): ^{1}H: 1.36 1.92 ppm (*m*, 10H), 3.23 ppm (tq, 12.9 Hz, 2.6 Hz, ^{1}H), $^{13}C\{^1H\}$: 26.3 ppm, (*s*), 27.82 (*d*, $^3J_{CP}$ = 11.2 Hz), 29.65 (*d*, $^2J_{CP}$ = 4.8 Hz), 33.85 (*d*, $^1J_{CP}$ = 15.0 Hz), $^{31}P\{^1H\}$: 25.1 ppm (*s*).

9.3.6 $[(Cy_3P)_2SbCl_3]$

$SbCl_3$ (0.11 g, 0.50 mmol) and PCy_3 (0.28 g, 1.0 mmol) were combined in a 3 mL of MeCN. The reaction mixture was stirred for 16 h to get a light yellow suspension. The supernatant was removed and the precipitate was washed with 3 mL of cold MeCN and pumped dry. The supernatant was concentrated under vacuum to obtain yellow needle-shaped crystals. The crystals and bulk powder exhibited identical NMR spectra, although trace amounts of $[(Cy_3P)SbCl_3]$ was also found in the bulk and

could not be separated by recrystallization. Yield (impure): 0.66 g. Melting point: 135-138 °C. Elemental Analysis (calcd./expt.): C (54.80/52.38), H (8.43/8.07). NMR (CD_2Cl_2, 298 K, 7.0 T field strength): ^{1}H: 1.34-2.56 ppm (*m*), ^{31}P{^{1}H}: 15.7 ppm (*s*).

9.3.7 $[(Me_3P)SbPhCl_2]$

A solution of PMe_3 (0.04 g, 0.50 mmol) in 1 mL MeCN was added to $PhSbCl_2$ (0.13 g, 0.50 mmol) dissolved in 3 mL MeCN. The clear colourless reaction mixture was allowed to stir for 15 minutes, filtered and concentrated under vacuum at room temperature to obtain clear colourless crystalline blocks that were washed with 0.5 mL cold MeCN and dried under vacuum. Yield: 0.30 g, 86 %. Melting point: 147-149 °C. Elemental Analysis (calcd./expt.): C (31.26/31.53), H (4.08/4.19). NMR (CD_3CN, 298 K, 300.3 MHz field strength): ^{1}H: 1.75 ppm (*d*, $^2J_{PH}$ = 13.9 Hz, 9H), 7.38-7.52 ppm (*m*, 3H), 8.29 ppm (*m*, 2H), ^{13}C{^{1}H}: 10.2 ppm, (*d*, $^1J_{CP}$ = 35 Hz), ^{31}P{^{1}H}: −9.2 ppm (*s*).

9.3.8 $[(Ph_3P)SbPhCl_2]_2$

A solution of PPh_3 (0.262 g, 1 mmol) in 2 mL CH_2Cl_2 was added to $PhSbCl_2$ (0.260 g, 1 mmol) dissolved in 2 mL CH_2Cl_2. The clear golden yellow reaction mixture was allowed to stir for 15 minutes, filtered and concentrated under vacuum to *ca.* 1 mL. Yellow crystalline blocks were obtained by diffusion of pentane vapour into this solution at −30°C over 24 h, and isolated by decanting the supernatant. Yield: 0. 217 g, 42 %. Melting point:118 °C dec.; Raman (normalized intensities): 91 (100), 128 (3), 150 (16), 181 (4), 198 (12), 217 (3), 249 (9), 267 (7), 311 (12), 343 (33), 410 (13), 444 (7), 518 (22), 617 (3), 685 (2), 714 (4), 749 (3), 998 (50), 1025 (18), 1096 (30), 1161 (6), 1184 (4), 1434 (4), 1480 (3), 1573 (4), 1584 (54), 3043 (4), 3057 (35), 3071 (2); NMR (CD_2Cl_2, 298 K, 8.45 T field strength): ^{1}H: 7.1-7.9 (*m*, PPh_3), ^{13}C{^{1}H}: 128.4 ppm (*d*, $^1J_{CP}$ = 25.0 Hz), ^{31}P{^{1}H}: 5.6 ppm (*s*) .

9.3.9 $[(Ph_3P)_2SbPhCl_2]$

This product could not be isolated as a pure substance and was formed together with $[(Ph_3P)Sb(Ph)Cl_2]$. A solution of PPh_3 (0.262 g, 1 mmol) in 2 mL MeCN was added to $PhSbCl_2$ (0.130 g, 1 mmol) to obtain a yellow solution, which was allowed to stir for 40 minutes. Upon concentration to 1 mL at −30°C for 72 h, a mixture of yellow

and colourless crystals was obtained and the colourless crystals were identified as $[(Ph_3P)_2SbPhCl_2]$ by X-ray crystallography. It was not possible to manually isolate a sufficient quantity of the colourless crystals to characterize the compound as a pure substance.

9.3.10 $[(Me_3P)SbCl_2][OTf]$

$SbCl_3$ (0.11 g, 0.50 mmol) and TMSOTf (0.11 g, 0.50 mmol) were combined in 2.5 mL of MeCN and stirred for 1 h. A solution of PMe_3 (0.04 g, 0.50 mmol) in 2 mL MeCN was added and the reaction mixtures was stirred for 1 h to obtain a clear, colourless solution. All volatiles were removed under vacuum to obtain a white powder (0.207 g, calcd. for product 0.209 g), which was recrystallized from MeCN at −30°C to obtain colourless block-shaped crystals, which were washed with cold MeCN and dried under vacuum. Yield: 0.19 g, 91 %. Melting point: 108-111 °C. Elemental Analysis (calcd./expt.): C (11.49/11.37), H (2.17/2.19). NMR (CD_3CN, 298 K, 8.45 T field strength): ^{1}H: 1.99 ppm (d, $^2J_{PH}$ = 14.7 Hz), ^{13}C{^{1}H}: 9.7 ppm (d, $^1J_{CP}$ = 34.1 Hz), ^{31}P{^{1}H}: 14.6 ppm (s), ^{19}F{^{1}H}: −80.0 ppm (s).

9.3.11 $[(Me_3P)_2SbCl_2][OTf]$

$SbCl_3$ (0.228 g, 1.00 mmol) and TMSOTf (0.222 g, 1.00 mmol) were combined in CH_2Cl_2 (4 mL) and stirred for 30 minutes to yield a clear and colourless solution. This was added drop-wise to a stirring solution of PMe_3 (0.228 g, 3.00 mmol) in CH_2Cl_2 (4 mL) over 30 seconds to produce a cloudy white suspension. The reaction mixture was allowed to stir for 1 hour yielding a fine white powder and a clear and colourless supernatant, the ^{31}P{^{1}H} NMR spectrum of which exhibited two signals (5.8 ppm, 85 % and−2.2 ppm, 15 %). Removal of solvent under dynamic vacuum at room temperature over 4 hours yielded a fine white powder (0.515 g), which was dissolved in MeCN (10 mL), filtered and placed in the freezer at −30°C for recrystallization. Highly-reflective colourless blocks were obtained after 5 days, isolated by decantation and washed with cold MeCN (3 x 3 mL). Yield: 0.401 g, 80 %; mp: 135 °C dec.; Elemental Analysis (calcd./expt.): C(17.02/16.97), H(3.67/3.41); Raman (normalized intensities): 84.8 (37), 115.2 (13), 123.4 (35), 140.7 (43), 184.6 (9), 208.7 (17), 212.1 (14), 250.2 (88), 272.4 (12), 317.7 (7), 350.4 (30), 520.6 (1), 576.1 (10), 674.4 (48),

757.8 (35), 765.6 (26), 1024.9 (85), 1226.9 (5), 1246.2 (3), 1415.9 (8), 1418.3 (8), 1433.3 (4), 2920.6 (100), 2989.6 (18), 2996.3 (31), 3006.9 (22); ^{1}H NMR (CD_3CN, 500 MHz, 293 K): 2.08 (*d*, 18H, $^{2}J_{PH}$ = 14.1 Hz); $^{13}C\{^{1}H\}$ NMR (CD_3CN, 125.8 MHz, 293 K): 11.6 (*d*, $^{1}J_{CP}$ = 34.4 Hz), 118.5 (*s*); $^{19}F\{^{1}H\}$ NMR (CD_3CN, 282.44 MHz, 293 K): −79.1 (*s*); $^{31}P\{^{1}H\}$ NMR (CD_3CN, 202.46 MHz, 293 K): 6.2 (*s*).

9.3.12 $[(Me_3P)_2SbCl][OTf]_2$

A solution of excess TMSOTf (0.67 g, 3.0 mmol) in 4 mL MeCN was added to solid $[(Me_3P)_2SbCl_3]$ (0.38 g, 1.0 mmol) and the clear, colourless solution was allowed to stir for 1 h. Volatiles were removed under vacuum to yield a sticky powder, which was redissolved in a minimum of MeCN and recrystallized via diffusion of Et_2O at −30°C to give colourless block-shaped crystals that were washed with 0.5 mL cold MeCN. Yield: 0.50 g, 82 %. Melting point: 157-160 °C. Elemental Analysis (calcd./expt.): C (15.81/15.45), H (2.99/2.83); I.R. (Nujol mull, KBr plates, cm^{-1}): 514, 573, 638, 667, 722, 754, 759, 786, 848, 857, 866, 961, 1019, 1027, 1077, 1157, 1169, 1207, 1268, 1287, 1339, 1366, 1376, 1456, 1464, 1717, 2040, 2340, 2360, 2670, 2726, 2852, 2923, 2952; Raman (normalized intensities): 79.9 (17), 86.4 (18), 109.9 (15), 129.1 (22), 143.6 (29), 148.4 (24), 166.7 (12), 177.3 (25), 196.6 (41), 218.8 (36), 226.7 (38), 262.2 (14), 265.1 (17), 275.7 (9), 317.2 (31), 342.2 (50), 347.1 (73), 355.7 (45), 514.8 (5), 575.6 (15), 636.3 (5), 671.0 (34), 756.9 (8), 763.6 (47), 1022.0 (27), 1028.8 (100), 2915.5 (39), 2923.5 (41), 2327.4 (41), 2932.2 (31), 2987.2 (13), 2990.1 (13), 2996.8 (20), 3006.5 (24), 3010.3 (15), 3020.9 (6); NMR (CD_3CN, 298 K, 8.45 T field strength): ^{1}H: 2.0 ppm (*d*, $^{2}J_{PH}$ = 14.6 Hz), $^{13}C\{^{1}H\}$: 9.6 ppm (*d*, $^{1}J_{CP}$ = 34.0 Hz), $^{31}P\{^{1}H\}$: 15.8 (*s*, broad).

9.3.13 $[(Me_3P)SbCl_2][OTf]$

$SbCl_3$ (0.11 g, 0.50 mmol) and TMSOTf (0.11 g, 0.50 mmol) were combined in 2.5 mL of MeCN and stirred for 1 h. A solution of PMe_3 (0.04 g, 0.50 mmol) in 2 mL MeCN was added and the reaction mixtures was stirred for 1 h to obtain a clear, colourless solution. All volatiles were removed under vacuum to obtain a white powder (0.207 g, calcd. for product 0.209 g), which was recrystallized from MeCN at −30°C to obtain colourless block-shaped crystals, which were washed with cold MeCN and dried under vacuum. Yield: 0.19 g, 91 %. Melting point: 108-111 °C. Elemental Analysis

(calcd./expt.): C (11.49/11.37), H (2.17/2.19). NMR (CD_3CN, 298 K, 8.45 T field strength): ^{1}H: 1.99 ppm (*d*, $^2J_{PH}$ = 14.7 Hz), $^{13}C\{^1H\}$: 9.7 ppm (*d*, $^1J_{CP}$ = 34.1 Hz), $^{31}P\{^1H\}$: 14.6 ppm (*s*), $^{19}F\{^1H\}$: −80.0 ppm (*s*).

9.3.14 $[(Ph_3P)_2SbCl_2][OTf]$

To a solution of $SbCl_3$ (0.09 g, 0.40 mmol) in CH_2Cl_2 (1 mL) was added a solution of PPh_3 (0.11 g, 0.40 mmol) in CH_2Cl_2 (1 mL). Neat TMSOTf (0.09 g, 0.40 mmol) was added and the clear, bright yellow solution stirred at room temperature. Following filtration through glass wool and concentration under reduced vacuum, crystalline yellow blocks were obtained after storage at room temperature for 24 h. The crystals were washed with 0.5 mL cold CH_2Cl_2 and dried under vacuum. Yield: 0.66 g, 76 %. Melting point: 105 °C (dec.). Elemental Analysis (calcd./expt.): C (51.30/51.05), H (3.49/3.01); IR (Nujol mull, cm^{-1}): 1450, 1436, 1419, 1395, 1298, 1226, 1212, 1165 , 1095, 1028, 1017, 998, 747, 725, 711, 691, 634, 619, 570, 516, 498, 493, 419, 398, 375, 354, 335, 328, 324, 304; NMR (298 K, 11.7 T field strength): ^{1}H ($CDCl_3$): 7.46-7.57 ppm (*m*, Ph), $^{13}C\{^1H\}$ ($CDCl_3$): 128.4 (*d*, $^1J_{CP}$ = 24 Hz), 129.2 (*d*, $^3J_{CP}$ = 10 Hz), 131.3 (*s*), 134.0 (*d*, $^2J_{CP}$ = 13 Hz), $^{31}P\{^1H\}$(CD_2Cl_2): −5.0 ppm (*s*, broad).

9.3.15 $[(Me_3P)SbPh_2][OTf]$

$Sb(OTf)_3$ (0.29 g, 0.50 mmol) and $SbPh_3$ (0.35 g, 1.0 mmol) were combined in MeCN (4 mL) and stirred for 1 h to get a pale yellow solution of Ph2SbOTf. Neat PMe_3 (0.11 g, 1.5 mmol) was added in three portions to obtain a clear, light yellow solution. This reaction mixture was stirred for 40 minutes, filtered through glass wool, concentrated under vacuum to approximately 2 mL. Colourless crystals were obtained upon storage −30°C for 24 h, isolated by removing the supernatant by pipette and washed with 0.5 mL cold MeCN and dried under vacuum. Yield: 0.42 g, 83 %. Melting point: 117-119 °C. Elemental Analysis (calcd./expt.): C (38.35/38.66) H (3.82/3.88); I.R. (Nujol mull, KBr plates): 448 (m), 515 (m), 571 (m), 637 (m), 664 (w), 695 (m), 728 (s), 756 (m), 853 (m), 959 (s), 996 (w), 1028 (m), 1064 (w), 1154 (s), 1223 (m), 1268 (s), 1294 (w), 1377 (s), 1460 (s), 1718 (m), 2725 (w), 2918 (s); NMR (CD_3CN, 298 K, 300.3 MHz field strength): ^{1}H: 1.60 ppm (*d*, $^2J_{PH}$ = 13.5 Hz, 9H), 7.52-7.57 ppm (*m* 6H), 7.67-7.72 (*m* 4H), $^{13}C\{^1H\}$: 10.3 ppm (*d*, $^1J_{CP}$ = 31.9 Hz), 130.9 ppm (*s*), 131.6

ppm (s), 138.1 ppm (s), $^{31}P\{^{1}H\}$: -21.2 ppm (s), $^{19}F\{^{1}H\}$: ppm (s): -79.2 ppm (s).

9.3.16 $[(Me_3P)_2SbPh_2][OTf]$

A solution of $Sb(OTf)_3$ (0.29 g, 0.50 mmol) and $SbPh_3$ (0.35 g, 1.0 mmol) were combined in MeCN (4 mL) and stirred for 1 h to get a pale yellow solution. All volatiles were removed under vacuum to yield an off-white powder, which was not isolated. The powder was redissolved in CH_2Cl_2 (3 mL) and a solution of PMe_3 (0.34 g, 4.5 mmol) in CH_2Cl_2 (3 mL) was dropwise added to get a clear, very light brown solution. This reaction mixture was stirred for 10 minutes, filtered, concentrated under vacuum to approximately 3 mL. Large, colourless blocks, obtained upon recrystallization at -30°C over 24 h, were isolated by removing the supernatant by pipette and were washed with 0.5 mL cold CH_2Cl_2 and dried under vacuum. Yield: 0.69 g, 80 %. Melting point: 98-100 °C. Elemental Analysis (calcd./expt.): C (39.54/39.96), H (4.89/4.68). NMR (CD_2Cl_2, 298 K, 8.45 T field strength): ^{1}H: 1.19 ppm (d, $^{2}J_{PH}$ = 7.9 Hz, 18H), 7.53-7.59 ppm (m, 6H), 7.65-7.69 (m, 4H), $^{13}C\{^{1}H\}$: 12.2 ppm (d, $^{1}J_{CP}$ = 12.1 Hz), 130.6 ppm (s), 131.0 ppm (s), 136.6 ppm (s), $^{31}P\{^{1}H\}$: -41.3 ppm (s), $^{19}F\{^{1}H\}$: -79.2 ppm (s).

9.3.17 $[(dmpe)SbCl_2][OTf]$

$SbCl_3$ (0.456 g, 2.00 mmol) and TMSOTf (0.446 g, 2.00 mmol) were combined in CH_2Cl_2 (7 mL) and stirred for 30 minutes to yield a clear and colourless solution. A solution of *dmpe* (0.300 g, 2.00 mmol) in CH_2Cl_2 (7 mL) was added drop-wise over 30 seconds. A mixture of brown and white precipitate formed immediately and the reaction was slightly exothermic. The reaction mixture was stirred for 3 h to yield a dark brown powder under a clear and colourless supernatant. The $^{31}P\{^{1}H\}$ NMR spectrum of this supernatant exhibited no signals. Removal of volatiles under dynamic vacuum at room temperature over 4 h yielded a brown powder (1.104 g) and the $^{31}P\{^{1}H\}$ NMR spectrum of this powder in MeCN exhibited one signal (34 ppm). The powder was dissolved in a 1:1 mixture by volume of MeCN and Et_2O and placed in the freezer at -30°C. Small colorless block shaped crystal were obtained after one week along with a small amount of insoluble black powder. The crystals were isolated by decantation and washed with a cold mixture of MeCN/Et_2O (3 x 1 mL). The yield

represents a total of three crops over 2 weeks, Yield: 0.691 g, 76 %; mp 175-220 °C darkens, 220-230 °C dec.; Elemental Analysis (calcd./expt.): C 17.09 (17.11), H 3.28 (3.02); Raman (normalized intensities): decomposition in laser; ^{1}H NMR (CD_3CN, 500 MHz, 293 K): 2.05 (*d*, 12H, $^{2}J_{PH}$ = 14.3 Hz), 2.72 (*m*, 4H); $^{13}C\{^{1}H\}$ NMR (CD_3CN, 125.8 MHz, 293 K): 8.9 (*d*, $^{1}J_{CP}$ = 36.8 Hz), 25.1 (*d*, $^{1}J_{CP}$ = 32.7 Hz), 118.4 (*s*); $^{19}F\{^{1}H\}$ NMR (CD_3CN, 282.44 MHz, 293 K): −79.0 (*s*); $^{31}P\{^{1}H\}$ NMR (CD_3CN, 202.46 MHz, 293 K): 34.1 (*s*).

9.3.18 [(*dmpm*)$SbCl_2$][OTf]

$SbCl_3$ (0.228 g, 1.00 mmol) and TMSOTf (0.223 g, 1.00 mmol) were combined in CH_2Cl_2 (7 mL) and stirred for 30 minutes to yield a clear and colourless solution. A solution of *dmpm* (0.136 g, 1.00 mmol) in CH_2Cl_2 (7 mL) was added drop-wise over 30 seconds. A white precipitate was immediately observed. The reaction mixture was stirred overnight to obtain a light yellow suspension. Removal of volatiles under dynamic vacuum at room temperature over 4 h yielded a light yellow powder, which was washed with CH_2Cl_2 (3 x 1 mL) and MeCN (3 x 1 mL), Yield: 0.400 g, 84 %; mp 166 °C dec.; Raman (normalized intensities): 83.8 (62), 114.2 (46), 151.8 (23), 169.2 (30), 196.2 (34), 216.9 (35), 255.5 (46), 276.7 (49), 310.9 (58), 338.4 (16), 350.9 (16), 364.9 (35), 511 (2), 573.2 (6), 615.6 (5), 656.1 (10), 694.7 (7), 725.1 (4), 743.9 (13), 761.2 (28), 1025.9 (45), 1162.3 (4), 1224.5 (8), 1298.8 (4), 1407.3 (9), 2770.7 (1), 2856 (25), 2910.5 (100), 2918.2 (36), 2972.7 (16), 3000.7 (15.3), 3012.2 (10).; ^{1}H NMR (CD_3CN, 300 MHz, 293 K): 2.13(*m* 12H), 4.05 (*t*, 2H, $^{2}J_{PH}$ = 12 Hz); $^{19}F\{^{1}H\}$ NMR (CD_3CN, 282.44 MHz, 293 K): −79.3 (*s*); $^{31}P\{^{1}H\}$ NMR (CD_3CN, 121.56 MHz, 293 K): 1.4 (*s*).

9.3.19 [(*dppm*)$SbCl_2$][$AlCl_4$]

$SbCl_3$ (1.140 g, 5.00 mmol) and $AlCl_3$ (0.666 g, 5.00 mmol) were combined in CH_2Cl_2 (45 mL) and stirred for 30 minutes to yield a yellow suspension. A solution of *dppm* (1.922 g, 5.00 mmol) in CH_2Cl_2 (15 mL) was added drop-wise over one minute and stirred for an additional 40 minutes. The resulting bright-yellow reaction mixture was clear and exhibited one signal in its $^{31}P\{^{1}H\}$ NMR spectrum (5 ppm). Removal of volatiles under dynamic vacuum at room-temperature over 16 hours yielded a

bright-yellow powder (3.844 g), which was re-dissolved in CH_2Cl_2 (12 mL), filtered, layered with pentane (3 mL) and stored in the freezer at −30°C. Large, yellow block shaped crystals were obtained after 3 days, isolated by decantation and washed with cold pentane (3 x 5 mL). Yield: 2.913 g, 78 %; mp 115 °C dec.; Elemental Analysis (calcd./expt.): C 40.26 (39.52), H 2.97 (2.89); Raman (normalized intensities): 83.8 (81), 116.6 (40), 136.9 (25), 176.4 (50), 205.8 (14), 218.4 (7), 268 (8), 301.3 (72), 329.2 (19), 334.5 (28), 346.1 (17), 407.3 (5), 420.4 (3), 434.8 (2), 452.2 (3), 464.2 (2), 491.7 (5), 493.2 (6), 527.4 (8), 614.2 (9), 671.5 (4), 693.2 (2), 740.9 (2), 748.7 (3), 983 (3), 998.4 (89.9), 1024.9 (37), 1034.1 (6), 1.87.6 (17), 1095.8 (22), 1158.9 (2), 1164.3 (6), 1188.8 (6), 1331.6 (2), 1435.7 (6), 1479.6 (4), 1573.6 (13), 1582.3 (100), 2918.2 (10), 2964.5 (5), 3001.1 (1), 3057.1 (45), 3061.9 (32), 3140.5 (1), 3157.3 (1).; ^{1}H NMR (CD_2Cl_2, 500 MHz, 293 K): 4.31 (*t*, 2H, $^{2}J_{PH}$ = 9.9 Hz), 7.50 (*t*, 8H, $^{3}J_{PH}$ = 7.4 Hz), 7.55-7.63 (*m*, 12H); ^{13}C{^{1}H} NMR (CD_2Cl_2, 282.44 MHz, 293 K): 23.5 (*t*, $^{1}J_{CP}$ = 10.4 Hz), 125.0 (*t*, $^{1}J_{CP}$ = 17.9 Hz), 130.4 (*t*, 2JPC = 5.1 Hz), 133.7 (*s*), 133.8 (*m*); ^{31}P{^{1}H} NMR (CD_2Cl_2, 202.46 MHz, 293 K): 5.2 (*s*).

9.3.20 [(*dppe*)$SbCl_2$][$AlCl_4$]

$SbCl_3$ (0.228 g, 1.00 mmol) and $AlCl_3$ (0.134 g, 1.00 mmol) were combined in CH_2Cl_2 (7 mL) and stirred for 30 minutes to yield a yellow suspension. A solution of *dppm* (0.399 g, 1.00 mmol) in CH_2Cl_2 (7 mL) was added drop-wise over 30 seconds. The resulting clear and light-yellow solution was stirred for an additional 20 minutes to give a clear orange solution, the ^{31}P{^{1}H} NMR spectrum of which exhibited one signal (17 ppm). Removal of volatiles under dynamic vacuum at room-temperature over 4 hours yielded an orange-brown powder (0.736 g), which was re-dissolved in CH_2Cl_2 (12 mL), filtered and stored in the freezer at −30°C. A small amount of light-orange crystals suitable for X-ray diffraction appeared on the walls of the vial over two weeks and were isolated by decantation. Yield: 0.135 g, 18 %; mp 104 °C dec.; Raman: decomposition in laser; ^{1}H NMR (CD_2Cl_2, 500 MHz, 293 K): 3.41 (*m*, 4H), 7.59-7.71 (*m*, 20H); ^{13}C{^{1}H} NMR (CD_2Cl_2, 125.8 MHz, 293 K): 130.6 (*t*, $^{1}J_{CP}$ = 5.4 Hz), 133.8 (*m*), 133.9 (*s*); ^{31}P{^{1}H} NMR (CD_2Cl_2, 202.46 MHz, 293 K): 17.5 (*s*). While it was not possible to recover the bulk of the material in this fashion, the NMR spectra of the bulk powder and the crystals were identical.

9.3.21 [(*dppm*)SbCl][$AlCl_4$]$_2$

$SbCl_3$ (0.228 g, 1.00 mmol) and $AlCl_3$ (0.532 g, 4.00 mmol) were combined in CH_2Cl_2 (8 mL) and stirred for 12 hours to obtain a light yellow suspension. A solution of *dppm* (0.384 g, 1.00 mmol) in CH_2Cl_2 (5 mL) was added at once to immediately yield a yellow, cloudy solution. The reaction mixture was allowed to stir for 30 minutes to give a light yellow solution, the $^{31}P\{^1H\}$ NMR spectrum of which exhibited one signal (-3 ppm). The slightly cloudy solution was filtered, concentrated to 4 mL under vacuum, layered with pentane (1 mL) and placed in the freezer at −30°C. A small amount of shiny transparent crystals formed below an orange oil after two weeks and isolated by removing the oil. The crystals were identified as [(*dppm*)SbCl][$AlCl_4$]2•CH_2Cl_2•C_5H_{12} by X-Ray crystallography. The oil was washed repeatedly with a 1:10 mixture of Et_2O and hexane and under vacuum gave a light yellow powder identified as [(*dppm*)SbCl][$AlCl_4$]$_2$•Et_2O, Yield: 0.784 g, 85 %; mp 100-104 °C; Elemental Analysis (calcd./expt.): C 36.54 (36.04), H 3.38 (3.22); ^1H NMR (CD_2Cl_2, 500 MHz, 293 K): 3.79 (*t*, 2H, $^2J_{PH}$ = 7.4 Hz), 7.35 (*m*, 8H), 7.44 (*m*, 4H), 7.59 (*m*, 8H); $^{31}P\{^1H\}$ NMR (CD_2Cl_2, 202.46 MHz, 293 K): −2.3 (*s*).

9.3.22 [(*dppe*)SbCl][Al_2Cl_7]$_2$

$SbCl_3$ (0.456 g, 2.00 mmol) and $AlCl_3$ (1.068 g, 8.00 mmol) were combined in CH_2Cl_2 (8 mL) and stirred for 40 minutes to obtain a light yellow suspension. A solution of *dppm* (0.797 g, 2.00 mmol) in CH_2Cl_2 (5 mL) was added at once to immediately yield a golden-yellow, clear solution. The reaction mixture was allowed to stir at room temperature for 1.5 hours and the resulting clear and yellow solution had a $^{31}P\{^1H\}$ NMR spectrum which exhibited one signal (49 ppm). The reaction mixture was filtered, concentrated to 5 mL under vacuum, layered with pentane (2 mL) and placed in the freezer at −30°C for recrystallization. A small amount of light orange block crystals were obtained after 10 days and isolated by removing the oil. The crystals were identified as 7b[AlCl4]2 by X-Ray crystallography. The remaining orange oil was washed repeatedly with a 1:10 mixture of Et_2O and hexane and under vacuum gave a light yellow powder identified as [(*dppe*)SbCl][Al_2Cl_7]$_2$•Et_2O, Yield: 0.294 g, 12 %; mp 77-79 °C; Elemental Analysis (calcd./expt.): C 29.20 (28.60), H 2.78 (2.24); Raman (normalized intensities): 123 (19), 174.9 (45), 182.2 (24), 191.8 (14), 216.9

(3), 247.3 (2), 269.5 (9), 316.7 (33), 366.8 (13), 370.7 (48), 426.6 (8), 435.3 (13), 457.5 (4), 523.4 (7), 615.5 (11), 682.6 (4), 810.9 (2), 999.38 (100), 1027.8 (32), 1100.1 (24), 1168.1 (7), 1198.5 (1), 1440.5 (4), 1578.9 (16), 1583.7 (76), 2909.5 (11), 2926.4 (5), 2941.4 (12), 2960.6 (4), 3062.4 (23), 3068.6 (40); ^{1}H NMR (CD_2Cl_2,500 MHz, 293 K): 3.89 (*m*, 4H), 7.68-7.72 (*m*, 8H), 7.81-7.84 (*m*, 8H) , 7.95-7.99 (*m*, 4H); ^{13}C{^{1}H} NMR (CD_2Cl_2, 282.44 MHz, 293 K): 26.6 (*d*, $^{1}J_{CP}$ = 32 Hz), 116.0 (*d*, $^{1}J_{CP}$ = 59 Hz), 132.3(*s*), 133.9 (*m*), 137.6 (*s*); ^{31}P{^{1}H} NMR (CD_2Cl_2, 202.46 MHz, 293 K): 49.1 (*s*).

9.3.23 $FSb(OTf)_2$

Into a rapidly stirred suspension of SbF_3 (41.4 mmol, 7.400 g) in MeCN (20 mL) was dropwise cannulated neat TMSOTf (83 mmol, 18.443 g) over 10 minutes, to obtain a clear, colourless solution. The reaction mixture was allowed to stir for 16 hours while attached to an oil bubbler to vent gaseous TMSF evolved during the course of the reaction. All volatiles were removed under dynamic vacuum at room temperature yielding a white solid. After crushing this crude product into a fine powder, dynamic vacuum at 100 °C was applied until an IR assay showed no evidence of residual MeCN. The fine, colourless powder was used without further purification. Yield: 17.975 g; Melting point: 260-263 °C; IR (ATR, 298 K, [cm^{-1}]): 219 (m), 227 (m), 251 (w), 297 (w), 331 (m), 344 (m), 365 (m), 511 (s), 582 (s), 587 (s), 623 (vs), 632 (m), 668 (vw), 775 (w), 964 (vs), 974 (vs), 1020 (s), 1034 (w), 1100 (s), 1127 (s), 1200 (vs), 1229, (m), 1311 (s), 1455 (vw); Raman (ranked intensities): 228.8 (12), 255.5 (14), 324.1 (7), 347.8 (6), 368.9 (13), 515.2 (16), 582.0 (5), 600.2 (2), 649.9 (16), 775.6 (1), 938.5 (22), 983.5 (21), 1018.7 (9), 1033.6 (8), 1104.1 (15), 1131.6 (3), 1173.2 (20), 1207.7 (17), 1228.5 (10), 1313.8 (4), 1361.0 (18), 2266.7 (4), 2295.7 (19), 2944.7 (11), 3011.5 (23); ^{13}C{^{1}H} (CD_3CN, 298 K, 125.8 MHz): 120.6 (*q*, $^{1}J_{CF}$ = 318 Hz, CF_3); ^{19}F{^{1}H} NMR (CD_3CN, 298 K, 282.4 MHz): −95.3 (broad *s*, SbF) −78.7 (*s*, CF_3).

9.3.24 $Sb(OTf)_3$

Into a rapidly stirred suspension of SbF_3 (50 mmol, 8.938 g) in MeCN (40 mL) was dropwise cannulated neat TMSOTf (150 mmol, 33.333 g) over five minutes yielding a clear effervescent solution. The reaction mixture was allowed to stir for 24 hours under argon while attached to an oil bubbler to vent gaseous TMSF formed during the

reaction. Removal of volatiles under dynamic vacuum at room temperature yielded a cream-coloured solid. The highly moisture and air-sensitive material was crushed into a fine powder and placed under dynamic vacuum at 80 °C until an IR assay showed no remaining MeCN. The product was obtained as a fine pale yellow powder and was used without further purification. Yield: 27.312 g; Melting point: 181 °C dec.; IR (ATR, 298 K, [cm^{-1}]): 240 (w), 255 (m), 326 (m), 344 (m), 359 (s), 399 (w), 511 (s), 573 (m), 588 (s), 618 (vs), 772 (m), 799 (s), 939 (vs), 958 (vs), 981 (vs), 1037 (vw), 1130 (vs), 1147 (s), 1195 (vs), 1323 (m), 1364 (w); Raman (ranked intensities): 75.2 (2), 117.3 (4), 144.9 (15), 180.3 (14), 266.4 (3), 326.7 (7), 388.2 (12), 536.6, 574.4 (13), 602.8 (9), 647.0 (10), 778.2 (1), 894.4 (16), 1013.4 (9), 1108.6 (5), 1132.2 (8), 1217.9 (6), 1245.0 (9), 1323.2 (11), 1374.9 (17), 1408.2 (18); $^{13}C\{^{1}H\}$ (CD_3CN, 298 K, 125.8 MHz): 120.5 (q, $^{1}J_{CF} = 318$ Hz, CF_3) ; $^{19}F\{^{1}H\}$ NMR (CD_3CN, 298 K, 282.4 MHz): -78.5 (s, CF_3).

9.3.25 [(*bipy*)SbF_2][OTf]

SbF_3 (0.179 g, 1 mmol) and *bipy* (0.156 g, 1 mmol) were added to a vial equipped with a stir-bar and MeCN (*ca.* 10 mL) was added. The resulting white suspension was stirred for 15 minutes before adding a solution of TMSOTf (0.222 g, 1 mmol) in MeCN (*ca.* 5 mL). A slight clearing of the suspension was observed. The reaction mixture was allowed to stir for 4 hours and then filtered to yield a clear and colourless solution, which was concentrated to approximately 5 mL. Recrystallization at -30°C overnight yielded shiny, colourless blocks identified as [(*bipy*)SbF_2][OTf]•MeCN by X-ray crystallography. Yield: 0.275 g, 59%; Melting point: 173-177 °C; Elemental Analysis (calcd./expt.): C (28.41/28.00), H (1.73/1.86), N (6.02/5.97); Raman (normalized intensities): 138 (13), 153 (10), 180 (9), 189 (9), 203 (6), 232 (6), 254 (5), 258 (6), 273 (3), 314 (10), 345 (7), 351 (9), 364 (12), 416 (3), 442 (4), 471 (4), 501 (6), 535 (5), 541 (10), 545 (13), 573 (6), 580 (5), 638 (6), 651 (6), 658 (7), 730 (4), 753 (4), 758 (15), 769 (21), 782 (4), 809 (5), 916 (4), 988 (4), 1094 (5), 1109 (5), 1159 (8), 1181 (5), 1222 (6), 1237 (5), 1253 (7), 1277 (12), 1290 (11), 1302 (9), 1324 (66), 1357 (4), 1423 (5), 1435 (6), 1480 (4), 1502 (40), 1567 (36), 1578 (9), 1601 (100), 1613 (19), 1669 (2), 1689 (3), 3000 (1), 3044 (1), 3075 (11), 3086 (6), 3105 (8), 3139 (2), 3157 (1); ^{1}H NMR (CD_3CN, 300 MHz, 298 K): 7.99 (m, 2H), 8.47 (td, 8.0 Hz, 1.6 Hz, 2H), 8.59 (dt, 8.2 Hz, 0.96 Hz, 2H), 9.15 (d, 5.0 Hz, 2H); $^{13C}\{^{1}H\}$ NMR (CD_3CN, 75.47 MHz, 298 K): 122.1 (q, $^{1}J_{CF}$

= 322 Hz), 125.4, 129.8, 145.5, 148.1. 149.3; $^{19}F\{^{1}H\}$ NMR (CD_3CN, 338.66 MHz, 298 K): −90.10 (broad), −79.51.

9.3.26 $[(bipy)_2SbF][OTf]_2$

SbF_3 (0.179 g, 1 mmol) and 2,2'-*bipy* (0.312 g, 2 mmol) were added to a vial equipped with a stir-bar and MeCN (*ca.* 10 mL) was added. The resulting white suspension was stirred for 15 minutes before adding a solution of TMSOTf (0.444 g, 2 mmol) in MeCN (*ca.* 5 mL). A slight clearing and appearance of yellow colour was observed. The reaction mixture was allowed to stir for 16 hours to yield a very light yellow suspension. Removal of volatiles under vacuum over 16 hours yielded a light peach coloured powder (0.757 g). The powder was dissolved in MeCN and recrystallized by vapour diffusion of Et_2O to yield very small white needles, which proved unsuitable for X-Ray diffraction. The crushed needles were washed with fresh MeCN (3 x 5 mL) and Et_2O (2 mL). Removal of all volatiles yielded the product as a fine white, analytically pure powder. Yield: 0.635 g, 84 %; Melting point: 170-173 °C; Elemental Analysis (calcd./expt.): C (35.17/35.02), H (2.15/2.16), N (7.46/7.50); Raman (normalized intensities): 145 (14), 164 (13), 179 (12), 187 (9), 212 (8), 254 (5), 262 (9), 314 (7), 318 (7), 348 (11), 354 (10), 363 (12), 421 (3), 427 (3), 446 (3), 468 (4), 520 (3), 535 (8), 546 (3), 553 (3), 575 (5), 627 (5), 636 (3), 638 (3), 646 (5), 651 (7), 659 (7), 730 (2), 749 (2), 758 (15), 766 (25), 783 (2), 814 (3), 988 (2), 1010 (56), 1027 (88), 1043 (10), 1064 (24), 1074 (9), 1155 (6), 1167 (5), 1229 (5), 1250 (7), 1270 (13), 1303 (13), 1312 (60), 1322 (59), 1436 (7), 1495 (34), 1503 (41), 1564 (55), 1577 (20), 1596 (81), 1600 (100), 1607 (33), 1668 (3), 2888 (2), 3036 (2), 3068 (13), 3074 (15), 3091 (10), 3097 (14), 3133 (4), 3153 (2); ^{1}H NMR (CD_3CN, 300 MHz, 298 K): 1.98 (*s* 3H), 8.07 (*m*, 4H), 8.63 (*dt*, 8.0 Hz, 1.4 Hz, 4H), 8.81 (*d*, 8.3 Hz, 4H), 8.89 (*d*, 5.4 Hz, 4H); $^{13}C\{^{1}H\}$ NMR (CD_3CN, 75.47 MHz, 298 K): 118.83, 121.6 (*q*, $^{1}J_{CF}$ = 317 Hz), 127.5, 131.8, 147.6, 149.7, 149.8; $^{19}F\{^{1}H\}$ NMR (CD_3CN, 338.66 MHz, 298 K): −93.17 (broad), −79.38.

9.3.27 $[(bipy)_2Sb][OTf]_3$

SbF_3 (1.785 g, 10 mmol) and *bipy* (3.130 g, 20 mmol) were added to a glass bulb equipped with a stir-bar. A solution of TMSOTf (4.000 g, 18 mmol) in MeCN (10

mL) was added to the bulb over 30 seconds and an exothermic reaction with copious amounts of bubbling proceeded. The white suspension was allowed to stir for 10 hours before a second addition of TMSOTf (4.000 g, 18 mmol) in MeCN (10 mL). The white suspension was allowed to stir for a further 4 hours. Removal of all volatiles under vacuum yielded a very faint pink powder (8.775 g, 95 %), which was recrystallized from a minimum amount of MeCN at −30°C over three days to give large colourless blocks identified as $[(bipy)_2Sb][OTf]_3$•MeCN by X-ray crystallography. Removal of coordinated acetonitrile under high vacuum for 48h gave the product as an analytically pure white powder. Yield: 7.611 g, 82 %; Melting point: 111-114 C; Elemental Analysis (calcd./expt.): C (31.34/31.55), H (1.83/1.72); Raman (normalized intensities): 84 (27), 95 (15), 132 (9), 156 (5), 166 (5), 189 (5), 194 (4), 211 (4), 255 (2), 273 (2), 315 (2), 323 (2), 346 (3), 350 (4), 356 (2), 366 (8), 415 (1), 427 (1), 477 (1), 577 (3), 639 (1), 645 (1), 650 (2), 660 (3), 761 (5), 763 (7), 767 (20), 1003 (4), 1026 (19), 1028 (24), 1036 (26), 1045 (11), 1067 (13), 1166 (4), 1231 (4), 1281 (7), 1327 (47), 1436 (3), 1502 (29), 1567 (41), 1604 (100), 1612 (22), 3043 (2), 3082 (12), 3090 (12), 3098 (13), 3136 (3); ^{1}H NMR (CD_3CN, 300 MHz, 298 K): 1.98 (*s* 3H), 8.07 (*m*, 4H), 8.63 (*dt*, 8.0 Hz, 1.4 Hz, 4H), 8.81 (*d*, 8.3 Hz, 4H), 8.89 (*d*, 5.4 Hz, 4H); $^{13}C\{^1H\}$NMR (CD_3CN, 75.47 MHz, 298 K): 118.83, 121.6 (*q*, $^1J_{CF} = 317$ Hz), 127.5, 131.8, 147.6, 149.7, 149.8; $^{19}F\{^1H\}$ NMR (CD_3CN, 298 K): −79.5.

9.3.28 [(*dppm*)Sb(OTf)$_3$]

SbF_3 (0.179 g, 1 mmol) and bis-(diphenylphosphino)methane (*dppm*) were combined in a vial equipped with a stir bar and 10 mL of MeCN was added. The mixture was stirred for 5 minutes to obtain a white suspension. A solution of TMSOTf (0.666 g, 3 mmol) in 7 mL MeCN was added dropwise over 30 seconds to obtain a clear yellow solution, which was allowed to stir for 16 h at room temperature. The slightly cloudy solution was filtered and slow removal of the solvent under dynamic vacuum yielded large colourless blocks identified as $[(dppm)Sb][OTf]_3$•MeCN by X-ray crystallography. A second crop was obtained by storing the mother liquor at −30°C for 4 days. Yield: 0.711 g, 79 %; Melting point: 182-184 °C dec.; Elemental Analysis (calcd./expt.): C (40.12/36.45), H (2.81/2.59), N (1.56/1.51); Raman (normalized intensities): 117 (41), 160 (18), 179 (44), 208 (10), 220 (10), 234 (9), 241 (8), 254 (11), 266 (5), 319 (9), 322 (9), 345 (10), 354 (8), 363 (13), 380 (5), 388 (6), 408 (19), 423 (10), 444 (7), 462

(6), 467 (4), 504 (14), 520 (3), 533 (16), 537 (7), 576 (5), 587 (3), 616 (12), 634 (3), 676 (6), 683 (4), 687 (7), 701 (5), 714 (2), 743 (4), 747 (3), 763 (15), 766 (20), 848 (2), 926 (5), 942 (4), 978 (9), 981 (10), 986 (10), 1002 (100), 1028 (7), 1044 (5), 1094 (33), 1103 (16), 1146 (4), 1165 (12), 1197 (6), 1231 (9), 1237 (7), 1315 (3), 1346 (6), 1373 (4), 1440 (6), 1486 (5), 1585 (87), 2255 (7), 2258 (19), 2298 (2), 2858 (4), 2941 (22), 2965 (3), 2996 (7), 3034 (3), 3069 (42), 3077 (26), 3152 (2), 3171 (3); ^{1}H NMR (CD_3CN, 300 MHz, 298 K): 1.98 (*s* 3H), 5.51 (*t*, 2H, $^{2}J_{PH}$ = 12.6 Hz), 7.58-7.85 (*m*, 10H); ^{31}P NMR (CD_3CN, 75.47 MHz, 298 K): 21.9; ^{19}FNMR (CD_3CN, 338.66 MHz, 298 K): −78.5.

9.3.29 $[Mg(MeCN)_6][(Me_3P)SbCl_4]_2$

$MgCl_2$ (0.10 g, 1.0 mmol) and $SbCl_3$ (0.46 g, 2.0 mmol) were combined in 8 mL MeCN. The reaction mixture was stirred for 16 h to obtain a white suspension. Neat PMe_3 (0.16 g, 2.0 mmol) was added to obtain a clear solution which became cloudy upon stirring for an additional 1 hour. The supernatant was removed from the white precipitate and filtered. Slow removal of acetonitrile at room temperature yielded colourless crystalline blocks. The dried precipitate and crystals gave identical ^{31}P, ^{1}H and ^{1}3C NMR spectra. Yield: 0.78 g, 74%. Melting point: 175-178 °C (dec.). Samples prepared for elemental analysis (dynamic vacuum for 24 h) show loss of one molecule of MeCN giving $[Mg(MeCN)_5][(Me_3P)SbCl_4]_2$ (calcd./expt.): C (21.14/21.27), H (3.66/3.49), N(7.71/7.84). NMR (CD_3CN, 298 K, 8.45 T field strength): ^{1}H: 1.95 ppm (*d*, 18H, $^{2}J_{PH}$ = 14.2 Hz, Me3P); 1.99 ppm (*s*, 18H, MeCN), ^{13}C{^{1}H}: 10.4 ppm (*d*, $^{1}J_{CP}$ = 36.2 Hz), ^{31}P{^{1}H}: 7.7 ppm (*s*, broad).

Table 9.3.1. Crystallographic details for compounds in Chapter 3.

	$[Me_3PSbCl_3]$	$[Ph_3PSbCl_3]$	$[Cy_3PSbCl_3]$	$[(Me_3P)_2SbCl_3]$	$[(Ph_3P)_2SbCl_3]$	$[(Cy_3P)_2SbCl_3]$
formula	$C_3H_9Cl_3PSb$	$C_{18}H_{15}Cl_3PSb$	$C_{18}H_{33}Cl_3PSb$	$C_6H_{18}Cl_3P_2Sb$	$C_{36}H_{30}Cl_3P_2Sb$	$C_{36}H_{66}Cl_3P_2Sb$
mw (g mol^{-1})	304.17	490.37	508.51	380.24	752.64	788.93
space group	P21/n	$P\bar{1}$	$P\bar{1}$	P21/n	I2/a	$P\bar{1}$
a /Å	7.9261 (11)	10.5374 (8)	10.376 (3)	7.6594 (4)	15.8017 (12)	9.7577 (7)
b /Å	19.089 (3)	10.5630 (8)	15.895 (4)	11.4178 (6)	9.5425 (8)	10.3383 (7)
c /Å	13.1115 (18)	10.6579 (8)	20.641 (5)	16.0941 (8)	22.4802 (18)	11.2342 (8)
α/°		92.9183 (8)	85.320 (4)			115.1065 (7)
β/°	100.8495 (17)	115.7836 (7)	80.800 (4)	96.3001 (5)	101.4987 (9)	104.6530 (7)
γ/°		113.9875 (7)	73.177 (4)			94.0515 (8)
V /$Å^3$	1948.3 (5)	937.79 (12)	3214.2 (14)	1398.98 (12)	3321.7 (5)	972.13 (12)
Z	8	2	6	4	4	1
ρ/g cm^{-3}	2.074	1.737	1.576	1.805	1.505	1.348
radiation /Å	0.71073	0.71073	0.71073	0.71073	0.71073	0.71073
T /K	173.15	173.15	173.15	173.15	173.15	173.15
G.O.F	1.036	1.102	0.872	1.048	1.068	1.079
R_1 [I > 2σ(I)]	0.0259	0.0190	0.0394	0.0123	0.0204	0.0250
wR_2 (all data)	0.0513	0.0455	0.0776	0.0295	0.0507	0.0672

Table 9.3.2. Crystallographic details for compounds in Chapter 3 (cont.).

	$[(Me_3P)SbCl][OTf]$	$[(Me_3P)SbPh_2][OTf]$	$[(Ph_3P)_2PSbCl_2][OTf]$	$[(Me_3P)_2SbPh_2][OTf]$	$[(Me_3P)_2SbCl][OTf]_2$	$[Mg(MeCN)_6][SbCl_4]_2$
formula	$C_4H_9Cl_2F_3O_3PSSb$	$C_{16}H_{19}F_3O_3PSSb$	$C_{37}H_{30}Cl_2F_3O_3P_2SSb$	$C_{19}H_{28}F_3O_3P_2SSb$	$C_8H_{18}ClF_6O_6P_2S_2Sb$	$C_{18}H_{36}Cl_8MgN_6P_2Sb_2$
mw (g mol^{-1})	417.79	501.09	866.26	577.16	607.48	949.88
space group	P21/c	$P\bar{1}$	$P\bar{1}$	P21/c	P21/n	P212121
a /Å	10.798 (2)	8.2553 (2)	9.5641 (7)	8.2974 (3)	13.5151 (8)	10.9776 (15)
b /Å	11.059 (2)	10.8326 (3)	12.0248 (8)	11.1805 (4)	11.4915 (7)	10.9983 (15)
c /Å	12.214 (3)	11.1367 (3)	17.5876 (12)	26.4962 (9)	13.9937 (8)	32.060 (4)
α/°		98.4361 (3)	94.0493 (9)			
β/°	114.382 (2)	97.6027 (3)	96.8668 (10)	93.3876 (4)	105.7092 (6)	
γ/°		93.1231 (3)	110.3615 (9)			
V /Å^3	1328.5 (5)	973.70 (4)	1869.0 (2)	2453.73 (15)	2092.2 (2)	3870.7 (9)
Z	4	2	2	4	4	4
ρ/g cm^{-3}	2.089	1.709	1.539	1.562	1.929	1.630
radiation /Å	0.71073	0.71073	0.71073	0.71073	0.71073	0.71073
T /K	173.15	173.15	173.15	173.15	173.15	173.15
G.O.F	1.081	1.063	1.062	1.050	1.037	1.063
R_1 [I $> 2\sigma$(I)]	0.0313	0.0157	0.0289	0.0201	0.0175	0.0367
wR_2 (all data)	0.0810	0.0413	0.0719	0.0506	0.0434	0.0797

Table 9.3.3. Crystallographic details for compounds in Chapter 3 (cont.).

	[(*dppm*)$SbCl_2$] [$AlCl_4$]	[(*dmpe*)$SbCl_2$] [OTf]	[(*dppe*)$_2SbCl_2$] [$AlCl_4$]•CH_2Cl_2	[$(Me_3P)_2SbCl_2$] [OTf]	[(*dppm*)SbCl] [$AlCl_4$]$_2$•CH_2Cl_2•C_5H_{12}	[(*dppe*)SbCl] [Al_2Cl_7]$_2$
formula	$C_{25}H_{22}AlCl_6P_2Sb$	$C_7H_{16}Cl_2F_3O_3P_2SSb$	$C_{27}H_{26}AlCl_8P_2Sb$	$C_7H_{18}Cl_2F_3O_3P_2SSb$	$C_{31}H_{36}Al_2Cl_9P_2Sb$	$C_{26}H_{24}Al_4Cl_{15}P_2Sb$
mw (g mol^{-1})	745.80	491.85	844.75	493.86	1090.16	1159.81
space group	$P\bar{1}$	P212121	$P\bar{1}$	C2/c	P21/n	$P\bar{1}$
a /Å	10.3131 (2)	11.1129 (3)	10.5270 (3)	25.4578 (11)	16.299 (2)	12.2162 (7)
b /Å	11.7645 (3)	11.3226 (3)	12.8155 (3)	6.4594 (3)	10.3844 (15)	12.2162 (7)
c /Å	13.2776 (3)	13.0683 (4)	14.0046 (3)	22.9155 (10)	25.251 (4)	17.8399 (11)
α/°	81.5321 (3)		74.3015 (3)			72.2279 (7)
β/°	73.3679 (3)		71.3838 (3)	113.8940 (4)	98.272 (2)	73.7807 (7)
γ/°	86.3619 (3)		87.5567 (3)			63.2388 (7)
V /Å^3	1526.32 (6)	1644.34 (8)	1721.72 (7)	3445.3 (3)	4229.3 (10)	2240.2 (2)
Z	2	4	2	8	4	2
ρ/g cm^{-3}	1.623	1.987	1.629	1.904	1.712	1.719
radiation /Å	0.71073	0.71073	0.71073	0.71073	0.71073	0.71073
T /K	173.15	173.15	173.15	173.15	173.15	173.15
G.O.F	1.023	1.117	1.021	1.116	1.063	1.062
R_1 [I > 2σ(I)]	0.0200	0.0131	0.0236	0.0156	0.0479	0.0262
wR_2 (all data)	0.0480	0.0329	0.0582	0.0400	0.1257	0.0652

Table 9.3.4. Crystallographic details for compounds in Chapter 3 (cont.).

	$[(Me_3P)SbPhCl_2]$	$[(Ph_3P)SbPhCl_2]$	$[(Ph_3P)_2SbPhCl_2]$	$[(bipy)SbF_2][OTf]$•MeCN	$[(bipy)_2Sb][OTf]_3$•MeCN	$[(dmap)_2Sb][OTf]_3$
formula	$C_9H_{14}Cl_2PSb$	$C_{24}H_{20}Cl_2PSb$	$C_{42}H_{35}Cl_2P_2Sb$	$C_{11}H_8F_5N_2O_3SSb$	$C_{25}H_{19}F_9N_5O_9S_3Sb$	$C_{17}H_{20}F_9N_4O_9S_3Sb$
mw (g mol^{-1})	345.82	532.02	794.29	465.01	922.39	813.30
space group	P21/n	P21/n	C2/c	P21/c	P$\bar{1}$	P$\bar{1}$
a /Å	6.8302(2)	10.3232(4)	12.9097(2)	9.1312(4)	9.0855(3)	12.1714(6)
b /Å	17.8515(5)	11.6723(4)	14.2568(2)	18.5598(9)	13.2629(4)	13.8281(7)
c /Å	10.5339(3)	18.4318(7)	19.9245(3)	8.9512(4)	13.8870(4)	19.0697(10)
α/°					81.6469(3)	70.2068(6)
β/°	93.8302(3)	90.4966(4)	96.6050(7)	110.1717(4)	86.8308(3)	77.4664(6)
γ/°					84.9286(3)	77.8872(6)
V /Å^3	1281.52(6)	2220.87(14)	3642.78(9)	1423.94(11)	1647.62(9)	2915.3(3)
Z	4	4	4	4	2	4
ρ/g cm^{-3}	1.792	1.591	1.448	2.169	1.859	1.853
radiation /Å	0.71073	0.71073	0.71073	0.71073	0.71073	0.71073
T /K	173.15	173.15	173.15	173.15	173.15	173.15
G.O.F	1.173	1.149	1.111	1.139	1.041	1.021
R_1 [I > 2σ(I)]	0.0163	0.0230	0.0195	0.0195	0.0187	0.0364
wR_2 (all data)	0.0480	0.0329	0.0485	0.0485	0.0501	0.1028

9.4 Compounds in Chapter 4

9.4.1 $[(THF)_2BiBr_2(OTf)]_2$

$BiBr_3$ (11.217 g, 25.00 mmol) was dissolved in THF (50 mL) in a schlenk bulb and stirred to obtain a clear, golden-yellow solution. A solution of MeOTf (4.103 g, 25.00 mmol) in THF (12 mL) was added over 20 minutes through an addition funnel with an oil bubbler attached to vent CH_3Br. Gaseous evolution and a slight exotherm was observed over the course of the addition. Stirring for an additional 16 h at room temperature produced a viscous white suspension. The slurry was pumped to dryness over 16 h under dynamic vacuum to yield a sticky light-grey solid (15.303 g). This product was recrystallized from a 1:1 v/v mixture of CH_2Cl_2/Et_2O at -30 °C over 72 h and the shiny, translucent blocks obtained were isolated by decantation. The crystals were identified as $[(THF)_2BiBr_2(OTf)]_2$ using X-ray crystallography. Due to the high degree of disorder in the THF molecules, precise bond-lengths and angles could not be obtained. The identity of the bulk was established via elemental Analysis and NMR spectroscopy, which confirmed that the coordinated THF molecules are not removed even after prolonged exposure to high-vacuum at room temperature. Yield: 10.031 g, 78%; Melting Point: $108 - 110$ °C ; Elemental Analysis (calcd./expt.): C (15.90/16.33), H (2.61/2.44); Raman (normalized intensities): 84.1 (45), 93.1 (28), 191.9 (52), 212.1 (100), 322.1 (6), 346.8 (5), 352.4 (11), 519.7 (1), 578.1 (3), 763.3 (24), 854.2 (6), 922.7 (6), 1022.6 (60), 1041.7 (4), 1185.4 (4), 1224.7 (7), 1347.0 (1), 1368.4 (4), 1450.3 (4), 1487.3 (5), 2880.5 (11), 2902.9 (18), 2936.6(19), 2954.6 (17), 2991.6 (23); ^{1}H NMR (300 MHz, CD_2Cl_2, 298 K): 2.00 (*m*, 4H, THF), 4.15 (*m*, 4H, THF); $^{13}C\{^1H\}$ NMR (75 MHz, CD_2Cl_2, 298 K): 26.1 (s), 71.1 (s), 116.8 (*q*, CF3, $^1J_{PC} =$ 319.8 Hz).

9.4.2 $[(dmpe)BiBr_2(OTf)]_2$

$[(THF)_2BiBr_2(OTf)]$ (0.662g, 1 mmol) in toluene (5 mL) was added dropwise to a solution of *dmpe* (0.150 g, 1 mmol) in toluene (5 mL). A bright yellow precipitate was obtained immediately. The reaction was allowed to stir for an additional hour to yield a light grey precipitate, which was filtered and washed with pentane (3 x 5 mL). Removal of solvent over 4 h gave a light grey powder together with some

insoluble black precipitate. The crude product was recrystallized from a minimum amount of MeCN at −30°C to yield translucent blocks which were identified as [(*dmpe*)$BiBr_2$(OTf)]•MeCN using X-ray crystallography. Yield (crystals): 0.548 g, 77 %; mp: 225 °C dec.; Elemental Analysis (calcd./expt.): C (15.25/16.54), H (2.70/2.65) sample shows visible decomposition (formation of an insoluble brown/black powder) under vacuum (10-2 mbar) and attempts to obtain better analytical results were unsuccessful; ^{1}H NMR (500 MHz, CD_3CN, 298 K): 2.41 (*d*, 12H, *dmpe*, $^2J_{PH}$ = 14.5 Hz), 3.06 (*m*, 4H, *dmpe*); ^{31}P NMR (200 MHz, CD_3CN, 298 K): 50.8 (broad). Raman: sample decomposes in the laser beam.

9.4.3 [(*dmpe*)$BiCl_2$(OTf)]$_2$

A solution of *dmpe* (0.150 g, 1 mmol) in toluene (5 mL) was added dropwise to a suspension of $BiCl_3$ (0.316 g, 1 mmol) and TMSOTf (0.222 g, 1 mmol) in toluene (10 mL). A yellow precipitate was observed immediately. The reaction was allowed to stir for 2 h to yield a yellow precipitate under a clear and colourless supernatant, which was filtered and washed with pentane (3 x 5 mL). Removal of solvent over 16 h yielded a fine yellow powder, which was recrystallized from a minimum amount of MeCN at −30°C over 48 h to yield large crystalline blocks, identified as [(*dmpe*)$BiCl_2$(OTf)]•MeCN using X-ray crystallography. Yield (crystals): 0.337 g, 54 %; mp: 220 °C dec; ^{1}H NMR (500 MHz, CD_3CN, 298 K): 2.30 (*d*, 12H, *dmpe*, $^2J_{PH}$ = 14.7 Hz), 3.10 (*m*, *dmpe*, 4H); ^{13}C{^{1}H} NMR (125 MHz, CD_3CN, 298 K): 9.8 (*d*, $^1J_{PC}$ = 28 Hz), 31.3 (*d*, $^1J_{PC}$ = 29 Hz); ^{31}P NMR (200 MHz, CD_3CN, 298 K): 80.7 (broad). Raman: sample decomposes in the laser beam.

9.4.4 [(*dmpe*)BiCl(OTf)$_2$]$_2$

A solution of *dmpe* (0.150 g, 1 mmol) in toluene (10 mL) was added dropwise to a suspension of $BiCl_3$ (0.316 g, 1 mmol) and TMSOTf (0.444 g, 2 mmol) in toluene (10 mL). A yellow precipitate was observed immediately. The reaction was allowed to stir for 1 h to yield a yellow suspension. The product was filtered and washed with pentane (3 x 5 mL). Removal of solvent over 24 h yielded a fine yellow powder, which was recrystallized from a minimum amount of MeCN at −30°C to yield colourless crystalline blocks, identified as [(*dmpe*)BiCl(OTf)$_2$]•MeCN using X-ray crystallography.

Yield (crystals): 0.496 g, 68 %; mp: 207-212°C dec.; Elemental Analysis (calcd./expt.) : C (16.37/16.20), H(2.61/2.79); ^{1}H NMR (CD_3CN, 300 MHz, 298 K): 1.94 (*s*, 3H, MeCN), 2.33 (*d*, 12H, *dmpe*), 3.19 (*m*, *dmpe*, 4H); $^{13}C\{^{1}H\}$ (CD_3CN, 75 MHz, 298 K): 10.2 (*d*, $^{1}J_{PC}$ = 29 Hz), 31.5 (*d*, $^{1}J_{PC}$ = 27 Hz); ^{31}P (CD_3CN, 120 MHz, 298 K): 90.8 (broad *s*).

Table 9.4.1. Crystallographic details for compounds in Chapter 4.

	$[(THF)_2BiBr_2(OTf)]$	$[(dmpe)BiBr_2(OTf)]$	$[(dmpe)BiCl_2(OTf)]$	$[(dmpe)BiCl(OTf)_2]$	$[(dmpe)_2Pd][Bi_2Cl_8(MeCN)_2]$
formula	$C_9H_{16}BiBr_2SO_5F_3$	$C_9H_{19}BiBr_2F_3O_3P_2SN$	$C_9H_{19}BiCl_2F_3NO_3P_2S$	$C_{10}H_{19}BiClF_6NO_6P_2S_2$	$C_{18}H_{38}Bi_2Cl_6F_6N_2O_6P_4PdS_2$
mw (g mol^{-1})	662.08	709.05	620.13	733.75	1417.56
space group	$P\bar{1}$	C2/c	C2/c	P2(1)/n	$P\bar{1}$
a /Å	8.088(2)	21.1892(16)	21.2850(16)	12.6020(15)	8.9289(4)
b /Å	10.539(4)	15.3454(16)	15.2439(16)	16.2877(19)	9.8177(4)
c /Å	11.746(3)	12.6533(11)	12.3056(10)	12.8527(15)	13.9674(6)
α/°	106.091(5)				106.6802(4)
β/°	97.960(4)	94.694(2)	95.629(2)	118.648(1)	94.1676(5)
γ/°	106.559(3)				107.2454(5)
V /Å^3	896.1(4)	4100.5(6)	3973.5(6)	2315.2(5)	1103.37
Z	2	8	8	4	1
ρ/g cm^{-3}	2.454	2.297	2.073	2.105	2.133
radiation /Å	0.71073	0.71073	0.71073	0.71073	0.71073
T /K	188(1)	198(1)	198(1)	173(1)	173(1)
G.O.F	1.048	1.032	1.037	1.058	1.106
R_1 [I > 2σ(I)]	0.0498	0.0397	0.0274	0.0320	0.0136
wR_2 (all data)	0.1222	0.0922	0.0583	0.0663	0.0331

9.5 Compounds in Chapter 5

9.5.1 $[(Me_3P)_2SbF][OTf]_2$

To a clear solution of $FSb(OTf)_2$ (1 mmol, 0.439 g) in MeCN (5 mL) was dropwise added a solution of PMe_3 (2 mmol, 0.152 g) in MeCN (2 mL) yielding a white suspension. The suspension was allowed to stir for 15 minutes and then allowed to settle for 30 minutes. The clear, pale-yellow coloured supernatant was removed and the remaining white precipitate washed with MeCN (2 mL) and Et_2O (2 mL). Removal of volatiles under dynamic vacuum over 2 hours yielded [**5.7(Me)**][$OTf]_2$ as an analytically pure powder. Yield: 0.443 g (75 %); Melting Point: 170 °C dec.; Elemental Analysis (calcd./expt.): C (16.26/15.87) H (3.07/3.04); IR (ATR, 298 K, [cm^{-1}]): 229 (m), 269 (vw), 318 (w), 350 (m), 514 (vs), 546 (s), 572 (m), 633 (vs), 758 (w), 788 (vw), 851 (w), 953 (s), 1016 (vs), 1155 (vs), 1202 (s), 1223 (s), 1243 (s), 1257 (s), 1301 (m), 1419 (w), 2850 (vw), 2920 (vw), 3000 (vw); Raman (ranked intensities): 199.0 (9), 223.9 (15), 269.7 (12), 319.1 (10), 348.4 (5), 516.6 (16), 546.7 (8), 574.7 (11), 638.4 (16), 671.1 (6), 761.9 (3), 955.4 (17), 974.9 (17), 1016.0 (16), 1030.6 (2), 1174.1 (13), 1223.7 (7), 1292.5 (16), 1313.7 (17), 1421.6 (8), 2801.8 (17), 2833.4 (17), 2880.7 (17), 2922.6 (1), 2995.6 (4), 3025.4 (14); ^{1}H NMR (CD_3CN, 298 K, 500.3 MHz): 2.2 (broad *d*, $^2J_{PH}$ = 14.1 Hz, CH3); $^{13}C\{^1H\}$ (CD_3CN, 298 K, 125.8 MHz): 9.7 (*d*, $^1J_{CP}$ = 32 Hz, CH3), 121.3 (*q*, $^1J_{CF}$ = 321 Hz, CF_3); $^{31}P\{^1H\}$ (CD_3CN, 298 K, 202.5 MHz): 15.9 (*d*, $^2J_{PF}$ = 44 Hz); $^{19}F\{^1H\}$ NMR (CD_3CN, 298 K, 282.5 MHz): −176.3 (*t*, $^2J_{PF}$ = 44 Hz, SbF), −79.0 (*s*, CF_3).

9.5.2 $[(Et_3P)_2SbF][OTf]_2$

To a clear solution of $FSb(OTf)_2$ (1 mmol, 0.439 g) in MeCN (5 mL) was dropwise added a solution of PEt_3 (2 mmol, 0.236 g) in MeCN (2 mL) yielding a pale-yellow coloured, clear solution. The solution was allowed to stir for further 30 minutes. The clear reaction mixture was filtered, layered with Et_2O and placed in the freezer to yield very fine, colourless needles over the course of 72 hours. Removal of solvent under dynamic vacuum yielded [**5.7(Et)**][$OTf]_2$ as an analytically pure fine white powder. Yield: 0.478 g (71 %); Melting Point: 93-95 °C dec.; Elemental Analysis (calcd./expt.): C (24.90/24.65) H (4.48/4.46); IR (ATR, 298 K, [cm^{-1}]): 227 (m),

320 (w), 349 (m), 360 (m), 512 (vs), 573 (m), 741 (m), 775 (m), 632 (vs), 878 (w), 1010 (vs), 1045 (m), 1150 (s), 1171 (s), 1202 (s), 1228 (s), 1294 (m), 1395 (w), 1417 (w), 1464 (m), 2885 (vw), 2947 (w), 2981 (vw); Raman (ranked intensities): 213.7 (9), 241.9 (10), 317.4 (10), 349.2 (10), 381.8 (14), 424.9 (15), 458.3 (18), 529.0 (11), 575.6 (13), 613.0 (7), 679.4 (23), 707.5 (22), 762.8 (6), 988.3 (17), 1020.4 (3), 1044.7 (8), 1167.3 (19), 1200.2 (19), 1229.0 (12), 1277.0 (20), 1298.0 (20), 1312.8 (20), 1395.3 (20), 1413.5 (16), 1464.4 (8), 2751.9 (21), 2765.7 (21), 2887.8 (5), 2920.9 (2), 2947.3 (1), 2985.7 (4); ^{1}H NMR (CD_3CN, 298 K, 500.3 MHz): 1.36 (*dt*, CH3,$^{3}J_{HH}$ = 7.8 Hz, $^{3}J_{HP}$ = 18.8 Hz, 18H), 2.51 (*dq*, CH2,$^{3}J_{HH}$ = 7.8 Hz, $^{2}J_{PH}$ = 8.7 Hz, 12H); ^{13}C{^{1}H} NMR (CD_3CN, 298 K, 125.8 MHz) : 8.2 (*d*, CH3 ,$^{2}J_{CP}$ = 7 Hz), 15.4 (*d*, CH2 ,$^{1}J_{CP}$ = 26 Hz), 121.3 (*q*, $^{1}J_{CF}$ = 321 Hz, CF_3); ^{31}P NMR (CD_3CN, 298 K, 202.5 MHz): 38.6 (*s*); ^{19}F{^{1}H} NMR (CD_3CN, 298 K, 282.5 Hz): −175.2 (broad *s*, SbF), −79.0 (*s*, CF_3).

9.5.3 $[(Me_3P)_4Sb_4][OTf]_4$

Freshly sublimed SbF_3 (48 mmol, 8.531 g) was added to a 250 mL 3-necked schlenk flask equipped with a Teflon stir bar. The flask was attached to the Schlenk manifold and appended with an oil bubbler (to vent formed TMSF) and a Schlenk frit (G3) with a 100 mL receiving flask. The apparatus was purged 3 times with fresh argon and then 55 mL of rigorously dried and deoxygenated MeCN was added via syringe to obtain a white suspension. Freshly distilled TMSOTf (96 mmol, 17.4 mL) was added via syringe over the course of 15 minutes and the resulting clear solution was allowed to stir for 24 h at room temperature to generate a clear solution of $FSb(OTf)_2$. The solution was concentrated to a volume of *ca.* 40 mL and cooled to 0 °C by applying an ice bath. Under rapid stirring, freshly distilled PMe_3 (106 mmol, 10.8 mL) was slowly injected under the surface of the solution (to minimize evaporative loss of PMe_3) with a syringe over a span of 5 minutes. A yellow-coloured suspension was obtained by the end of addition, which was allowed to stir for a further 0.5 h at 0 °C.* The reaction mixture was filtered *via* the attached Schlenk frit to yield a fine, yellow-coloured powder and a yellow-orange filtrate in the receiving flask. The frit was separated from

*During stirring, occasionally, the suspension starts to turn dark orange. This is a sign that the concentration of free PMe_3 (reducing agent) in the mixture is too high, resulting in the formation of elemental antimony. It is vital to immediately apply slight vacuum to remove some of the volatile phosphine.

the receiving flask and the yellow powder was dried under vacuum. The filtrate was concentrated to *ca.* 50 % of its original volume and cooled to 0 °C. Thus, a second crop of yellow-coloured powder, which was isolated by carefully removing the dark orange supernatant via a filter-tipped cannula, was obtained. The combined crops were dried under vacuum. A ^{31}P NMR assay showed the presence of a small amount of [**5.12(Me)**][OTf] which was removed washing with cold MeCN (15 mL). After drying for 16 h under dynamic vacuum at room temperature, [**5.10(Me)**][OTf]$_4$ was obtained as a fine yellow powder. Yield: 13.87 g, (83 %); Melting Point: 116 °C dec.; Elemental Analysis (calcd./expt.): C (13.85/13.52) H (2.61/2.58); IR (cm^{-1}, CsI plates, Nujol mull): 514, 571, 634, 667, 674, 722, 756, 849, 953, 1019, 1154, 1231, 1296, 1376, 1455, 1547, 1594, 1716, 1784, 2341, 2357, 2725, 2917, 3411, 3617; ^{1}H NMR (CD_3CN, 300K, 500.1 MHz): 2.24 (*m*, 12H); ^{13}C{^{1}H} NMR (CD_3CN, 300 K, 126.6 MHz): 14.1 (*m*), 120.8 (*q*, $^1J_{CF}$ = 319 Hz, CF_3); ^{31}P NMR (CD_3CN, 300 K, 202.5.9 Hz): −24.5 (*s*); ^{19}F{^{1}H} NMR (CD_3CN, 339 K, 376.5 MHz): −79.0 (*s*, CF_3).

9.5.4 $[(Et_3P)_4Sb_4][OTf]_4$

A solution of $FSb(OTf)_2$ in 60 mL of MeCN was generated as described above using 8.8951 g (50 mmol) of SbF_3 and 18 mL (100 mmol) of TMSOTf. The solution was concentrated to a volume of *ca.* 45 mL and cooled to 0 °C by applying an ice bath. With rapid stirring, PEt_3 (105 mmol, 12.3 mL) was injected over 2 minutes. The resulting slightly yellow-coloured reaction mixture was stirred for an additional 15 minutes at 0 °C and then warmed to room temperature. Stirring was continued for 24 hours and the resulting clear, orange-coloured solution was placed under vacuum with stirring until the formation of large amount of yellow-coloured precipitate was observed. This yellow precipitate was separated by filtration (G3 frit) from the orange supernatant. The frit was removed from the receiving flask and the residue dried under vacuum. A second crop of product was optained by concentrating the dark orange-coloured filtrate and separating the mother liquor via a filter-tipped cannula to give a yellow-coloured precipitate. The combined crops were dried under vacuum to yield a very bright yellow-coloured powder (12.105 g). A ^{31}P NMR assay of the product indicated trace amounts of [**5.12(Et)**][OTf]. The product was recrystallized from a minimum amount of thoroughly dried MeCN and washed with fluorobenzene (2 x 25 mL) and Et_2O (2 x 25 mL). Application of dynamic vacuum over the course

of 16 hours at room temperature yielded analytical grade [**5.10(Et)**][OTf]$_4$ as a bright yellow-coloured powder. Yield: 9.505 g, (49 %); Melting Point: 161.2 °C dec.; Elemental Analysis (calcd./expt.): C (21.62/21.76) H (3.89/4.26); Raman (ranked intensities): 186.4 (5), 218.1 (7), 267.1 (16), 315.4 (10), 349.3 (9), 374.8 (15), 427.2 (17), 457.8 (18), 517.8 (22), 574.7 (12), 620.5 (13), 684.7 (24), 720.4 (24), 759.7 (8), 978.0 (14), 1030.0 (3), 1169.5 (23), 1185.0 (24), 1227.0 (11), 1289.9 (18), 1385.6 (20), 1412.7 (15), 1466.1 (10), 2252.2 (25), 2745.6 (19), 2760.3 (20), 2812.2 (21), 2880.8 (6), 2911.4 (1), 2944.6 (2), 2979.5 (4); ^{1}H NMR (CD_3CN, 300K, 400.1 MHz): 1.34 (*m*, 12H), 2.6 (*m*, 8H); $^{13}C\{^1H\}$ NMR (CD_3CN, 300 K, 100.6 MHz): 8.2 (*s*, CH3), 16.8 (*m*, CH2), 120.8 (*q*, $^1J_{CF}$ = 319 Hz, CF_3); ^{31}P NMR (CD_3CN, 300 K, 161.9 Hz): 8.8 (*s*); $^{19}F\{^1H\}$ NMR (CD_3CN, 300 K, 376.5 MHz): −79.1 (*s*, CF_3).

9.5.5 $[Et_3PPEt_3][OTf]_2$

Ph_3SbCl_2 (0.43 mmol, 0.183 g) and AgOTf (0.86 mmol, 0.222 g) were combined under the exclusion of light and 5 mL CH_2Cl_2 was added yielding which resulted in the formation of a white suspension. The reaction mixture was stirred for additional 60 minutes under the exclusion of light and then filtered to remove the formed AgCl. To the clear and colourless filtrate neat PEt_3 (0.86 mmol, 0.101 g) was dropwise added, which resulted in the formation of a white suspension. After stirring for 15 minutes the colourless precipitate was isolated by filtration and washed with CH_2Cl_2 (2 mL). After removing of all volatiles under dynamic vacuum [**5.11(Et)**][OTf]$_2$ was obtained as an analytically pure colourless powder. Yield: 0.212 g (46 %); Melting Point: 169-170 °C; Elemental Analysis (calcd./expt.): C (31.46/31.68) H (5.66/5.75); IR (ATR, 298 K, [cm^{-1}]): 210 (w), 228 (w), 248 (w), 347 (m), 421 (w), 516 (vs), 572 (s), 633 (vs), 698 (w), 734 (w), 755 (m), 780 (m), 877 (w), 961 (m), 1025 (vs), 1050 (w), 1149 (vs), 1217 (s), 1256 (s), 1306 (w), 1394 (w), 1465 (w), 2889 (vw), 2917 (w), 2954 (w), 2990 (vw); Raman (ranked intensities): 262.0 (9), 313.2 (7), 348.1 (4), 387.3 (20), 422.3 (21), 504.6 (15), 519.6 (18), 574.8 (10), 595.1 (21), 625.5 (8), 683.9 (23), 726.4 (22), 757.2 (5), 789.4 (24), 973.8 (17), 994.9 (16), 1030.3 (1), 1056.5 (14), 1162.8 (21), 1223.1 (12), 1273.0 (18), 1384.2 (18), 1400.1 (15), 1454.2 (13), 1469.3 (11), 2760.9 (19), 2889.1 (6), 2907.7 (3), 2920.9 (3) , 2957.6 (2), 2994.5 (6), 3004.0 (8); ^{1}H NMR (CD_3CN, 298 K, 500.3 MHz): 1.43 (*m*, 18H), 2.84 (*m*, 12H); $^{13}C\{^1H\}$ NMR (CD_3CN, 298 K, 125.8 MHz): 8.1 (*s*, CH3), 12.2 (*t*, $^1J_{CP}$ = 17 Hz, CH2), 125.1 (*q*, $^1J_{CF}$ = 321 Hz, CF_3);

$^{31}P\{^{1}H\}$ NMR (CD_3CN, 298 K, 202.5 MHz): 39.3 (*s*), $^{19}F\{^{1}H\}$ NMR (CD_3CN, 298 K, 282.5 MHz): −79.2 (*s*, CF_3). Crystals suitable for XRD were obtained as colourless blocks from a concentrated MeCN solution at −30°C and exhibited the same ^{31}P NMR chemical shift as the bulk material.

9.5.6 NMR data for $[Pr_3PPPr_3][OTf]_2$

The formation of this compounds in the reaction mixture was confirmed by an NMR assay of the reaction mixture containing PPr_3 and $Sb(OTf)_3$ in a 3:1 stoichiometry. The observed chemical shift shows an excellent match with reported NMR data. ^{1}H NMR (CD_2Cl_2, 298 K, 300 MHz): 2.72-2.60 (*m*, 12H), 1.82-1.65 (*m*, 12H), 1.11 (*tt*, $^{3}J_{HH}$ = 7 Hz, $^{4}J_{PH}$ = 1 Hz, 18H), ^{31}P NMR (CD_2Cl_2, 298 K, 146 MHz): 31.2 (*s*).

9.5.7 [(*dmpe*)SbF][OTf]$_2$

To a solution of $FSb(OTf)_2$ (3 mmol, 1.317 g) in MeCN (6 mL) was added a solution of *dmpe* (3 mmol, 0.450 g) in MeCN (2 mL) yielding a clear, pale yellow-coloured solution. The reaction mixture was allowed to stir for an additional 60 minutes after which a ^{31}P NMR assay showed complete consumption of *dmpe* (δ = −48.4 ppm) and the appearance of a broad *d* as the major phosphorus containing product. The reaction mixture was concentrated to 3 mL, filtered and placed in the freezer at −30°C. A fine white powder precipitated, which was isolated by decanting the mother liquor and identified as analytically pure [**5.13**][$OTf]_2$. Yield: 1.152 g (65 %); Melting point: 104 °C dec.; Elemental Analysis (calcd./expt.): C (16.31/16.13) H (2.74/2.71); IR (ATR, 298 K, [cm^{-1}]): 218 (m), 226 (m), 246 (w), 268 (vw), 276 (vw), 303 (vw), 321 (w), 350 (m), 440 (w), 514 (vs), 541 (s), 575 (m), 631 (vs), 728 (w), 761 (w), 773 (w), 796 (vw), 819 (vw), 852 (m), 876 (m), 911 (m), 927 (m), 942 (s), 960 (m), 1012 (vs), 1021 (vs), 1114 (w), 1154 (vs), 1184 (s), 1207 (vs), 1232 (vs), 1280 (s), 1293 (s), 1304 (m), 1415 (w), 1430 (vw), 2923 (vw), 2959 (vw), 3000 (vw); Raman (ranked intensities): 187.0 (4), 209.0 (8), 246.6 (11), 266.3 (14), 318.3 (5), 350.0 (3), 441.8 (19), 517.6 (17), 543.6 (11), 576.2 (12), 652.8 (10), 733.8 (13), 764.4 (6), 795.6 (19), 927.5 (18), 1025.2 (2), 1114.8 (19), 1167.3 (16), 1180.1 (15), 1196.0 (17), 1231.1 (11), 1305.1 (15), 1412.6 (10), 2816.4 (18), 2925.1 (1), 2957.9 (9), 2965.6 (9), 3000.0 (7), 3029.7 (15); ^{1}H NMR (CD_3CN, 298 K, 500.3 MHz): 1.86 (broad *d*, $^{2}J_{PH}$ = 12.4 Hz, 6H), 2.1

(broad *d*, $^{2}J_{\mathrm{PH}}$ = 12.9 Hz, 6H), 2.75 (broad *m*, 4H); ^{13}C{^{1}H} NMR (CD_3CN, 298 K, 125.8 MHz): 6.1 (*m*), 7.2 (*m*), 24.3 (*m*), 120.1 (*q*, $^{1}J_{\mathrm{CF}}$ = 320 Hz, CF_3); ^{31}P NMR (CD_3CN, 298 K, 202.5 MHz): 41.2 (broad *d*, $^{2}J_{\mathrm{PF}}$ = 39 Hz); ^{19}F{^{1}H} NMR (CD_3CN, 298 K, 282.5 MHz): −186.3 (broad *t*, $^{2}J_{\mathrm{PF}}$ = 41 Hz, SbF), −78.1 (*s*, CF_3). Fine, needle-like crystals suitable for XRD were obtained by diffusion of Et_2O vapour into a concentrated MeCN solution at −30°C and exhibited the same ^{31}P NMR chemical shift as the bulk material.

9.5.8 [(*nacnac*$^{(dipp)}$)(Me_3P)$_3Sb_4$][OTf]$_3$

Solid [**5.10(Me)**][OTf]$_4$ (0.50 mmol, 0.692 g) and [Li][*nacnac*$^{(}$*dipp*)] (1.10 mmol, 0.467 g) were combined in a Schlenk flask equipped with a Teflon stir bar. The flask was attached to a Schlenk line and freshly distilled MeCN (10 mL) was added at 0 °C under argon with rapid stirring to yield an orange-coloured suspension. The flask was placed under a mild dynamic vacuum to effect removal of the evolved PMe_3. After stirring for four hours, the orange suspension was filtered to obtain a red-coloured filtrate, which was stored at −30°C for 48 hours to yield a light brown-coloured precipitate. The precipitate was removed by filtration and washed with Et_2O (3 x 5 mL). After removal of all volatiles under dynamic vacuum, analytically pure [**5.15(Me)**][OTf]$_3$ was obtained as brown-coloured, powder. Yield: 0.412 g (52 %); Melting point: 164-165 °C, dec.; Elemental Analysis (calcd./expt.): The reactivity of the compound precluded the determination of satisfactory elemental Analysis; Raman (ranked intensities): 74.9 (2), 94.8 (3), 144.6 (1), 199.8 (5), 268.2 (17), 293.9 (22), 314.6 (20), 345.9 (12), 444.7 (28), 489.6 (27), 573.7 (26), 649.0 (13), 668.4 (14), 757.8 (9), 884.9 (23), 910.6 (29), 1025.9 (6), 1108.1 (18), 1163.5 (21), 1183.4 (10), 1213.1 (11), 1242.3 (16), 1312.1 (24), 1440.0 (19), 1464.0 (25), 1591.0 (7), 1645.4 (8), 2869.9 (30), 2912.9 (4), 3059.9 (15); ^{1}H NMR (CD_3CN, 298 K, 400.1 MHz): 1.08 (*d*, H11/12/14/15, $^{3}J_{\mathrm{HH}}$ = 4.6 Hz, 6H), 1.10 (*d*, H11/12/14/15, $^{3}J_{\mathrm{HH}}$ = 4.6 Hz, 6H), 1.26 (*d*, H11/12/14/15, $^{3}J_{\mathrm{HH}}$ = 6.82 Hz, 6H), 1.28 (*d*, H11/12/14/15, $^{3}J_{\mathrm{HH}}$ = 6.75 H, 6H), 1.99 (*d*, (PMe_3)1, $^{2}J_{\mathrm{PH}}$ = 13.5 Hz, 18H), 2.07 (*s*, H3, 6H), 2.27 (*d*, (PMe_3)2, $^{2}J_{\mathrm{PH}}$ = 14.39 Hz, 9H), 2.93 (*sept.*, H10, $^{3}J_{\mathrm{HH}}$ = 6.75 Hz, 4H), 6.20 (*s*, H1, ^{1}H), 7.14-7.27 (broad *m*, H6/7/8, 6H); ^{13}C{^{1}H} NMR (CD_3CN, 298 K, 100.6 MHz): 14.0 (*d*, 2 x (PMe_3)1, $^{1}J_{\mathrm{CP}}$ = 34 Hz), 14.1 (*d*, (PMe_3)2, $^{1}J_{\mathrm{CP}}$ = 35 Hz), 23.9 (C3), 24.0 (C11/12/14/15), 24.1 (C11/12/14/15), 24.4 (C11/12/14/15), 25.2 (C11/12/14/15), 29.0 (C10/13), 29.1 (C10/13), 57.0 (C1), 124.6

(C6/8), 121.9 (q, $^1J_{CF}$ = 320 Hz, CF_3) 124.9 (C6/8), 126.0 (C7), 137.6 (C5/9), 138.4 (C5/9), 174.6 (C2); ^{31}P $\{^1H\}$ NMR (CD_3CN, 300 K, 161.9 MHz): −33.6 (d, $(PMe_3)1$, 3JPP = 32 Hz, 2P), −26.6 (t, $(PMe_3)2$, 3JPP = 32 Hz, 1P); $^{19}F\{^1H\}$ NMR (CD_3CN, 298 K, 376.5 MHz): −79.1 (s, CF_3). Colourless block shaped crystals suitable for XRD were obtained upon recrystallization from a concentrated MeCN solution at −30°C and exhibited the same ^{31}P NMR chemical shifts as the bulk material.

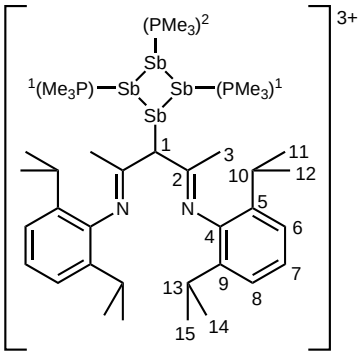

9.5.9 [(*nacnac*$^{(dipp)}$)Sb(OTf)$_2$]

Solid $Sb(OTf)_3$ (11 mmol, 6.259 g) and [Li][*nacnac*$^{(}$*dipp*)] (11 mmol, 4.671 g) were combined in a Schlenk flask equipped with a Teflon stir bar. The flask was attached to a Schlenk line and 35 mL fluorobenzene was added under argon yielding an orange-coloured suspension. Upon stirring for 24 hours a dark orange-coloured suspension was obtained which was filtered via a glass frit (G3) to remove LiOTf. The resulting filtrate was concentrated to 10 mL, cooled to 0 °C and Et_2O (10 mL) was added under argon to yield a yellow suspension upon stirring for 20 minutes. This suspension was filtered via a glass frit (G3) and the residue washed with pentane (10 mL). Removal of all volatiles under dynamic vacuum at room temperature yielded the product as an analytically pure yellow-coloured powder. Yield: 6.171 g (67 %); Melting point: 144-145 °C, dec.; Elemental Analysis (calcd./expt.): C (44.46/43.62) H (4.93/4.72) N (3.34/3.61); Raman (ranked intensities): 441.3 (7), 453.1 (6), 501.3 (15), 527.8 (9), 550.1 (2), 590.4 (14), 630.9 (17), 645.7 (14), 690.2 (19), 727.1 (21), 764.5 (5), 793.6 (23), 817.4 (21), 868.9 (24), 888.2 (10), 937.4 (26), 956.9 (22), 997.3 (6), 1031.9 (12), 1046.8, 1110.0 (12), 1165.9 (13), 1186.0 (4), 1244.2 (1), 1298.2 (11), 1320.5 (12), 1346.9

(17), 1371.2 (16), 1389.2 (17), 1442.7 (7), 1470.0 (9), 1530.6 (18), 1560.7 (20), 1590.7 (3), 2720.2 (28), 2766.3 (29), 2869.9 (25), 2913.6 (8), 2942.3 (7), 2968.9 (18), 2983.7 (26), 3031.6 (28), 3070.8 (27), 3170.8 (30); ^{1}H NMR (CD_2Cl_2, 300 K, 400.1 MHz): 1.21 (*d*, H8/9/11/12, $^{3}J_{HH}$ = 6.8 Hz, 6H), 1.28 (*d*, H8/9/11/12, $^{3}J_{HH}$ = 6.5 Hz, 6H), 1.35 (*d*, H8/9/11/12, $^{3}J_{HH}$ = 6.9 Hz, 6H), 1.37 (*d*, H8/9/11/12, $^{3}J_{HH}$ = 6.5 Hz, 6H), 2.16 (*s*, H15, 6H), 2.98 (*sept*, H7/10, $^{3}J_{HH}$ = 6.8 Hz, 2H), 3.36 (*sept.*, H7/10, $^{3}J_{HH}$ = 6.6 Hz, 2H), 5.91 (*s*, H13, ^{1}H), 7.36-7.38 (*m*, H3/5, 4H), 7.46-7.50 (*t*, H4, $^{3}J_{HH}$ = 7.8 Hz, 2H); ^{13}C{^{1}H} NMR (CD_2Cl_2, 100.6 MHz, 300 K): 24.4 (C15), 24.9 (C8/9/11/12), 25.5 (C8/9/11/12), 25.7 (C8/9/11/12), 25.4 (C8/9/11/12), 29.0 (C7/10), 29.3 (C7/10), 108.5 (C13), 119.0 (*q*, COTf1/OTf2, $^{1}J_{CF}$ = 319 Hz), 120.3 (*q*, COTf1/OTf2, $^{1}J_{CF}$ = 317 Hz), 126.3 (C3/5), 126.7 (C3/5), 130.9 (C4), 134.5 (C1), 145.2 (C2/6), 146.5 (C2/6), 170.5 (C14); ^{19}F{^{1}H} NMR (CD_3CN, 300 K, 376.5 MHz): −78.4 (*s*), −78.3 (*s*). Crystals suitable for XRD were grown from a saturated hexane solution at −30°C and exhibited the same ^{1}H NMR chemical shifts as the bulk material.

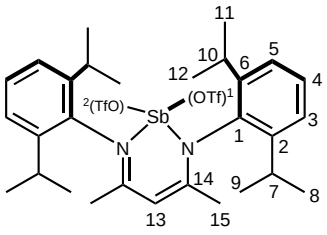

9.5.10 [Me$_3$PPCy$_2$][OTf]

To a bright yellow solution of [**5.10(Me)**][OTf]$_4$ (0.25 mmol, 0.347g) in MeCN (5 mL) was dropwise added neat Cy_2PCl (1 mmol, 0.233 g) yielding a black suspension. The reaction mixtures was stirred for a further 10 minutes and then allowed to settle yielding a clear and colourless supernatant above a fine black precipitate. A ^{31}P NMR assay of the supernatant showed quantitative consumption of [**5.10(Me)**][OTf]$_4$ and two coupled doublets indicating the formation of only one phosphorus containing species. The reaction mixture was filtered and all volatiles were removed under dynamic vacuum to yield a fine colourless powder. This powder was washed with Et_2O (2 x 1 mL) and dried to obtain analytically pure [Me_3PPCy_2][OTf]. Yield: 0.339 g (80 %); Melting point: 110-112 °C; Elemental Analysis (calcd./expt.): C (45.39/45.48)

H (7.62/8.14); IR (ATR, 298 K, [cm^{-1}]): 297 (w), 335 (vw), 516 (s), 572 (w), 635 (vs), 678 (vw), 756 (vw), 849 (w), 889 (w), 958 (s), 1029 (s), 1151 (s), 1224 (s), 1255 (vs), 1282 (m), 1306 (w), 1323 (w), 2918 (m), 1420 (vw), 1449 (w), 2845 (w), 3000 (vw); Raman (ranked intensities): 205.4 (13), 225.9 (6), 275.6 (11), 301.5 (13), 316.7 (11), 349.7 (11), 383.1 (13), 418.4 (10), 481.5 (10), 513.5 (13), 573.3 (12), 679.5 (6), 702.2 (9), 757.9 (10), 770.7 (13), 815.9 (8), 847.3 (10), 1002.1 (12), 1029.3 (3), 1081.1 (12), 1117.9 (13), 1173.5 (12), 1192.0 (13), 1226.0 (12), 1269.5 (10), 1297.8 (9), 1327.3 (12), 1344.5 (12), 1405.3 (11), 1421.8 (13), 1444.9 (4), 2710.8 (13), 2799.1 (13), 2848.3 (2), 2882.8 (5), 2919.7 (1), 2949.5 (6), 2974.1 (8), 3001.2 (7); ^{1}H NMR (CD_3CN, 298 K, 500.3 MHz): 1.22-1.54 (broad *m* 10H), 1.66-1.74 (broad *m*, 2H), 1.75-1.86 (broad overlapping *m*, H2/6, 6H), 1.92 (overlapping *dd* 9 x H7, $^{2}J_{PH}$ = 13.3 Hz, $^{3}J_{PH}$ = 2.7 Hz, 11H), 2.22 (broad *m*, H1/2, 2H); ^{13}C{^{1}H} NMR (CD_3CN, 298 K, 125.8 MHz): 12.3 (*dd*, C7, $^{1}J_{CP}$ = 43 Hz, $^{2}J_{CP}$ = 7 Hz), 26.6 (*s*, C4), 27.9 (*d*, C3/5, $^{3}J_{CP}$ = 10 Hz), 28.1 (*d*, C3/5, $^{3}J_{CP}$ = 10 Hz), 32.1 (*dd*, C1, $^{1}J_{CP}$ = 11 Hz, $^{2}J_{CP}$ = 8 Hz), 32.9-33.4 (overlapping *m*, C2/6); ^{31}P NMR (CD_3CN, 298 K, 202.5 MHz): −5.7 (broad *d*, $^{1}J_{PP}$ = 328 Hz), 11.9 (*d* of decets, $^{1}J_{PP}$ = 328 Hz, $^{2}J_{PH}$ = 13 Hz); ^{19}F{^{1}H} NMR (CD_3CN, 298 K, 282.5 MHz): −79.3 (*s*, CF_3).

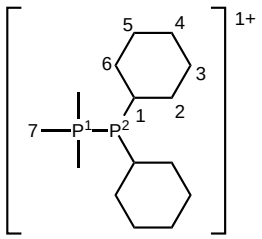

9.5.11 [Me_3PF][OTf]

To a solution of PMe_3 (1 mmol, 0.076 g) in CH_2Cl_2 (5 mL) was added solid XeF_2 (1 mmol, 0.169 g) in 10 equal portions over 10 minutes. Effervescence was observed with each addition and a clear colourless solution was obtained by the end of the addition. The reaction mixture was allowed to stir for 20 minutes and then neat TMSOTf was added to obtain a white suspension. The suspension was allowed to stir for 15 minutes and then hexane was added to aid settling of the precipitate. After settling for 20 minutes at −30°C, the clear and colourless supernatant was removed by pipette and

the precipitate was dried under vacuum to yield analytically pure [**5.12(Me)**][OTf] as a very fine white powder. Yield: 0.201 g (82 %); Melting Point: 180-182 °C; Elemental Analysis (calcd./expt.): C (19.68/19.36) H (3.72/3.78); IR (ATR): 218 (w), 254 (w), 297 (m), 318 (vw), 336 (m), 516 (s), 573 (m), 634 (vs), 668 (vw), 759 (w), 875 (s), 967 (vs), 994 (s), 1029 (s), 1153 (s), 1225 (vs), 1245 (s), 1306 (w), 1427 (w), 2918 (vw), 3000 (w), 3146 (vw); Raman (ranked intensities): 260.0 (9), 288.2 (11), 316.7 (6), 336.4 (8), 351.6 (5), 521.0 (12), 574.7 (8), 640.2 (4), 674.8 (3), 760.0 (5), 783.6 (11), 878.6 (11), 972.7 (12), 1032.9 (2), 1228.6 (8), 1260.5 (10), 1410.1 (7), 1422.7 (7), 1885.1, 2923.8 (1), 3003.8 (4); ^{1}H NMR (CD_3CN, 298 K, 300.3 MHz): 2.15 (*dd*, $^{1}J_{HP}$ = 14.5 Hz, $^{2}J_{HF}$ = 12.6 Hz, CH3); $^{13}C\{^{1}H\}$ NMR (CD_3CN, 298 K, 75.5 MHz) : 11.9 (*dd*, $^{1}J_{CP}$ = 62 Hz, 2JCF = 9 Hz), 120.5 (*q*, $^{1}J_{CF}$ = 322 Hz, CF_3); $^{31}P\{^{1}H\}$ (CD_3CN, 298 K, 146.2 MHz): 145 (*d*, $^{1}J_{PF}$ = 951 Hz), $^{19}F\{^{1}H\}$ NMR (CD_3CN, 298 K, 282.5 MHz): −137.9 (*d*, $^{1}J_{PF}$ = 951 Hz, PF), −79.4 (*s*, CF_3). Colourless crystals suitable for XRD were obtained from a concentrated MeCN solution at −30°C and exhibited the same ^{31}P NMR chemical shift as the bulk material.

9.5.12 $[(Ph_3P)_4Sb_6][OTf]_4$

$FSb(OTf)_2$ (5 mmol, 2.195 g) and PPh_3 (10 mmol, 2.620 g) were combined in 10 mL MeCN in a thick walled glass tube equipped with a stir bar. The tube was sealed and the reaction mixture was stirred for 20 minutes at room temperature to give a clear yellow solution. The tube was then placed in an oil bath (90 °C) for 1.5 hours to obtain a deep red solution. The solution was filtered, concentrated to half its volume, layered with 5 mL Et_2O and placed in the freezer at −30 ° C for 72 hours giving a fine orange powder. The supernatant was decanted and the powder was washed five times with *ca.* 3 mL MeCN and dried under vacuum to give the product as a fine orange powder. Yield: 328 mg, 17 %; Melting Point: 114 °C, dec.; Elemental Analysis (calcd./expt.): C (38.42/38.42) H (2.55/2.41) N (0.00/<0.3); IR (ATR, 298 K, [cm^{-1}]): 220 (m), 248 (w), 311 (vw), 347 (w), 451 (m), 480 (s), 502 (vs), 514 (vs), 571 (m), 634 (s), 689 (s), 713 (m), 746 (m), 749 (m), 996 (s), 998 (m), 1024 (s), 1093 (m), 1151 (s), 1199 (m), 1235 (m), 1240 (s), 1268 (w), 1436 (w), 1480 (w); ^{1}H NMR (CD_3CN, 298 K, 300.3 MHz): 7.01 (pseudo *dd*, 14 Hz, 8 Hz, 6H), 7.38-7.51 (overlapping *m*, 18H), 7.52-7.68 (overlapping *m*, 24H), 7.68-7.80 (overlapping *m*, 12H); $^{13}C\{^{1}H\}$ NMR (CD_3CN, 298 K, 75.5 MHz): 120.9 (*q*, $^{1}J_{CF}$ = 322 Hz), 120.6 (*d*, $^{1}J_{CP}$ = 58 Hz), 121.3 (*d*, $^{1}J_{CP}$ = 54

Hz), 122. 8 (d, $^{1}J_{CP}$ = 54 Hz), 130-131.3 (overlapping m), 133.3-135.5 (overlapping m); $^{31}P\{^{1}H\}$ (CD_3CN, 298 K, 121.5 MHz): -3.2 (d, 15 Hz, 1P), -2.1 (s, 2P), 7.62 (broad s, 1P); $^{19}F\{^{1}H\}$ NMR (CD_3CN, 298 K, 282.5 MHz): -78.0 (s); Crystallographic details for $[(Ph_3P)_4Sb_6][OTf]_4$•2MeCN•2EtCN: formula = $C_{87}H_{78}F_{12}N_4O_{12}P_4S_4Sb_6$, mw = 2582.15 $gmol^{-1}$, P-1, a = 13.3675(5) Å, b = 16.4283(7) Å, c = 23.2356(9) Å, α = 88.9560(10)°, β = 73.9250(10)°, γ = 81.9460(10)°, V = 4853.7(3) $Å^3$, T = 153.0 K, Z = 2, μ = 1.880, 76380 reflections measured, 28141 unique ($R_{int.}$ = 0.0243), R_1 = 0.0322, wR_2 = 0.0794 (all data).

Table 9.5.1. Crystallographic details for compounds in Chapter 5.

	[(*dmpe*)SbF][OTf]$_2$	[Et$_3$PPEt$_3$][OTf]$_2$	[Me$_3$PF][OTf]	[(Me$_3$P)$_4$Sb$_4$][OTf]$_4$•3MeCN	[(Et$_3$P)$_4$Sb$_4$][OTf]$_4$•MeCN	[(Me$_3$P)$_3$(*nacnac*)Sb$_4$][OTf]$_3$	[(*nacnac*)Sb(OTf)$_2$]
formula	$C_8H_{16}F_7O_6P_2S_2Sb$	$C_{14}H_{30}P_2S_2O_6F_6$	$C_4H_9O_3F_4PS$	$C_{22}H_{45}F_{12}N_3O_{12}P_4S_4Sb_4$	$C_{58}H_{123}F_{24}NO_{24}P_8S_8Sb_8$	$C_{43}H_{71}F_9N_3O_9P_3S_3Sb_4$	$C_{31}H_{41}F_6N_2O_6S_2Sb$
mw (g mol^{-1})	589.02	534.44	244.14	1387.62	3152.81	1621.12	837.53
space group	P21/n	P21/n	P21/m	P21	P21/c	P-1	P21/c
a /Å	14.5029(6)	13.4271(9)	10.2147(7)	12.8449(6)	23.986(16)	11.4789(3)	12.3127(4)
b /Å	8.9034(4)	11.8532(8)	8.6511(6)	21.7755(9)	21.830(14)	11.9874(3)	17.4575(6)
c /Å	14.9927(6)	15.7504(11)	11.0323(7)	18.1186(8)	22.193(15)	26.0864(7)	17.0214(6)
α/°						91.8200(10)	
β/°	97.2600(10)	110.9930(10)	94.5503(8)	96.9576(6)	106.570(14)	97.5640(10)	91.030(2)
γ/°						112.0740(10)	
V /Å^3	1920.41(14)	2340.4(3)	971.83(11)	5030.6(4)	11138(13)	3284.57(15)	3658.1(2)
Z	4	4	4	4	4	2	4
ρ/g cm^{-3}	2.037	1.517	1.669	1.995	1.880	1.639	1.521
radiation /Å	0.71073	0.71073	0.71073	0.71073	0.71073	0.71073	0.71073
T /K	173.15	173.15	173.15	173.15	173.15	173.15	
G.O.F	1.023	1.030	1.055	1.053	1.225	1.173	1.046
R_1 [I > 2σ(I)]	0.0214	0.0372	0.0303	0.0322	0.0560	0.0405	0.0271
wR_2 (all data)	0.0490	0.0961	0.0890	0.0787	0.1485	0.1174	0.0684

9.6 Compounds in Chapter 6

9.6.1 [(*triphos*−Cl)P][OTf]$_2$

AgOTf (2.00 mmol, 514 mg) and PCl_3 (1.00 mmol, 137 mg) were combined in *ca.* 5 mL CH_2Cl_2 in the dark and stirred for 10 minutes. A solution of *triphos* (1 mmol, 535 mg) in 5 mL CH_2Cl_2 was dropwise added over one minute and the reaction mixture was allowed to stir for 16 hours in the dark. The resulting white suspension was filtered on a G3 frit to remove insoluble AgCl. The filtrate was concentrated to *ca.* 5 mL, layered with pentane and placed in the freezer at −30 °C for one week to obtain white crystalline material. The mother liquor was decanted and the solids were washed twice with 3 mL hexane and dried to constant mass under dynamic vacuum. Yield = 766 mg, 85 %; Melting Point = 168-171 °C; Elemental Analysis (calcd./expt.): C (47.88/47.88) H (4.13/3.91) N(0.00/<0.30); IR (ATR, 298 K, [cm^{-1}]): 215 (s), 220 (w), 233 (m), 244 (m), 255 (m), 279 (w), 289 (w), 343 (w), 354 (w), 379 (w), 419 (vw), 440 (vw), 476 (w), 485 (w), 497 (w), 533 (m), 559 (m), 583 (s), 539 (vs), 703 (m), 797 (s), 825 (w), 1028 (vs), 1170 (s), 1227 (vs), 1237 (vs), 1281 (s), 1458 (w), 1616 (vw); ^{1}H NMR (CD_3CN, 298 K, 300 MHz): 2.66-2.85 (*m*, 2H), 2.95-3.16 (overlapping *m*, 3H), 3.19-3.52 (overlapping *m*, 3H), 7.44-7.63 (overlapping *m*, 8H), 7.63-7.85 (overlapping *m*, 14H), 7.85-7.95 (*m*, 3H); ^{13}C{^{1}H} NMR (CD_3CN, 298 K, 500 MHz): 23.1 (*dd*, $^1J_{CP}$ = 43 Hz, $^2J_{CP}$ = 10 Hz), 24.3 (*d*, $^1J_{CP}$ = 50 Hz), 27.4 (*dt*, $^1J_{CP}$ = 37 Hz, $^nJ_{CP}$ = 5 Hz), 29.7 (*dt*, $^1J_{CP}$ = 41 Hz, $^nJ_{CP}$ = 5 Hz), 122.2 (*q*, $^1J_{CF}$ = 323 Hz), 125.6 (*m*, C_{ipso}-P), 126.31 (*ddd*, $^1J_{CP}$ = 29 Hz, $^2J_{CP}$ = 9 Hz, $^3J_{CP}$ = 4 Hz), 126.9 (*ddd*, $^1J_{CP}$ = 31 Hz, $^2J_{CP}$ = 8 Hz, $^3J_{CP}$ = 4 Hz), 130.6-130.9 (*m*), 131.7 (*d*, 15 Hz), 133.1 (*dd*, 10.7 Hz, 4 Hz), 133.5 (*dd*, 11 Hz, 2 Hz), 133.6 (*dd*, 11 Hz, 2 Hz), 134.2 (*d*, 13 Hz), 134.7 (*dd*, 14 Hz, 3 Hz), 135.0 (*d*, 3 Hz), 138.4 (*s*); ^{31}P{^{1}H} NMR (CD_3CN, 298 K, 202.5 MHz): -249.9 (*dd*, $^1J_{PP}$ = 442 Hz), 66.7 (*dd*, $^1J_{PP}$ = 442 Hz, $^2J_{PP}$ = 15 Hz), 72.4 (*ddd*, $^1J_{PP}$ = 442 Hz, $^3J_{PP}$ = 67 Hz, $^2J_{PP}$ = 15 Hz, 75.5 (*d*, $^3J_{PP}$ = 68 Hz); ^{19}F{^{1}H} NMR (CD_3CN, 298 K, 282.5 MHz) = -78.5 (*s*).

9.6.2 [(*triphos*−Cl)As][OTf]$_2$

This compound was made using a similar procedure as [(*triphos*−Cl)P][OTf]$_2$, using $AsCl_3$ (1 mmol, 181 mg) instead of PCl_3 and stirring for 2 hours. The product was

obtained as a light yellow powder. Yield = 498 mg, 53 %; Melting Point = 99-101 °C dec.; IR (ATR, 298 K, [cm^{-1}]): 222 (m), 235 (w), 254 (w), 280 (w), 356 (m), 477 (s), 514 (s), 571 (m), 632 (vs), 686 (s), 733 (m), 996 (w), 1023 (vs), 1100 (s), 1150 (s), 1221 (s), 1235 (s), 1436 (m), 1482 (w); ^{1}H NMR (CD_3CN, 298 K, 500 MHz): 2.93-3.16 (*m*, 2H), 3.28-2.58 (*m*, 4H), 3.65-3.86 (*m*, 2H), 7.58 (*dt*, 7.9 Hz, 3.5 Hz, 2H), 7.62-7.69 (overlapping *m*, 4H), 7.69-7.77 (overlapping *m*, 3H), 7.77-7.83 (overlapping *m*, 4H), 7.84-8.04 (overlapping *m*, 9H); ^{13}C{^{1}H} (CD_3CN, 298 K, 125.81 MHz): 22.9 (*d*, $^{1}J_{CP}$ = 34 Hz), 23.7 (*d*, $^{1}J_{CP}$ = 48 Hz), 24.7 (*dd*, $^{1}J_{CP}$ = 33 Hz, $^{2}J_{CP}$ = 4 Hz), 28.6 (*dd*, $^{1}J_{CP}$ = 37 Hz, $^{2}J_{CP}$ = 4 Hz), 121.2 (*q*, $^{1}J_{CF}$ = 321 Hz), 123.2 (*dd*, J_{CP} = 61 Hz, J_{CP} = 2 Hz), 124.8 (*dd*, J_{CP} = 65 Hz, J_{CP} = 2 Hz), 130.0, 130.1, 130.2, 130.3, 130.3, 130.4, (overlapping *m*), 130.9 (*dd*, J_{CP} = 15 Hz, J_{CP} = 5 Hz), 132.4 (*d*, J_{CP} = 10 Hz), 132.8 (*d*, J_{CP} = 11 Hz), 133.0 (*d*, J_{CP} = 11 Hz), 133.3 (*dd*, J_{CP} = 13 Hz, J_{CP} = 3 Hz), 134.4 (*dt*, J_{CP} = 22 Hz, J_{CP} = 4 Hz), 137.5 (*s*); ^{31}P{^{1}H} NMR (CD_3CN, 298 K, 202.5 MHz): 56.6 (*s*), 62.4 (*d*, $^{3}J_{PP}$ = 64 Hz), 74.7 (*d*, $^{3}J_{PP}$ = 64 Hz); ^{19}F{^{1}H} NMR (CD_3CN, 298 K, 282.5 MHz) = -78.5 (*s*).

9.6.3 [(*triphos*)Sb][OTf]$_3$

Solid SbF_3 (1.00 mmol, 179 mg) was suspended in 5 mL MeCN and TMSOTf (3 mmol, 666.66 mg) was added as a neat liquid. A clear, pale yellow solution was obtained upon stirring for 16 hours and then all volatiles were removed to obtain a pale yellow powder. The powder was suspended in 2 mL CH_2Cl_2 and a solution of triphos (1 mmol, 535 mg) in CH_2Cl_2 (2 mL) was added to obtain a white suspension. To overcome the low solubility of the solids, 4 mL MeCN was added and after stirring for 1.5 h a clear, pale yellow solution was obtained. This solution was concentrated to half its volume, and allowed to settle overnight at −30 °C. The supernatant was decanted and the solids were washed twice with 2 mL Et_2O and dried to constant mass under vacuum. Yield: 1.012 g, 91 %; Melting Point: 112 °C, dec.; Elemental Analysis with half molecule of MeCN (calcd./expt.): C (40.50/40.28) H (3.35/3.03) N(0.62/0.61); IR (ATR, 298 K, [cm^{-1}]): 223 (m), 234 (w), 260 (w), 280 (w), 316 (m), 352 (m), 364 (w), 404 (w), 416 (w), 428 (w), 444 (w), 470 (s), 484 (s), 512 (vs), 573 (m), 629 (vs), 682 (s), 692 (w), 710 (s), 721 (m), 742 (s), 753 (w), 814 (m), 860 (m), 883 (w), 998 (vs), 1017 (vs), 1034 (w), 1094 (s), 1113 (m), 1154 (s), 1192 (vs), 1206 (vs), 1216 (vs), 1230 (s), 1290 (s), 1306 (m), 1343 (w), 1407 (w), 1438 (m), 1487 (w),

1575 (w); ^{1}H NMR (CD_3CN, 298 K, 300.27 MHz): 3.56 (broad *m*, 4H), 3.84 (broad *m*, 4H), 7.19 (pseudo *tt*, 8 Hz, 4H), 7.43 (pseudo *q*, 8 Hz, 4H), 7.49 (*t*, 8 Hz), 7.61 (*m*, 2 H), 7.64-7.68 (broad *t*, 8 Hz, 4H), 7.58 (broad *t*, 8 Hz, 3H), 7.83-7.90 (overlapping *m*, 2 H), 8.07 (broad *q*, 8 Hz, 4H), ^{13}C{^{1}H} (CD_3CN, 298 K, 125.81 MHz): 120.2 (*dt*, $^{1}J_{CP}$ = 59 Hz, $^{3}J_{CP}$ = 2 Hz), 121.1 (*d*, $^{1}J_{CP}$ = 51 Hz), 123.2 (*d*, $^{1}J_{CP}$ = 58 Hz), 130.9 (pseudo *d*, J_{CP} = 14 Hz), 131.6-131.9 (overlapping *m*), 133.5 (*t*, J_{CP} = 5 Hz), 134.7 (*t*, J_{CP} = 5 Hz), 135.0 (*d*, $^{n}J_{CP}$ = 10 Hz), 135.9 (*d*, J_{CP} = 34 Hz), 136.0 (*s*); ^{31}P NMR (CD_3CN, 298 K, 202.5 MHz, [ppm]): 31.1 (*s*, 2P), 53.4 (*s*, 1P). Crystals suitable for diffraction were obtained by slow evaporation of solvent from a concentrated MeCN solution and exhibited the same NMR resonances as the bulk material.

9.6.4 $[(tbbipy)_2P][OTf]_3$

To a rapidly stirred suspension of PCl_3 (5.00 mmol, 0.687 g) and AgOTf (15 mmol, 3.854 g) in 20 mL MeCN was added solid *tbbipy* (10.00 mmol, 2.684 g) in five portions to yield a yellow suspension. The suspension was allowed to stir for 2 hours and allowed to settle. The orange supernatant was separated via filtration and concentrated under dynamic vacuum to *ca.* 10 mL when a large amount of yellow precipitate appeared. The precipitate was allowed to settle over 48 hours at -30 °C and separated by decanting the light orange supernatant. The precipitate was washed with Et_2O (10 mL), filtered, and dried under dynamic vacuum for 8 hours to yield the product as a fine yellow powder. Yield: 3.560 g (70 %); Melting Point: 257 °C dec.; Elemental Analysis with one molecule of MeCN (calcd./expt.): C (46.59/46.70) H (4.96/5.28) N(6.63/6.34); IR (ATR, 298 K, [cm^{-1}]): 238 (w), 279 (vw), 298 (w), 315 (vw), 340 (vw), 418 (vw), 455 (m), 493 (m), 517 (s), 539 (w), 550 (w), 574 (s), 612 (w), 634 (vs), 697 (vw), 727 (w), 740 (w), 758 (w), 846 (s), 901 (m), 932 (m), 969 (w), 1025 (vs), 1071 (w), 1118 (w), 1163 (s), 1219 (s), 1232 (s), 1257 (s), 1293 (m), 1372 (w), 1385 (w), 1464 (w), 1483 (w), 1515 (w), 1543 (vw), 1592 (m), 1615 (m); ^{1}H NMR (CD_3CN, 298 K, 500 MHz, [ppm]): 1.53 (*s*, 2 × $C(CH_3)_3$, 18H), 1.60 (*s*, 2 × $C(CH_3)_3$, 18H), 8.04 (dt, 6.9 Hz, 1.7 Hz, 2H), 8.34 (*dd*, 6.3 Hz, 1.7 Hz, 2H), 8.64 (*dd*, 6.9 Hz, 2.3 Hz, 2H), 9.02 (*m*, 4H), 9.17 (*dd*, 6.3 Hz, 2.9 Hz, 2H); ^{13}C{^{1}H} (CD_3CN, 298 K, 125.81 MHz, [ppm]): 29.3 (*s*, $C(CH_3)_3$), 29.7 (*s*, $C(CH_3)_3$), 37.2 (*s*, $C(CH_3)_3$), 28.1 (*s*, $C(CH_3)_3$), 121.1 (*q*, CF_3, $^{1}J_{CF}$ = 321 Hz), 123.4 (*d*, J_{CP} = 6 Hz), 124.3 (*d*, J_{CP} = 4 Hz), 127.9 (*d*, J_{CP} = 3 Hz), 129.2 (*d*, J_{CP} = 5Hz), 142.7 (*d*, J_{CP} = 3 Hz), 143.5

(d, J_{CP} = 13 Hz), 146.3 (s), 147.0 (d, J_{CP} = 2 Hz), 174.0 (d, J_{CP} = 4 Hz), 178.2 (d, J_{CP} = 3 Hz); ^{31}P NMR (CD_3CN, 298 K, 202.5 MHz, [ppm]): 30.7 (s); $^{19}F\{^1H\}$ NMR (CD_3CN, 298 K, 282.5 Hz, [ppm]): -79.2 (s).

9.6.5 $[(tbbipy)_2As][OTf]_3$

AsCl3 (1 mmol, 181 mg) and AgOTf (3 mmol, 771 mg) were combined in 5 mL MeCN and stirred for 5 minutes. Solid *tbbipy* (2 mmol, 537 mg) was added in five small portions and the resulting white suspension was allowed to stir for 4 h and then filtered. The clear and colourless filtrate was concentrated to *ca.* 3 mL, layered with Et_2O and placed in the freezer at −30 °C for 16 hours to obtain white crystalline material. The supernatant was decanted and the solids were washed twice with 2 mL Et_2O. Removal of all volatiles under vacuum gave the product as a fine white powder. Yield = 677 mg, 64 %; Melting Point: 245 °C dec.; IR (ATR, 298 K, [cm^{-1}]): 210 (s), 219 (s), 236 (w), 251 (w), 292 (w), 330 (w), 350 (w), 368 (w), 414 (w), 483 (w), 516 (s), 545 (m), 573 (m), 602 (m), 634 (vs), 720 (w), 742 (w), 755 (w), 846 (m), 896 (m), 936 (w), 1017 (vs), 1071 (w), 1154 (s), 1210 (s), 1229 (s), 1252 (s), 1277 (s), 1370 (w), 1421 (m), 1484 (w), 1545 (w), 1614 (m); Elemental Analysis (calcd./expt.): C (44.24/43.91) H (4.57/4.86) N (5.29/5.26); ^{1}H NMR (CD_3CN, 298 K, 500 MHz, [ppm]): 1.52 (broad s, 18H), 7.68-8.71 (broad overlapping m, 3H), 2.32 (s, 2H), 8.98-9.76 (broad s, 1H); $^{13}C\{^1H\}$ (CD_3CN, 298 K, 125.81 MHz, [ppm]): 29.5 (s), 37.4 (s), 120.8 (q, $^1J_{CF}$ = 322 Hz), 123.9 (s), 127.9 (broad s), 146.6 (s), 147.2 (broad s), 173.6 (broad s); $^{19}F\{^1H\}$ NMR (CD_3CN, 298 K, 282.5 Hz, [ppm]): −79.3 (s). Crystals suitable for diffraction were obtained from a MeCN solution and exhibited the same NMR resonances as the bulk material.

9.6.6 $[(tbbipy)_2Sb][OTf]_3$

$Sb(OTf)_3$ (1 mmol, 569 mg) and *tbbipy* (2 mmol, 537 mg) were combined in 5 mL CH_2Cl_2 to obtain a clear and colourless solution which was stirred for 2 hours. Upon filtration, the colourless filtrate was concentrated to 2 mL under vacuum, layered with pentane, and placed at −30 °C for 72 hours to obtain a fine white powder. Yield: 857 mg, 77 %; Melting Point: 159-163 °C dec.; Elemental Analysis (calcd./expt.): C (42.32/41.41) H (4.46/4.09) N(5.06/5.03); IR (ATR, 298 K, [cm^{-1}]): 220 (vw),

Table 9.6.1. Crystallographic details for compounds in Chapter 6.

	[(*triphos*)Sb][OTf]$_3$•MeCN	[(*tbbipy*)$_2$As][OTf]$_3$•2.833MeCN	[(*tbbipy*)$_2$P][OTf]$_3$•MeCN
formula	$C_{39}H_{36}F_9N$ $O_9P_3S_3Sb$	$C_{44.67}H_{56.50}$ AsF9N$_{6.83}$O9S3	$C_{41}H_{51}O_9F_9PS_3$
mw (g mol^{-1})	1144.53	1175.23	1056.01
space group	Pbcn	P$\bar{1}$	*P*
a /Å	12.2821(2)	15.0217(6)	11.6535(4)
b /Å	16.7365(3)	18.4434(8)	14.5562(5)
c /Å	44.4675(8)	31.1243(13)	14.5880(5)
α/°		93.9090(6)	88.2712(4)
β/°		101.3392(6)	80.7875(4)
γ/°		99.3536(6)	88.0482(4)
V /Å^3	9140.7(3)	8297.5(6)	2440.47(15)
Z	8	6	2
ρ/g cm^{-3}	1.663	1.411	1.437
radiation /Å	1.54178	0.71073	0.71073
T /K	173.15	173.15	173.15
G.O.F	1.191	1.039	1.047
R_1 [I > 2σ(I)]	0.0415	0.0451	0.0502
wR_2 (all data)	0.0956	0.1208	0.1398

228 (vw), 236 (vw), 259 (vw), 316 (w), 350 (w), 396 (w), 515 (s), 548 (w), 573 (m), 605 (m), 634 (vs), 719 (w), 849 (m), 898 (m), 1015 (vs), 1153 (s), 1199 (s), 1223 (s), 1262 (s), 1369 (w), 1416 (m), 1483 (w), 1546 (w), 1614 (m);^{1}H NMR (CD_2Cl_2, 298 K, 300.15 MHz): 1.47 (broad *s*, 18H), 7.91 (broad *s*, 4H), 8.52 (broad *s*, 4H), 8.75 (broad (*s*), 4H); ^{13}C{^{1}H} (CD_2Cl_2, 298 K, 75.5 MHz, [ppm]): 29.8 (*s*), 36.6 (*s*), 119.9 (*q*, CF_3, $^1J_{CF}$ = 323 Hz), 122.3 (broad *s*), 126.8 (broad *s*), 147.0 (broad *s*), 148.4 (*s*), 170.8 (broad *s*); ^{19}F{^{1}H} NMR (CD_2Cl_2, 298 K, 282.5 Hz, [ppm]): −78.9 (*s*).

Bibliography

[1] Haaland, A. (1989) *Angewandte Chemie International Edition in English* **28(8)**, 992–1007.

[2] Himmel, D., Krossing, I., and Schnepf, A. (2014) *Angewandte Chemie International Edition* **53(2)**, 370–374.

[3] Frenking, G. (2014) *Angewandte Chemie International Edition* **53(24)**, 6040–6046.

[4] Himmel, D., Krossing, I., and Schnepf, A. (2014) *Angewandte Chemie International Edition* **53(24)**, 6047–6048.

[5] Köppe, R. and Schnöckel, H. (2015) *Chemical Science* **6**, 1199–1205.

[6] Zhang, X. M. and Bordwell, F. G. (1994) *Journal of the American Chemical Society* **116(3)**, 968–972.

[7] Weigand, J. J., Riegel, S. D., Burford, N., and Decken, A. (2007) *Journal of the American Chemical Society* **129(25)**, 7969–7976.

[8] Power, P. P. (2010) *Nature* **463**, 171–177.

[9] Dunn, N. L., Ha, M., and Radosevich, A. T. (2012) *Journal of the American Chemical Society* **134(28)**, 11330–11333.

[10] Less, R. J., Melen, R. L., and Wright, D. S. (2012) *Royal Society of Chemistry Advances* **2**, 2191–2199.

[11] Penafiel, J., Maron, L., and Harder, S. (2015) *Angewandte Chemie International Edition* **54**, 201–206.

[12] Kühl, O. (2008) Phosphorus-31 NMR Spectroscopy, Springer-Verlag Berlin Heidelberg, .

[13] Whitmire, K. H. Bismuth: Inorganic Chemistry John Wiley & Sons, Ltd (2011).

[14] Weston, R. E. (1954) *Journal of the American Chemical Society* **76(10)**, 2645–2648.

[15] Swalen, J. D. and Ibers, J. A. (1962) *The Journal of Chemical Physics* **36(7)**, 1914–1918.

[16] Haynes, W. (2012) CRC Handbook of Chemistry and Physics, 93rd Edition, CRC Handbook of Chemistry and Physics.Taylor & Francis, .

[17] Kaupp, M. Chemical Bonding of Main-Group Elements pp. 1–24 Wiley-VCH Verlag GmbH & Co. KGaA (2014).

[18] Burt, J., Levason, W., and Reid, G. (2014) *Coordination Chemistry Reviews* **260(0)**, 65–115.

[19] Robertson, A. P. M., Gray, P. A., and Burford, N. (2014) *Angewandte Chemie International Edition* **53(24)**, 6050–6069.

[20] Higelin, A., Sachs, U., Keller, S., and Krossing, I. (2012) *Chemistry A European Journal* **18(32)**, 10029–10034.

[21] Shapiro, I. R., Jenkins, D. M., Thomas, J. C., Day, M. W., and Peters, J. C. (2001) *Chemical Communications* pp. 2152–2153.

[22] Chitnis, S. S., Carpenter, Y.-Y., Burford, N., McDonald, R., and Ferguson, M. J. (2013) *Angewandte Chemie International Edition* **52(18)**, 4863–4866.

[23] Bissinger, P., Braunschweig, H., Kraft, K., and Kupfer, T. (2011) *Angewandte Chemie International Edition* **50(20)**, 4704–4707.

[24] Curran, D. P., Boussonnière, A., Geib, S. J., and Lacôte, E. (2012) *Angewandte Chemie International Edition* **51(7)**, 1602–1605.

[25] Kinjo, R., Donnadieu, B., Celik, M. A., Frenking, G., and Bertrand, G. (2011) *Science* **333(6042)**, 610–613.

[26] Zhu, H., Chai, J., Stasch, A., Roesky, H. W., Blunck, T., Vidovic, D., Magull, J., Schmidt, H.-G., and Noltemeyer, M. (2004) *European Journal of Inorganic Chemistry* **2004(20)**, 4046–4051.

[27] Nakai, H., Tang, Y., Gantzel, P., and Meyer, K. (2003) *Chemical Communications* pp. 24–25.

[28] Holzmann, N., Dange, D., Jones, C., and Frenking, G. (2013) *Angewandte Chemie International Edition* **52(10)**, 3004–3008.

[29] duMont, W.-W. and Ruthe, F. (1999) *Coordination Chemistry Reviews* **189(1)**, 101 – 133.

[30] Barnes, N. A., Godfrey, S. M., Khan, R. Z., Pierce, A., and Pritchard, R. G. (2012) *Polyhedron* **35(1)**, 31–46.

[31] Núñez, R., Farràs, P., Teixidor, F., Viñas, C., Sillanpää, R., and Kivekäs, R. (2006) *Angewandte Chemie International Edition* **45(8)**, 1270–1272.

[32] Hendrickson, J. B. and Schwartzman, S. M. (1975) *Tetrahedron Letters* **16(4)**, 277–280.

[33] Kilah, N. L., Petrie, S., Stranger, R., Wielandt, J. W., Willis, A. C., and Wild, S. B. (2007) *Organometallics* **26(25)**, 6106–6113.

[34] Burford, N., Herbert, D., Ragogna, P., McDonald, R., and Ferguson, M. (2004) *Journal of the American Chemical Society* **126(51)**, 17067–17073.

[35] Schmidpeter, A., Lochschmidt, S., and Sheldrick, W. S. (1982) *Angewandte Chemie International Edition in English* **21(1)**, 63–64.

[36] Chitnis, S. S., Burford, N., McDonald, R., and Ferguson, M. J. (2014) *Inorganic Chemistry* **53(10)**, 5359–5372.

[37] Wang, Y. and Robinson, G. H. (2011) *Inorganic Chemistry* **50(24)**, 12326–12337.

[38] Kretschmer, R., Ruiz, D. A., Moore, C. E., Rheingold, A. L., and Bertrand, G. (2014) *Angewandte Chemie International Edition* **53(31)**, 8176–8179.

[39] Aprile, A., Corbo, R., Vin Tan, K., Wilson, D. J. D., and Dutton, J. L. (2014) *Dalton Transactions* **43**, 764–768.

[40] Bamford, K. L., Robertson, A. P., Jenkins, H. A., Patrick, B. O., and Burford, N. (2015) *Canadian Journal of Chemistry* **93(0)**, 1–5.

[41] Beattie, I. R., Ozin, G. A., and Blayden, H. E. (1969) *Journal of the Chemical Society A* pp. 2535–2536.

[42] MacDonald, E., Doyle, L., Chitnis, S. S., Werner-Zwanziger, U., Burford, N., and Decken, A. (2012) *Chemical Communications* **48**, 7922–7924.

[43] Klein, S., Tonner, R., and Frenking, G. (2010) *Chemistry A European Journal* **16(33)**, 10160–10170.

[44] Beckmann, J., Bolsinger, J., Duthie, A., Finke, P., Lork, E., Lüdtke, C., Mallow, O., and Mebs, S. (2012) *Inorganic Chemistry* **51(22)**, 12395–12406.

[45] Boyle, P. D., Cross, W. I., Godfrey, S. M., McAuliffe, C. A., Pritchard, R. G., Sarwar, S., and Sheffield, J. M. (2000) *Angewandte Chemie* **112(10)**, 1866–1868.

[46] Barnes, N. A., Godfrey, S. M., Halton, R. T. A., Mushtaq, I., Pritchard, R. G., and Sarwar, S. (2006) *Dalton Transactions* pp. 1517–1523.

[47] Taouss, C. and Jones, P. G. (2011) *Dalton Transactions* **40**, 11687–11689.

[48] Dutton, J. L. and Ragogna, P. J. (2009) *Inorganic Chemistry* **48(4)**, 1722–1730.

[49] Dube, J. W., Hänninen, M. M., Dutton, J. L., Tuononen, H. M., and Ragogna, P. J. (2012) *Inorganic Chemistry* **51(16)**, 8897–8903.

[50] Núñez, R., Teixidor, F., Kivekäs, R., Sillanpää, R., and Viñas, C. (2008) *Dalton Transactions* pp. 1471–1480.

[51] Burford, N., Cameron, T. S., Ragogna, P. J., Ocando-Mavarez, E., Gee, M., McDonald, R., and Wasylishen, R. E. (2001) *Journal of the American Chemical Society* **123(32)**, 7947–7948.

[52] Carpenter, Y.-y., Dyker, C. A., Burford, N., Lumsden, M. D., and Decken, A. (2008) *Journal of the American Chemical Society* **130(46)**, 15732–15741.

[53] Slattery, J. M. and Hussein, S. (2012) *Dalton Transactions* **41**, 1808–1815.

[54] Slattery, J. M., Fish, C., Green, M., Hooper, T. N., Jeffery, J. C., Kilby, R. J., Lynam, J. M., McGrady, J. E., Pantazis, D. A., Russell, C. A., and Willans, C. E. (2007) *Chemistry A European Journal* **13(24)**, 6967–6974.

[55] Abrams, M. B., Scott, B. L., and Baker, R. T. (2000) *Organometallics* **19(24)**, 4944–4956.

[56] Ellis, B. D., Ragogna, P. J., and Macdonald, C. L. B. (2004) *Inorganic Chemistry* **43(24)**, 7857–7867.

[57] Chitnis, S., Peters, B., Conrad, E., Burford, N., McDonald, R., and Ferguson, M. (2011) *Chemical Communications* **47**, 12331–12333.

[58] Chitnis, S. S., Peters, B., Conrad, E., Burford, N., McDonald, R., and Ferguson, M. J. (2011) *Chemical Communications* **47**, 12331–12333.

[59] Conrad, E., Burford, N., McDonald, R., and Ferguson, M. J. (2009) *Journal of the American Chemical Society* **131(46)**, 17000–17008.

[60] Burford, N., Dyker, C. A., and Decken, A. (2005) *Angewandte Chemie International Edition* **44(16)**, 2364–2367.

[61] Swarnakar, A. K., McDonald, S. M., Deutsch, K. C., Choi, P., Ferguson, M. J., McDonald, R., and Rivard, E. (2014) *Inorganic Chemistry* **53(16)**, 8662–8671.

[62] Breitsameter, F., Schrödel, H.-P., Schmidpeter, A., Nöth, H., and Rojas-Lima, S. (1999) *Zeitschrift für anorganische und allgemeine Chemie* **625(8)**, 1293–1300.

[63] Frenking, G., Tonner, R., Klein, S., Takagi, N., Shimizu, T., Krapp, A., Pandey, K. K., and Parameswaran, P. (2014) *Chem. Soc. Rev.* **43**, 5106–5139.

[64] Rutsch, P. and Huttner, G. (2002) *Zeitschrift für Naturforschung* **57B**, 25–42.

[65] Nguyen, T. A. N. and Frenking, G. (2012) *Chemistry A European Journal* **18(40)**, 12733–12748.

[66] Burford, N., Losier, P., Sereda, S. V., Cameron, T. S., and Wu, G. (1994) *Journal of the American Chemical Society* **116(14)**, 6474–6475.

[67] Holthausen, M. H., Feldmann, K.-O., Schulz, S., Hepp, A., and Weigand, J. J. (2012) *Inorganic Chemistry* **51(6)**, 3374–3387.

[68] Vogt, R., Jones, P. G., and Schmutzler, R. (1993) *Chemische Berichte* **126(6)**, 1271–1281.

[69] Dillon, K. B., Goeta, A. E., Howard, J. A. K., Monks, P. K., Shepherd, H. J., and Thompson, A. L. (2008) *Dalton Transactions* pp. 1144–1149.

[70] Dube, J. W., Macdonald, C. L. B., Ellis, B. D., and Ragogna, P. J. (2013) *Inorganic Chemistry* **52(19)**, 11438–11449.

[71] Surgenor, B. A., Chalmers, B. A., Athukorala Arachchige, K. S., Slawin, A. M. Z., Woollins, J. D., Bühl, M., and Kilian, P. (2014) *Inorganic Chemistry* **53(13)**, 6856–6866.

[72] Karsch, H. H., Keller, U., Gamper, S., and Müller, G. (1990) *Angewandte Chemie International Edition in English* **29(3)**, 295–296.

[73] Gau, D., Kato, T., Saffon-Merceron, N., Cossío, F. P., and Baceiredo, A. (2009) *Journal of the American Chemical Society* **131(25)**, 8762–8763.

[74] Gau, D., Rodriguez, R., Kato, T., Saffon-Merceron, N., deCózar, A., Cossío, F. P., and Baceiredo, A. (2011) *Angewandte Chemie International Edition* **50(5)**, 1092–1096.

[75] Rodriguez, R., Gau, D., Kato, T., Saffon-Merceron, N., De Cózar, A., Cossío, F. P., and Baceiredo, A. (2011) *Angewandte Chemie International Edition* **50(44)**, 10414–10416.

[76] Dyker, C. A., Burford, N., Lumsden, M. D., and Decken, A. (2006) *Journal of the American Chemical Society* **128(30)**, 9632–9633.

[77] Kölmel, C., Ochsenfeld, C., and Ahlrichs, R. (1992) *Theoretica Chimica Acta* **82(3-4)**, 271–284.

[78] Carpenter, Y.-y., Burford, N., Lumsden, Michael, D., and McDonald, R. (2011) *Inorganic Chemistry* **50(8)**, 3342–3353.

[79] Robertson, A. P. M., Burford, N., McDonald, R., and Ferguson, M. J. (2014) *Angewandte Chemie International Edition* **53(13)**, 3480–3483.

[80] Mundt, O., Riffel, H., Becker, G., and Simon, A. (1988) *Zeitschruft für Naturforschung Teil B* **43b**, 952–958.

[81] McAdam, A., Beagley, B., and Hewitt, T. G. (1970) *Transactions of the Faraday Society* **66**, 2732–2739.

[82] Gruber, M., Jones, P. G., and Schmutzler, R. (1990) *Chemische Berichte* **123(6)**, 1313–1317.

[83] Lee, J. D. and Goodacre, G. W. Feb 1971 *Acta Crystallographica Section B* **27(2)**, 302–307.

[84] Weigand, J. J., Burford, N., Mahnke, D., and Decken, A. (2007) *Inorganic Chemistry* **46(19)**, 7689–7691.

[85] Wickham-Jones, C. T., Moran, S., and Ellison, G. B. (1989) *The Journal of Chemical Physics* **90(2)**, 795–806.

[86] Scott, J. D., Causley, G. C., and Russell, B. R. (1973) *The Journal of Chemical Physics* **59(12)**, 6577–6586.

[87] Borisenko, K. B. and Rankin, D. W. H. (2002) *Journal of the Chemical Society, Dalton Transactions* , 3135–3141.

[88] Pietschnig, R. (2007) *Journal of Organometallic Chemistry* **692(16)**, 3363 – 3369.

[89] Wolstenholme, D. J., Weigand, J. J., Davidson, R. J., Pearson, J. K., and Cameron, T. S. (2008) *The Journal of Physical Chemistry A* **112(15)**, 3424–3431.

[90] Maaliki, C., Lepetit, C., Duhayon, C., Canac, Y., and Chauvin, R. (2012) *Chemistry A European Journal* **18(50)**, 16153–16160.

[91] Dyker, C. A. and Burford, N. (2008) *Chemistry An Asian Journal* **3(1)**, 28–36.

[92] Kapustinskii, A. F. (1956) *Q. Rev. Chem. Soc.* **10**, 283–294.

[93] Glasser, L. and Jenkins, H. D. B. (2011) *Journal of Chemical & Engineering Data* **56(4)**, 874–880.

[94] Gutowski, K. E., Holbrey, J. D., Rogers, R. D., and Dixon, D. A. (2005) *The Journal of Physical Chemistry B* **109(49)**, 23196–23208.

[95] Shi, Q., Tan, Z.-C., Di, Y.-Y., Tong, B., Li, Y.-S., and Wang, S.-X. (2007) *Journal of Chemical & Engineering Data* **52(3)**, 941–947.

[96] Pan, X., Wang, X., Zhao, Y., Sui, Y., and Wang, X. (2014) *Journal of the American Chemical Society* **136(28)**, 9834–9837.

[97] Sasaki, S., Sutoh, K., Murakami, F., and Yoshifuji, M. (2002) *Journal of the American Chemical Society* **124(50)**, 14830–14831.

[98] Ménard, G., Hatnean, J. A., Cowley, H. J., Lough, A. J., Rawson, J. M., and Stephan, D. W. (2013) *Journal of the American Chemical Society* **135(17)**, 6446–6449.

[99] Blount, J. F., Maryanoff, C. A., and Mislow, K. (1975) *Tetrahedron Letters* **16(11)**, 913 – 916.

[100] Nenajdenko, V. G., Shevchenko, N. E., Balenkova, E. S., and Alabugin, I. V. (2003) *Chemical Reviews* **103(1)**, 229–282.

[101] Nikitin, E., Romakhin, A., Zagumennov, V., and Babkin, Y. (1997) *Electrochimica Acta* **42(1314)**, 2217 – 2224 Electrochemistry in Organic Synthesis.

[102] Menschutkin, N. (1890) *Zeitschrift für Physikalische Chemie* **5**, 589 – 590.

[103] Reed, R., Réau, R., Dahan, F., and Bertrand, G. (1993) *Angewandte Chemie International Edition in English* **32(3)**, 399–401.

[104] Seidel, W. (1964) *Zeitschrift für anorganische und allgemeine Chemie* **330(3-4)**, 141–150.

[105] Spangenberg, S. F. and Sisler, H. H. (1969) *Inorganic Chemistry* **8(4)**, 1006–1010.

[106] Summers, J. C. and Sisler, H. H. (1970) *Inorganic Chemistry* **9(4)**, 862–869.

[107] Boon, J. A., Byers, H. L., Dillon, K. B., Goeta, A. E., and Longbottom, D. A. (2000) *Heteroatom Chemistry* **11(3)**, 226–231.

[108] Dillon, K. B. and Monks, P. K. (2007) *Dalton Transactions* pp. 1420–1424.

[109] Coffer, P. K. and Dillon, K. B. (2013) *Coordination Chemistry Reviews* **257(56)**, 910 – 923 Recent Developments in Main Group Chemistry.

[110] Knackstedt, D. (2011) Investigations of Phosphenium Insertion into P-P Bonds, Dalhousie University, Halifax, .

[111] Bondi, A. (1964) *The Journal of Physical Chemistry* **68(3)**, 441–451.

[112] Long, L. H. and Sackman, J. F. (1957) *Transactions of the Faraday Society* **53**, 1606–1611.

[113] Burg, A. B. and Slota, P. J. (1958) *Journal of the American Chemical Society* **80(5)**, 1107–1109.

[114] Pervova, Y., Korobov, M., and Sidorov, L. (1992) *Zhurnal Fizicheskoi Khimii* **66(5)**, 1199–1204.

[115] Jonas, V., Frenking, G., and Reetz, M. T. (1994) *Journal of the American Chemical Society* **116(19)**, 8741–8753.

[116] Durig, J. R. and DiYorio, J. S. (1969) *Inorganic Chemistry* **8(12)**, 2796–2802.

[117] Johnston, D. H. and Shriver, D. F. (1993) *Inorganic Chemistry* **32(6)**, 1045–1047.

[118] Huang, W., Frech, R., and Wheeler, R. A. (1994) *The Journal of Physical Chemistry* **98(1)**, 100–110.

[119] Miles, M., Doyle, G., Cooney, R., and Tobias, R. (1969) *Spectrochimica Acta Part A: Molecular Spectroscopy* **25(9)**, 1515 – 1526.

[120] (1977) *Journal of Crystal and Molecular Structure* **7**, 295 – 306.

[121] McKean, D. C., McQuillan, G. P., Murphy, W. F., and Zerbetto, F. (1990) *The Journal of Physical Chemistry* **94(12)**, 4820–4831.

[122] Clegg, W., Elsegood, M. R. J., Norman, N. C., and Pickett, N. L. (1994) *Journal of the Chemical Society, Dalton Transactions* pp. 1753–1757.

[123] Clegg, W., Elsegood, M. R. J., Graham, V., Norman, N. C., Pickett, N. L., and Tavakkoli, K. (1994) *Journal of the Chemical Society, Dalton Transactions* pp. 1743–1751.

[124] Genge, A. R. J., Hill, N. J., Levason, W., and Reid, G. (2001) *Journal of the Chemical Society, Dalton Transactions* pp. 1007–1012.

[125] Streuli, C. A. (1960) *Analytical Chemistry* **32(8)**, 985–987.

[126] Wilson, D. J. D., Couchman, S. A., and Dutton, J. L. (2012) *Inorganic Chemistry* **51(14)**, 7657–7668.

[127] Cordero, B., Gomez, V., Platero-Prats, A. E., Reves, M., Echeverria, J., Cremades, E., Barragan, F., and Alvarez, S. (2008) *Dalton Transactions* pp. 2832–2838.

[128] Wielandt, J. W., Kilah, N. L., Willis, A. C., and Wild, S. B. (2006) *Chemical Communications* pp. 3679–3680.

[129] Feng, W.-J., Shu, Z., Ma, X.-J., and Jin, Z.-M. Sep 2007 *Acta Crystallographica Section E* **63(9)**, m2411.

[130] Ghoulili, A., Chaari, N., and Zouari, F. (2010) *X-ray Structure Analysis Online* **26**, 21–22.

[131] Haiges, R., Vij, A., Boatz, J. A., Schneider, S., Schroer, T., Gerken, M., and Christe, K. O. (2004) *Chemistry A European Journal* **10(2)**, 508–517.

[132] Benjamin, S. L., Burt, J., Levason, W., Reid, G., and Webster, M. (2012) *Journal of Fluorine Chemistry* **135(0)**, 108 – 113.

[133] Merritt, L. L. and Schroeder, E. Oct 1956 *Acta Crystallographica* **9(10)**, 801–804.

[134] Edwards, A. J. and Sills, R. J. C. (1971) *Journal of the Chemical Society A* pp. 942–945.

[135] Holz, K. and Mattes, R. (1989) *Zeitschrift für anorganische und allgemeine Chemie* **578(1)**, 133–142.

[136] Mattes, R. and Holz, K. (1983) *Angewandte Chemie International Edition in English* **22(11)**, 872–873.

[137] Palmer, R. A. and Piper, T. S. (1966) *Inorganic Chemistry* **5(5)**, 864–878.

[138] Broomhead, J. A., Young, C. G., and Hood, P. (2007) Tris(2,2-Bipyridine)Ruthenium(II) Dichloride Hexahydrate, John Wiley & Sons, Inc., .

[139] Molnár, J., Kolonits, M., and Hargittai, M. (1997) *Journal of Molecular Structure* **413414(0)**, 441 – 446 Structural Chemistry.

[140] Edwards, A. J. (1970) *Journal of the Chemical Society A* pp. 2751–2753.

[141] Lindqvist, I. and Niggli, A. (1956) *Journal of Inorganic and Nuclear Chemistry* **2(56)**, 345 – 347.

[142] Sidiropoulos, A., Osborne, B., Simonov, A. N., Dange, D., Bond, A. M., Stasch, A., and Jones, C. (2014) *Dalton Transactions* **43**, 14858–14864.

[143] Ollevier, T. (2013) *Org. Biomol. Chem.* **11**, 2740–2755.

[144] Raț, C. I., Silvestru, C., and Breunig, H. J. (2013) *Coordination Chemistry Reviews* **257(5-6)**, 818–879 Recent Developments in Main Group Chemistry.

[145] Nema, M. G., Breunig, H. J., Soran, A., and Silvestru, C. (2012) *Journal of Organometallic Chemistry* **705(0)**, 23–29.

[146] Silvestru, C., Breunig, H. J., and Althaus, H. (1999) *Chemical Reviews* **99(11)**, 3277–3328.

[147] Woodhouse, M. E., Lewis, F. D., and Marks, T. J. (1982) *Journal of the American Chemical Society* **104(21)**, 5586–5594.

[148] Clegg, W., John Errington, R., Fisher, G. A., Green, M. E., Hockless, D. C. R., and Norman, N. C. (1991) *Chemische Berichte* **124(11)**, 2457–2459.

[149] Clegg, W., Errington, R. J., Flynn, R. J., Green, M. E., Hockless, D. C. R.,

Norman, N. C., Gibson, V. C., and Tavakkoli, K. (1992) *Journal of the Chemical Society, Dalton Transactions* pp. 1753–1754.

[150] Willey, G. R., Daly, L. T., and Drew, M. G. B. (1996) *Journal of the Chemical Society, Dalton Transactions* pp. 1063–1067.

[151] Beckmann, J., Bolsinger, J., Duthie, A., Finke, P., Lork, E., Lüdtke, C., Mallow, O., and Mebs, S. (2012) *Inorganic Chemistry* **51(22)**, 12395–12406.

[152] Mazières, S., Le Roux, C., Peyronneau, M., Gornitzka, H., and Roques, N. (2004) *European Journal of Inorganic Chemistry* **2004(14)**, 2823–2826.

[153] Louër, M., Le Roux, C., and Dubac, J. (1997) *Chemistry of Materials* **9(12)**, 3012–3016.

[154] Malmros, G. (1970) *Acta Chemica Scandinavica* **24**, 384–396.

[155] Hanna, T. A., Keitany, G., Ibarra, C., Sommer, R. D., and Rheingold, A. L. (2001) *Polyhedron* **20(19)**, 2451–2455.

[156] Rogers, R. D., Bond, A. H., Aguinaga, S., and Reyes, A. (1992) *Journal of the American Chemical Society* **114(8)**, 2967–2977.

[157] Carmalt, C. J., Clegg, W., Elsegood, M. R. J., Errington, R. J., Havelock, J., Lightfoot, P., Norman, N. C., and Scott, A. J. (1996) *Inorganic Chemistry* **35(12)**, 3709–3712.

[158] Schultz, G., Kolonits, M., and Hargittai, M. (1999) *Structural Chemistry* **10(4)**, 321–325.

[159] Clegg, W., Errington, R. J., Fisher, G. A., Hockless, D. C. R., Norman, N. C., Orpen, A. G., and Stratford, S. E. (1992) *Journal of the Chemical Society, Dalton Transactions* pp. 1967–1974.

[160] Schafer, M., Frenzen, G., Neumuller, B., and Dehnicke, K. (1992) *Angewandte Chemie International Edition in English* **31(3)**, 334–335.

[161] Strobele, M. and Meyer, H.-J. (2009) *Zeitschrift fur anorganische und allgemeine Chemie* **635(11)**, 1517–1519.

[162] Petuškova, J., Patil, M., Holle, S., Lehmann, C. W., Thiel, W., and Alcarazo, M. (2011) *Journal of the American Chemical Society* **133(51)**, 20758–20760.

[163] Carreras, J., Patil, M., Thiel, W., and Alcarazo, M. (2012) *Journal of the American Chemical Society* **134(40)**, 16753–16758.

[164] Coffer, P. K., Deng, R. M. K., Dillon, K. B., Fox, M. A., and Olivey, R. J. (2012) *Inorganic Chemistry* **51(18)**, 9799–9808.

[165] Levason, W. and Reid, G. (2006) *Coordination Chemistry Reviews* **250(1920)**, 2565 – 2594.

[166] Champness, N. R. and Levason, W. (1994) *Coordination Chemistry Reviews* **133(0)**, 115 – 217.

[167] Braunschweig, H., Cogswell, P., and Schwab, K. (2011) *Coordination Chemistry Reviews* **255(12)**, 101 – 117.

[168] Lin, T.-P., Ke, I.-S., and Gabbaï, F. P. (2012) *Angewandte Chemie International Edition* **51(20)**, 4985–4988.

[169] Tschersich, C., Limberg, C., Roggan, S., Herwig, C., Ernsting, N., Kovalenko, S., and Mebs, S. (2012) *Angewandte Chemie International Edition* **51(20)**, 4989–4992.

[170] Fernández, E. J., Laguna, A., López-deLuzuriaga, J. M., Monge, M., Nema, M., Olmos, M. E., Pérez, J., and Silvestru, C. (2007) *Chemical Communications* pp. 571–573.

[171] Berning, D. E., Noll, B. C., and DuBois, D. L. (1999) *Journal of the American Chemical Society* **121(49)**, 11432–11447.

[172] Alcock, N. W., Ravindran, M., and Willey, G. R. (1989) *Journal of the Chemical Society, Chemical Communications* pp. 1063–1065.

[173] D. Kushch, N., A. Dyachenko, O., V. Gritsenko, V., Cassoux, P., Faulmann, C., Kobayashi, A., and Kobayashi, H. (1998) *Journal of the Chemical Society, Dalton Transactions* pp. 683–688.

[174] Breunig, H. J., Denker, M., Schulz, R. E., and Lork, E. (1998) *Zeitschrift für anorganische und allgemeine Chemie* **624(1)**, 81–84.

[175] Chivers, T. and Manners, I. Inorganic rings and polymers of the p-block elements: from fundamentals to applications RSC Publications (2009).

[176] He, G., Shynkaruk, O., Lui, M. W., and Rivard, E. (2014) *Chemical Reviews* **114(16)**, 7815–7880.

[177] Brownridge, S., Krossing, I., Passmore, J., Jenkins, H., and Roobottom, H. (2000) *Coordination Chemistry Reviews* **197(1)**, 397 – 481.

[178] Inoue, S., Ichinohe, M., Yamaguchi, T., and Sekiguchi, A. (2008) *Organometallics* **27(23)**, 6056–6058.

[179] Ichinohe, M., Igarashi, M., Sanuki, K., and Sekiguchi, A. (2005) *Journal of the American Chemical Society* **127(28)**, 9978–9979.

[180] Sekiguchi, A., Tsukamoto, M., and Ichinohe, M. (1997) *Science* **275(5296)**, 60–61.

[181] Breunig, H. and Raţ, C. (2013) Catenated compounds from group 15 In Jan Reedijk Kenneth Poeppelmeier, (ed.), Comprehensive Inorganic Chemistry {II}, pp. 151 – 178 Elsevier Amsterdam second edition.

[182] Althaus, H., J. Breunig, H., and Lork, E. (1999) *Chemical Communications* pp. 1971–1972.

[183] Breunig, H. J., Denker, M., and Lork, E. (1996) *Angewandte Chemie International Edition in English* **35(9)**, 1005–1006.

[184] Hering, C., Lehmann, M., Schulz, A., and Villinger, A. (2012) *Inorganic Chemistry* **51(15)**, 8212–8224.

[185] Minkwitz, R. and Hirsch, C. (1999) *Zeitschrift für anorganische und allgemeine Chemie* **625(10)**, 1674–1682.

[186] Conrad, E., Burford, N., Werner-Zwanziger, U., McDonald, R., and Ferguson, M. J. (2010) *Chemical Communications* **46**, 2465–2467.

[187] Lindsjö, M., Fischer, A., and Kloo, L. (2004) *Angewandte Chemie International Edition* **43(19)**, 2540–2543.

[188] Carpenter, Y. (2010) Investigations Into the Reactivity and Structure of Phosphinophosphonium Cations and Related Species, Dalhousie University, Halifax:Canada, .

[189] Marcoux, D. and Charette, A. B. (2008) *The Journal of Organic Chemistry* **73(2)**, 590–593.

[190] Goodson, F. E., Wallow, T. I., and Novak, B. M. (1997) *Journal of the American Chemical Society* **119(51)**, 12441–12453.

[191] Bellachioma, G., Cardaci, G., Macchioni, A., Venturi, C., and Zuccaccia, C. (2006) *Journal of Organometallic Chemistry* **691(18)**, 3881 – 3888.

[192] Filippou, A. C., Fischer, E. O., and Alt, H. G. (1988) *Journal of Organometallic Chemistry* **344(2)**, 215 – 225.

[193] Takaoka, A., Mendiratta, A., and Peters, J. C. (2009) *Organometallics* **28(13)**, 3744–3753.

[194] Bedford, R. B., Betham, M., Butts, C. P., Coles, S. J., Cutajar, M., Gelbrich, T., Hursthouse, M. B., Scully, P. N., and Wimperis, S. (2007) *Dalton Transactions* pp. 459–466.

[195] Avis, M. W., Vrieze, K., Ernsting, J. M., Elsevier, C. J., Veldman, N., Spek, A. L., Katti, K. V., and Barnes, C. L. (1996) *Organometallics* **15(9)**, 2376–2392.

[196] Acosta-Ramirez, A., Flores-Alamo, M., Jones, W. D., and Garcia, J. J. (2008) *Organometallics* **27(8)**, 1834–1840.

[197] Morita, D. K., Stille, J. K., and Norton, J. R. (1995) *Journal of the American Chemical Society* **117(33)**, 8576–8581.

[198] Siddique, R. M. and Winfield, J. M. (1989) *Canadian Journal of Chemistry* **67(11)**, 1780–1784.

[199] Fryzuk, M. D. (1992) *Canadian Journal of Chemistry* **70(12)**, 2839–2845.

[200] Liang, L.-C. (2006) *Coordination Chemistry Reviews* **250(910)**, 1152 – 1177 Recent Developments in Organometallic Chemistry: 2006.

[201] Man, P. P. Quadrupole Couplings in Nuclear Magnetic Resonance, General John Wiley & Sons, Ltd (2006).

[202] Roering, A. J., Davidson, J. J., MacMillan, S. N., Tanski, J. M., and Waterman, R. (2008) *Dalton Transactions* pp. 4488–4498.

[203] Waterman, R. and Tilley, T. D. (2006) *Angewandte Chemie International Edition* **45(18)**, 2926–2929.

[204] Lipkowski, J., Fonari, M. S., Kravtsov, V. C., Simonov, Y. A., Ganin, E. V., and Gelmboldt, V. O. (1996) *Journal of Chemical Crystallography* **26(12)**, 823–833.

[205] Becker, I., Windhaus, M., and Mattes, R. (1994) *Zeitschruft für Naturforschung Teil B* **49b**, 870–876.

[206] Schafer, M., Pebler, J., Borgsen, B., Weller, F., and Dehnicke, K. (1990) *Zeitschruft für Naturforschung Teil B* **45b**, 1243–1250.

[207] Fonari, M. S., Ganin, E. V., Gelmboldt, V. O., Lipkowski, J., Kotlyar, S. A., and Kamalov, G. L. May 2006 *Acta Crystallographica Section E* **62(5)**, m1021–m1023.

[208] Levason, W., Light, M. E., Maheshwari, S., Reid, G., and Zhang, W. (2011) *Dalton Transactions* **40**, 5291–5297.

[209] Yow, H. and Bartell, L. (1973) *Journal of Molecular Structure* **15(2)**, 209 – 215.

[210] Bernhardt, T. M., Stegemann, B., Kaiser, B., and Rademann, K. (2003) *Angewandte Chemie International Edition* **42(2)**, 199–202.

[211] Wang, X., Kunc, K., Loa, I., Schwarz, U., and Syassen, K. Oct 2006 *Phys. Rev. B* **74**, 134305.

[212] Kornath, A. J., Kaufmann, A., and Cappellacci, S. (2009) *Journal of Molecular Spectroscopy* **255(2)**, 189 – 193.

[213] M J. (1981) *Surface Science* **106(13)**, 18 – 26.

[214] Schwarzmaier, C., Sierka, M., and Scheer, M. (2013) *Angewandte Chemie International Edition* **52(3)**, 858–861.

[215] Hendrickson, J. B. and Schwartzman, S. M. (1975) *Tetrahedron Letters* **16(4)**, 277 – 280.

[216] Burford, N., Ragogna, P. J., McDonald, R., and Ferguson, M. J. (2003) *Journal of the American Chemical Society* **125(47)**, 14404–14410.

[217] Weigand, J. J., Burford, N., Decken, A., and Schulz, A. (2007) *European Journal of Inorganic Chemistry* **2007(31)**, 4868–4872.

[218] Bourget-Merle, L., Lappert, M. F., and Severn, J. R. (2002) *Chemical Reviews* **102(9)**, 3031–3066.

[219] Lesikar, L. A. and Richards, A. F. (2006) *Journal of Organometallic Chemistry* **691(20)**, 4250 – 4256.

[220] Balázs, G., Breunig, H. J., Lork, E., and Mason, S. (2003) *Organometallics* **22(3)**, 576–585.

[221] Balázs, G., Breunig, H. J., and Lork, E. (2003) *Zeitschrift für anorganische und allgemeine Chemie* **629(11)**, 1937–1942.

[222] Breunig, H. J., Rösler, R., and Lork, E. (1999) *Zeitschrift für anorganische und allgemeine Chemie* **625(10)**, 1619–1623.

[223] Westerhausen, M., Weinrich, S., and Mayer, P. (2003) *Zeitschrift für anorganische und allgemeine Chemie* **629(7-8)**, 1153–1156.

[224] Karsch, H. H. (1979) *Zeitschruft für Naturforschung Teil B* **34b**, 31–43.

[225] Burford, N., Losier, P., Phillips, A. D., Ragogna, P. J., and Cameron, T. S. (2003) *Inorganic Chemistry* **42(4)**, 1087–1091.

[226] Breunig, H. J., Ebert, K. H., Gülec, S., and Probst, J. (1995) *Chemische Berichte* **128(6)**, 599–603.

[227] Hanauer, T. and Korber, N. (2006) *Zeitschrift f'ur anorganische und allgemeine Chemie* **632(7)**, 1135–1140.

[228] Breunig, H. J., Ghesner, M. E., and Lork, E. (2005) *Zeitschrift f'ur anorganische und allgemeine Chemie* **631(5)**, 851–856.

[229] Doskocz, M., Malinowska, B., Młynarz, P., Lejczak, B., and Kafarski, P. (2010) *Tetrahedron Letters* **51(26)**, 3406 – 3411.

[230] Fey, N., Garland, M., Hopewell, J. P., McMullin, C. L., Mastroianni, S., Orpen, A. G., and Pringle, P. G. (2012) *Angewandte Chemie International Edition* **51(1)**, 118–122.

[231] Chitnis, S. S. and Burford, N. (2015) *Dalton Transactions.* **44**, 17–29.

[232] Wang, Y., Xie, Y., Abraham, M. Y., Gilliard, R. J., Wei, P., Schaefer, H. F., Schleyer, P. v. R., and Robinson, G. H. (2010) *Organometallics* **29(21)**, 4778–4780.

[233] Burford, N., Cameron, T. S., LeBlanc, D. J., Phillips, A. D., Concolino, T. E., Lam, K.-C., and Rheingold, A. L. (2000) *Journal of the American Chemical Society* **122(22)**, 5413–5414.

[234] Schwedtmann, K., Holthausen, M. H., Feldmann, K.-O., and Weigand, J. J. (2013) *Angewandte Chemie International Edition* **52(52)**, 14204–14208.

[235] Deng, R. M. K. and Dillon, K. B. (1984) *Journal of the Chemical Society, Dalton Transactions* pp. 1911–1916.

[236] Chitnis, S. S., Burford, N., and Ferguson, M. J. (2013) *Angewandte Chemie International Edition* **52(7)**, 2042–2045.

[237] Donath, M., Conrad, E., Jerabek, P., Frenking, G., Frhlich, R., Burford, N., and Weigand, J. J. (2012) *Angewandte Chemie International Edition* **51(12)**, 2964–2967.

[238] Tohm, A., Grelaud, G., Argouarch, G., Roisnel, T., Labouille, S., Carmichael, D., and Paul, F. (2013) *Angewandte Chemie International Edition* **52(16)**, 4445–4448.

[239] Frisch, M. J., Trucks, G. W., Schlegel, H. B., Scuseria, G. E., Robb, M. A., Cheeseman, J. R., Scalmani, G., Barone, V., Mennucci, B., Petersson, G. A., Nakatsuji, H., Caricato, M., Li, X., Hratchian, H. P., Izmaylov, A. F., Bloino, J., Zheng, G., Sonnenberg, J. L., Hada, M., Ehara, M., Toyota, K., Fukuda, R., Hasegawa, J., Ishida, M., Nakajima, T., Honda, Y., Kitao, O., Nakai, H., Vreven, T., Montgomery Jr., J. A., Peralta, J. E., Ogliaro, F., Bearpark, M. J., Heyd, J., Brothers, E. N., Kudin, K. N., Staroverov, V. N., Kobayashi, R., Normand, J., Raghavachari, K., Rendell, A. P., Burant, J. C., Iyengar, S. S., Tomasi, J., Cossi, M., Rega, N., Millam, N. J., Klene, M., Knox, J. E., Cross, J. B., Bakken, V.,

Adamo, C., Jaramillo, J., Gomperts, R., Stratmann, R. E., Yazyev, O., Austin, A. J., Cammi, R., Pomelli, C., Ochterski, J. W., Martin, R. L., Morokuma, K., Zakrzewski, V. G., Voth, G. A., Salvador, P., Dannenberg, J. J., Dapprich, S., Daniels, A. D., Farkas, d., Foresman, J. B., Ortiz, J. V., Cioslowski, J., and Fox, D. J. Gaussian 09 (2009).